A NUMERICAL STUDY OF CARDIAC ARRHYTHMIA AND DEFIBRILLATION VALIDATED BY EXPERIMENTS

A Dissertation
Presented to
The Academic Faculty

By

Yanyan Claire Ji

In Partial Fulfillment
of the Requirements for the Degree
Doctor of Philosophy in the
School of Physics

Georgia Institute of Technology

December 2018

A NUMERICAL STUDY OF CARDIAC ARRHYTHMIA AND DEFIBRILLATION VALIDATED BY EXPERIMENTS

Approved by:

Dr. Flavio Fenton, Advisor
School of Physics
Georgia Institute of Technology

Dr. Roman Grigoriev
School of Physics
Georgia Institute of Technology

Dr. Simon Sponberg
School of Physics
Georgia Institute of Technology

Dr. Elizabeth Cherry
School of Mathematical Sciences
Rochester Institute of Technology

Dr. Richard A Gray
Center for Devide and Radiological Health
Food and Drug Administration

Date Approved: December 11, 2018

”Great power comes with great responsibility”

I dedicate this thesis to my xiao xiong Anthony and everyone who supported me through the darkest days.

ACKNOWLEDGEMENTS

I thank my adviser Flavio Fenton, post-doc Abouzar Kaboudian from my lab and my thesis committee for their valuable input.

TABLE OF CONTENTS

LIST OF TABLES

LIST OF FIGURES

SUMMARY

Defibrillation is termination of arrhythmias by altering the transmembrane voltage through the delivery of electric shocks. It has been known for over 100 years that electrical shocks can both initiate and terminate fibrillations. Debates on the mechanisms behind defibrillations, however, have never ceased. More recent studies affirmed the contribution of inhomogeneities to depolarization in tissues during a defibrillation shock, stating the heterogeneities, such as vessels and bundles, which have different electrical conductivities than cardiac tissue, serve as virtual electrodes during an electric shock, creating excitations in tissues far away from the anode and cathode [1].

Low energy anti-fibrillation pacing (LEAP) has been suggested as an alternative method to traditional defibrillation method, which applies a strong electric pulse to terminate the arrhythmia. LEAP delivers multiple low amplitude electric shocks through field electrodes close to, or inside the tissue [2, 3]. The main goal of this thesis is to investigate the mechanism of LEAP and to suggest ways to improve it.

The main finding is that LEAP works by gradually synchronizing the electric activity to the same frequency through each additional shock. Because the tissue is synchronized to the same frequency, both depolarization and repolarization are synchronized and additional shocks will not restart arrhythmia. Modified Kuramoto phase diagrams showed that, during arrhythmias, phase is relatively evenly distributed, and once LEAP is applied, the phase over the domain is increasingly focused with each shock. To further quantify this synchronicity, we calculated the fraction of tissue excited (FTE) as a function of time. The FTE peak progressively increases to one with each pulse for successful LEAP and its derivative indicates how fast the tissue synchronizes. In contrast, during one-shock defibrillation, the FTE upstroke is much slower compared to LEAP, indicating that all cells are eventually excited but not at the same time. Therefore, the mechanism of one-shock defibrillation is not through synchronization but rather by resetting all cells to an excited state,

which requires the use of stronger electrical shocks, as some cells are less excitable than the others due to the repolarization gradients during fibrillation.

Numerical simulations in this study suggested some ways to improve LEAP by adjusting the pacing period as well as the shock timings. The success rate is higher when the pacing cycle length is close to the dominant period of the arrhythmia and when the first shock was applied at the downslope of the fraction of tissue excited (FTE) curve.

CHAPTER 1
MOTIVATION

1.1 Current situation

Cardiovascular disease is the leading cause of death in the United States, accounting for over 800,000 deaths in 2014 [4]. Atrial fibrillation (AF) is the most common sustained cardiac arrhythmia affecting between 2.7 to 6.1 million Americans with a projected increase to approximately 12.1 million by 2030 [4]. Complications associated with chronic AF include an increased risk for both thromboembolism and stroke due to clot formation [5] and was the underlying cause of death for 21,713 Americans in 2014 [4]. Ventricular fibrillation (VF) is the most commonly identified arrhythmia in cardiac arrest patients, mentioned on 353,427 death certificates in the US in 2014 [4]. It is crucial to identify the mechanisms of AF and VF and find more effective treatments.

Using computational simulations we can reduce the number of animal experiments, easily adjust parameters and shed light on problems that are difficult to experiment. Since in simulations it is much easier to control the environment to allow varying only a few important factors, they are particularly useful in offering insights into the mechanism of fibrillation and optimizing parameters for defibrillation.

1.2 Problem description

Standard defibrillation, which resets the heart with one strong shock, remains the mainstay treatment for symptomatic patients [6, 7]. However, acute electrical shocks are associated with severe side effects including electroporation, tissue damage, conduction disturbance, and pain in patients [8, 9, 10].

Recently, low energy anti-fibrillation pacing (LEAP) has been suggested as an alterna-

tive method. LEAP delivers multiple low amplitude electric shocks through field electrodes close to, or inside the tissue [2, 3]. The central mechanism behind defibrillation lays on the generations of virtual electrodes [11, 12, 13] or secondary excitation sources originating at heterogeneities in tissue such as trabecula, vessels, bundles, and abrupt changes in fiber direction. Excitations from virtual electrodes act as a multitude of intramural implanted defibrillation electrodes that allow to terminate arrhythmias inside the tissue. An otherwise entirely homogeneous heart will only be activated at boundaries by electric field and defibrillation would never be possible. For single defibrillation shocks to work, they have to provide enough energy to synchronize the whole domain in one single shock while for multiple shocks as in LEAP, we hypothesize that each low energy pulse gradually recruits more tissue to a given frequency until all tissue has been synchronized [2, 3].

To acquire trustworthy results from simulations for defibrillation studies, it requires using realistic cardiac models in both physiology and geometry.

At present, there are close to a hundred mathematical models describing the electrophysiology and dynamics of single cardiomyocyte. However, most of them focus only on ion channels and sarcoplasmic reticulum (SR) dynamics without including the equations to simulate the contraction. This is a considerable drawback since electrical activities and mechanics are closely related.

In addition, there exists a large discrepancy in the results between single cell and tissue simulations for recently developed and widely used models[14]. It is necessary to compare them with experiments and validate them.

1.3 Outline

In this thesis, I first give an introduction to normal and abnormal heart rhythm and review the theories of one major abnormal function: fibrillation (Chapter 2). Then I review equations and numerical schemes used in cardiac modeling for this thesis (Chapter 3). Next, in Chapter 4, we developed a systematic methodology to implement contraction into electro-

physiology models and validate their calcium and contraction behaviors comparing them with experiments. In Chapter 5, we compared the voltage and calcium alternans dynamics from a widely used calcium model with dual voltage-calcium optical mapping experiments. In Chapter 6, we combined experiments with simulations to discover the mechanism of low-energy anti-fibrillation. In Chapter 7, we used the WebGL-accelerated simulations to explore the influence of multiple factors on the defibrillation results. And we draw conclusions and suggestions for future studies in Chapter 8.

CHAPTER 2
INTRODUCTION

In this Chapter, I first give a brief description of normal and abnormal heart functions. Then I discuss the induction of alternans, and its relation to the calcium signaling in the heart. Then we review the current major theories on fibrillation and defibrillation.

2.1 Normal heart function

The human heart is composed of four chambers: the right/left atria (RA/LA), which collect deoxygenated/oxygenated blood from the body/lungs, and the right/left ventricle (RV/LV), which pump the blood to the lungs/body. Contraction of the heart is the driving force for the circulation system.

The contraction of the heart is coordinated by electric signals, represented by the transmembrane voltage, a voltage difference between the intracellular and extracellular space. The elevated transmembrane voltage is called an action potential (AP). In a single cell, the AP is created by ions entering and exiting the membrane and this process can be divided into five phases. Phase 4 is when AP is at its resting value (about $-84mV$). With some perturbations, the AP rises above the excitation threshold (about $-65mV$) which activates the Na^+ channel. Large amount of Na^+ ions flowing into the cell causes the AP to rise rapidly. This is the depolarization (upstroke), phase 0, of an AP. Then Na^+ channels close and K^+ channels open. K^+ ions flow out of the cell, causing the AP to drop. This is the peak, phase 1, of an AP. While K^+ ions keep flowing out, Ca^{2+} enters the cytoplasmic space, balancing K^+, causing a flat plateau of AP; this is phase 2. Then phase 3 starts when both Ca^{2+} and K^+ are exiting the intracellular space, causing AP to drop; this is the repolarization of AP. After that, AP drops back to resting state and the process goes back to phase 4 again (Fig. 2.1).

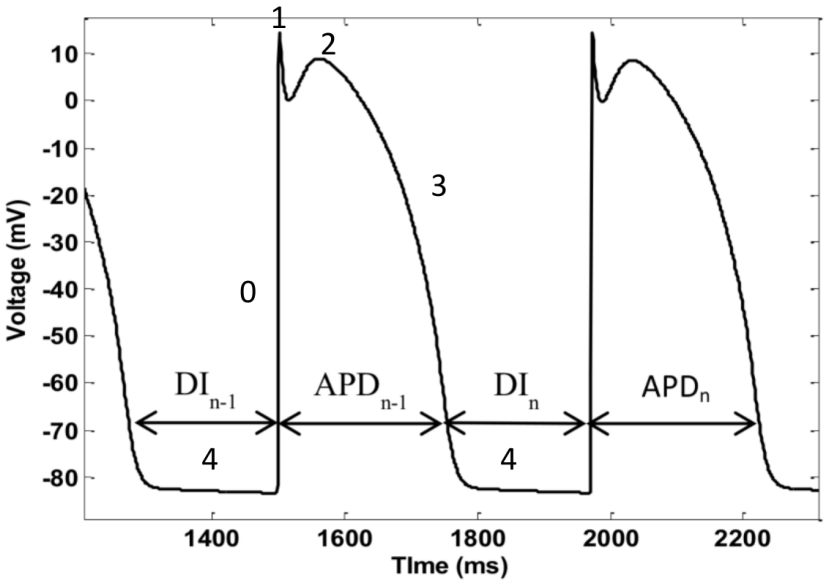

Figure 2.1: Action potential, action potential duration and diastolic interval

The duration of the action potential above a chosen threshold is called an action potential duration (APD), during which the ventricles are contracting, ejecting blood out of the heart. The interval between two adjacent APs (phase 4) is called a diastolic interval (DI), during which the ventricles are relaxed and blood refill the heart. The duration of a whole cycle is called a cycle length (CL=APD+DI, see Fig. 2.1). If APD is not adjusted at a faster heart rate, DI will be reduced, leading to insufficient refill of the blood. In reality, when the heart beats at a higher frequency, the ionic gates are not fully recovered, resulting in a reduced ionic current, and thus shortened both APD and DI, therefore adequate time is distributed between systoles and diastoles.

In normal hearts, action potentials are generated in a regular rhythm from only the sinoatrial (SA) node (a patch of natural pacemaker cells located on the upper part of the RA), meaning APD, DI and CL are kept relatively constant, and APs only propagate from the base (top) to the apex (bottom) of the heart through the atrioventricular (AV) node located at the bottom part of the RA.

Intracellular calcium handling plays an essential role in cardiac cell dynamics, includ-

ing ion homeostasis, intracellular signaling, and contraction.

Figure 2.2 shows the different compartments and ion channels in a cell involved in the intracellular calcium cycling during an action potential [15]. During the depolarization, L-type calcium channels are activated and the influx of calcium current into the narrow dyadic space induces a large calcium release from the Junctional Sarcoplasmic Reticulum (JSR) through clusters of Ryanodine Receptors (RyRs). Intracellular calcium concentration is thus greatly increased immediately following the depolarization of the transmembrane action potential. Some of these calcium ions bind to affinity sites on myofilament protein Troponin C therefore enable myosin heads, which contain cross-bridges, to attach to actin. Myosin heads walk on actin generating force, transforming chemical energy to mechanical energy resulting in cell contraction. Then during the repolarization of the action potential, calcium leaves the cytoplasmic compartment into either the Network Sarcoplasmic Reticulum (NSR) through the Ca-ATPase pump or out of the cell membrane though Na-Ca exchangers. The decreased intracellular calcium concentration causes calcium to detach from troponin C, inducing uncoupling of Myosin heads and actin, which ends the contraction process. Calcium is deeply involved in both the electrical activation and the tension generation.

2.2 Abnormal heart function

Abnormalities in the initiation or propagation of APs can cause pathologic heart rhythms, called **cardiac arrhythmias**. For example, action potentials can be fired from pulmonary veins other than the SA node [16]; and they can be propagated to ventricles through accessory pathways by the bundle of Kent rather than the AV node (the Wolff-Parkinson-White syndrome [17]).

Arrhythmias can be classified in different ways. One way is based on the heart rate. **Bradycardias** refer to heart rates slower than normal (below 60 beats per minute). It is usually caused by abnormally slow sinus rhythm, secondary slower pacemaker (such as the

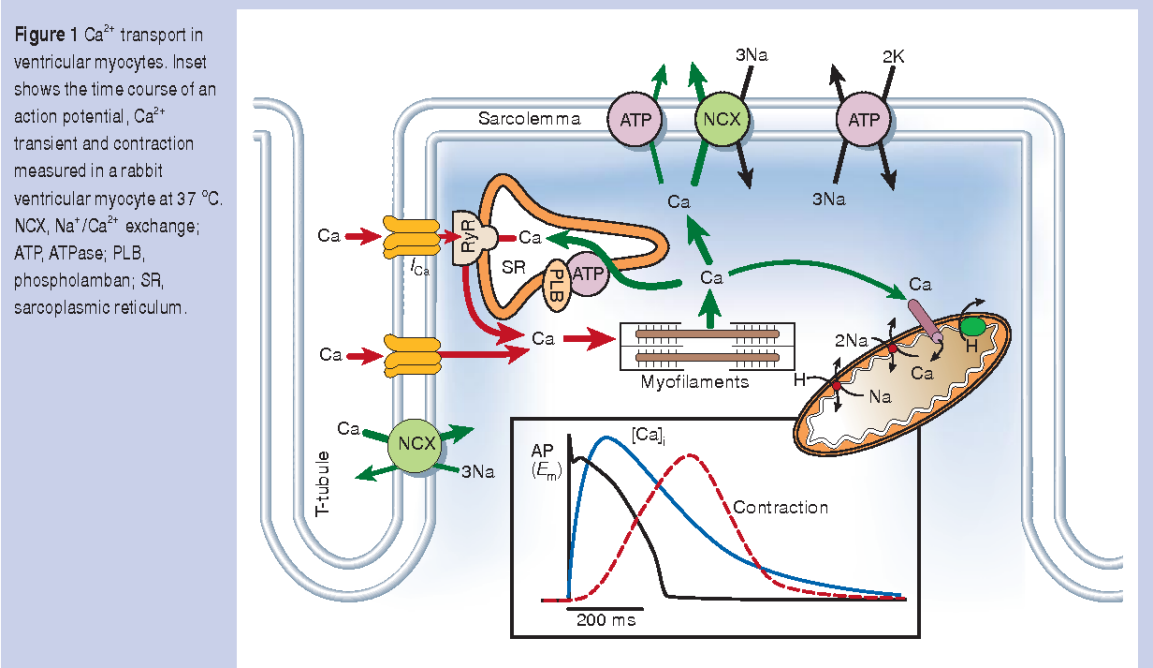

Figure 2.2: Intracellular calcium signaling. Figure from [15]

AV node) taking over or normal sinus rhythm being blocked. Patients with bradycardias are usually treated with drugs that can increase the heart rate or implanted pacemakers that can take over the heart to maintain a normal heart rate [18].

Tachycardias refer to the heart rates faster than normal (above 100 beats per minute). During ventricular tachycardia (VT), blood is not pumped efficiently by the heart, which will cause less oxygenated blood delivered to the body therefore patients will feel weakness and dizziness. Tachycardias can degenerated into **fibrillations** during which patients have completely disorganized rhythms and ventricular fibrillations (VF) can lead to sudden cardiac arrests when no blood is pumped [18].

Tachycardia and fibrillation can be induced in many ways. One way is through reentry. In a normal heart, action potentials propagate as an almost simultaneous wave. Under pathological conditions, however, an action potential might not complete its normal pathway but rather circles back upon itself, forming long-lasting self-sustained excitations, taking the form of a spiral wave (2D) or a scroll wave (3D). It has been shown that spiral waves in the heart could be responsible for deadly arrhythmias such as tachycardias and

fibrillations [19].

Alternans happens when the action potential duration varies from one beat to the next. This long-short alternation in duration and in some cases amplitude has been shown to arise from a period-doubling bifurcation [20, 21], originating at the cellular level [22]. In space, alternans can lead to complex spatiotemporal patterns along the epicardium and endocardium [23] and eventually to conduction block and fibrillation [24, 25].

2.3 Mechanism of alternans and reentry

During fast pacing, alternate patterns of APD in space can be classified as concordant alternans (CA), in which all the tissue responds with a long APD on one beat and with a short APD on the following beat with the sequence repeating, or discordant alternans (DA), in which one section of tissue responds with a long APD and another with a short APD on the same beat followed by the reverse on the next beat. Figure 2.3 shows an example of concordant and discordant alternans from a simulation. A 3cm long 1D cable is paced from the left end. The left panels show the APD over the cable for two consecutive beats and the right panel shows the action potential time sequence in two cells located at the left and right end of the cable. In Fig. 2.3a, the pacing cycle length is 300ms. The APD alternates between long and short for two consecutive beats and the whole cable follows the same pattern thus it is in concordant alternans. In Fig. 2.3b the pacing cycle length is 260ms. The APD profile along the cable for two consecutive even and odd beats intersect at a nodal point, indicating when part of the cable undergoes a long, the other part undergoes a short APD, which means the cable is in discordant alternans.

To date, two main mechanisms for the development of discordant alternans have been proposed, one driven by voltage and another by calcium [26, 27]. The first mechanism identified [21] was purely voltage-driven [20]; in space it is coupled through the dynamical interaction between the APD restitution curve and the conduction velocity (CV) restitution curve.

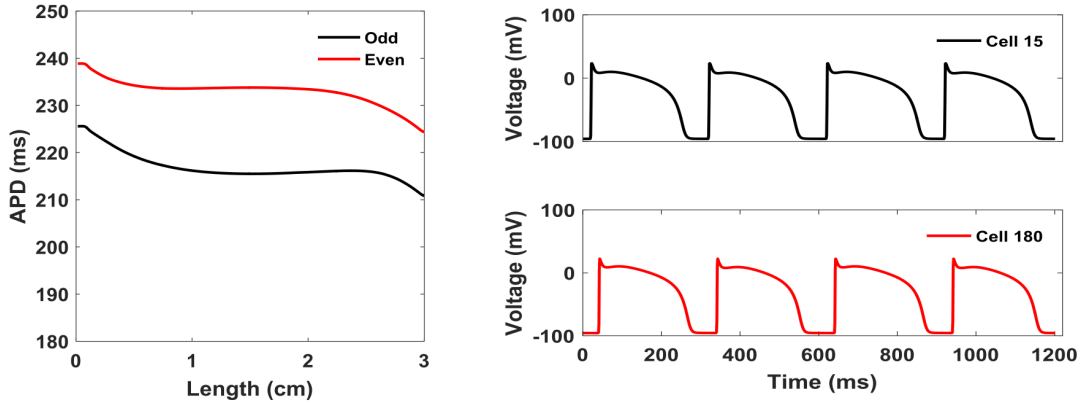

(a) Concordant alternans, T = 300ms

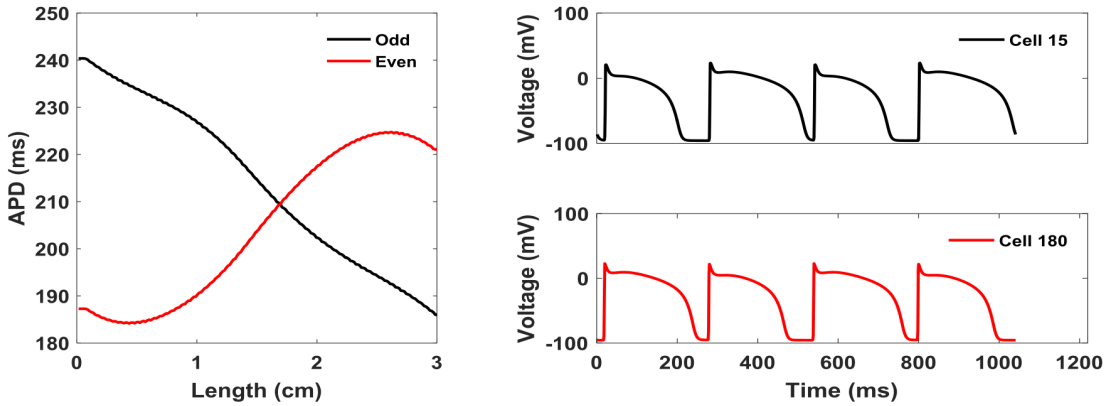

(b) Discordant alternans, T = 260ms

Figure 2.3: Demonstration of concordant and discordant alternans. Left panel: APD over a 3cm 1D cable. Right panel: action potential of two cells, one at the left side and one at the right side of the cable.

The APD-DI restitution curve is the relation between APD and its preceding DI. It shows $\mathrm{APD_n}$ as a function of $\mathrm{DI_{n-1}}$ (Fig. 2.1). The preceding DI will not only affect APD, but will also influence the propagating speed. The conduction velocity restitution curve shows the wave front conduction velocity (CV) at a given site as a function of the proceeding DI at that site.

When tissue is paced rapidly, diastolic intervals are shorter, causing slower CV near the stimulating site while CV increases downstream along wavefront propagation, causing a large spatial dispersion in the APD that can lead to DA [28, 29].

The other mechanism, calcium-driven, is considered more complex, with DA caused by instabilities in calcium cycling that in turn impacts APD through Ca - Vm coupling [30]. Ca - Vm coupling depends on a dynamical balance between the influx through the L-type calcium current (ICaL) and the outflux through the Na-Ca exchanger current (INCX) [31]. If the effect of INCX dominates, positive Ca - Vm coupling will occur, where a large calcium causes prolonged APD by an enhanced calcium outflux through INCX. Otherwise, when a large Ca transient reduces ICaL through increased calcium-dependent inactivation, APD will be shortened [30]. Ca instability is another multifactorial process. The key components are the fractional Ca release from the sarcoplasmic reticulum (SR), which refers to the relation between the Ca released from the SR and the SR calcium load, and the cytosolic Ca sequestration, which refers to the efficiency of Ca removal from the cytosol through the reuptake to the SR and the outflux through the Na-Ca exchanger [32]. In general, factors increasing fractional Ca release promote Ca alternans and factors increasing Ca sequestration reduce alternans [30]. Many studies have attributed cardiac alternans to disturbances of calcium signaling, with APD alternans considered a secondary effect [33, 34, 35, 36, 37].

There are two types of reentry. The anatomic reentry has a fixed anatomic pathway [38]. For example, in the Wolff-Parkinson-White syndrome mentioned before, an extra electrical pathway connects the atria and ventricles, allowing electrical impulses to bypass the AV

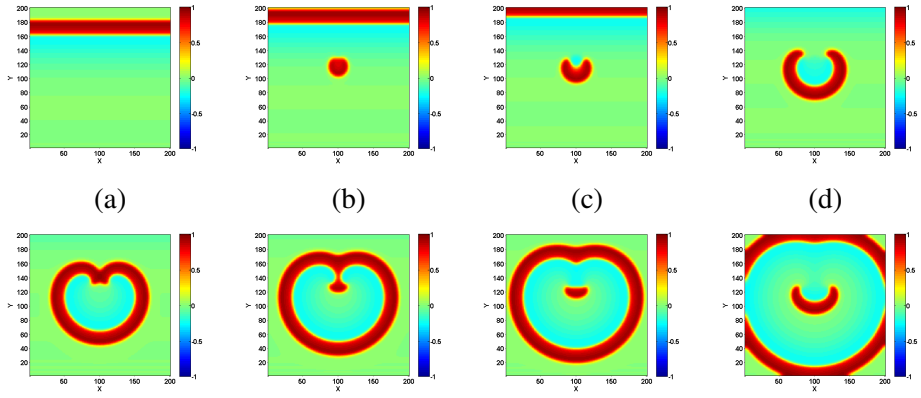

(a) (b) (c) (d)

(e) (f) (g) (h)

Figure 2.4: Demonstration of functional reentry

node. When the electrical impulses use this detour through the heart, the ventricles are activated too early [39]. In this case it develops a global anatomic reentry pathway between the atria and the ventricles. Another typical example of anatomic reentry is a spiral wave pinned at an unexcitable obstacle (ischemia or scar tissue for example) after a normal plane wave passing through.

The functional reentry does not require an anatomic obstacle or pathway [40]. Instead, the excitation waves rotate around a functional obstacle called the core of the spiral wave. A common mechanism to generate functional reentry is through the **S1-S2 pacing protocol** shown in Fig. 2.4. The protocol is composed of two beats. The first beat S1 generates a normal plane wave (Fig. 2.4a); the second stimuli S2 is delivered at the tail of S1 (Fig. 2.4b) and it will curve around the refractory areas created by the S1 stimuli (Fig. 2.4c) and generate a spiral. The obstacle in this situation is functional, created by the refractory period. In Fig. 2.4 the spiral wave is self-sustainable and it will never die out.

Alternans and functional reentries are closely related. Discordant alternans increases the vulnerability to reentry by increasing the spatial dispersion of refractoriness, thus it makes it more likely for the next premature beat to generate reentry [28].

The reentry-based tachycardia can cause a quickly rotating spiral wave in the atria (atrial flutter) or ventricles (VT). And fibrillation is degenerated from tachycardia when

the spiral wave breaks into multiple wavelets [41].

2.4 Existing theory on mechanism of fibrillation and defibrillation

Defibrillation is termination of arrhythmias by altering the transmembrane voltage through the delivery of electric shocks [41]. It has been known for over 100 years that electrical shocks can both initiate and terminate fibrillations [42][43]. Debates on the mechanisms behind defibrillation, however, have never ceased. Ideker et al [44] had an excellent analogy, comparing different hypotheses to "blind men feeling the elephant": "investigators performed their own research studying different aspects of defibrillation but no one can see the whole picture".

From the "minimum energy necessary in defibrillation" point of view, it has been shown that the strength of electrical shocks can be greatly reduced. Dudel [45] hypothesized the minimum electric field needs to paralyze the entire ventricle. Wiggers [46] proposed the field only needs to halt the activation fronts. Zipes et al [47] and Mower et al [48] suggested a even weaker field halting activation fronts only in a critical mass. Recently even lower energy was proposed utilizing multiple shocks and combined stages of treatment to further reduce the energy needed [49][50].

From the "initiation and termination of fibrillation" point of view, several hypotheses were proposed in the 70s and 80s that associated the induction and termination of arrhythmias by shocks to the same mechanisms. The "upper limit of vulnerability" hypothesis [51] claimed the upper limit of the strength of shocks that induce fibrillations is approximately the same as the defibrillation threshold. The "field-recovery critical point" hypothesis [52] stated that the critical variables in both induction and termination of fibrillation are the dispersion of recovery and the potential gradient field. However, this hypothesis suggested the nonuniform dispersion of refractoriness is induced by the S2 shock itself while another hypothesis called the "nonuniform dispersion of refractoriness" hypothesis [46][53] suggested the premature S2 stimuli only initiates the fibrillation, the dispersion of refrac-

toriness is inherited from the ionic channels, conductivity and other properties in the tissue. This "nonuniform dispersion of refractoriness" implied much smaller electrical stimuli induce fibrillations from a mechanism different than strong shocks halt fibrillations.

From the 90s, optical mapping techniques using potentiometric fluorescent dyes to record transmembrane potential changes in defibrillation shocks revealed the effect of prolongation of action potential by the shock followed by simultaneous AP recovery, indicating simultaneous recovery through the whole myocardium after shock as essential in successful defibrillations [54][55][56].

More recent studies suggested the contribution of inhomogeneities to depolarization in tissues during a defibrillation shock, stating the heterogeneities, such as vessels and bundles, serve as virtual electrodes during an electric shock, enhancing the depolarization and hyperpolarization in tissues far away from the anode and cathode [1].

The theory of primary and secondary sources of electric field in excitable tissues can be tracked down from Maxwell equations [57]. The primary source arises from the combination of an ohmic current due to the resistivity of tissue and a nonohmic current due to active transport, which is the movement of ions or molecules across a cell membrane into a region of higher concentration ($\vec{J} = \sigma\vec{E} + \vec{J^i}$). The secondary source arises from the boundaries where electrical discontinuities occur. For example, on the interface between two media with different conductivities σ_1 and σ_2, a current layer lies with the density of $\vec{K} = \phi(\sigma_2 - \sigma_1)\hat{n}$, ϕ being the potential and $\hat{n}$ being the normal vector of the surface. Theoretical analysis using geometries and conductive properties from cardiac cells showed that secondary sources are more significant than the primary ones [57]. These secondary current sources will occur at any interface separating two media with different electrical conductivities, such as the gap junction that serves as connection between two adjacent cells, inhomogeneities in tissues like vessels and bundles, and changes in fiber orientations [58]. Due to the secondary sources provided by heterogeneities, electric field can penetrate through tissues without dying out at the boundary exponentially. The secondary

source is also called virtual electrode.

Experiments confirmed secondary sources on cellular levels. Fast el al [59] studied the effect of defibrillation shocks on monolayer cells cultured with specifically designed clefts. The results found depolarization and hyperpolarization on each side of the cleft and a linear relationship between the strength of the secondary source and the obstacle length but a nonlinearly increase of the source strength with respect to the strength of the shock.

Experiments also found a dog-bone shaped depolarization (or hyperpolarization region dependent on the polarity of the stimulation) in transmembrane potential for a point-size stimulus due to the anisotropy in cardiac tissue [60][1]. It is called a virtual electrode polarization (VEP) pattern. The VEP plays key role in electrical stimulation in heart and experiment showed damaged tissue can eliminate VEP and increase the defibrillation pacing threshold [61].

Several simulation studies showed the effect of fiber orientations and curvatures on defibrillation shocks. Trayanova et al [58] demonstrated shock-induced electrodes associated with fiber curvature can extinguish a recirculating spiral wave. Bittihn et al [12] showed an optimal negative curvature for which the effect of electric filed is the largest in defibrillation shocks, suggesting negative curvature structures such as papillary or trabecular muscles can be employed to facilitate defibrillation.

2.5 Optical mapping and pacing protocols

Optical mapping techniques use potentiometric fluorescent dyes to record transmembrane potential changes. Tissue is perfused with voltage (or calcium) sensitive dye, whose emission intensity shifts when transmembrane voltage changes. By recording the emitted light intensity with a high speed camera, we can recover the transmembrane voltage signal. In this thesis, we compare our simulation results directly with optical mapping experiments. Here we briefly describe the procedures of the optical mapping experiments.

All experiments conform to the current Guide for Care and Use of Laboratory Animals

published by the National Institutes of Health (NIH Publication No. 85-23, revised 1996), and approved by the Office of Research and Integrity Assurance at Georgia Tech. Animals (New Zealand white rabbits or Mongrel dogs) were anesthetized and euthanized. Hearts were then quickly removed and perfused with cardioplegic solution, gassed with 95% O_2 and 5% CO_2. Then the hearts (for rabbits) or separated ventricle or atria (for dogs) were immersed in a chamber kept at $37°C$ and perfused with Tyrode's solution. Tissue contraction was suppressed by using blebbistatin. For imaging, the heart was stained with the voltage-sensitive dye Di-4-ANEPPS or JPW-6003 and intracellular calcium-sensitive dye Rhod-2.

For defibrillation experiments, ventricular arrhythmias were induced by fast pacing (60-150ms) while atrial arrhythmias were induced by applying acetylcholine before pacing (30-65ms) [62]. Both VF and AF featured multiple spiral waves. Pacing and defibrillation shocks consisted of rectangular pulses. For the LEAP experiments, a sequence of at least 5 pulses was applied with a 5-ms pulse duration and a cycle length 5-10 ms below or above the dominant period of the arrhythmia. The minimum energy required to terminate fibrillation by standard one-shock defibrillation was obtained on the same hearts.

CHAPTER 3

COMPUTATIONAL MODEL OF THE HEART

In this Chapter, I will briefly describe computational cardiac models. I will first review the mathematical equations that are used to model a single cardiomyocyte, then further extend them to modeling multi-dimensional tissue from 1D cable to 3D geometry. Then I will introduce Web Graphic Library (WebGL), a library for computation using GPU.

3.1 Cardiac cell modeling

The single cell membrane potential can be described by the following current conservation law in which the cell membrane is modeled by a capacitor:

$$C_m \frac{dV_m}{dt} = -I_{ion} + I_{stim}, \tag{3.1}$$

where C_m is the membrane capacitance (unit:$\mu F/cm^2$), V_m is the transmembrane voltage (unit:mV), I_{ion} and I_{stim} correspond to the membrane ionic current and stimulus current, respectively (unit:$\mu A/cm^2$). Figure 3.1 shows the circuit representation of Eq. 3.1.

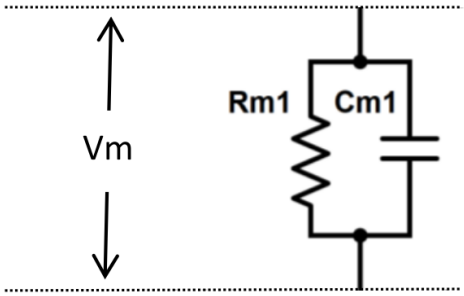

Figure 3.1: Circuit representation of the membrane

The ionic current I_{ion} is usually a sum of several different current. Depending on the complexity of the ionic current, single cell models can be classified into two types: electrophysiological (EP) models and phenomenological models [63].

EP models try to simulate actual ionic concentrations and currents. The ionic current is usually comprised of a large number of individual currents that represent specific Na^+, K^+, Ca^{2+} current and are often inherited or modified from previous generations of models [64][63][65][66]. Earlier models, known as the first generation [64][63][65], had fixed intracellular ion concentrations with classic Hodgkin-Huxley(HH) [67] type of equations based on experimental voltage clamp data to describe their ion channels [68][69][70]. The second generation models improved on the first generation by allowing changing ion concentrations [71][72][73]. And some more recent models, the third generation, include more detailed mathematical descriptions using advanced multi-state Markov-chain equations [74][75][76].

One thing to note is the enormous complexity more recent models acquired, some have multiple compartments within the cell such as the sarcoplasmic reticulum (SR) and mitochondria [75][77]. Including detailed subcellular processes into EP models, on one hand, enables us to have a complete picture of cell activities, providing potential explanations of experimental phenomenon from a subcellular point of view [75][76][77], on the other hand, however, it greatly increases the computational cost for some models have over 50 variables [78] and the large number of parameters also greatly increases the difficulty to understand the dynamics of the model.

Phenomenological models tend to use simple expressions to reproduce fundamental experimental characteristics without imitating actual ionic currents [63]. A frequently used model is the FitzHugh-Nagumo (FHN) model [79]. The motivation of this model is to simplify the process of representing a class of excitable-oscillatory systems. The model only has two variables: one voltage (u) and one gating (v) variable; they represent excitability and refractoriness respectively. Other phenomenological models include Rogers-modified

FitzHugh-Nagumo model [80] and Fenton-Karma model [81]. Due to its simplicity, phenomenological models of cardiac cells are often coupled to produce higher dimensional tissues. The downside of phenomenological models is that they are usually too simple to produce some complicated dynamics.

Single cell models usually only involve ordinary differential equations (ODE) with time (t) being the independent variable. ODE solvers with various orders of accuracy such as forward Euler (1st order), backward Euler (2nd order) and Runge-Kutta (4th order usually) are commonly used [82]. The Rush-Larson method is used to improve the stability of integrators such as the forward Euler [83].

3.2 Tissue modeling

Cardiac cells are connected through gap junctions, which allow molecules and ions to pass through so the electrical signals can propagate from cell to cell. The propagation of action potential can be modeled using a reaction-diffusion equation:

$$C_m \frac{dV_m}{dt} = \bigtriangledown \cdot (D \bigtriangledown V_m) - I_{ion} + I_{stim} \tag{3.2}$$

This equation is like Eq. 3.1 with an addition of the term $\bigtriangledown \cdot (D \bigtriangledown V_m)$, which is used to model the diffusion (propagation) of the transmembrane voltage through the tissue. The boundary condition is $\hat{n} \cdot (D \bigtriangledown V_m) = 0$. Figure 3.2 shows a schematic circuit diagram for Eq. 3.2 in a 1D case. The intracellular space is modeled with resisters in series and the extracellular potential is grounded.

Equation 3.2 only models the transmembrane potential, assuming the potential of the extracellular space is proportional to the potential of the intracellular space, scaled by the conductivities. This assumption is true if the ratio of conductivities parallel and perpendicular to the fibers is the same in the intracellular and extracellular space [63]. In a 1D cable, this assumption is automatically satisfied because there is only one direction. This equation

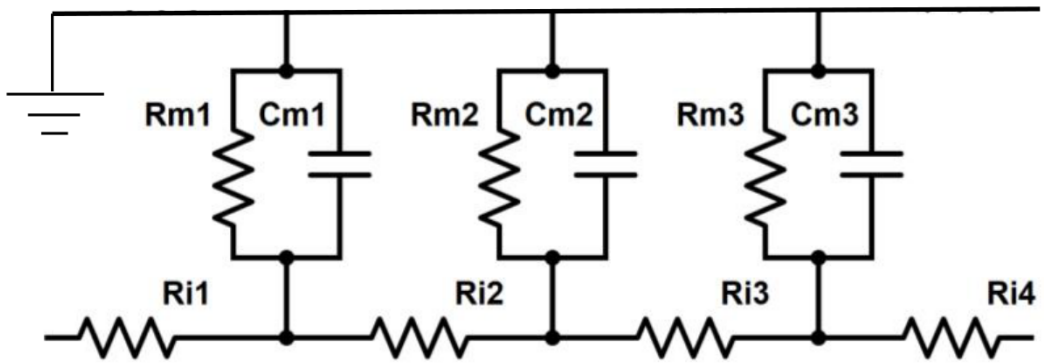

Figure 3.2: Circuit representation of the monodomain model

is also called the monodomain model. In higher dimensions, experimental results showed this ratio in intracellular domain is usually five times that of the extracellular domain for cardiac tissues [84]. If the anisotropy is not important to the study, monodomain model is sufficient. Otherwise bidomain models need to be used. Bidomain models simulate potentials in both the intracellular and the extracellular domain (Figure 3.3):

$$C_m \partial V_m / \partial t = -I_{ion} + \nabla \left(D_i \nabla V_m \right) + \nabla \left(D_i \nabla V_e \right) \tag{3.3a}$$

$$\nabla \left(D_i \nabla V_m \right) + \nabla \left((D_i + D_e) \nabla V_e \right) = 0 \tag{3.3b}$$

where V_i and V_e are the intracellular and extracellular potentials, the membrane potential is given by $V_m = V_i - V_e$, and the intra- and extracellular diffusions are given by D_i and D_e.

Traditionally, defibrillation simulations require using bidomain models due to the effect of electric field on conductive heterogeneities that we mentioned in the previous Chapter. Figure 3.4 demonstrates the bidomain circuit with unexcitable gap in the intracellular domain (heterogeneity). When external electric shock is applied, current will flow from the anode to cathode in the extracellular space. It will enter the intracellular space when it

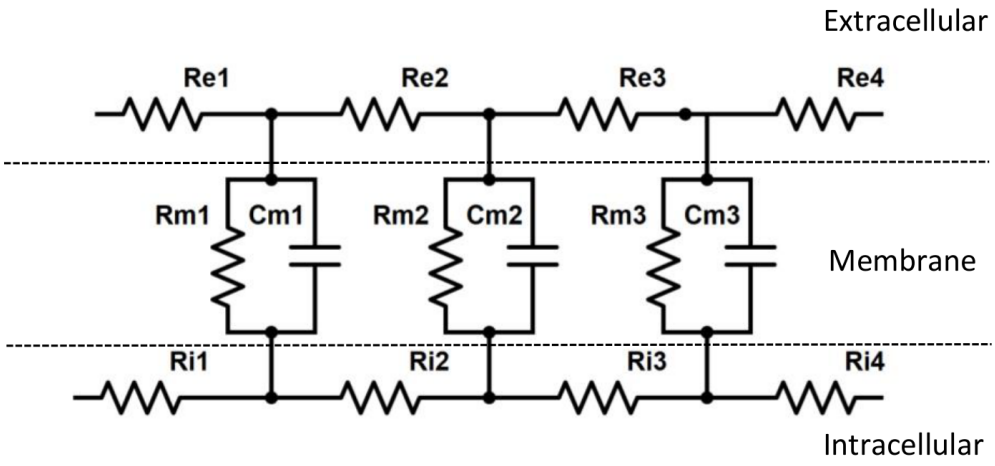

Figure 3.3: Circuit representation of the bidomain model

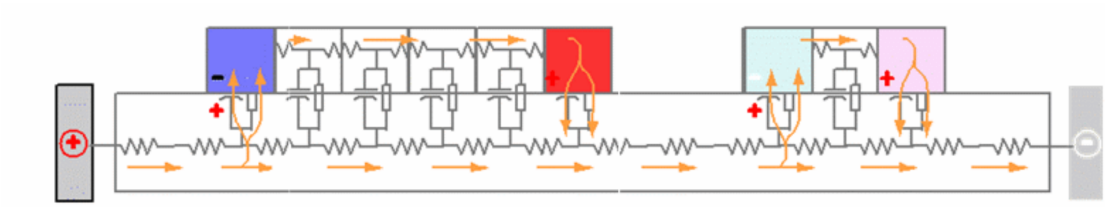

Figure 3.4: Circuit representation of the effect of electric field on unexcitable gaps in the intracellular space

reaches the intracellular boundary and it will be forced to flow outside of the intracellular space when it reaches the unexcitable gap, which will create repolarization and depolarization of the transmembrane potential at those two sites and secondary sources can be produced at the depolarization sites. Traditional monodomain model will not be able to reproduce that.

Recently Pumir et al [85] proposed using monodomain equations with appropriate boundary conditions for simulating the effect of external electric field on heart tissue. In the presence of an external electric field, E_0, at both the domain boundary and the interface between two conduction discontinuities, the boundary condition reads [85]:

$$\hat{\boldsymbol{n}} \cdot (\bigtriangledown V_m - \boldsymbol{E_0}) = 0 \tag{3.4}$$

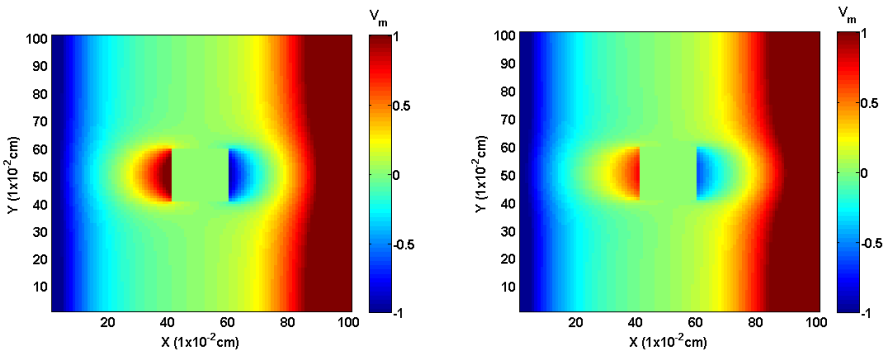

(a) Monodomain (b) Bidomain

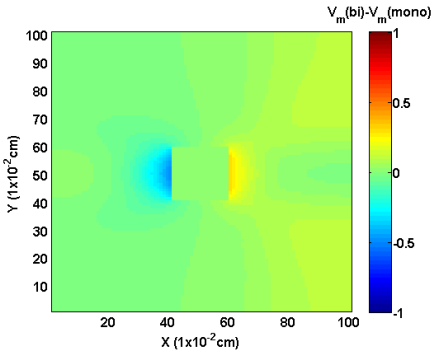

(c) Difference between bidomain and monodomain

Figure 3.5: Comparison of the transmembrane potentials under the steady-state electric field on the 2D domain between monodomain and bidomain simulation. (a) Monodomain steady state (b) Bidomain steady state (c) The difference between the bidomain and the monodomain.

By using this boundary condition, the monodomain model can generate secondary sources at the conduction heterogeneities. Figure. 3.5 shows the transmembrane potentials on a 2D domain with an unexcitable square (heterogeneity) under a constant electric field, solved from the monodomain equation (Fig. 3.5a), bidomain equation (Fig. 3.5b), and Fig. 3.5c shows the difference between the bidomain and the monodomain. We can see that the monodomain and the bidomain models produce similar results. I used the monodomain equations with Pumir's boundary conditions for most part of this thesis.

Equation (3.2) is a parabolic equation which contains first order derivative in time and second in space. Finite difference solvers for parabolic equations based on Taylor expansions include forward Euler (first order accuracy in Δt and second in Δx), backward Euler

and Crank-Nicolson method (second order accuracy in both Δt and Δx) [82]. In this thesis, I used the forward Euler solver with the Rush-Larson method.

3.3 Accelerating simulation with WebGL

To obtain reliable defibrillation results that can shed light on the mechanism of fibrillation and defibrillation and provide guidance for future experiments, we need to run realistic simulations, with respect to both the ionic model and the geometry of the heart. Running complex cardiac models on realistic heart geometry with sufficient resolution is computationally costly.

Graphic Processing Units (GPUs) can provide high levels of parallelization. Each GPU contains thousands of cores, which can perform calculations of each computational element simultaneously. There are many GPU programing languages. In my work, I used WebGL to accelerate defibrillation simulations.

WebGL (web graphic library) is a JavaScript API for rendering interactive 3D and 2D graphics within any compatible web browser. It's fast speed, free, and independence of operating systems.

The essence of WebGL programing is the implementation of "Fragment Shader". A fragment shader is a part of the WebGL application that is in charge of coloring each pixel on a surface using four values: red (r), green (g), blue (b), and transparency (α).

For example, if I would like to simulate FitzHugh-Nagumo [79] model on a 100 by 100 square domain, I can define a canvas with the size of 100 by 100. For each pixel on the canvas, I assign its "red" value to represent the membrane voltage (u) and assign the "green" value to represent the refractory gate (v). The algorithm for solving the PDE of u and the ODE of v is implemented in WebGL in the same way as in any other programing language.

CHAPTER 4

CALCIUM DYNAMICS AND CONTRACTION

4.1 Motivation for this chapter

Electrical stimulation such as cardiac resynchronization therapy (CRT) and cardiac contractility modulation (CCM) have shown success in treating patients with heart failure (HF) [86, 87]. CRT is a current treatment for patients with congestive heart failure (CHF) for a wide QRS complex, where biventricular pacemakers are used to improve electrical synchrony and presumably ejection fraction [86, 88]. However, the response to CRT varies greatly among patients. Improvements are quite variable with up to 30% of patients being non-responders to this treatment at all [86, 89]. Nevertheless, the efficacy and optimization of CRT continues to being improved [90, 91]. For example, it has been shown that extensive electrical remodeling is significantly associated with better survival rates after CRT [90]. Other measurements than electrical dyssynchrony have been investigated as identifications for CRT implantation estimation. It has been suggested that mechanical dyssynchrony is as well essential in prediction of CRT response [91]. An alternate electrical therapy for HF is cardiac contractility modulation (CCM) which delivers electric fields to the heart during its refractory period. Although its mechanism of action was initially thought to result from increased calcium flux from Sarcoplasmic Reticulum (SR) [92, 87], recent studies suggest this is not the case, but that increased contractile function is the result of β adregenergic stimulation [93]. Clinical studies have showed that CCM therapy improved quality of life, exercise capacity, New York Heart Association (NYHA) class, and ejection fraction (EF) during long-term follow up [94]. However, other clinical studies have reported contradictory evidence where CCM did not change effects on hospitalization or mortality [95], and it did not increase myocardial oxygen consumption [96]. It is clear then, that optimization

of CRT and CCM therapies require an understanding of the effects of electric fields on myocyte dynamics especially for inotropicity as regulated by intracellular calcium. Computer simulations have the potential to improve these therapies through clarification of the underlying mechanisms [97]. For example, one challenge in CRT is to determine the optimal pacing locations; Miri et al. provided an optimization strategy to find the best pacing sites and timing delays in CRT based on biventricular-paced activation sequences and ECGs obtained from simulations using patient-specific anatomy and pathophysiology models [98]. Computer simulations can also be beneficial to help to predict the response of patients to certain therapies [99, 100]. For instance, Niederer et al. have designed an electromechanical heart model based on clinical observations [101]. The model predicted that patients with dyssynchronous electrical activation but effective length-dependent tension regulation at the cellular scale are less likely to respond to CRT treatment than patients with attenuated or no length dependent of tension.

Such simulations of electrical therapy require a robust model of cellular excitation-contraction coupling that occurs in the cardiac myocyte such that the electrical and contraction predictions are both accurate. From the introduction to the intracellular calcium handling in Chapter 2, we can see that calcium is deeply involved in two highly non-linear systems: the electrical activation and the force generation. Calcium binding with troponin C is the key component linking the electrical signals to the activation of tension.

While there are close to a hundred cell models describing the detailed electrophysiology (EP) of cardiac cells, the majority of cell models do not include the equations to reproduce the contractile force [102, 103]. This is a considerable drawback. In this Chapter, I first introduce a protocol for testing contraction behaviors, then I prescribe a systematic methodology to implement contraction into EP models. Then I evaluate the contraction behavior of 14 models and conclude with the criteria for EP models that are most suitable to implement contraction. Table 4.1 listed all the terminology used in this chapter.

While there are close to a hundred cell models describing the detailed electrophysi-

ology (EP) of cardiac cells, the majority of cell models do not include the equations to reproduce contractile force[19,20]. This is a considerable drawback. We suggest the most appropriate and challenging test for Electrical-contractile coupled (ECC) cell models derived from EP models is to reproduce the ”postextrasystolic potentiation” (PESP) behavior of the heart [104]. PESP is an example of the changes in stimulation pattern on contractile strength. The effect can be demonstrated with the PESP pacing protocol [105]. First, a train of stimuli is delivered with a fixed basic cycle length called the priming period (PP). Second, an extrasystolic (ES) beat is delivered after the last priming stimulus by an interval called extrasystolic interval (ESI). Following the ES beat, a postextrasystolic (PES) beat is then delivered after another interval called the postextrasystolic interval (PESI). In normal hearts the strength of postextrasystolic contraction is a function of both ESI and PESI. If ESI is fixed, postexatrasystolic strength increases as PESI is lengthened. If PESI is fixed, postextrasystolic strength increases as ESI is shortened. This effect includes mechanical restitution and pause dependence and it captures the important heart dynamics involving force generation and calcium cycling that occurs over multiple beats. Just like the electrical restitution protocol is a stringent test for electrical rate dependence, we believe that reproducing the PESP protocol is essential for an electromechanical cell model. In contrast to electrical restitution in which action potential duration is recorded for a single extrasystolic beat, the purpose of the PESP protocol is to study the contractile strength as a function of a single extrasystolic followed by a compensatory pause. The idea is to capture the full cycle Ca handling, specifically the release of calcium from the SR as a function of timing and the dynamics of the restoration of releasable SR during (and following) action potential repolarization. The basic theory lies in the fact that release from the SR is determined by two factors: the recovery of Ryanodine Receptor’s (RyR’s) which is a function of interbeat interval; and the amount of Ca in the SR. When ESI>PP, RyRs are more recovered from the last priming beat, resulting in a bigger Ca release from SR for the ES beat. Consequently, the Ca content in SR will be smaller compared to the priming period, and may lead to a

smaller or larger Ca release (compared to PP) for the next PES beat depending on the PESI.

In this chapter, we first present a systematical methodology to incorporate mechanical models into various existing EP models. We chose fourteen of the most recently developed EP models with multiple cellular compartments, advanced ionic currents and more realistic subcellular dynamics because they include the essential elements required to couple contraction models (e.g., SR dynamics and calcium buffers). We studied these models under the isometric condition by 1) evaluating how their calcium dynamics are affected by the inclusion of the contraction and 2) assessing how well these electromechanical models simulate contraction by comparing their PESP contractile response with experiments from Yue et al. and 3) analyzing the mechanism of PESP by finding the correlation between the calcium release from SR and the contractile strength. Finally we concluded with insights regarding the suitability of various models to reproduce electromechanical activities and the underlying mechanism of PESP, which may provide guidelines for future experiments.

4.2 Methods

In this section we introduced the contraction model that we implemented to EP models and the experiment we compared our simulations to, then we described our classification of EP models and corresponding strategy for contraction implementation, the numerical methods used to solve the models as well as the pacing protocols and data analysis.

4.2.1 The contraction model

We chose the Negroni_Lascano_1996 (NL96) [106] contraction model to represent the coupling of cross-bridge dynamics and intracellular calcium kinetics. The muscle unit structure and cross-bridge dynamics are shown in Figure 4.1.

The muscle unit is composed of an inflexible thick filament (myosin), a thin filament (actin) and an elastic paralleled element (titin). The cross-bridges are attached to the thick element on one end and can slide on the thin element on the other end. The total force is

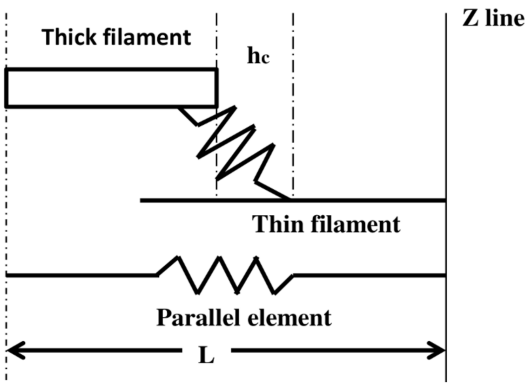

Figure 4.1: Muscle unit structure

contributed by two parts: force generated from the elastic element (F_p) and force generated by the cross-bridges (F_b):

$$F = F_b + F_p \tag{4.1a}$$

$$F_p = K(L - L_0)^5 \tag{4.1b}$$

$$F_b = A([TCa^*] + [T^*])h \tag{4.1c}$$

where K, A and L_0 are constants; L is the sarcomere length; $[TCa^*]$ and $[T^*]$ are two states associated with troponin C sites on the thin filament (defined below); h is the elongation of the muscle unit. The fifth order nonlinear term in F_p is due to the simplification to avoid discontinuity in the representation [106]. For "isometric" contraction where the sarcomere length is fixed, F_p is constant, and the total force is determined only by the force generated from the cross-bridges. We study the isometric case because for a physiological work-loop styple contraction, the first phase is isovolumetric contraction. Cross-bridge grabbing and sliding on the thin element will generate force F_b, which is proportional to the elongation (h) and the total number of attached cross-bridges. The number of attached cross-bridges is determined by the interaction with Ca^{2+} and the relevant buffers, which is represented by a four-state system comprised of:1) sites on the thin element with free troponin C ($[T]$);

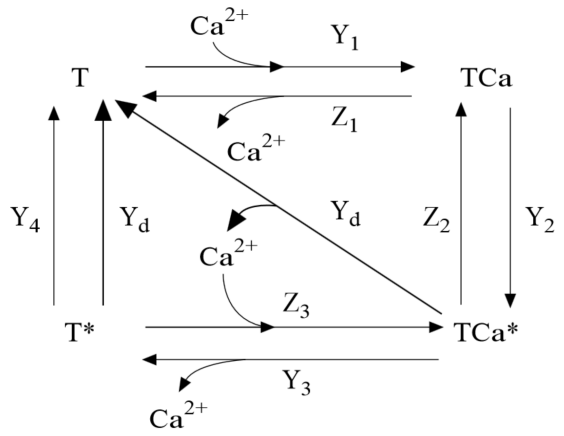

Figure 4.2: Transition among the four states

2) sites with Ca^{2+} bound to troponin C ($[TCa]$); 3) sites with Ca^{2+} bound to troponin C and attached cross-bridges ($[TCa^*]$); and 4) sites with troponin C not bound to Ca^{2+} but attached cross-bridges ($[T^*]$). The transitions happen among these four states via the binding and releasing of Ca^{2+} and attaching and detaching of cross-bridges (Figure 4.2).

The number of total cross-bridges is the sum of the two states that associated with cross-bridges ($[TCa^*] + [T^*]$). Equations representing the transitions among the four states are:

$$\frac{d[T^*]}{dt} = (Y_3[TCa^*] - Z_3[T^*][Ca^{2+}]_i) - Y_4[T^*] - Y_d(dX/dt)^2[T^*] \tag{4.2a}$$

$$\frac{d[TCa]}{dt} = (Y_1[Ca^{2+}]_i[T] - Z_1[TCa]) - (Y_2[TCa]_{eff} - Z_2[TCa^*]) \tag{4.2b}$$

$$\frac{d[TCa^*]}{dt} = -(Y_3[TCa^*] - Z_3[T^*][Ca^{2+}]_i) + (Y_2[TCa]_{eff} - Z_2[TCa^*]) - Y_d(dX/dt)^2[TCa^*] \tag{4.2c}$$

$$[T] = [Troponin]_{total} - [T^*] - [TCa] - [TCa^*] \tag{4.2d}$$

These are reaction equations among the states of $[T]$, $[T^*]$, $[TCa]$, and $[TCa^*]$; all with units of mM/ms. $[TCa]_{eff}$ is the effective $[TCa]$ where cross-bridge attachment can occur and its dependent on the sarcomere length (see Eq. (10) in [106]). $X = L - h$, which is the inextensible length in the muscle unit. $Y_1 \sim Y_4$, $Z_1 \sim Z_3$ and Y_d are rate constants.

The NL96 model includes feedback from force on $[Ca^{2+}]$; therefore it is, in general, a "strongly coupled" contraction model, but under isometric condition it is weakly coupled since $dX/dt = 0$ [66].

There are three reasons why we chose the NL96 model. First, it shares common elements with the EP models; this greatly simplifies the implementation procedure. For example, the four states in the Ca^{2+} kinetics are closely related to intracellular Ca^{2+} concentration and Troponin concentration, both of which are common elements in advanced EP models. Second, even though NL96 model is a simplified model of the average effect of the interaction between myosin and actin, it can effectively reproduce basic physiological findings, such as time course of isometric force, intracellular Ca^{2+} transient and force-length-Ca^{2+} relation. Third, our method to incorporate NL96 can be easily applied to other contraction models as long as they use ODEs to describe the Ca-Troponin (CaTRPN) states, like [107, 108, 109].

4.2.2 The contraction experiments

We implemented contraction into 14 electrophysiology models. To evaluate the ability of these fourteen models to reproduce experimental findings, we compared the results of the simulations with the isovolumetric canine ventricular experiments from Yue et al. [105]. We chose Yue et al. because their paper includes not only a comprehensive experimental exploration of the relation between the contractile strength and pacing intervals, but also a concise mathematical framework that allows quantitative comparisons of model predictions.

We applied the same PESP pacing protocol employed by Yue et al. [105], which was introduced in the Introduction section. By fixing ESI and varying PESI, Yue et al. [105] measured the rate of pressure change of the PES beat as a function of PESI; then by changing ESI to another value and repeatedly varying PESI, a family of curves can be constructed showing the effect of both ESI and PESI on pressure change. Figure 4.3 shows an example

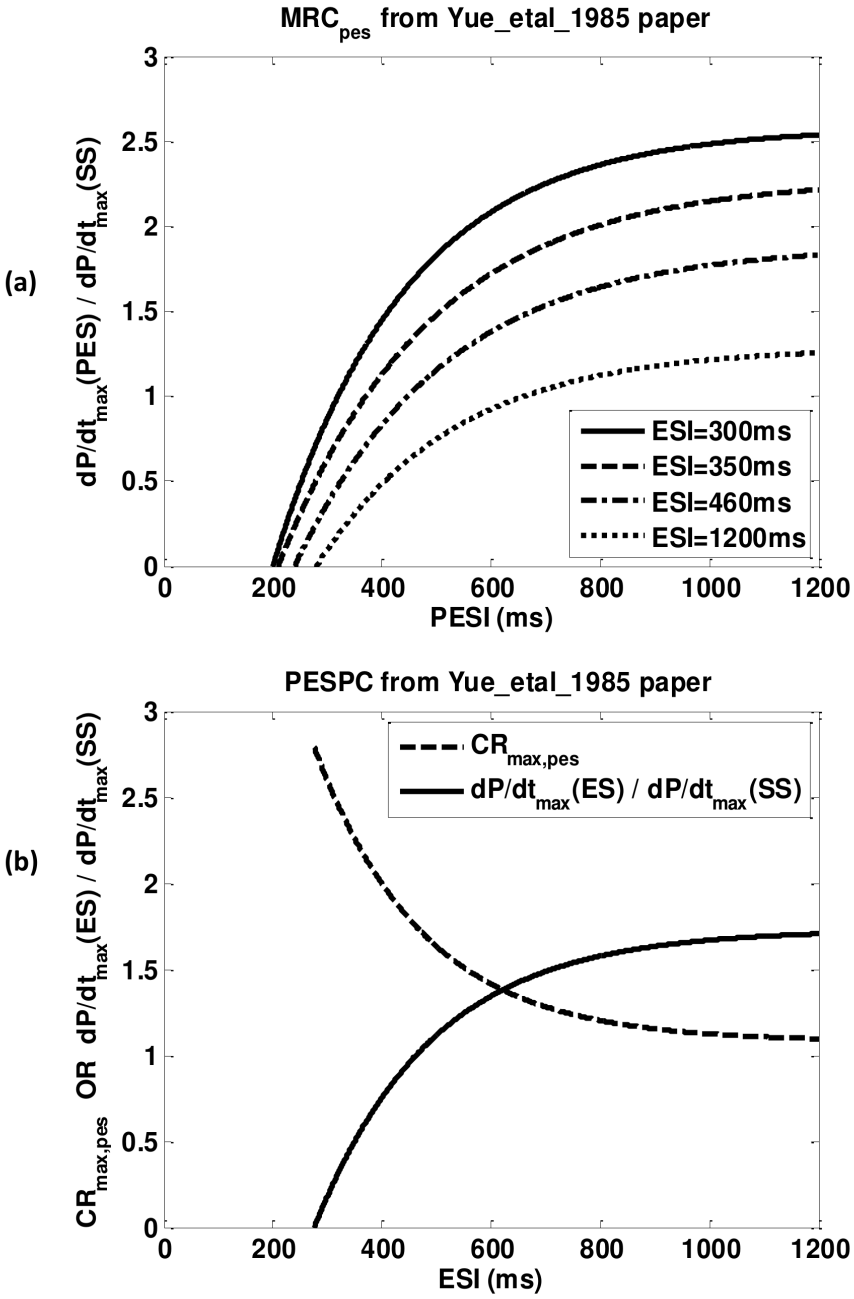

Figure 4.3: Contractile characteristic curves generated from equations in Yue experiments: (a) Postextrasystolic mechanical restitution curves (MRC_{pes}) using ESI equal to 300ms (solid line), 350ms (dash line), 460ms (dash-dot line) and 1200ms (dot line). (b) Postextrasystolic potentiation curve (PESPC, dash line) and extrasystolic mechanical restitution curve (MRC_{es}, solid line).

of the results from Yue et al. [105].

In Yue's experiments, they measured the maximum rate of pressure change in fourteen isolated perfused left canine ventricles under the isovolumetric conditions. In the NL96 contraction model, force (normalized to muscle cross section area) is the variable to quantify the contractile strength; therefore to correlate with Yue's experiment results, we assumed a linear relationship between the force generated from a single cell and the ventricular pressure [110], thus we compared the normalized maximum rate of force change in our simulations with the normalized maximum rate of pressure change in Yue's paper.

4.2.3 Ventricular models and electrophysiological contraction implementation

We studied fourteen ventricular cell models, which include four species: guinea pig (n=4) [76, 111, 112, 113], rabbit (n=2) [114, 115], dog (n=2) [116, 117] and human (n=6) [118, 78, 77, 119, 120, 121]. We classified the models into five categories based on the type of their calcium buffers and designed corresponding strategies to implement NL96. The complexity of the implementation of contraction into these five types of models is listed in ascending order. The flowchart 4.4 illustrates steps of the implementation. We provide the essential equations, initial conditions and choice of parameters below. Table 4.2 lists general information about all models including classification, species, buffer information, number of variables, stimulus current amplitudes and durations; rate constants for CaTRPN can be found in Table 4.3.

Type One: models with contraction

Two of the fourteen models have contraction in their original versions: Iribe_etal_2006 [111] and Matsuoka_etal_2003 [76]. Matsuoka_etal_2003 already has NL96 contraction in the original version. However, to investigate how much influence the contraction has on this model, we removed the NL96 model (the four-state variable dynamic buffer as in Eq. (4.2))

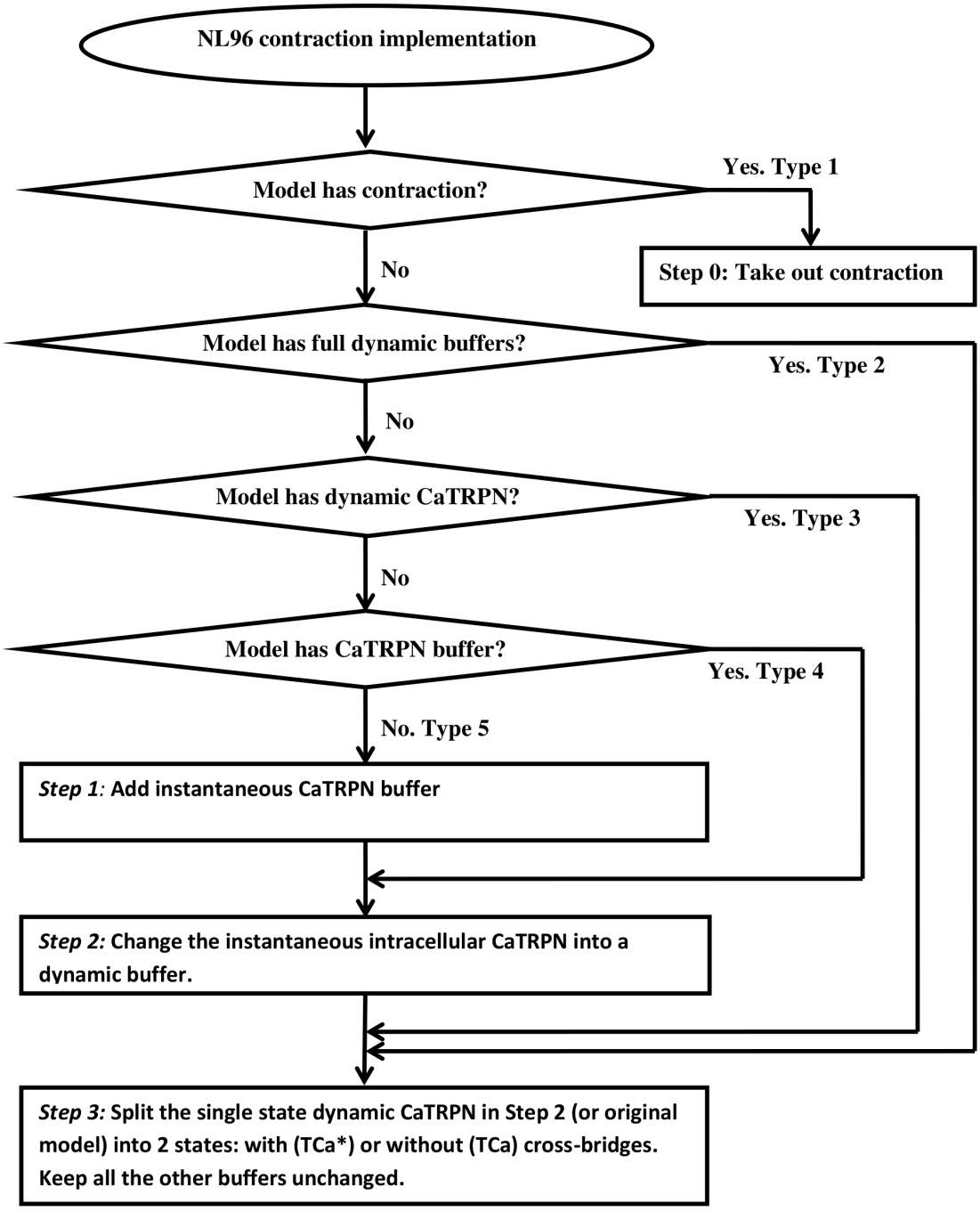

Figure 4.4: Flowchart of systematically implement contraction into EP models

and made CaTRPN a single-state-variable dynamic buffer:

$$\frac{d[CaTRPN]}{dt} = K_{on}[Ca^{2+}]_i(B_{max,trop} - [CaTRPN]) - K_{off}[CaTRPN] \qquad (4.3)$$

$[Ca^{2+}]_i$ is the intracellular Ca^{2+} concentration; $B_{max,trop}$ is the total Troponin concentration; K_{on} and K_{off} are rate constants for the chemical reaction:

$$\mathrm{Ca}^{2+} + \mathrm{TRPN} \underset{K_{off}}{\overset{K_{on}}{\leftrightarrows}} \mathrm{CaTRPN} \qquad (4.4)$$

We set K_{on} and K_{off} to the values of Y_1 and Z_1 and B_{max} to the value in the original model. We call this new model Matuoska_etal_2003 without Contraction. Iribe_etal_2006 includes the contraction model of Rice et al. (RWH99) [107] in the original version [111]. For RWH99, CaTRPN is expressed by a single-state dynamic equation like Eq. (4.3) but with a dynamic rate constant K_{off} that depends on force, hence it is strongly coupled even for isometric contractions. Also the RWH99 model has six tropomyosin/cross-bridge states with rate constants that are functions of the CaTRPN concentration. To simulate this model without contraction, we eliminated the six tropomyosin/cross-bridge states and set K_{off} for CaTRPN to a constant value by fixing the force in the K_{off} expression to half of its maximum value. We then compared simulations of the original model and the version without contraction as well as the one with the NL96 contraction model (implemented as described in the next "Type Two" section).

Type Two: models with full dynamic buffers

Two of the models incorporate ordinary differential equations (ODEs) for all the buffers: Shannon_etal_2004 [114] and Grandi_etal_2010 [118]. The equations for the original CaTRPN in these models are the same as Eq. (4.3). For models of Type Two we added the four-state NL96 model using Eqs. (4.2) above; this is done by splitting the dynamical CaTRPN in the

original model into two states: with (TCa^*) or without (TCa) cross-bridges:

$$\frac{d[CaTRPN]}{dt} = \frac{dTCa}{dt} + \frac{dTCa^*}{dt} \tag{4.5}$$

and adding the other two states T and T^*. There are multiple K_{on} and K_{off} in Eqs. (4.2). They are kept the same as original NL96 paper [106] except for Y_1 and Z_1, which are chosen to match the values of K_{on} and K_{off} in Eq. (4.3) from the original model (see Table 4.3). This is to preserve the dynamics of Ca as similar as possible to the original model.

Type Three: models with dynamic CaTRPN

Two of the models use ODEs for CaTRPN but instantaneous forms for all the other buffers: Mahajan_etal_2008 [115] and Iyer_etal_2004 [78].

For this type of models we followed the same step regarding the dynamic CaTRPN in Type Two above and kept all the other buffers instantaneous. The only difference between Type Three and Type Two is that there are instantaneous buffer factors in Type Three models (see Eq. (4.6) below) but not in Type two.

Type Four: models with instantaneous CaTRPN

Five of the models have instantaneous CaTRPN: Hund_etal_2004 [116], Faber_etal_2000 [112], Livshitz_etal_2007 [113], Ohara_etal_2011 [77] and Priebe_etal_1998 [119]. The buffering of Ca^{2+} by Troponin is represented using the following equations:

$$\frac{d[Ca^{2+}]_i}{dt} = \beta I_{total}^{Ca} \tag{4.6a}$$

$$\beta = 1/(1 + \sum_j \frac{B_{max,j} K_{d,j}}{([Ca^{2+}]_i + K_{d,j})^2}) \tag{4.6b}$$

I_{total}^{Ca} is the total intracellular Ca^{2+} current; β is the instantaneous buffer factor; index j represents each type of intracellular Ca^{2+} buffer; $B_{max,j}$ and $K_{d,j}$ are the total concentration

and the affinity constant for buffer j. For this type of model we first changed the instantaneous intracellular CaTRPN into a dynamic buffer by eliminating the CaTRPN term from the instantaneous buffer factor β and by adding a dynamic CaTRPN current into the $\frac{d[Ca^{2+}]_i}{dt}$ equation:

$$\frac{d[Ca^{2+}]_i}{dt} = \beta'(I^{Ca}_{total} - I_{CaTRPN}) \tag{4.7a}$$

$$\beta' = 1/(1 + \sum_{j'} \frac{B_{max,j'} K_{d,j'}}{([Ca^{2+}]_i + K_{d,j'})^2}) \tag{4.7b}$$

$$I_{CaTRPN} = \frac{d[CaTRPN]}{dt} = K_{on}[Ca^{2+}]_i(B_{max,trop} - [CaTRPN]) - K_{off}[CaTRPN] \tag{4.7c}$$

in which j' goes through all Ca^{2+} buffers except for CaTRPN. The way to choose K_{on} and K_{off} here is not unique as long as $\frac{K_{off}}{K_{on}} = K_d$ in the original model. We chose $K_{off} = \sqrt{\sigma} K_{off,s}$ and $K_{on} = 1/\sqrt{\sigma} K_{on,s}$, where the subscript 's' indicates the values from the Shannon_etal_2004 model and $\sigma = \frac{K_d}{K_{d,s}}$. We used the values from Shannon_etal_2004 as the standard values here because they have been widely used to simulate dynamic CaTRPN. After changing the instantaneous CaTRPN into a dynamical buffer, we followed the same procedure as for Type Three models to incorporate the NL96 contraction.

Type Five: models without Ca troponin buffers

Three of the models do not have CaTRPN, but they do have other intracellular Ca^{2+} buffers: Fox_etal_2002 [117], TenTusscher_etal_2006 [120] and Fink_etal_2008 [121].

For this type of models, we first added the instantaneous CaTRPN into the models. If the model has one general Ca^{2+} buffer (referred as "General") representing the average effect of all intracellular Ca^{2+} buffers (e.g. TenTusscher_etal_2006 and Fink_etal_2008), we split the general buffer into two parts: CaTRPN and "Other". We kept $K_{d,TRPN}$ and $K_{d,Other}$ to be the same as $K_{d,General}$ from the original model so that the Ca affinity of the instantaneous buffer will be retained. $B_{max,TRPN}$ was set to be 0.07mM, which is

a standard value in most models. $B_{max,Other} = B_{max,General} - B_{max,TRPN}$ so that the concentration of the total intracellular Ca^{2+} buffer is the same as in the original model. If the model has other Ca^{2+} buffers (such as CMDN) but no CaTRPN (e.g. Fox_etal_2002), we kept the other buffers unchanged and add a CaTRPN buffer. For the new CaTRPN buffer we also set $B_{max,TRPN} = 0.07mM$ and $K_{d,TRPN} = 0.6\mu M$, which are both common values in many models. After adding an instantaneous CaTRPN to the model, we followed the steps for Type Four to implement NL96.

4.2.4 Numerical integration

Except for one model (Iyer_etal_2004), all the code for the original single cell models were downloaded from www.cellml.org in CELLML format. Then they were translated into .m files (MATLAB files) using a PYCML program [122, 123]. Simulations were run in MATLAB and integrated using the forward Euler integration method with time steps of 0.0001ms. The Iyer_etal_2004 model consists of 67 variables and requires a dt integration step as low as 1×10^5 to converge using forward Euler, thus becoming impractically slow to simulate in MATLAB. Therefore as in [124] the Iyer_etal_2004 model was written in FORTRAN using a semi-implicit integration method that allows a much larger (while still convergent) integration time step of dt.

4.2.5 Pacing protocol and initial conditions

Our pacing protocol is composed of three steps and similar to the pacing protocol from Yue et al [105] except that we chose to use a priming period of 500ms. The stimulus currents and durations for the different models were selected to ensure excitation and the values are provided in Table 4.2. All simulations were run for isometric contraction of a single cell, where the half sarcomere length is fixed to be $1.05\mu m$.

Step one: Quiescent

In this step, EP models without contractions were run with no stimulus current until quiescent steady states were reached (i.e., no state variable changed by more than 0.01%). Initial values for state variables in each model were directly loaded from CellML code. The time for each model to reach the quiescent state is listed in Table 4.3, and it ranges from 10min of real time (as in the Mahajan_etal_2008 model) to up to 100min (as in the Hund_etal_2004 model). Note that these are real times and not simulation times. Steady state quiescent values for voltage, intracellular Ca^{2+} and JSR (or SR) Ca^{2+} concentrations vary considerably among models as shown in Table 4.4.

Step Two: Priming Cycle

During the priming pacing cycle, all models (with and without contractions) were paced with priming period T=500ms starting from the quiescent states at the end of Step one, until a new priming steady state was achieved. The number of pacing required to reach this priming steady state for each model is listed in Table 4.2. For models incorporating NL96 contraction, state variables for the four states of CaTRPN buffer were calculated by solving Eqs. (4.2) for steady state using the quiescent value of $[Ca^{2+}]_i$. The total CaTRPN buffer (TCa + TCa^*) calculated using this method was verified to be similar to the quiescent value in the original EP model if the original model had a CaTRPN buffer. We used this method to ensure that the initial conditions for the original models and the corresponding contraction models were as close as possible.

Step Three: Postextrasystolic pacing protocol

For all models, an extrasystolic (ES) and a postextrasystolic (PES) beat were delivered in sequence after the last priming beat as described in Section 4.2.1. We held ESI at a constant value and varied PESI to record the transients of transmembrane potential, $[Ca^{2+}]_i$, CaTRPN and generated force; we then changed ESI to a different value and repeated the

process using the priming steady state as initial conditions. The shortest PESI is the refractory period of the ES beat so it is just long enough that the PES beat is separated from the ES beat. The longest PESI (ESI) value was chosen as 1200ms, 1500ms or 2000ms, depending on the time it took for the MRC_{pes} (MRC_{es}) to converge to a plateau level, as some models took longer than others to reach it.

4.2.6 Data Analysis

Our analysis is divided into two parts: Ca^{2+} **dynamics** and **Contraction**.

To analyze the **calcium dynamics** we compare the intracellular Ca^{2+} transients for the priming beats and during postextrasystolic potentiation between the original models and models with contraction. The purpose is to see how much change there is in the calcium dynamics after contraction is implemented. For example, we do not want to completely distort the calcium transient after implementing contraction.

To analyze **Contraction** we generate four characteristic contraction curves: Postextrasystolic Mechanical Restitution Curve (MRC_{pes}), Postextrasystolic Potentiation Curve (PESPC), Minimum-value Axis Intercept Curve ($t_{o,pes}$ plotted vs ESI) and Time Constant Curve ($T_{mrc,pes}$ plotted vs ESI). These curves capture important characteristics of contraction responding to pacing intervals. Yue et al. paper [105] has a complete description of the definition. We validate the contraction behaviors of our model by comparing the curves with the experiments.

For the curve fitting we used MATLAB's built-in function "fit", whose default curve fit algorithm is the Trust-Region method. The value of r^2 was given for each fit and 95% confidence bounds were provided for each fitted coefficient.

Ca^{2+} Dynamics

Priming Ca^{2+}: For each model, we plotted the intracellular Ca^{2+} of the last priming beat, i.e. priming steady state, for both the original model and the one with contraction

implemented in the same plot. We quantified the transient by calculating the following: 1) minimum (diastolic) [Ca^{2+}]$_i$; 2) maximum (systolic) [Ca^{2+}]$_i$; 3) the duration for which [Ca^{2+}]$_i$ was above its half amplitude level, i.e. $[Ca^{2+}]_i > [Ca^{2+}]_{diastolic} + ([Ca^{2+}]_{diastolic} + [Ca^{2+}]_{systolic})/2$; 4) the time at which [Ca^{2+}]$_i$ reached its maximum systolic value (t_{peak}); and 5) the amplitude of the total Ca^{2+} charge delivered to the cytoplasmic compartment during one beat (Q) that was calculated by integrating the area underneath the $[Ca^{2+}]_i + [Ca^{2+}]_{diastolic}$ transient. We quantified the difference of the parameter between the original model and the model with contractions by the relative difference, defined as $\Delta Parameter = (P_{with\_contraction} - P_{without\_contraction})/P_{without\_contraction}$.

Postextrasystolic Potentiation in [Ca^{2+}]$_i$: For each model, we plotted the intracellular Ca^{2+} transient for the last 3 priming beats, along with multiple ES/PES beat pairs overlaid on the same graph for each model (without contraction on the left and with contraction of the right).

Contraction

Following the data fitting and analysis from Yue paper [105] with modification, we generated four characteristic curves for each model after the implementation of contraction: Postextrasystolic Mechanical Restitution Curve (MRC_{pes}), Postextrasystolic Potentiation Curve (PESPC), Minimum-value Axis Intercept Curve ($t_{o,pes}$ plotted vs ESI) and Time Constant Curve ($T_{mrc,pes}$ plotted vs ESI).

Postextrasystolic (PES) Mechanical Restitution Curves ($\mathbf{MRC_{pes}}$) are a family of curves of maximum force change rate of postextrasystolic beats normalized to the last priming beat plotted vs PESI. For a fixed ESI, MRC_{pes} increases monoexponentially to a plateau level (the fully restituted value) as PESI increases. The equation for this is:

$$MRC_{pes} = \frac{dF/dt_{max}(PES)}{dF/dt_{max}(SS)} = CR_{max,pes}\left(1.0 - exp\left(-\frac{PESI - t_{o,pes}}{T_{mrc,pes}}\right)\right) + C_0 \tag{4.8}$$

where F denotes the force generated from NL96 model; PES denotes that it is the postextrasystolic beat; SS denotes the steady state during the priming period; $CR_{max,pes}$ is the plateau amplitude, termed as Maximum Postextrasystolic Contractile Response; C_0 is the minimum value of MRC_{pes}, in Yue et al. [105], $C_0 = 0$; $\mathbf{t_{o,pes}}$ is the minimum-value axis intercept where MRC_{pes} intercepts the minimum value line $MRC_{pes} = C_0$; and $\mathbf{T_{mrc,pes}}$ is the time constant for MRC_{pes}. All terminology can be found in Table 4.1. Figure 4.3 shows one set of MRC_{pes} generated using equations and parameters in Yue et al. [105].

Extrasystolic (ES) Mechanical Restitution Curves (MRC_{es}) presents the maximum rates of change of force of extrasystolic beats normalized to the last priming beat as a function of ESI. Since it is a subset of MRC_{PES} with ESI equal to the priming cycle length, we did not present them separately.

Postextrasystolic Potentiation Curve (PESPC) is the maximum postextrasystolic contractile response ($CR_{max,pes}$) plotted vs ESI. $CR_{max,pes}$ is the plateau amplitude of the above MRC_{pes} for a fixed ESI and this amplitude decreases to a plateau value as ESI increases. Figure 4.3 shows the PESPC and the simultaneously determined MRC_{es}, both generated from the equations in Yue et al. [105]. The equation for PESPC fitting is:

$$CR_{max,pes} = B + A\left(exp\left(\frac{ESI - t_{o,es}}{T_{pespc}}\right)\right) \tag{4.9}$$

where B is the plateau level; A is the amplitude; $t_{o,es}$ is the ESI-axis intercept for the simultaneously determined Extrasystolic Mechanical Restitution Curve; T_{pespc} is the time constant for PESPC.

4.3 Results

The Results section is divided into three parts: Calcium Results, Contraction Results, and the Underlying Mechanism for PESP. In the **Calcium Results** section we first compared the Priming Ca^{2+} transients between the original EP models and the corresponding mod-

els with the NL96 contraction to investigate the influence of including contraction on EP models. Then we studied the Postextrasystolic Potentiation behavior in intracellular Ca^{2+} before and after the implementation of contraction. In the **Contraction Results** section we compared the four characteristic contractile curves with the Yue et al. experiments. In the **Underlying Mechanism for PESP** section we analyzed the mechanism of PESP by finding the correlation between the calcium release from SR and the contractile strength.

4.3.1 Ca^{2+} Results

Priming Ca^{2+} properties are undisturbed after the implementation of contraction for models with dynamic buffers

We present the priming Ca^{2+} data in Figure 4.5, Table 4.5, Table 4.6, Table 4.7 and Section B.1 in Appendix B. Figure 4.5 illustrates $Ca2+$ transients for the last priming beat for six representative models with (dashed lines) and without (solid lines) contraction. They are chosen to include five of the different EP types: (a) Matsuoka_etal_2003 (Type One: with contraction (NL96)); (b) Iribe_etal_2006 (Type One: with contraction (RWH99)); (c) Shannon_etal_2004 (Type Two: full dynamic Ca^2+ buffers); (d) Mahajan_etal_2008 (Type Three: dynamic CaTRPN); (e) Ohara_etal_2004 (Type Four: instantaneous CaTRPN); (f) TenTusscher_etal_2006 (Type Five: no CaTRPN). The corresponding plots for all the fourteen models are provided in Section B.1 in Appendix B. The five quantities computed to quantify the priming Ca^{2+} transient for all EP models without (with) contraction are provided in Table 4.5 (Table 4.6) and the relative differences between before and after contraction are shown in Table 4.7, where double dagger symbols (‡) indicate the differences larger than 50%; single dagger symbols (†) indicate differences larger than 10% but less than 50%.

$[Ca^{2+}]_i$ differs substantially among the original EP models (without contraction) as shown in Table 4.5. For example, for systolic $[Ca^{2+}]_i$, Grandi_etal_2010 and Shannon_etal_2004 have values in the [0.3, 0.5]$\times 10^{-3}$ mM range while Faber_etal_2000

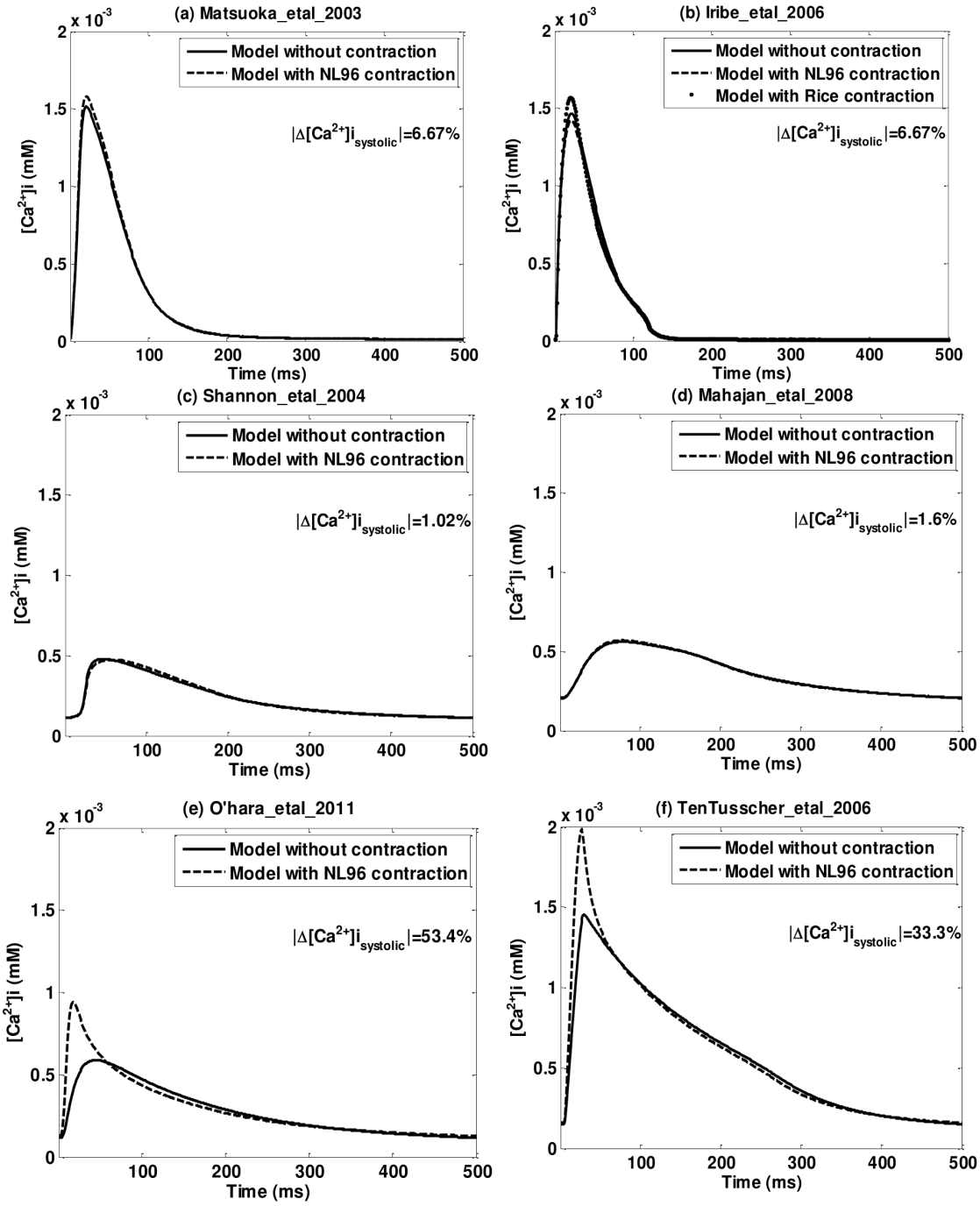

Figure 4.5: Priming Ca^{2+} transient for six representative models: (a) Matsuoka_etal_2003 (Type One: with contraction (NL96)); (b) Iribe_etal_2006 (Type One: with contraction (RWH99)); (c) Shannon_etal_2004 (Type Three: with full dynamic calcium buffers); (d) Mahajan_etal_2008 (Type Three: with dynamic calcium troponin buffer) ; (e) Ohara_etal_2011 (Type Four: with instantaneous calcium troponin buffer) ; (f) TenTusscher_etal_2006 (Type Five: with no calcium troponin buffer). Solid lines are models without contraction; dash lines are models with NL96 contraction. All figures have the same ranges in x and y axis. The insets show the relative difference in systolic Ca^{2+} between models with contractions and without contractions.

is up to four times larger at 2.0×10^{-3} mM; for diastolic $[Ca^{2+}]_i$, the maximum value is 2.0×10^{-3} mM for Faber_etal_2000 and the minimum value is 3.82×10^{-4} mM for Grandi_etal_2010, which is one fifth of the maximum value.

The original models that include dynamic CaTRPN buffers (Type One to Three) do not exhibit a significant change in the shape of the priming Ca^{2+} transient after implementing contraction (adding NL96 model), but the models with instantaneous, or no CaTRPN (Type Four and Five), demonstrate large differences in the transient shape (Figure 4.5).

The most significant changes tended to be an increase in the maximum $[Ca^{2+}]_i$, always accompanied by a decrease in the time of this peak (t_{peak}). As shown in Table 4.7, all six models with dynamic CaTRPN have relative differences of less than 10% in systolic $[Ca^{2+}]_i$ and five out them have relative differences less than 10% in t_{peak}. On the other hand, among the eight models with instantaneous or none CaTRPN, six models show differences larger than 50% and none has a difference less than 10% in systolic $[Ca^{2+}]_i$; in t_{peak}, one of the eight models (Fink_etal_2008) has a relative difference less than 10% and three of them have differences of more than 50%. In addition, except for one model (Fox_etal_2002), all of them have positive relative differences in systolic $[Ca^{2+}]_i$, indicating a systolic $[Ca^{2+}]_i$ increase after the implementation of the NL96 contraction; and all eight models have negative Δt_{peak}, meaning the time of the peak is decreased by the implementation of contraction. The increase in maximum $[Ca^{2+}]_i$ and the decrease in t_{peak} in models with instantaneous or none CaTRPN after the implementation of NL96 is due to an increased and fast rate change of the intracellular calcium after its dynamics has been modified from Eqs. (4.6) (before the implementation) to Eqs. (4.7) (after the implementation) to account for the contraction. Figure 4.6 shows, as an example, the $[Ca^{2+}]_i$ and $d[Ca^{2+}]_i/dt$ respectively for the Ohara_etal_2011 model before (solid lines) and after (dashed line) the NL96 implementation. It can be seen that after the implementation of NL96: (i) the instantaneous buffer factor β increases due to the elimination of the instantaneous CaTRPN from the denominator (see Eqs. (4.7)); and (ii) the current I_{total}^{Ca} is reduced due to the addition of

the negative dynamic CaTRPN current (see Eqs. (4.7)). The current I_{total}^{Ca} decreases by less than 50% of the original value but β increases by more than 200% (Figure 4.6) resulting in an sharp increase in $[Ca^{2+}]_i$ amplitude. And the time for β to reach its peak is clearly shortened, resulting in the decrease of Ca^{2+} peak (t_{peak}).

Results for the priming $[Ca^{2+}]_i$ duration ($t_{1/2}$) are similar to those of systolic $[Ca^{2+}]_i$ (see Table 4.7). All six models that have dynamic CaTRPN show little change in $t_{1/2}$ (less than 10%). Among the eight models with instantaneous or no CaTRPN, six have differences more than 50% and none has a difference less than 10%. Seven out of eight have negative $\Delta t_{1/2}$, indicating the shortening in the time duration when $[Ca^{2+}]_i$ stays above half the amplitude. This large difference in $t_{1/2}$ is closely related to the change in systolic $[Ca^{2+}]_i$. A sharp increase in systolic $[Ca^{2+}]_i$ greatly raises the half amplitude level; this together with the large and narrow spike in $[Ca^{2+}]_i$ generated by the inclusion of contraction, significantly decrease the time duration where $[Ca^{2+}]_i$ stay above the half amplitude level.

The diastolic $[Ca^{2+}]_i$ and the $[Ca^{2+}]_i$ charge (Q) during one beat are the two parameters that do not change much after implementing NL96 contraction in all of the models. Thirteen out of fourteen models have diastolic $[Ca^{2+}]_i$ changes of less than 10%, with only one model having a difference larger than 50% (Fox_etal_2002). Q for eleven out of fourteen models changes by less than 10% and only one model (Fox_etal_2002) has a change of more than 50% (see Table 4.7). This is because, although the systolic $[Ca^{2+}]_i$ is greatly increased for models with instantaneous or none CaTRPN, its increase is localized to a relatively narrow spike with an area that is negligible comparing with that of the rest of the transient.

Models with dynamic buffers show significant Postextrasystolic Potentiation in $[Ca^{2+}]_i$

Postextrasystolic potentiation exists in intracellular Ca^{2+} transients, where giving a fixed and long enough PESI, as the ESI increases, the amplitudes of the $[Ca^{2+}]_i$ of the ES beats

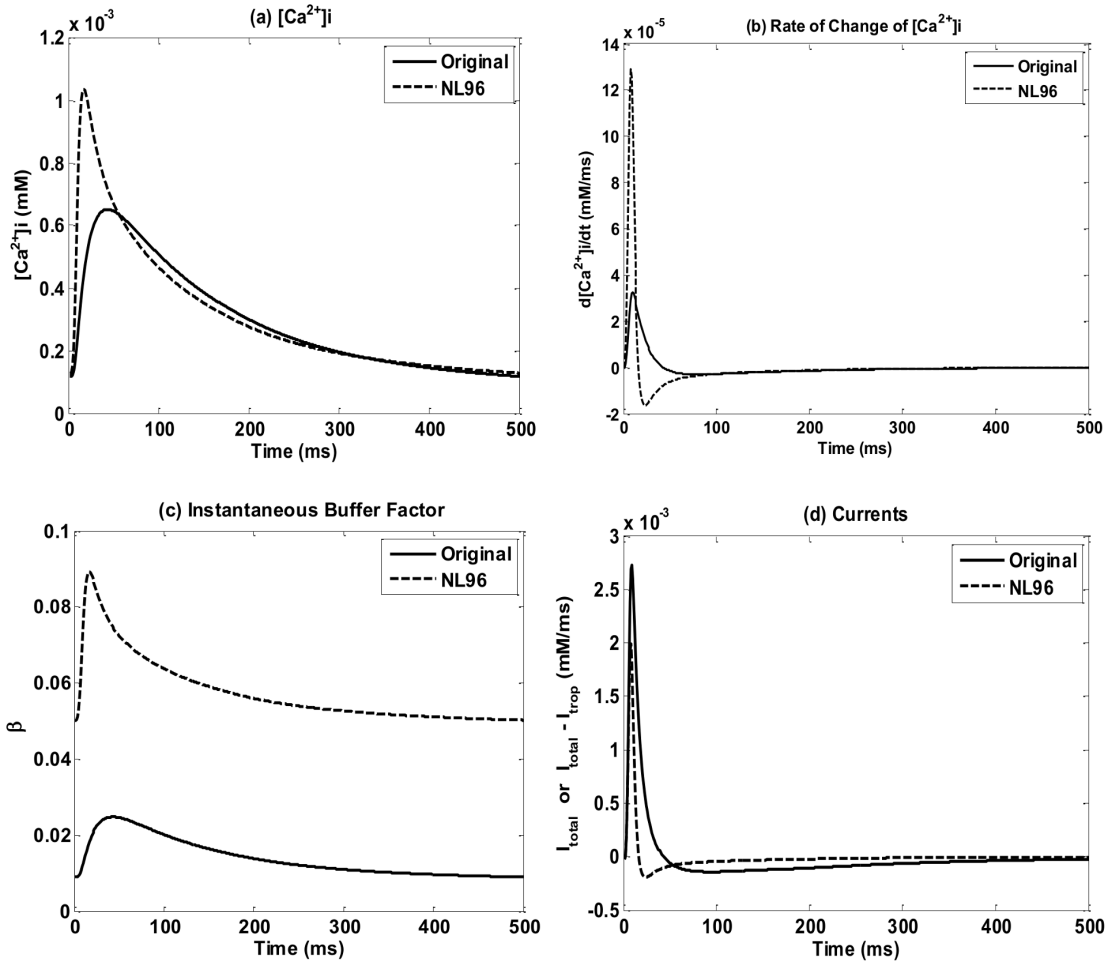

Figure 4.6: $[Ca^{2+}]_i$ shape changes for models with instantaneous buffers. Figures show the Ohara_etal_2008 model for: (a) $[Ca^{2+}]_i$ (grey lines) and $d[Ca^{2+}]_i/dt$ (black lines), before (solid lines) and after (dash lines) the implementation of NL96; (b) zoom in of $d[Ca^{2+}]_i/dt$; (c) the instantaneous buffer factor β before (solid line) and after (dash line) the implementation of NL96; (d) intracellular Ca^{2+} current before (solid line) and after (dash line) the implantation of NL96.

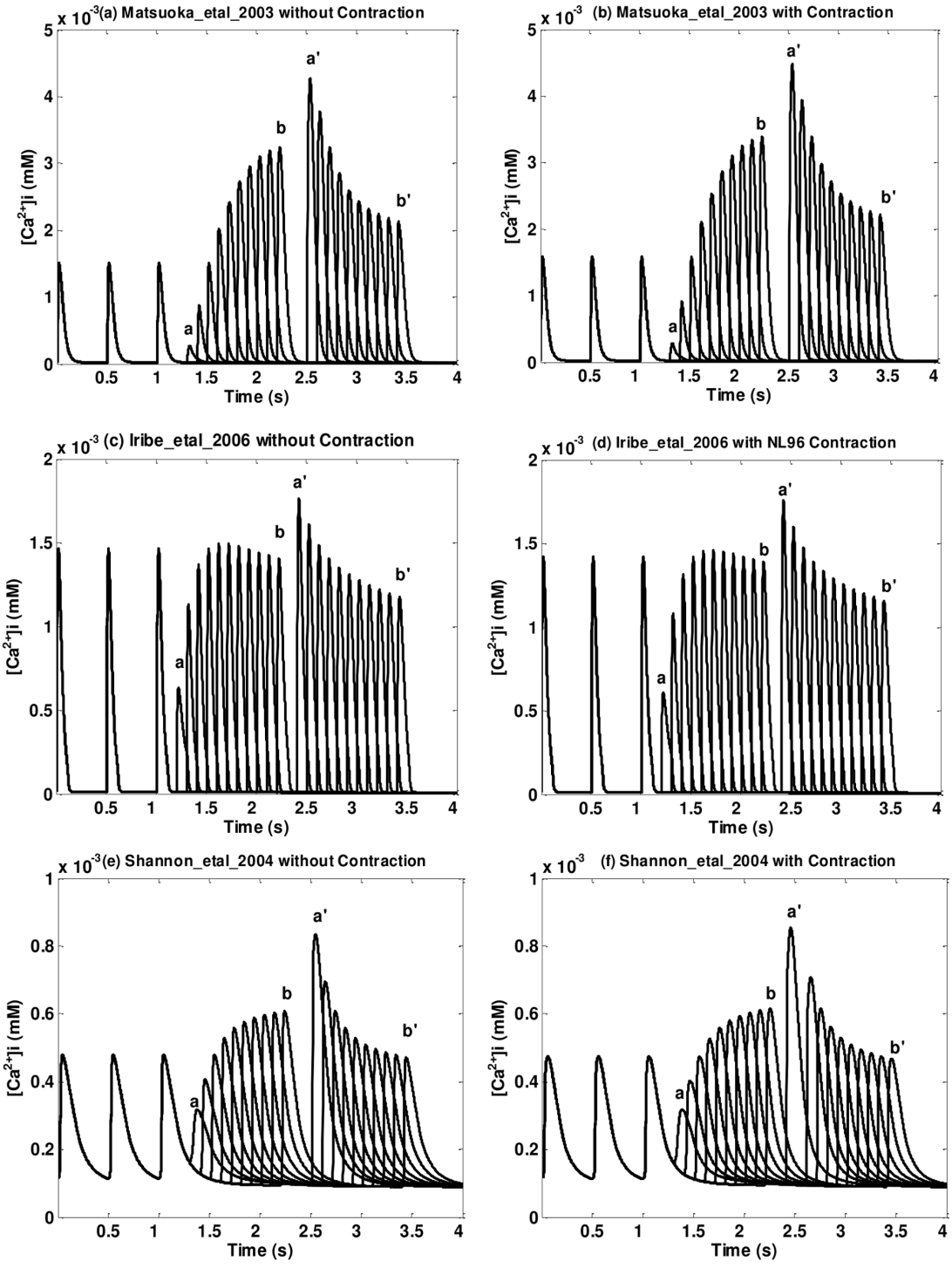

Figure 4.7: Postextrasystolic potentiation in $[Ca^{2+}]_i$ transient for three models of Type One and Two: (a)(b) Matsuoka_etal_2003 without/with contraction; (c)(d) Iribe_etal_2006 without/with contraction (NL96); (e)(f) Shannon_etal_2004 without/with contraction. The first three beats are priming beats; from beat a to beat b are ES beats with different ESIs; from a' to b' are PES beats with a fixed PESI (fully restituted PESI, defined in Step Three in Section 4.2.5); a and b are corresponding ES and PES beats; so are a' and b'. Note that each pair of figures (without/with contraction) has the same axis range.

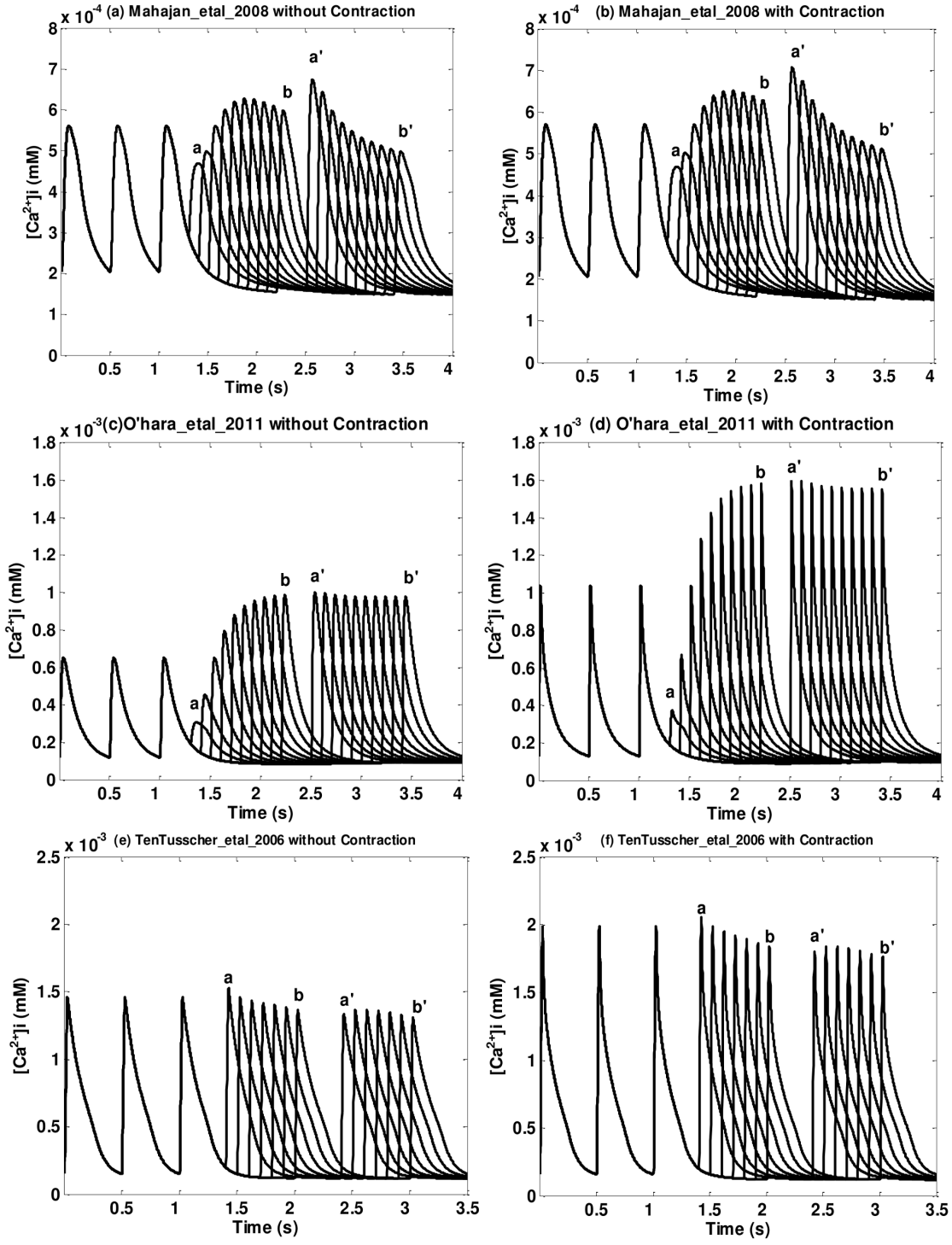

Figure 4.8: Postextrasystolic potentiation in $[Ca^{2+}]_i$ transient for three models of Type Three, Four and Five: (a)(b) Mahajan_etal_2008 without/with contraction; (c)(d) Ohara_etal_2006 without/with contraction; (e)(f) TenTusscher_etal_2006 without/with contraction. As in the previous figure, the first three beats are priming beats; from beat a to beat b are ES beats with different ESIs; from a' to b' are PES beats with a fixed PESI. And each pair of figures (without/with contraction) has the same axis range.

will increase while the PES beats will show the opposite trend. Representative examples of the differences in postextrasystolic potentiation before and after the implementation of NL96 contraction of Type One and Two (Type Three, Four, and Five) models are shown in Figure 4.7 (Figure 4.8). Figures for all models are in Section B.2 in Appendix B. ES beats with different ESIs are labeled from a to b; PES beats with a fixed PESI are labeled from a' to b' (see Step Three in Section 4.2.5); a and b (a' and b') correspond to ES and PES paired beats for the shortest (longest) ESI.

From Figure 4.7, Figure 4.8 and Section B.2 in Appendix B we can see that models with dynamic CaTRPN show a significant postextrasystolic potentiation in the Ca^{2+} transients. As ESI increases, the amplitudes of the ES beats increase while the corresponding PES beats decrease. In addition, there's no notable difference in Ca^{2+} transient before and after the implementation of NL96 contraction (see Figure 4.7 and Section B.2 in Appendix B). On the other hand, models with instantaneous or none CaTRPN do not show a significant postextrasystolic potentiation in the Ca^{2+} transients. Among the eight models, only one model (Livshitz_etal_2007, see Section B.2 in Appendix B) shows notable amplitude change in both ES beats and PES beats. Three models (Hund_etal_2004, Faber_etal_2000 and Ohara_etal_2011, see Figure 4.8 and Section B.2 in Appendix B) show increase in ES beats but no noticeable decrease in PES beats. Four models (Priebe_etal_1998, Fox_etal_2002, TenTusscher_etal_2006 and Fink_etal_2008, see Figure 4.8 and Section B.2 in Appendix B) show neither considerable increase in ES beats nor decrease in PES beats. Note that these types of models, as discussed before, show a change in the shape of $[Ca^{2+}]_i$ when contraction is included. However it does not change the postextrasystolic potentiation behavior much, namely, if the original model has a clear PESP trend, after the implementation, the new model will still maintain that behavior and vice versa.

4.3.2 Contraction Results

To investigate how well our EP models with updated contraction can represent postextrasystolic dynamics, we calculated the four characteristic curves, for all fourteen models with the NL96 contraction and compared them with the experimental data from Yue et al. [105]. Models that can reproduce Yue et al. experiments are considered more physiologically correct.

Postextrasystolic Mechanical Restitution Curve (MRC_{pes})

Representative examples of $MRC_{pes}(dF/dt_{max}(PES)/dF/dt_{max}(SS))$ for six models are shown in Figure 4.9. For all the models, MRC_{pes} are given in Section B.3 in Appendix B.

For all models MRC_{pes} is well described ($r^2 > 0.99$; averaged over all ESI values) by a monotonically increasing curve with respect to PESI (Eq. (4.8)) as shown in Table 4.8, after the elimination of some data points (see the example of Mahajan_eral_2008 below). However not all models were consistent with the experimental findings of Yue et al. [105] whose $C_0 = 0$. Among the six models with dynamic CaTRPN (Type One, Two, Three), four satisfy this condition, while among the eight models with instantaneous or none CaTRPN (Type Four and Five), only one satisfies $C_0 = 0$ (see Table 4.8). Here we provide a brief explanation why C_0 does not go to zero for some models in our simulations. We use Mahajan_etal_2008 with NL96 as an example to demonstrate. In Figure 4.10(a)(b)(c) we plotted the Action Potential (AP), Ca^{2+} transient and normalized dF/dt transient of Mahajan_etal_2008 with NL96 for ESI=500ms. The first beat is the steady priming beat, the second beat is the ES beat with ESI=500ms and from a' to d' are PES beats with PESI from 200 to 650ms. We can observe that the dF/dt$_{max}$ increases with PESI from beat c' to d' but there is no well-defined trend before c'. Beat a' and b' are not clearly separated from the ES beat and a' is even almost fused into the ES beat. However, even though beat a' is very close to the ES beat, dF/dt$_{max}$ still does not go to zero. We plotted normalized dF/dt$_{max}$ (normalize to steady priming beat) for ESI=500ms and PESI ranges from 200ms to 1200ms

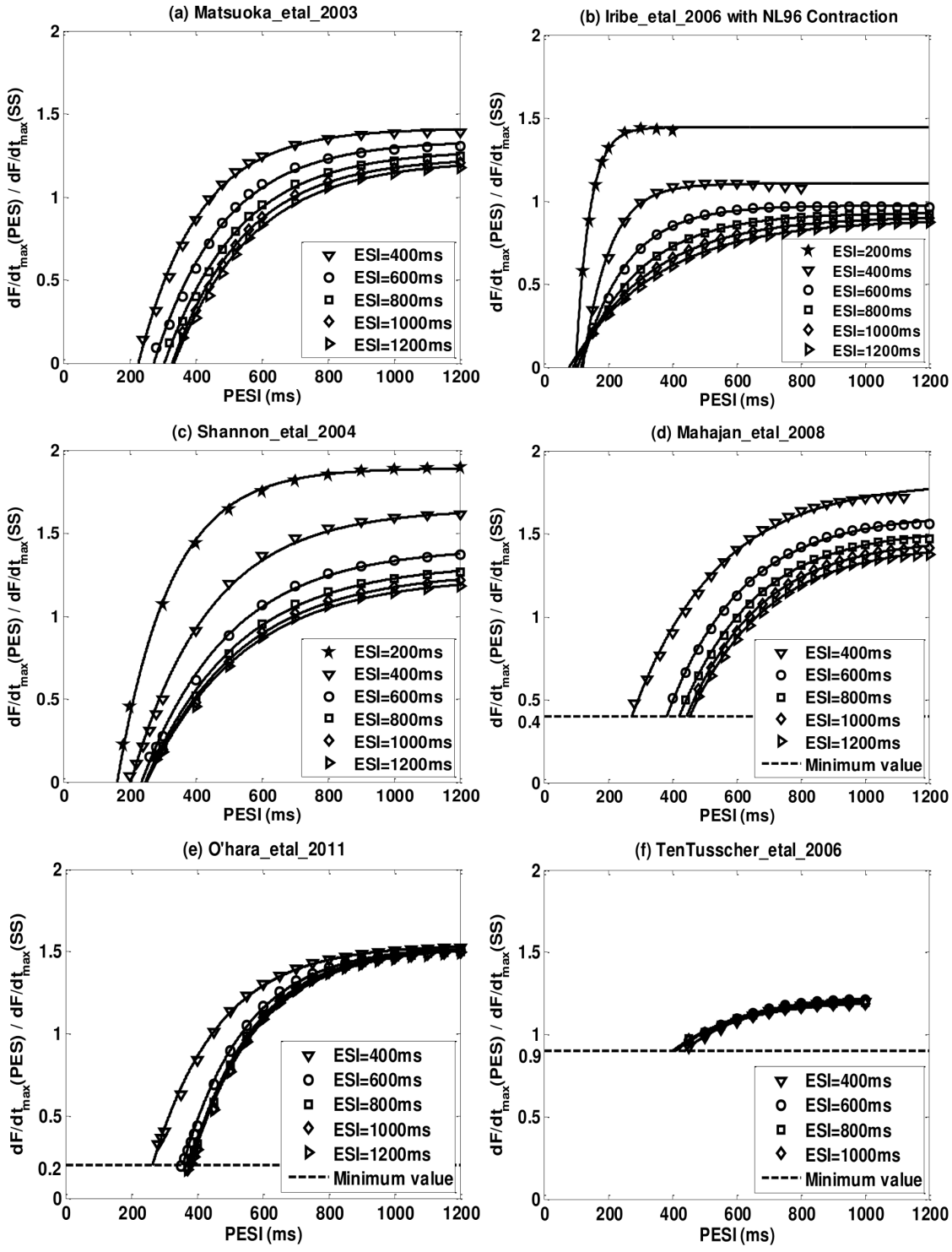

Figure 4.9: Representative postextrasystolic mechanical restitution curves (MRC_{pes}) for six models after implementation of the NL96 contraction: (a) Matsuoka_etal_2003; (b) Iribe_etal_2006; (c) Shannon_etal_2004; (d) Mahajan_etal_2008; (e) Ohara_etal_2011; (f) TenTusscher_etal_2006.

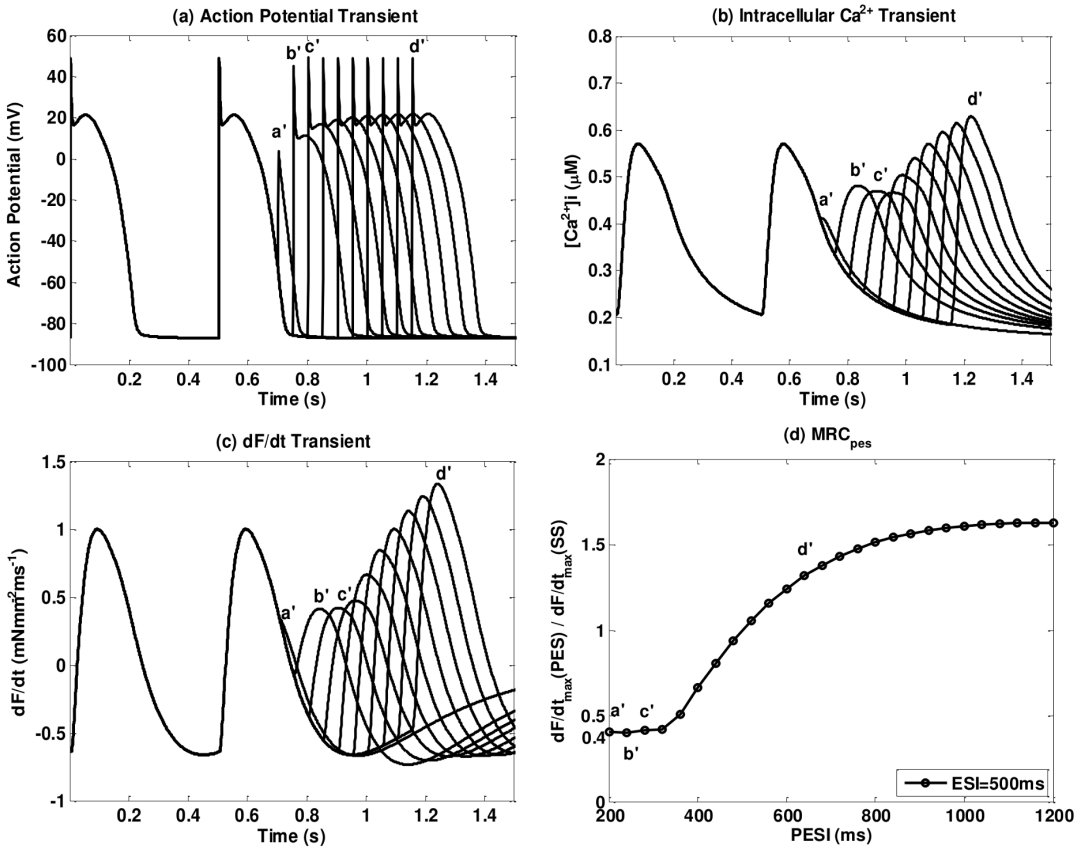

Figure 4.10: Details for cases where C_0 does not go to zero. We use as example the Mahajan_etal_2008 for ESI=500ms: (a) the action potential (AP), (b) Ca^{2+} transient; (c) normalized dF/dt transient (d) normalized dF/dt$_{max}$ of the PES beats. In (a) (b) and (c), the first beat is the priming beat; the second beat is the ES beat with ESI=500ms; from a' to d' are PES beats with PESI ranges from 200ms to 650ms.

in Figure 4.10(d). We can see that dF/dt$_{max}$ stops decreasing when PESI is below 300ms and the minimum value is about 0.4. In order to fit this into Eq. (4.8) we exclude data with PESI lower than 300ms and set $C_0 = 0.4$. That is the reason for Mahajan_etal_2008 and other eight models, that C_0 does not go to zero and also an example of how we choose the shortest ESI and PESI values.

The experimental results of Yue et al. [105] showed that the fully restituted plateau value of MRC_{pes} (CR$_{max,pes}$) decreased as ESI increased. From Figure 4.9 and Section B.3 in Appendix B we can see that all models with dynamic CaTRPN show unique plateau val-

ues for different ESIs while models with instantaneous or no CaTRPN converge to the same plateau values for different ESIs; this property will be further discussed in Section 4.3.2.

The time constant for MRC_{pes} ($T_{mrc,pes}$) did not vary much as a function of ESI in the experiment of Yue et al. [105]. In addition, a leftward shift of the MRC_{pes} was observed as ESI decreased, presented as an increase of $t_{o,pes}$ as ESI increased. The fourteen models behave differently regarding these two parameters. We will discuss these in detail in the $t_{o,pes}$ and $T_{mrc,pes}$ subsections.

Postextrasystolic Potentiation Curve (PESPC)

Figure 4.11 shows representative postextrasystolic potentiation curves (PESPCs) for six models. Figures for all the models can be found in Section B.4 in Appendix B. To provide a better picture of the amplitude and time constant of the PESPC we simultaneously plotted the PESPC and the Extrasystolic Mechanical Restitution Curve (MRC_{es}). Note that for those models with $C_0 \neq 0$ in the MRC_{es}, we have shifted the curves upward by C_0 when plotting the PESPC (star *) on the same graph with the MRC_{es} (open circle o) for comparison. We also use 95% confidence bounds as error bars for each data point on PESPC, which is the fitting confidence bound for $CR_{max,pes}$ of each ESI value. Note that confidence bounds are relatively small compared to the scale of the graph.

A list of all parameters for the curve fitting of Eq. (4.9) are listed in Table 4.8 for all the models along with the experimental data of Yue et al. [105] to allow comparison between our simulation results and those from the experiments. The values without any symbol match the experiment results well. They are either parameters with 95% confidence bounds overlapping the mean plus/minus standard deviation (mean$\pm$SD) range from Yue et al. or they have r^2 values that are higher than 0.99. The double and the triple star (** and ***) means the 95% confidence bound overlaps Yue et al. datas mean$\pm$2SD and the mean$\pm$3SD respectively. The X mark means the confidence bound overlaps the mean$\pm$SD but the confidence bound is too large (more than 50% of the center value) so that we did not

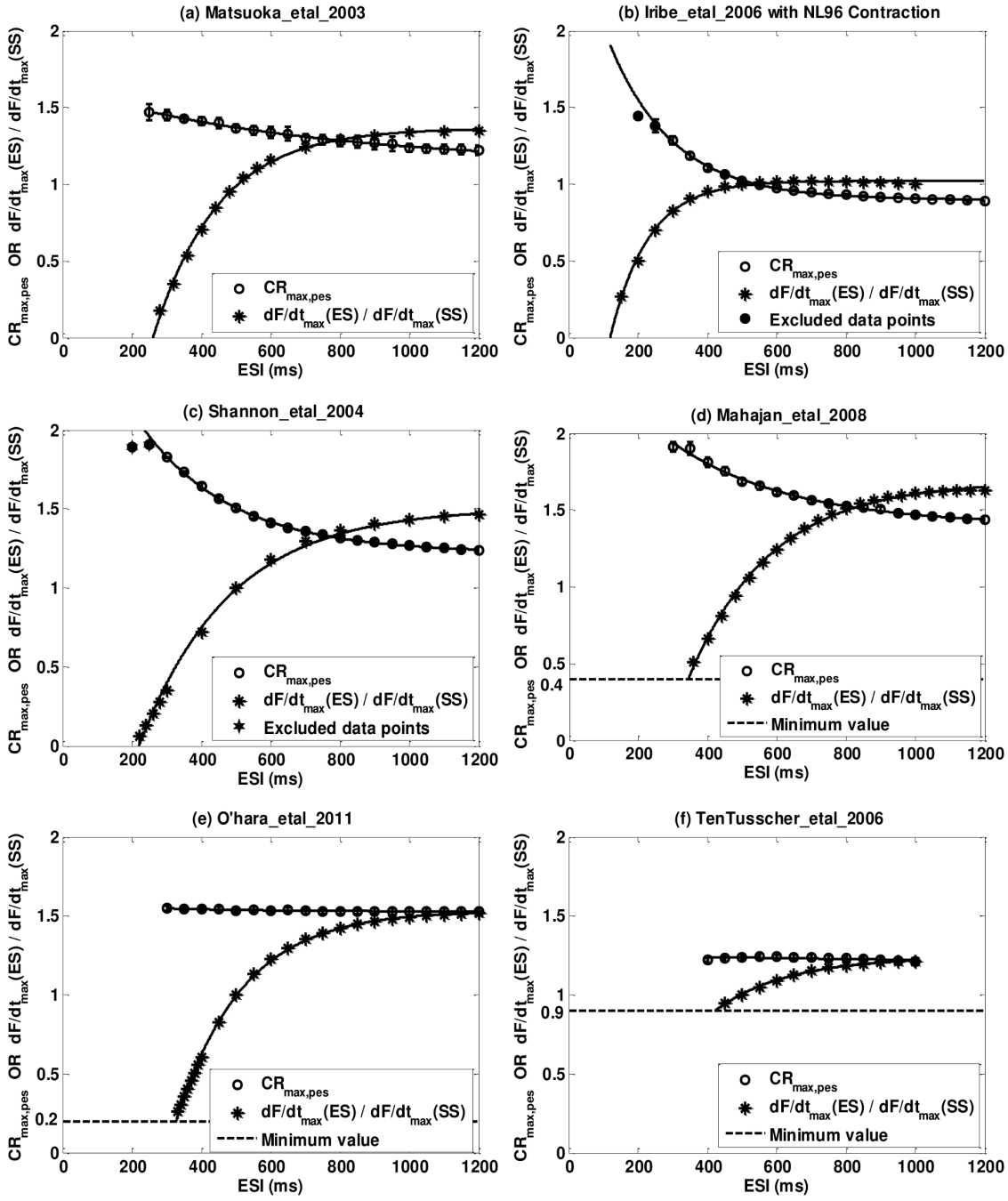

Figure 4.11: Representative postextrasystolic potentiation curve (PESPC, circles o) and extrasystolic mechanical restitution curve (MRC_{es}, stars *) for six models: (a) Matsuoka_etal_2003; (b) Iribe_etal_2006; (c) Shannon_etal_2004; (d) Mahajan_etal_2008; (e) Ohara_etal_2011; (f) TenTusscher_etal_2006. 95% confidence bounds of $CR_{max,pes}$ are plotted as error bars on PESPC but since the confidence bounds are small compared to the entire scale, they are not clearly observed in the figures.

consider this as a real overlapping. The double X mark (XX) means the confidence bound does not overlap the mean±nSD from Yue experiment with $n \leq 3$. The single-dagger (†) means the r^2 is less than 0.99 but more than 0.9 and the double-dagger (‡) means it's less than 0.9.

The experiments of Yue et al. showed that PESPC decreased monoexponentially to a plateau level as ESI increases (Eq. (4.9) and Figure 4.3(b)), meaning that when PESI is fixed and long enough, the maximum force changing rates of the PES beats will decrease as ESI increases. Models with dynamic CaTRPN (Type One, Two and Three) have PESPCs well described by Eq. (4.9); all six models have r^2 values larger than 0.99. On the other hand, models with instantaneous or no CaTRPN (Type Four and Five) are not well fit by Eq. (4.9). Four of the eight models have r^2 values lower than 0.9 with one of them as low as 0.0048 (Priebe_etal_1998). However, the poor quality of the fitting is not evident on Figure 4.11 or Section B.4 in Appendix B)) because the amplitude of the PESPC is much smaller than the scale of the figure.

The plateau levels (B) of $\mathrm{CR}_{max,pes}$ for the fourteen contraction models are more similar to the experiment results compared to the other parameters. In Yue et al. [105], the mean value (±SD) for B is 1.05±0.13. In our simulations, two out of the six models with dynamic CaTRPN (Type One, Two and Three) have 95% confidence bounds overlap the mean±SD range of Yue et al. [105] and four have confidence bounds overlap the mean±2SD range. On the other hand, only two out of eight models with instantaneous or no CaTRPN (Type Four and Five) have 95% confidence bounds overlap the mean±2SD range.

Parameter *A* has the least matching degree with Yue et al. [105] where the mean value (± SD) is 1.68±0.32. Only one out of the six models with dynamic CaTRPN (Type One, Two and Three) have 95% confidence bounds overlap the mean±2SD range from Yue paper and none of the models with instantaneous or none CaTRPN have confidence bounds overlapping this range (see Table 4.8). The values of A from our contraction models are

significantly smaller than Yue paper. This feature is well depicted in Figure 4.11 and Section B.4 in Appendix B in which the PESPCs of the models with instantaneous buffers have slopes of approximate zero while in the Yue et al. paper there exhibited a pronounced monoexponentially decay (Figure 4.3). The insufficient change in fully-restituted contractile strength of postextrosystoles with respect to varied ESIs indicates a clear limitation of these models as we will further comment in the discussions section.

$\boldsymbol{t_{o,pes}}$ is obtained by calculating where the Extrasystolic Mechanical Restitution Curve (MRC_{es}) intercepts the line $\frac{dF/dt_{max,es}}{dF/dt_{max,ss}} = C_0$. The mean value ($\pm$SD) in the Yue et al. [105] is 284$\pm$32ms. Four out of six models with dynamic CaTRPN (Type One, Two and Three) and five out of eight models with instantaneous buffers (Type Four and Five) are in the mean$\pm$2SD range. For this parameter, it seems that the dynamic buffers do not show much advantage over instantaneous buffers. However, in the Yue et al. paper, this interception is where MRC_{es} intercepts with the line $\frac{dF/dt_{max,es}}{dF/dt_{max,ss}} = 0$, so are four out of the six models with dynamic CaTRPN. But for most models with instantaneous buffers, this parameter is where MRC_{es} intercepts with the line $\frac{dF/dt_{max,es}}{dF/dt_{max,ss}} = C_0$ with $C_0 \neq 0$. Therefore models with dynamic buffers still match this parameter better to the experimental data of Yue et al. [105].

The mean value ($\pm$SD) of **the time constant for PESPC** (T_{pespc}) is 176$\pm$18ms in Yue et al. [105]. Only two out of the six models with dynamic CaTRPN (Type One, Two, Three) and none of the models with instantaneous or none buffers (Type Four and Five) have 95% confidence bounds that overlap the experimental mean$\pm$2SD range. Ten other models have time constants much larger (50% more) than Yue et al. [105]. This parameter is also the worst fit for models with instantaneous or no CaTRPN; five out of eight models have 95% confidence bounds larger than 50% of the center values, indicating a poor fit.

Minimum-value Axis Intercept Curve ($t_{o,pes}$)

Figure 4.12 shows Minimum-value Axis Intercept Curves for six models. Open circles (o) are for different ESI values. Error bars are 95% confidence bounds. Figures for all models are provided in Section B.4 in Appendix B and the summarized data is in Table 4.9.

In the Yue et al. paper [105], $t_{o,pes}$ increased as ESI increased. They explained this trend by suggesting that the refractory period is an increasing function of ESI. Five out of six models with dynamic CaTRPN (Type One, Two and Three) show the same trend as Yue et al. paper with $t_{o,pes}$ increasing exponentially with ESI; only the Iribe_etal_2006 model shows a non-monotonic behavior. Three out of eight models with instantaneous buffers (Type Four and Five) show the same trend as Yue et al. (Hund_etal_2004, Livshitz_etal_2007 and Ohara_etal_2011) while three models show a monotonically decreasing trend (Faber_etal_2000, TenTusscher_etal_2006 and Fink_etal_2008) and two (Priebe_etal_1998 and Fox_etal_2002) do not have monotonic behaviors. The range of $t_{o,pes}$ of the models match Yue et al. paper well as thirteen out of fourteen models fall within the experimental range.

Time Constant Curve ($T_{mrc,pes}$)

Figure 4.13 shows six Time Constant Curves, i.e. time constants of MRC_{pes} ($T_{mrc,pes}$) vs ESI for 6 models, where the dash line indicates the mean $T_{mrc,pes}$ from the Yue et al. paper; the gray area denotes the range of the mean$\pm$SD range. Open circles (o) are $T_{mrc,pes}$ from curve fitting for different ESI values. Error bars are 95% confidence bounds. Figures for all the models are in Section B.6 in Appendix B. There were two major results in Yue et al. [105] regarding $T_{mrc,pes}$. First, $T_{mrc,pes}$ varied little with ESI; the mean ($\pm$SD) was 181$\pm$41ms and the normalized mean (normalize to $T_{mrc,es}$) was 1.01$\pm$0.12. In our simulations, all of the models have their normalized time constant values overlap the mean$\pm$2SD range from Yue paper while ten of the models have their $T_{mrc,es}$ (identical to $T_{mrc,pes}$ with ESI=500ms in simulations) overlap the mean$\pm$2SD range from Yue paper. Therefore our

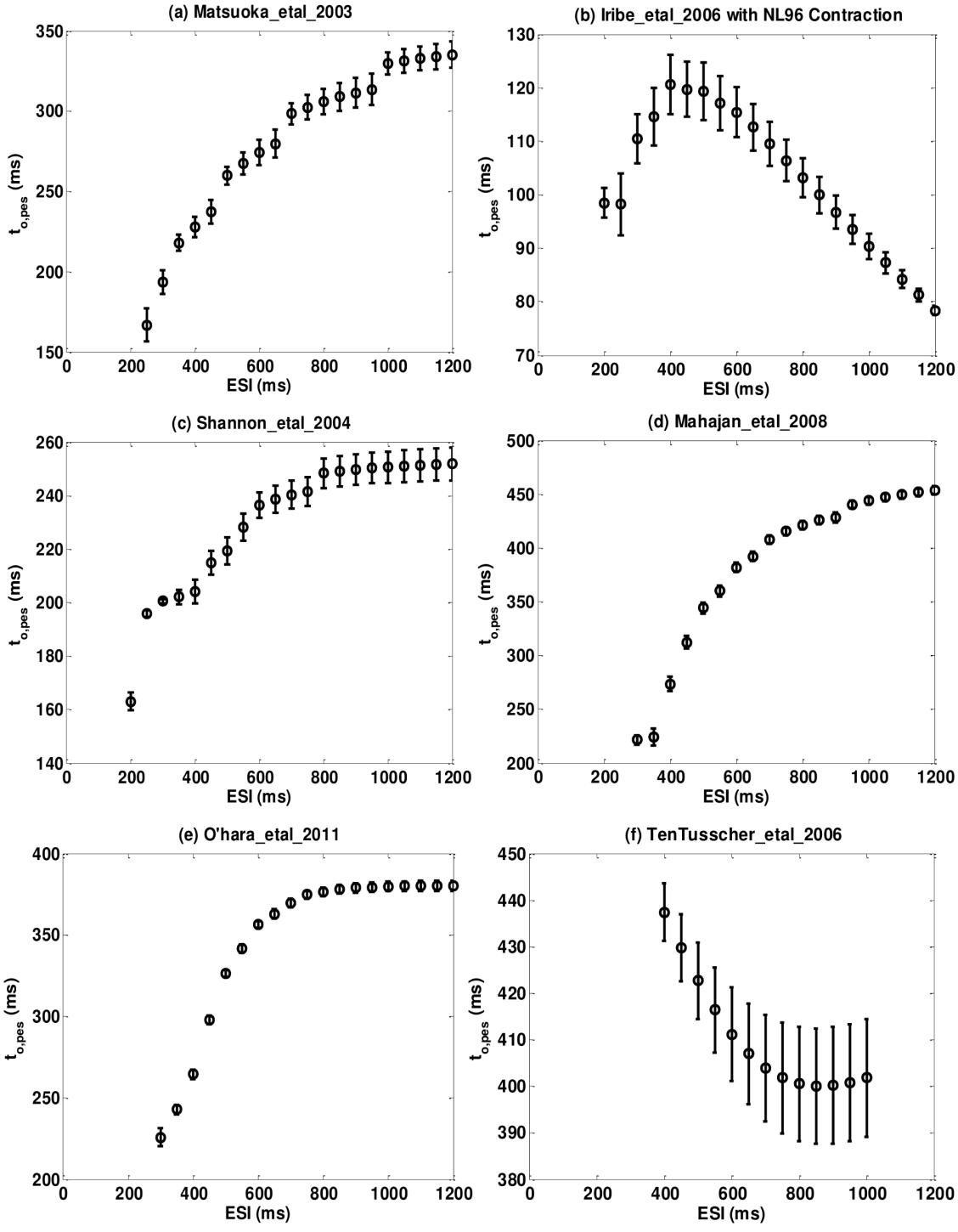

Figure 4.12: Representative minimum-value axis intercept curve ($t_{o,pes}$) for six models: (a) Matsuoka_etal_2003; (b) Iribe_etal_2006; (c) Shannon_etal_2004; (d) Mahajan_etal_2008; (e) Ohara_etal_2011; (f) TenTusscher_etal_2006. 95% confidence bounds of $t_{o,pes}$ are plotted as error bars.

contraction models fit this property with Yue paper quite well. The second major result from Yue paper is that the time constants of PESPC and MRC_{pes} were close; the mean difference between the two time constants ($\pm$SD) was 13$\pm$23ms. Models with dynamic CaTRPN (Type One, Two and Three) are more consistent with the experiments than instantaneous buffers (Type Four and Five) in this respect. Three out of six models with dynamic buffers have 95% confidence bounds that overlap Yues mean$\pm$2SD range while only one out of eight models with instantaneous buffers overlaps that. Six of them have large 95% confidence bounds inherited from the large T_{pespc} bounds, so we marked them by a symbol $\aleph$, indicating the 95% confidence bounds overlap Yue's mean$\pm$SD but the confidence bound is so large (more than 3SD) that we do not consider this as a real overlapping.

4.3.3 Underlying mechanism for postextrasystolic potentiation

There is a clear resemblance between the intracellular Ca^{2+} dynamic and the force dynamics. And since the Ca^{2+} released from SR (J_{rel}) is the main source for intracellular Ca^{2+}, we propose that J_{rel} dynamics, which depends on RyR, Ca^{2+}_{SR}, among others, is the primary determinant of PESP dynamics.

To verify this hypothesis, we analyzed, for each model, the correlation between the dependence of the potentiation in Ca^{2+} released from SR (J_{rel}) and the contractile strength on pacing intervals. In this study we have shown two sets of curves demonstrating the potentiation strength: the Postextrasystolic Mechanical Restitution Curve (MRC_{pes}) and the Postextrasystolic Potentiation Curve (PESPC). The former demonstrates how postextrasystolic contractile strength changes with respect to various PESI for a fixed ESI. From Figure 4.9 and Section B.3 in Appendix B, it can be seen the consistency of the increasing trend of the normalized force changing rate with respect to PESI for all models studied. However, the PESPC, which shows how postextrasystolic contractile strength changes with respect to various ESI values for a fixed and long PESI, differs among models: models with dynamic buffers showed significant variation in contractile strength with respect to

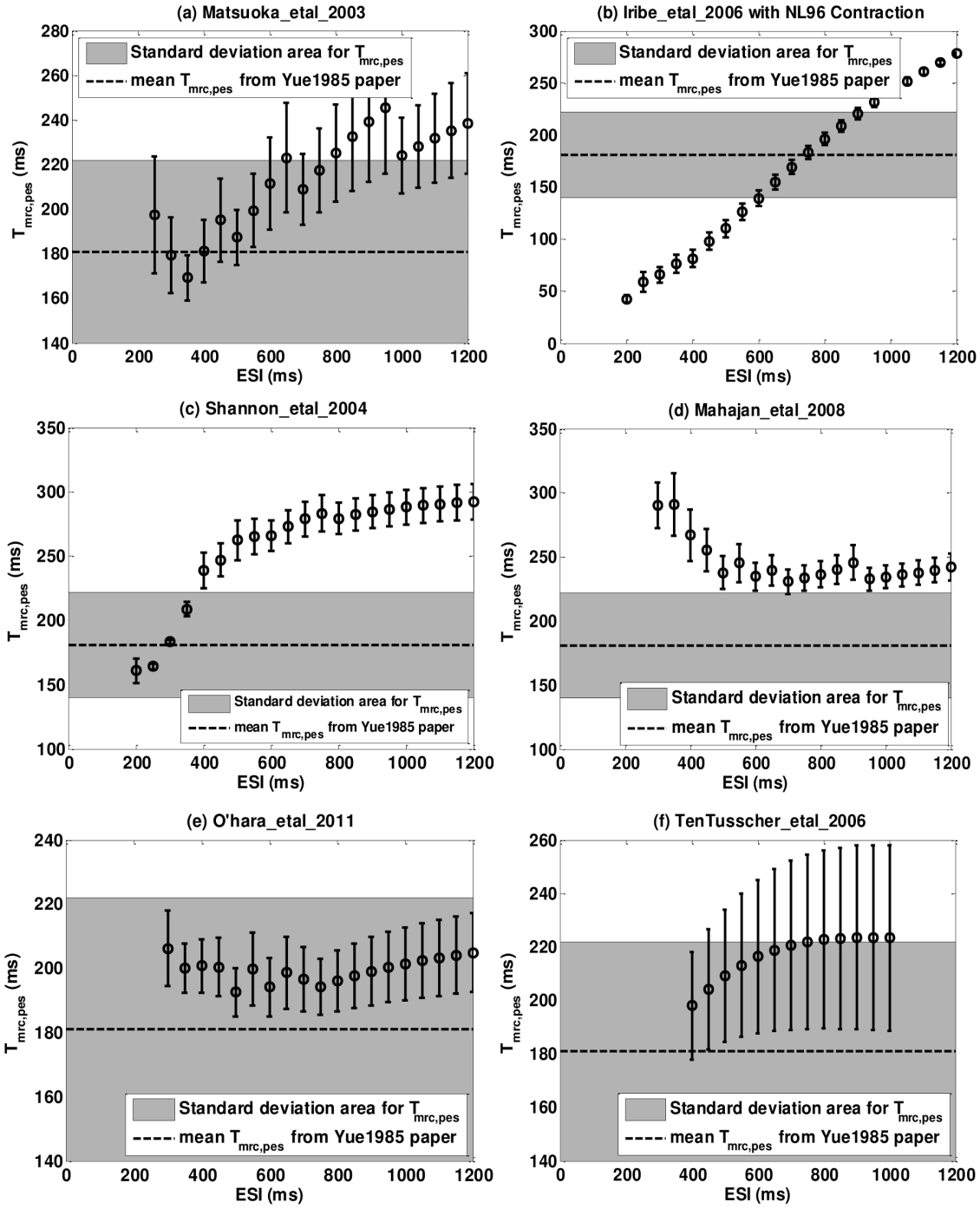

Figure 4.13: Representative time constant for MRC_{pes} curve ($T_{mrc,pes}$) for six models: (a) Matsuoka_etal_2003; (b) Iribe_etal_2006; (c) Shannon_etal_2004; (d) Mahajan_etal_2008; (e) Ohara_etal_2011; (f) TenTusscher_etal_2006. Error bars are 95% confidence bounds. The dash line indicates mean $T_{mrc,pes}$ for ESI=460ms from Yue et al. The gray area denotes their standard deviation range.

Table 4.1: Terminology: definition of variables. Yue et al. 1985 paper measured pressure changing rate. In our simulations we calculate tension changing rate and we replace P with F

Type	Name	Definition
Pacing interval	SSI (PI,PP)	Steady state interval (or priming interval/priming period): interval between steady state stimuli. It's 500ms in our simulations
	ESI	Extrasystolic interval: interval between extrasystolic and the last steady state stimuli
	PESI	Postextrasystolic interval: interval between postextrasystolic and extrasystolic stimuli
Measured quantity	dP/dt$_{max}$(SS)	Maximum pressure rising rate of steady state beats
	dP/dt$_{max}$(ES)	Maximum pressure rising rate of extrasystolic beats
	dP/dt$_{max}$(PES)	Maximum pressure rising rate of postextrasystolic beats
	$[Ca^{2+}]_i$	Intracellular calcium concentration
Force-interval relations	MRC_{pes}	Postextrasystolic mechanical restitution curve: normalized dP/dt$_{max}$ of postextrasystoles plotted vs PESI
	MRC_{es}	Extrasystolic mechanical restitution curve: normalized dP/dt_{max} of extrasystoles plotted vs ESI
	PESPC	Postextrasystolic potentiation curve: normalized dP/dt_{max} of fully restituted postextrasystoles ($CR_{max,pes}$) plotted vs ESI
Parameters for MRC_{pes}	$CR_{max,pes}$	Maximum postextrasystolic contractile response: plateau value for MRC_{pes}
	$T_{mrc,pes}$	Time constant for MRC_{pes}
	$t_{o,pes}$	PESI-axis intercept value
Parameters for PESPC	A	Amplitude
	B	Plateau value
	T$_{pespc}$	Time constant

Table 4.2: General information of 14 electrophysiological models including classification of models (model type, model name, species, type of intracellular Ca buffers) and model properties (number of variables in the original model, stimulus current amplitude and duration).

Model Type	Model Name	Species	CaTRPN Buffer	Other Ca^{2+} Buffer	No. of Variables	Stimulus Current (A/F)	Stimulus Duration (ms)
Type One	Matsuoka_etal_2003	guinea pig	NL96	none	37	-8	1
	Iribie_etal_2006	guinea pig	RWH99	dynamic	23	-4	2
Type Two	Shannon_etal_2004	rabbit	dynamic	dynamic	39	-15	4
	Grandi_etal_2010	human	dynamic	dynamic	39	-9.5	4
Type Three	Mahajan_etal_2008	rabbit	dynamic	instantaneous	26	-30	2
	Iyer_etal_2004	human	dynamic	instantaneous	67	-25	2
Type Four	Hund_etal_2004	dog	instantaneous	instantaneous	29	-30	2
	Faber_etal_2000	guinea pig	instantaneous	instantaneous	25	-25.5	2
	Livshitz_etal_2007	guinea pig	instantaneous	instantaneous	18	-15	2
	Ohara_etal_2011	human	instantaneous	instantaneous	41	-80	0.5
	Priebe_etal_1998	human	instantaneous	instantaneous	22	-30	2
Type Five	Fox_etal_2002	dog	none	instantaneous	13	-80	1
	TenTusscher_etal_2006	human	none	instantaneous	19	-51	1
	Fink_etal_2008	human	none	instantaneous	27	-24	2

Table 4.3: General information of 14 electrophysiological models including parameters of CaTRPN (K_d, K_{on}, K_{off}), approximate time to reach quiescent states, beat number to reach priming steady states and ESI,PESI ranges.

Model Type	Model Name	K_d (mM)	K_{on} ($mM^{-1}ms^{-1}$)	K_{off} (ms^{-1})	Quiescent time	Prime beat No	ESI(ms)	PESI(ms)
Type One	Matsuoka_etal_2003	7.69E-04	3.90E+01	3.00E-02	20min	500	250-1200	100-1200
	Iribie_etal_2006	function of F	8.00E+01	3.00E-01	10min	500	200-1200	100-1200
Type Two	Shannon_etal_2004	6.00E-04	3.27E+01	1.96E-02	20min	1500	200-1200	100-2000
	Grandi_etal_2010	6.00E-04	3.27E+01	1.96E-02	20min	500	300-1200	200-1200
Type Three	Mahajan_etal_2008	6.00E-04	3.27E+01	1.96E-02	10min	1500	300-1200	200-1200
	Iyer_etal_2004	1.00E-03	4.00E+01	4.00E-02	40min	15000	250-1500	200-1500
Type Four	Hund_etal_2004	5.00E-04	3.58E+01	1.79E-02	80min	6000 10500	250-1200	150-1200
	Faber_etal_2000	5.00E-04	3.58E+01	1.79E-02	20min	1500	200-1500	350-1500
	Livshitz_etal_2007	5.00E-04	3.58E+01	1.79E-02	20min	1500	200-1200	200-1200
	Ohara_etal_2011	5.00E-04	3.58E+01	1.79E-02	20min	1000	300-1200	200-1200
	Priebe_etal_1998	5.00E-04	3.58E+01	1.79E-02	20min	1500	400-2000	400-2000
Type Five	Fox_etal_2002	6.00E-04	3.27E+01	1.96E-02	20min	1500	200-2000	200-2000
	TenTusscher_etal_2006	1.00E-03	2.53E+01	2.50E-02	20min	1500	400-1000	450-1000
	Fink_etal_2008	1.00E-03	2.53E+01	2.50E-02	40min	1500	350-1200	350-1200

Table 4.4: Quiescent state variables: membrane voltage, intracellular calcium condensation and JSR (or SR) calcium condensation. If the original model does not have contraction, we run the original model to get quiescent state. If the original model has contraction, we take out the contraction part and run that to quiescent state.

Model Type	Model Name	whether original	V_m (mV)	$[Ca^{2+}]_i$ (mM)	$[Ca^{2+}]_{JSR}$ (mM)	$[Ca^{2+}]_{SR}$ (mM)
Type One	Matsuoka_etal_2003	No	-85.9	2.92E-06	4.76E+00	5.50E+00
	Iribie_etal_2006	No	-94.3	5.50E-06	NA	6.82E-03
Type Two	Shannon_etal_2004	Yes	-85.4	7.06E-05	NA	4.58E-01
	Grandi_etal_2010	Yes	-81.0	7.08E-05	NA	4.60E-01
Type Three	Mahajan_etal_2008	Yes	-86.4	5.31E-05	3.68E-02	7.36E-02
	Iyer_etal_2004	Yes	-91.6	1.40E-05	3.92E-02	7.84E-02
Type Four	Hund_etal_2004	Yes	-86.9	8.34E-05	1.27E+00	2.54E+00
	Faber_etal_2000	Yes	-85.3	7.19E-05	1.09E+00	2.18E+00
	Livshitz_etal_2007	Yes	-90.0	8.00E-05	7.20E+00	8.40E+00
	Ohara_etal_2011	Yes	-88.3	5.58E-05	9.82E-01	1.96E+00
	Priebe_etal_1998	Yes	-91.6	9.26E-05	1.58E+00	3.17E+00
Type Five	Fox_etal_2002	Yes	-94.3	5.02E-05	NA	1.11E+00
	TenTusscher_etal_2006	Yes	-87.5	2.58E-05	NA	1.87E-01
	Fink_etal_2008	Yes	-86.8	9.05E-05	NA	2.05E+00

Table 4.5: Data for steady priming beat: EP models without contraction.

Model Type	Model Name	$[Ca^{2+}]_i$_diastolic(mM)	$[Ca^{2+}]_i$_systolic(mM)	$t_1/2$(ms)	t_{peak}(ms)	Q (mM*ms)
Type One	Matsuoka_etal_2003	1.46E-05	1.50E-03	5.69E+01	2.02E+01	9.80E-02
	Iribie_etal_2006	1.03E-05	1.50E-03	5.25E+01	2.08E+01	8.40E-02
Type Two	Shannon_etal_2004	1.13E-04	4.80E-04	1.41E+02	4.60E+01	5.90E-02
	Grandi_etal_2010	1.11E-04	3.82E-04	1.42E+02	5.49E+01	4.49E-02
Type Three	Mahajan_etal_2008	2.04E-04	5.61E-04	1.94E+02	7.90E+01	7.57E-02
	Iyer_etal_2004	2.33E-04	9.90E-04	2.23E+02	7.80E+01	1.80E-01
Type Four	Hund_etal_2004 1.86E-04	7.37E-04	1.64E+02	4.27E+01	1.02E-01	
	Faber_etal_2000	2.45E-04	2.00E-03	9.75E+01	1.47E+01	2.04E-01
	Livshitz_etal_2007	1.73E-04	1.40E-03	1.20E+02	2.20E+01	1.61E-01
	Ohara_etal_2011	1.18E-04	6.52E-04	1.37E+02	4.31E+01	8.74E-02
	Priebe_etal_1998	4.31E-04	9.73E-04	1.75E+02	1.52E+01	1.10E-01
Type Five	Fox_etal_2002	3.80E-05	1.62E-03	8.22E+01	1.75E+01	1.52E-01
	TenTusscher_etal_2006	1.51E-04	1.50E-03	1.38E+02	2.93E+01	2.10E-01
	Fink_etal_2008	1.42E-04	1.50E-03	1.02E+02	3.43E+01	1.72E-01

Table 4.6: Data for steady priming beat: models with NL96 contraction.

Model Type	Model Name	$[Ca^{2+}]_i$ diastolic (mM)	$[Ca^{2+}]_i$ systolic (mM)	$t_1/2$(ms)	t_{peak}(ms)	Q (mM*ms)
Type One	Matsuoka_etal_2003	1.49E-05	1.60E-03	5.65E+01	2.01E+01	1.02E-01
	Iribie_etal_2006	1.04E-05	1.40E-03	5.26E+01	2.06E+01	8.19E-02
Type Two	Shannon_etal_2004	1.12E-04	4.75E-04	1.46E+02	5.80E+01	5.99E-02
	Grandi_etal_2010	1.14E-04	3.87E-04	1.35E+02	5.48E+01	4.38E-02
Type Three	Mahajan_etal_2008	2.06E-04	5.70E-04	1.89E+02	7.80E+01	7.49E-02
	Iyer_etal_2004	2.41E-04	1.00E-03	2.16E+02	7.60E+01	1.83E-01
Type Four	Hund_etal_2004	1.95E-04	1.20E-03	7.05E+01	1.18E+01	1.06E-01
	Faber_etal_2000	2.27E-04	4.80E-03	6.90E+00	3.79E+00	1.80E-01
	Livshitz_etal_2007	1.86E-04	2.30E-03	2.99E+01	1.60E+01	1.19E-01
	Ohara_etal_2011	1.29E-04	1.00E-03	5.81E+01	1.66E+01	9.00E-02
	Priebe_etal_1998	4.23E-04	1.60E-03	1.93E+01	1.01E+01	1.11E-01
Type Five	Fox_etal_2002	1.16E-04	2.79E-04	1.86E+02	1.38E+01	3.35E-02
	TenTusscher_etal_2006	1.59E-04	2.00E-03	7.47E+01	2.59E+01	2.15E-01
	Fink_etal_2008	1.49E-04	2.00E-03	5.99E+01	3.14E+01	1.75E-01

Table 4.7: Data for steady priming beat: relative differences between EP models and models with NL96 contractions. † inidcates the relative difference is between 10% and 50%. ‡ indicates the relative difference is more than 50%

Model Type	Model Name	Δ $[Ca^{2+}]_i$ diastolic	$\Delta[Ca^{2+}]_i$ systolic	$\Delta t_1/2$	Δt_{peak}	ΔQ
Type One	Matsuoka_etal_2003	1.80E-02	6.67E-02	-7.33E-03	-7.52E-03	3.78E-02
	Iribie_etal_2006	1.06E-02	-6.67E-02	1.54E-03	-9.41E-03	-2.55E-02
Type Two	Shannon_etal_2004	-5.31E-03	-1.02E-02	3.55E-02	2.61E-01‡	1.53E-02
	Grandi_etal_2010	2.23E-02	1.23E-02	-4.68E-02	-2.31E-03	-2.45E-02
Type Three	Mahajan_etal_2008	1.03E-02	1.60E-02	-2.58E-02	-1.27E-02	-9.66E-03
	Iyer_etal_2004	3.31E-02	1.03E-02	-3.15E-02	-2.56E-02	1.72E-02
Type Four	Hund_etal_2004	4.82E-02	6.28E-01‡	-5.71E-01‡	-7.25E-01‡	3.53E-02
	Faber_etal_2000	-7.55E-02	1.60E+00‡	-9.29E-01‡	-7.43E-01‡	-1.21E-01†
	Livshitz_etal_2007	7.47E-02	6.43E-01‡	-7.51E-01‡	-2.73E-01†	-2.61E-01†
	Ohara_etal_2011	9.24E-02	5.34E-01‡	-5.75E-01‡	-6.15E-01‡	2.97E-02
	Priebe_etal_1998	-1.69E-02	6.44E-01‡	-8.90E-01‡	-3.36E-01†	1.46E-02
Type Five	Fox_etal_2002	2.05E+00‡	-8.28E-01‡	1.26E+00‡	-2.12E-01†	-7.79E-01‡
	TenTusscher_etal_2006	5.20E-02	3.33E-01†	-4.59E-01†	-1.15E-01†	2.43E-02
	Fink_etal_2008	4.86E-02	3.33E-01†	-4.11E-01†	-8.53E-02	2.10E-02

Table 4.8: Contraction parameters: MRC_{pes} and PESPC. ** indicates the models 95% confidence bound overlaps the mean±2SD value in Yue et al 1985 experiment. *** indicates the models 95% confidence bound overlaps the mean±3SD value in Yue et al 1985 experiment. XX indicates the models 95% confidence bound does not overlap the mean±nSD value in Yue et al 1985 experiment with n3. X indicates the models 95% confidence bound overlaps the mean±SD value in Yue et al 1985 but the bound is more than 50% of the center value. † indicates 0.9 $r^2 \leq 0.99$. ‡ indicates $r^2 < 0.9$.

Model Type	Model Name	MRC_{pes}		PESPC				
		Mean r square	C_0	B	A	$t_{o,es}$(ms)	T_{pespc}(ms)	r square
Experiment	Yue et al 1985	NA	0	1.05±0.13	1.68±0.32	284±32	176±18	NA
Type One	Matsuoka_etal_2003	0.9967	0	1.13±0.05	0.34±0.04 XX	260±6	704±156 XX	0.9944
	Iribie_etal_2006	0.9953	0	0.90±0.01 **	1.01±0.09 **	119±6 XX	184±13	0.9969
Type Two	Shannon_etal_2004	0.9988	0	1.22±0.01 **	0.83±0.02 ***	219±6 **	263±9 XX	0.9996
	Grandi_etal_2010	0.9991	0	1.47±0.01 XX	0.65±0.02 XX	297±4	221±13 **	0.9983
Type Three	Mahajan_etal_2008	0.9987	0.4 XX	1.00±0.03	0.47±0.03 XX	344±6 **	346±49 XX	0.9938
	Iyer_etal_2004	0.9987	0.4 XX	1.49±0.05 XX	0.48±0.05 XX	366±3 ***	608±96 XX	0.9933
Type Four	Hund_etal_2004	0.9991	0	1.47±0.01 XX	0.02±0.01 XX	233±4 **	471±320 X	0.9043 †
	Faber_etal_2000	0.9986	0.7 XX	0.74±0.01 ***	-0.01±0.01 XX	334±6 **	323±46 XX	0.9865 †
	Livshitz_etal_2007	0.9998	0.5 XX	0.80±0.01 **	0.04±0.01 XX	312±1	413±100 XX	0.9814 †
	Ohara_etal_2011	0.9988	0.2 XX	1.33±0.01 ***	0.02±0.01 XX	326±3 **	322±196 X	0.8848 ‡
	Priebe_etal_1998	0.9992	1.1 XX	0.77±0.01 ***	-0.00±0.01 XX	566±4 XX	232±7809 X	0.0048 ‡
Type Five	Fox_etal_2002	0.9991	0.5 XX	1.32±0.01 **	0.01±0.01 XX	321±4 **	328±94 XX	0.9156 †
	TenTusscher_etal_2006	0.9971	0.9 XX	0.01±32.8 X	0.33±32.8 X	423±9 XX	1.04e4±1e6X	0.4278 ‡
	Fink_etal_2008	0.9977	0.9 XX	0.31±0.01 XX	0.01±0.01 XX	392±6 XX	190±121 X	0.8208 ‡

Table 4.9: Contraction parameters: $t_{o,pes}$ and $T_{mrc,pes}$. ** indicates the models 95% confidence bound overlaps the mean±2SD value in Yue et al 1985 experiment. *** indicates the models 95% confidence bound overlaps the mean±3SD value in Yue et al 1985 experiment. XX indicates the models 95% confidence bound does not overlap the mean±nSD value in Yue et al 1985 experiment with n3. X indicatese the models 95% confidence bound overlaps the mean±SD value in Yue et al 1985 but the bound is more than 50% of the center value. indicates the models 95% confidence bound overlaps the mean±SD value in Yue et al 1985 but the bound is more than 3SD. • indicates the plus/minus is the standard deviation. The other plus/minus are 95% confidence range.

Model Type	Model Name	$t_{o,pes}$		$T_{mrc,pes}$		
		Trend w.r.t. ESI	Range(ms)	$T_{mrc,es}$(ms)	Mean±SD •	T_{pespc}-$T_{mrc,es}$(ms)
Experiment	Yue et al. 1985	Monotonic increase	180-420	181±41	1.01±0.12	13±23
Type One	Matsuoka_etal_2003	Monotonic increase	167-335	187±13	1.15±0.12	517±156 XX
	Iribie_etal_2006	Not monotonic XX	78-120 XX	110±9 **	1.52±0.71	74±13 ***
Type Two	Shannon_etal_2004	Monotonic increase	163-252	262±16 **	0.98±0.17	1±16
	Grandi_etal_2010	Monotonic increase	245-350	234±10 **	1.01±0.11	-13±13
Type Three	Mahajan_etal_2008	Monotonic increase	221-454	238±14 **	1.04±0.08	108±49 **
	Iyer_etal_2004	Monotonic increase	305-498	333±10 XX	1.04±0.04	275±96 XX
Type Four	Hund_etal_2004	Monotonic increase	126-242	234±9 **	1.00±0.02	237±320 א
	Faber_etal_2000	Monotonic decrease XX	297-342	300±13 ***	1.02±0.04	23±46
	Livshitz_etal_2007	Monotonic increase	232-333	203±3	1.02±0.06	210±100 XX
	Ohara_etal_2011	Monotonic increase	226-380	193±8	1.04±0.02	129±196 א
	Priebe_etal_1998	Not monotonic XX	377-624	438±14 XX	1.04±0.03	-206±7809 א
Type Five	Fox_etal_2002	Not monotonic XX	244-380	370±8 XX	1.00±0.02	-4294 א
	TenTusscher_etal_2006	Monotonic decrease XX	402-437	209±25	1.04±0.04	1.02e4±1e6 א
	Fink_etal_2008	Monotonic decrease XX	341-420	256±18 **	1.0±0.03	-66±121 א

ESI while models with instantaneous buffers showed little variation (Figure 4.11 and Section B.4 in Appendix B). The amplitude (parameter A) in PESPC captures this difference. Since we are interested in what causes the difference in models, we studied the correlation between the Ca^{2+} released from SR (J_{rel}) and the contractile strength of the postextrasystoles with various ESIs and fixed a PESI. We designed an analogous parameter A_J for the J_{rel} amplitude. Similar to our dF/dt$_{max}$ fit, for a fixed ESI, we first fitted the normalized J_{rel_max} (to the prime beats) of the postextrasystolic beats to a mono-exponentially increasing curve with respect to PESI (analogous to MRC_{pes}). For most models, J_{rel_max} was well described by a mono-exponential increasing curve, similar to the contractile strength. Then we fitted the plateau values of these curves to a mono-exponentially decreasing curve with respect to ESI (analogous to PESPC); we define the amplitude of this curve as A_J. Models with larger A_J suggest that their fully-restituted J_{rel_max} vary with respect to ESI. Therefore the correlation between A and A_J can be used as a gauge for the correlation between the dependence of J_{rel} and the contractile strength on pacing intervals. We performed a linear regression for A_J and A for thirteen (out of the fourteen) electromechanical models as shown in Fig 11. We found a strong positive correlation (r^2=0.848) between the two parameters. In addition, data from models with instantaneous buffers clustered around the origin while data from models with dynamic buffers were distributed along the regression curve. **This means for models with instantaneous buffers, the insufficient variation in the fully-restituted postextrasystolic contractile strength responding to various ESI is a direct result of the J_{rel} dynamics**. Note that the model excluded from the linear regression was TenTusscher_etal_2006 (upward triangular mark in Figure 4.14) because the curve fitting for parameter A in this model is not reliable due to its large 95% confidence bound (see Table 4.8).

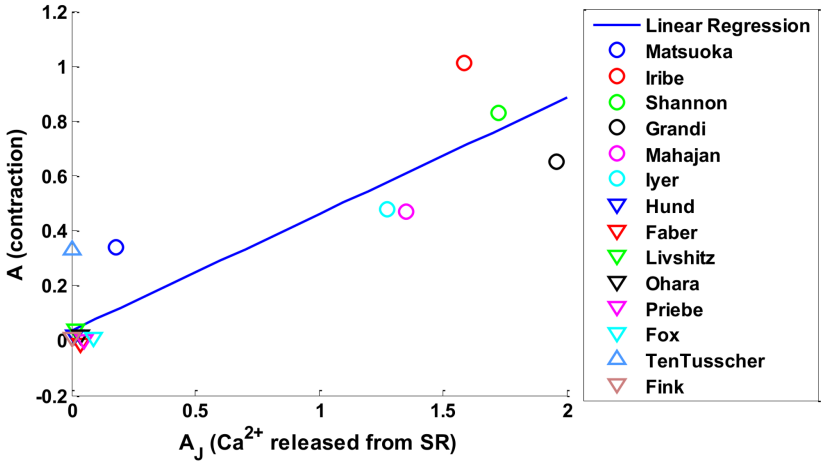

Figure 4.14: Correlation between the potentiation in J_{rel} and contractile strength: the Postextrasystolic Potentiation Curves (PESPC) amplitude of contractile strength (A) vs that of calcium released from SR (A_J).

4.4 Discussion

4.4.1 Verifying the choice of contraction model

To assess the robustness of the contraction model we use, we conducted more careful verifications in Appendix C and Appendix D.

In Appendix C, we compared NL96 with two other contraction models: i) NL96 and RWH99 implemented in Iribe_etal_2006; ii) dynamic (original) NL96 and instantaneous NL96 implemented in Ohara_etal_2011. In the first set of comparison, we conclude that under the isometric condition there are no significant differences between NL96 and RWH99 under the scope of this study in the sense that each one matches different parameters with experiments better than the other. In the second set of comparison we find that although including NL96 in models with instantaneous CaTRPN distort their Ca^{2+} shape, the poor contraction behaviors of these models are not directly related to that. Two simulation results support this conclusion. First, their original models do not show clear postextrasystolic potentiation behavior in Ca^{2+} (see Figure 4.8), which is directly related to the lack of

variation in contractile strength and second, Ca^{2+} shape is retained after the implementation of the instantaneous NL96 yet the contraction behavior of Ohara_etal_2011 is still not optimal.

Finally in Appendix D, we conducted verifications of physiological parameters such as different priming period, low temperature and cooperativity of the contraction model. By comparing simulation results before and after modification of these physiological parameters, we showed that the choice of parameters did not change quantitatively the PESP behavior.

4.4.2 Conclusion and limitation

Simulations of electrical therapies for HF (e.g., CRT and CCM) require models that accurately reproduce the excitation-contraction coupling that occurs in the cardiac myocyte. While action potential duration restitution curves tend to be used to help validate EP models, there has been no systematic method to validate cellular contraction models. We suggest that the PESP protocol can be used in the validation process of mathematical models of cellular electromechanics and we present a methodology to include mechanics into cellular EP models of various types and compare results among the models with and without contraction. The results from this study suggest four reasons why electrophysiology models with dynamic CaTRPN are much better candidates to implement contraction than EP models with instantaneous or none CaTRPN.

First, the complexity in implementation is greatly reduced since the original models are already equipped with dynamic equations for CaTRPN. Type Two and Type three models only take one step in the implementation flowchart while Type Four and Type Five require one or two more steps to add in instantaneous CaTRPN and change that into a dynamic form (see Appendix A).

Second, the inclusion of contraction does not disturb properties in the original models. The Ca^{2+} shape shows minimum change for models with dynamic buffers while it

is largely distorted for models with instantaneous or none CaTRPN (Figure 4.5 and Section B.1 in Appendix B). This is closely related to the first benefit as it requires adding extra terms into Type Four and Type Five models to incorporate contraction and therefore Ca^{2+} shapes are more likely to be unphysiologically deformed.

Third, models with dynamic CaTRPN show clear postextrasystolic potentiation in Ca^{2+} with or without contraction implemented (see Figure 4.7, Figure 4.8 and Section B.2 in Appendix B). Therefore these models show desired variation in contractile strength of extrasystoles and postextrasystoles because of the close relationship between Ca^{2+} and contraction.

Fourth, contraction properties of models with dynamic CaTRPN fit experimental results better (see Figure 4.9 comapring with Figur 4.3(a), Figure 4.11 comparing with Figure 4.3(b), Figure 4.12, and Figure 4.13). This has been shown in the four characteristic curves (Postextrasystolic Mechanical Restitution Curve (MRC_{pes}); Postextrasystolic Potentiation Curve (PESPC); Minimum-value Axis Intercept Curve ($t_{o,pes}$) and Time Constant Curve ($T_{mrc,pes}$)) and their various parameters.

To unveil the mechanism why model with dynamic buffers reproduce PESP better than models with instantaneous buffers, we studied the correlation between contraction and calcium release from SR. We found a strong positive correlation (r^2=0.848). This means for models with instantaneous buffers, the insufficient variation in contractile strength responding to various pacing cycle length is a direct result of the Ca^{2+} dynamics. The interpretation for this result is twofold. First, Ca^{2+} release from SR is the main source for intracellular Ca^{2+}, therefore J_{rel} can be the direct reason of contraction behaviors. Second, time constants play a crucial role in cell contraction. The time constants of binding with troponin C in Eq. (4.3) in models with dynamic buffers are in the order of 10ms, which is the same order of the time scales of the upstroke of Ca^{2+}, CaTRPN and tension development. The RyR release kinetics is highly timing sensitive and strongly coupled to the binding process. Therefore models with dynamic buffers, which can describe the timing of interaction

among different cell compartments more accurately, reproduce correct contraction behaviors. This has biological significance since most electrophysiological models incorporate instantaneous buffering due to their simplicity and lower computational cost.

Limitation

Yue's experiments are based on dog ventricles in iso-volume conditions, but our simulations are on isometric single cells. However similar experiment results have been observed in smaller tissue sizes. Wier et al. [110] measured tension in perfused ferret papillary muscles 0.67 ± 0.05mm in external diameter and reported similar monoexponential curves as Yue et al.. We do consider the size to be a potential limitation of our work. Qualitatively we get similar characteristic curves in our simulations as in the experiment but quantitatively none of our models show as much variation in contraction strength with respect to changing stimulus rate (see Figure 4.9 and Figure 4.11) as in Yue's experiment. One possible reason might be that the coupling and isotropy in tissues reinforce the variation in contractile strength, which suggests tissue simulations should be one direction for future work.

Another limitation on using some of the cell models is the coupling of cross species models and the comparison to experimental data from another species. The argument is that, first, the parameters in the experiment and simulations that we performed quantitatively cross species comparisons on are all normalized to their own priming beats (Figure 4.9 and Figure 4.11); the normalization should reduce the species sensitive factors. Second, the quantities that are not normalized are either compared before and after the contraction implementation within each own individual model (Figure 4.5, Figure 4.7, Figure 4.8) or compared qualitatively with the experiment (trends with respect to ESI in Figure 4.12 and Figure 4.13). Nevertheless we admit this is a limitation in our work due to the lack of experiment data for all species.

In our study, we chose a hybrid approach to implement contraction that we only changed CaTRPN into a dynamic buffer while kept all the other buffers instantaneous. The reason

for that is because we want to change the original model as little as possible. Since only CaTRPN is presented in the contraction model, we think it should be enough to change only that into a dynamic buffer. We did conduct simulations on O'Hara et al. that we changed both of the instantaneous intracellular calcium buffers in the model (troponin and calmodulin) into dynamic buffers using the same strategy described in Section 4.2.3. We found that the shapes of both voltage and calcium are significantly retorted (not shown). It is not surprising because the more changes we make, the less the model's behavior will resemble the original model. That's why we think our study is informative and important for people in the field to realize the importance of models with dynamic buffers in reproducing contraction behaviors since the form of the equations for CaTRPN in those models is compatible with contraction models therefore little changes are required.

CHAPTER 5
CALCIUM ALTERNANS

5.1 Introduction to this Chapter

Long-QT syndrome (LQTS), characterized by abnormal prolongation of the QT interval [125], is a result of delayed repolarizations in the heart and can increase the risk of life-threatening arrhythmias, with a mortality rate of 20% within the first year after first detection and up to 50% in the next 10 years for untreated patients [126]. The known dangers of LQTS have resulted in guidelines by the FDA concerning the design and testing of any new drug and in the interpretation and analysis of these drugs in clinical trials [127]. In addition, many currently available medications can be very dangerous to some patients with heart problems, as they are known to further prolong QT intervals as shown in the compendium maintained by the Sudden Arrhythmia Death Syndromes Foundation (sads.org). LQTS is usually accompanied by T-wave alternans [128] where the duration of the T wave can vary from one beat to the next [129]. This long-short alternation in duration and in some cases amplitude has been shown to arise from a period-doubling bifurcation [20, 21] originating at the cellular level [22]. In space, alternans can lead to complex spatiotemporal patterns along the epicardium and endocardium [23] and eventually to conduction block and fibrillation [24, 25].

Alternans was observed in cardiac tissue as early as 1872 [130], and some of the earliest mathematical models of cardiac action potentials were able to produce such phenomena [69, 68]. However, later generations of models often failed to produce alternans [71, 112, 70, 73], with more detailed species-specific models for rabbit [74, 114], dog [131] and human [78, 119, 75] ventricular action potentials among them. In time, other models have been specifically designed to account for alternans [117, 115, 77, 132].

Recently the FDA's sponsored Cardiac Safety Research Consortium [133] proposed a new initiative, the Comprehensive in-Vitro Pro-arrhythmia Assay (CiPA), which specifies the use of mathematical models of cardiac action potentials in the aid of pro-arrhythmic drug risk assessments. Many recently developed ionic models are complex single-cell models with a large number of variables. There exists a large variability in dynamics between them as well as failures to reproduce key physiological features when they are tested in tissue (alternans, reentrant wave dynamics, dominant frequencies, etc.). **The known differences between many cell and tissue models make it imperative to validate and verify models with experiments**.

In this chapter, we compared the voltage and calcium alternans in Sato et al. [132] model with dual optical mapping recordings for $[Ca^{2+}]_i$ and V_m during discordant alternans in Langendorff-perfused rabbit hearts to verify if the model can produce correct dynamics of the development of alternans.

5.2 Experimental setup

The heart preparations and optical mapping setups were described in Chapter 2. New Zealand white rabbits (2-3 kg, n=8) were used. A total of six high-power LEDs were used for excitation, three were for voltage imaging and the other three were used for calcium imaging.

External bipolar stimuli (3-5 ms, strength is twice of the diastolic threshold) were applied from the apex or the base using a downsweep pacing protocol with the pacing cycle length (PCL) starting from 400ms. For each PCL, 150 to 200 stimuli were delivered to allow the system to reach steady state. The PCL was gradually shortened with decreasing steps once alternans started to appear until the occurrence of VF or wave block at any point along the wavefront propagation, usually between 150ms to 130ms.

Alternans in voltage was quantified by measuring the action potential duration (APD) and the alternans in calcium by measuring the the calcium transient duration (CaD). When

calculating the APD and CaD, the voltage and calcium signals were first normalized between 0 and 1 for each pixel. Then the APD was calculated using a threshold of 0.5, and the CaD was calculated using a threshold of 0.4.

5.3 Simulation setup

The Sato et al. model (Sato et al., 2013) for rabbit ventricular cells in space was used under conditions similar to those of the rabbit experiments. For the details of the ionic current, please see reference [132]. Briefly, each cardiac cell of a one-dimensional cable of tissue is modeled by 75 sarcomeres connected through the diffusion of cytosolic calcium (Cai) and network sarcoplasmic reticulum (NSR) calcium. The diffusion strengths are $8 \times 10^{-9} cm^2/ms$ and $4 \times 10^{-10} cm^2/ms$ respectively. Voltage in the 75 sarcomeres within one cell is considered to be the same due to the fast diffusion inside a cell. Each sarcomere consists of four compartments: cytosol, submembrane, NSR and junctional SR (JSR). See Figure 5.1. The calcium fluctuation is model by the Langevin equation with a noise term depending on the number of SERCA pumps.

One-dimensional tissue is modeled by the cable equation 3.2, in which the ionic current is

$$I^i_{ion} = I^i_{Na} + I^i_K + \sum_{j=1}^{M} \left(I^{i,j}_{Ca} + I^{i,j}_{Na,Ca} \right) \tag{5.1}$$

Index i indicates the ith cell in the 1D cable and the index j indicates the jth sarcomere in one cell. M is the total number of sarcomeres in one cell (i.e. 75 in our simulations). The cable equation is integrated using an operator splitting approach with Δx = 0.015cm and Δt = 0.1ms. The diffusion of calcium between cells is considered negligible. The cable length is 3cm. Neumann boundary condition is used.

In the previous chapter, we have emphasized on the importance of including contraction in electrophysiology models. We did not include contraction in Sato et al. model because in our experiments, we used blebbistatin to suppress the contraction for better visualization

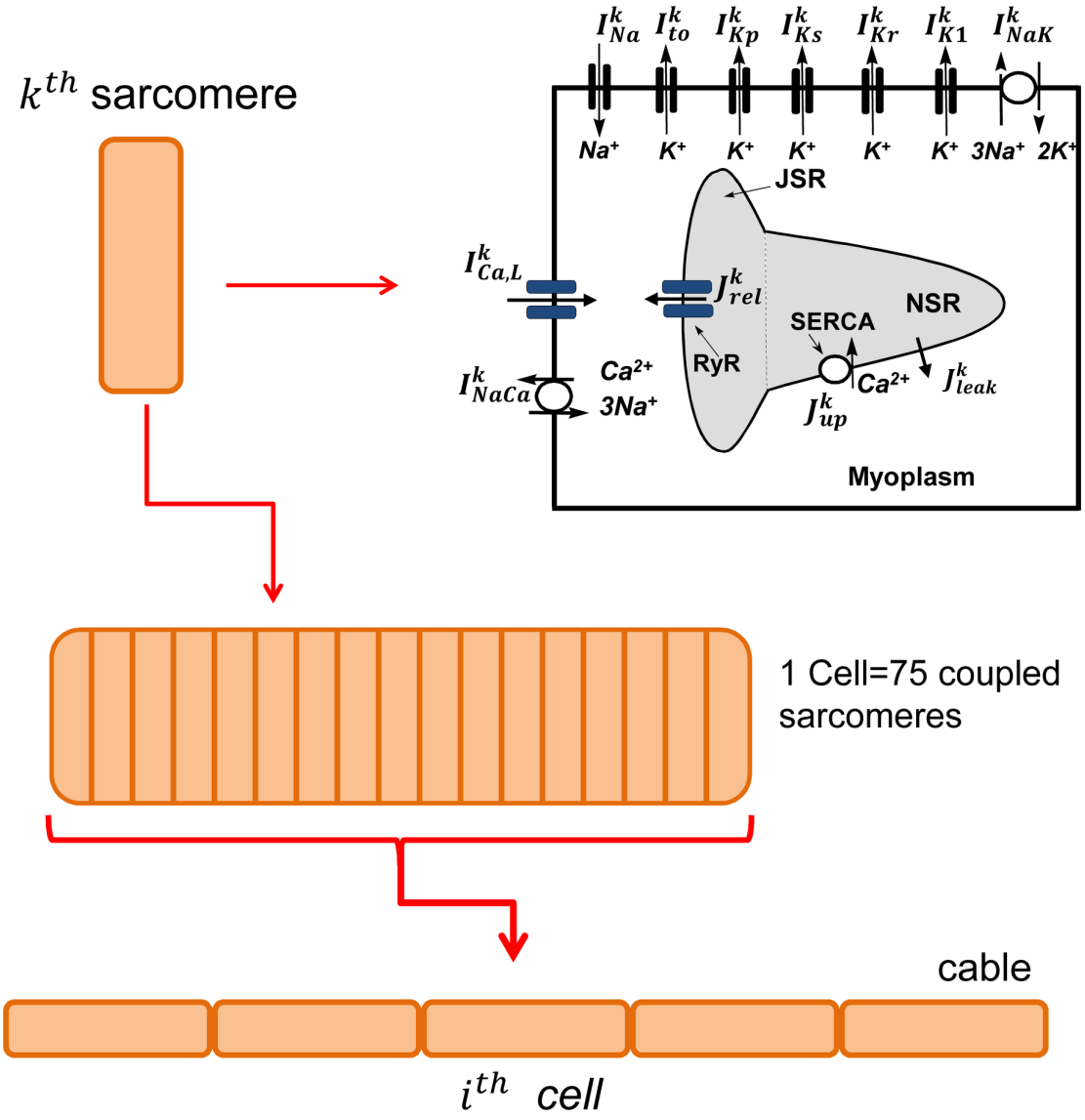

Figure 5.1: Schematic illustration of the multi-scale computational model. Figure from Sato et al. [132]

of the electrical signals.

Three different pacing protocols were used for the 1D simulations, with each using a stimulus current applied to the five leftmost cells for a duration of 2ms. In the first pacing protocol, we started with PCL = 600ms until steady state was reached, then decreased the PCL to 300ms and paced until steady state was reached. In the second pacing protocol, we initially assigned to the whole cable the steady state variables for the leftmost cell for PCL = 600ms, then we gradually decreased the PCL to 300, 295, 290, 285, 280, 270, and 260ms. For PCLs longer than 300ms, we used the third pacing protocol, in which we used the steady state of PCL = 300ms from the second protocol as the initial condition. When calculating APD, -80mV (about 80% repolarization) was used as the threshold. When calculating CaD, the threshold was set to be between 10% and 20% of the repolarization, adjusted among different pacing cycle lengths to make sure both even and odd beats can be captured.

5.4 $[Ca^{2+}]_i$ alternans develops at longer PCLs than APD alternans in experiments

The spatiotemporal dynamics of voltage and calcium in cardiac tissue depends on the pacing period. Figure 5.2A shows snapshots of voltage (upper two rows) and calcium (lower two rows) in a rabbit ventricle for a series of PCLs from 350 to 140 ms when stimulation was applied at the base of the heart. Each column shows consecutive even and odd images during steady state 120 ms after stimulus application; all frames over two successive beats at steady state are shown in Movie 1 in Appendix G. Figure 5.2B shows the same situation but when the stimulus was applied to the apex, and Movie 2 shows all frames over two successive beats at steady state for this case. In all rabbit experiments, Ca alternans clearly developed at longer PCLs than voltage alternans. As the tissue was paced more rapidly, inhomogeneity emerged in both voltage and calcium patterns with calcium displaying more spatial heterogeneity compared to voltage. Figure 5.3 shows the voltage and calcium signals, respectively, over time for one pixel indicated by a marker in Figure 5.2 for all PCLs.

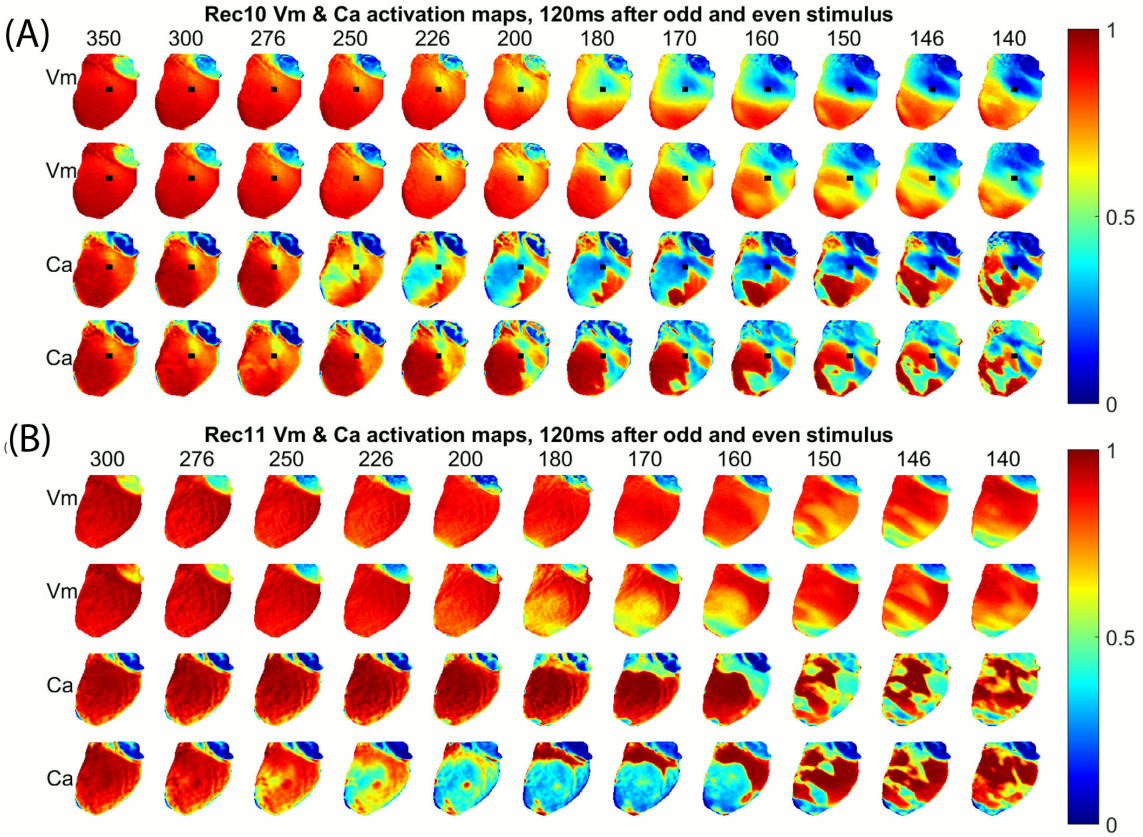

Figure 5.2: Snapshots of normalized voltage (upper two rows) and intracellular Ca (lower two rows) 120 ms after stimulus application on consecutive beats for decreasing pacing cycle lengths (PCL) from 350ms to 146ms (left to right). Rabbit ventricle is shown here from experiments. The long axis of the heart is about 4cm (see Figure 5.5). Stimulus was applied at (A) the base and (B) the apex.

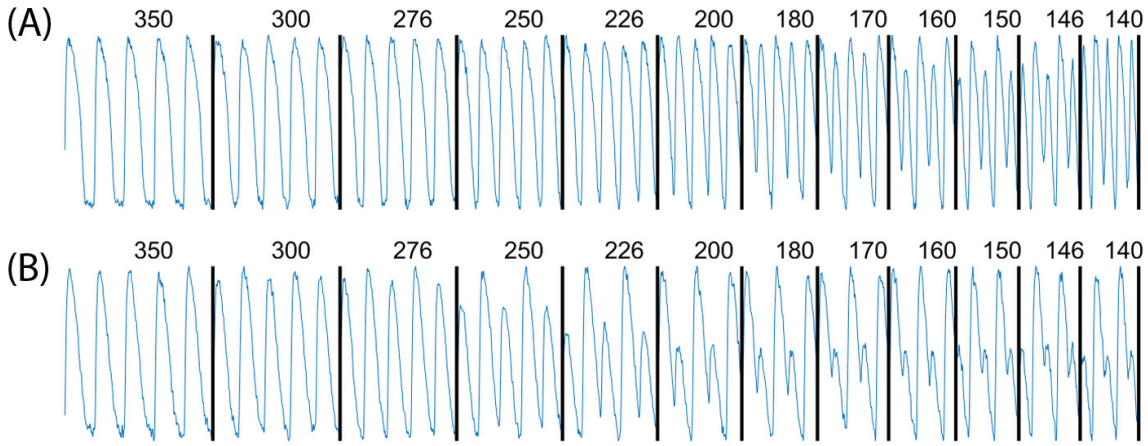

Figure 5.3: Time traces of normalized voltage (top) and $[Ca^{2+}]_i$ (bottom) signals from a single pixel marked in Figure 5.2 for the same PCLs.

As the PCL decreases, alternans was detected first in calcium amplitude (250$\pm$10 ms), then in calcium duration (220$\pm$15ms), and finally in APD (200$\pm$15ms). The shortest PCLs can barely generate an excitation in calcium for the short beats (last two panels in Figure 5.3B), and alternans is more pronounced in both duration and amplitude for the calcium signal.

5.5 Discordant alternans nodes are more pronounced in $[Ca^{2+}]_i$ than in APD

Figure 5.4A shows the spatial dispersion of APD for successive beats at steady state. Several important features are worth noticing. At long PCLs (e.g., PCL>250 ms), there is no difference between even and odd beats (no alternans), but there is an intrinsic smooth spatial dispersion of APDs in the range of 15ms for each beat. As concordant alternans and then discordant alternans develop, the gradient of APD increases to around 30ms as the PCL decreases. The distance between the locations of the longest and shortest APD decreases during Discordant alternans (DA), similar to what has been observed in canine hearts [23]. During DA, the regions of long-short and short-long APD are separated by a collection of nodes (nodal lines) where the APD remains constant from beat to beat (shown as white lines in Figure 5.4), with more nodes forming as the PCL decreases. Figure 5.4B shows the CaD dispersion in tissue, similar to Figure 5.4A. However, during DA, the nodal lines

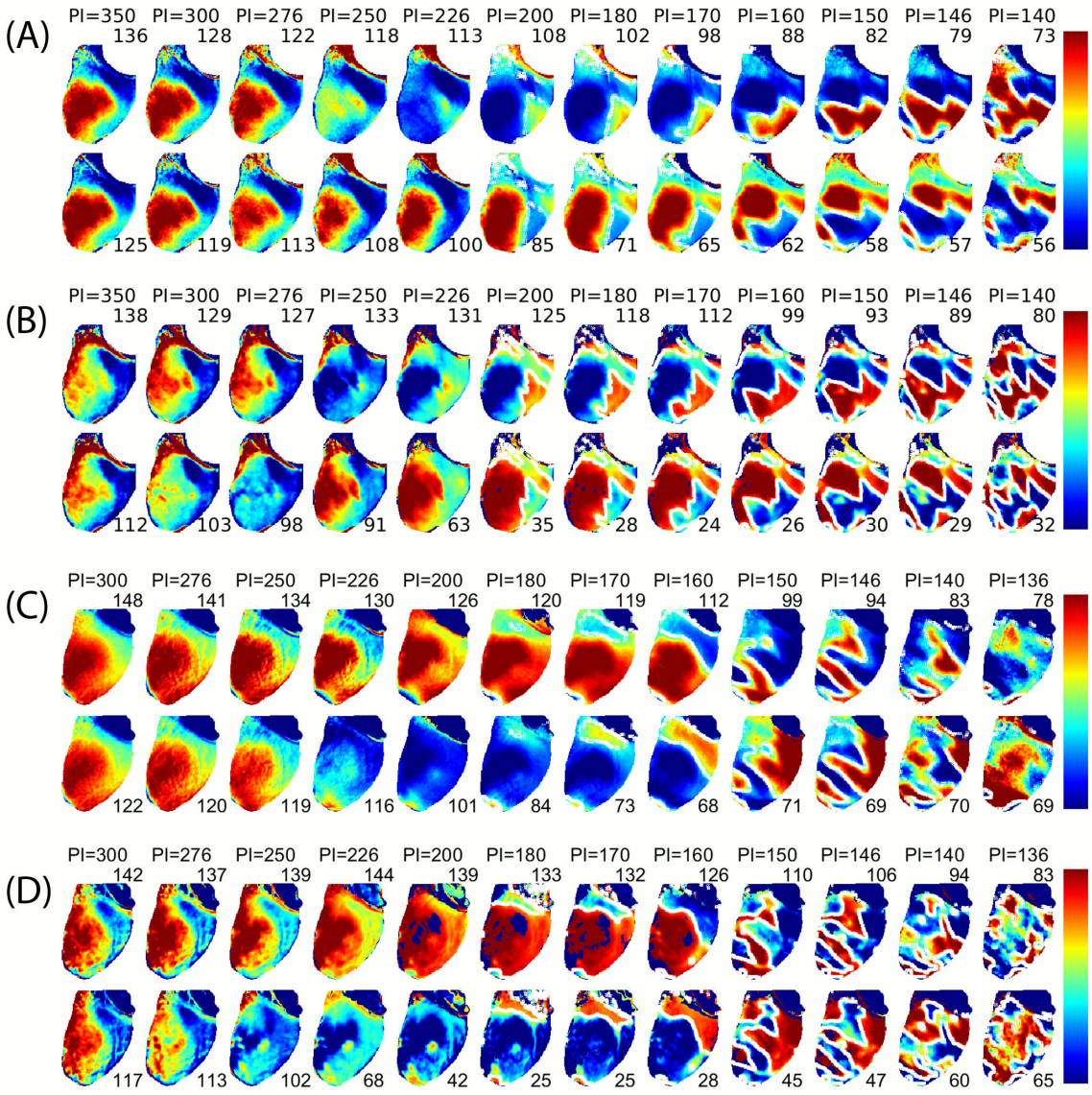

Figure 5.4: (A) Spatial distribution in APD for even (top) and odd (bottom) beats at various PCLs with stimulation applied to the base. Rabbit ventricle is shown from experiments. The long axis of the tissue is about 4cm (see Figure 5.5). Numbers next to the maps indicate the maximum and minimum values used in the color map. Notice there is no alternans for PCL>275 ms, concordant alternans for PCL between 250 and 225 ms, and discordant alternans for PCLs below 225 ms. Nodal lines are shown in white. (B) $[Ca^{2+}]_i$ spatial distribution for even (top) and odd (bottom) beats as in A, but transitions between discordant alternans phases are sharper and nodes are more pronounced. (C-D) Spatial distributions as in (A-B) but for pacing from the apex.

are thicker and more pronounced compared to voltage nodal lines. Figure 5.4C-D show plots similar to Figure 5.4A-B for the same preparation but with the pacing site located at the apex instead of the base. The progression from no alternans to concordant alternans (CA) and then to DA occurs at the same PCLs, but the spatial patterns are different. This difference of patterns depending on pacing site was observed in all 8 rabbit experiments as well as in previous studies [23, 134].

Previous numerical studies of alternans [28, 29, 25, 135] have used one-dimensional cables to quantify the spatial profiles of APDs, including the number of nodes present. In the same way, Figure 5.5 and Figure 5.6 displays the values of APD and CaD along a line across the heart's surface for two successive beats during alternans. As in Figure 5.4, it can be seen that there is no alternans for PCL $>$ 250 ms, then concordant alternans in voltage and calcium appears for PCLs between 200 and 180ms. At 170ms, there is CA in voltage but DA for calcium, and for PCL $<$ 170 ms DA is present for both voltage and calcium. We calculated in Table 5.1 the steepness (slope) of the APD and CaD nodal lines for PCL between 160ms and 146ms corresponding to Figure 5.6I-L when the DA are most pronounced. Data was presented as mean$\pm$s.d. (standard deviation), averaged among the slopes at each node for even and odd beats for each pacing cycle length. It clearly shows that CaD nodal lines are about one order of magnitude steeper than APD nodal lines, indicating the diffusive connection among cells differs in voltage and calcium signals [136, 137], as the insufficient of diffusion in calcium leads to calcium profiles that are sharper in space compared to voltage.

5.6 Experimental alternans features smoother spatial profiles and slower alternans amplitude growth than simulated alternans

Simulation results using the Sato et al. model confirm that alternans appear as the PCL is decreased. However, the PCLs at which they appear are much longer compared to experiments. Figures 5.7 and Figure 5.8 show the voltage and the calcium alternans in a 1D cable

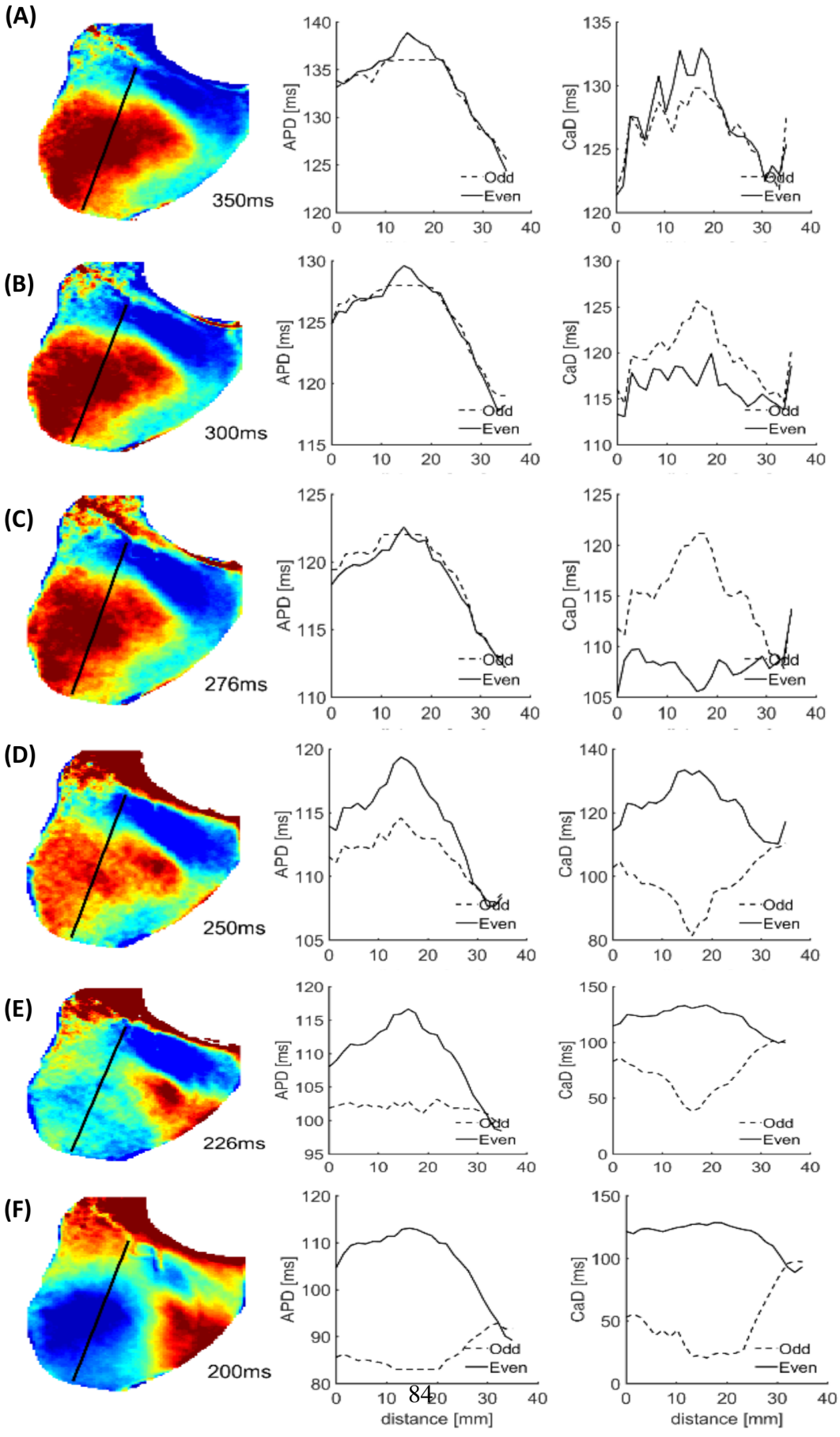
(A)
350ms
APD [ms]
CaD [ms]
Odd
Even
(B)
300ms
(C)
276ms
(D)
250ms
(E)
226ms
(F)
200ms
distance [mm]
distance [mm]

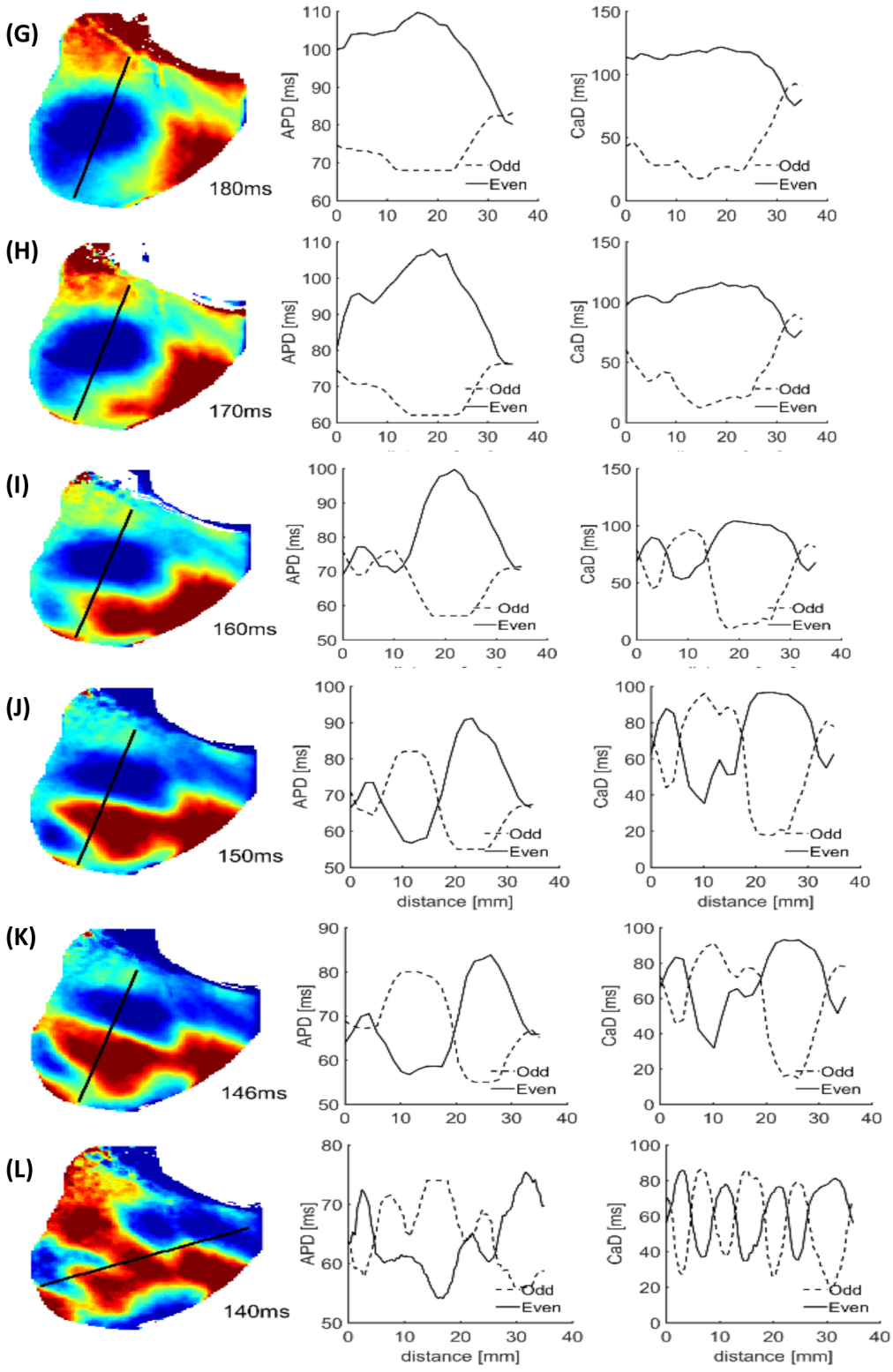

Figure 5.6: APD contour and APD and $[Ca^{2+}]_i$ alternans duration in ms for even and odd beats measured along a one-dimensional line shown in black for different PCLs as in Figure 5.4 (Continue). Data from rabbit ventricle experiment.

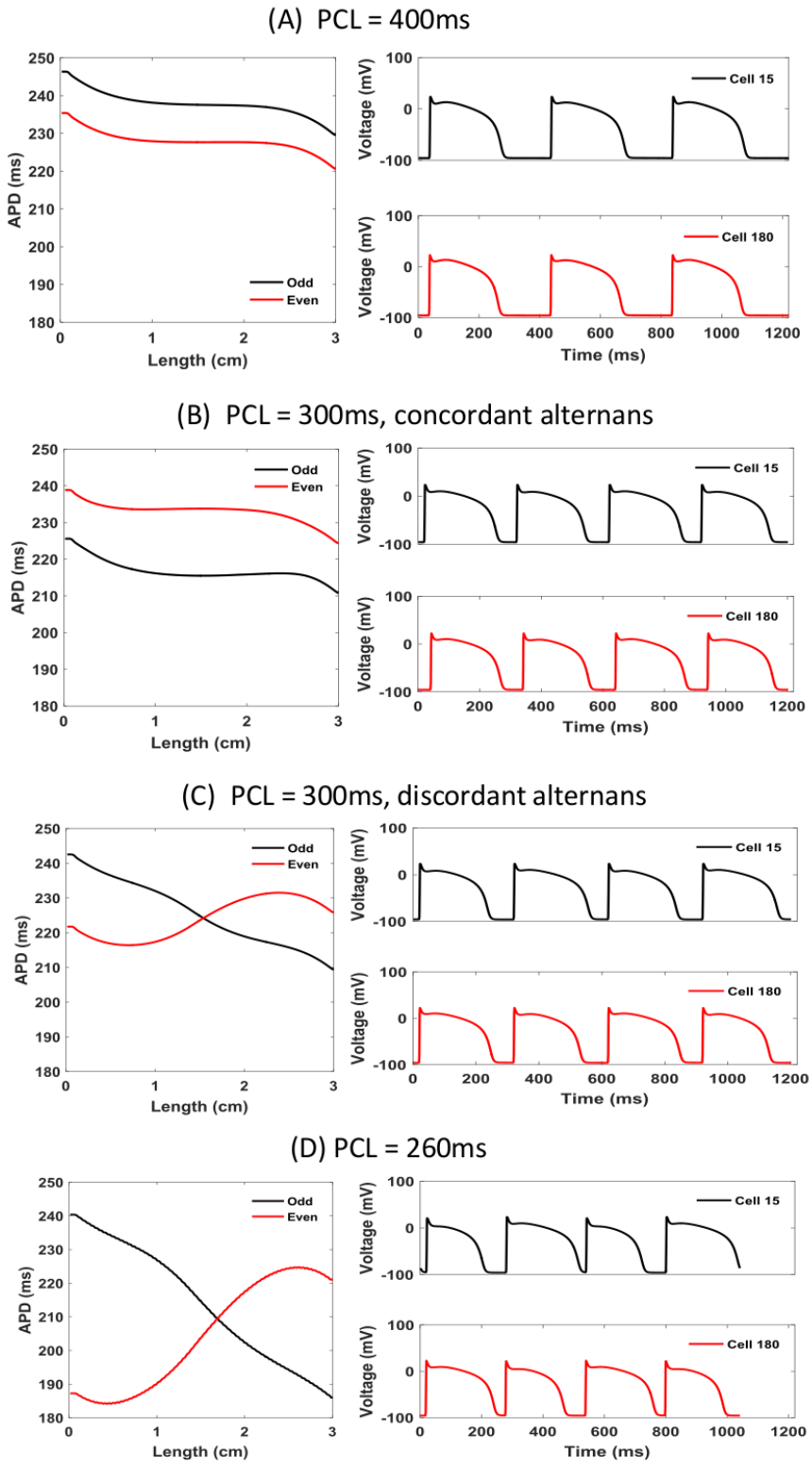

Figure 5.7: Voltage alternans in a 1D cable (L = 3cm, 200 cells) of the Sato et al. model for decreasing PCLs: (A) PCL=400 ms, (B) PCL=300 ms (concordant alternans), (C) PCL=300 ms (discordant alternans), and (D) PCL=260 ms (discordant alternans). Left column: spatial profile of APD for odd (black) and even (red) beats. The amplitude of discordant alternans increases as PCL decreases. Right column: voltage over time at two cells, one near the left end and the other near the right end of the cable.

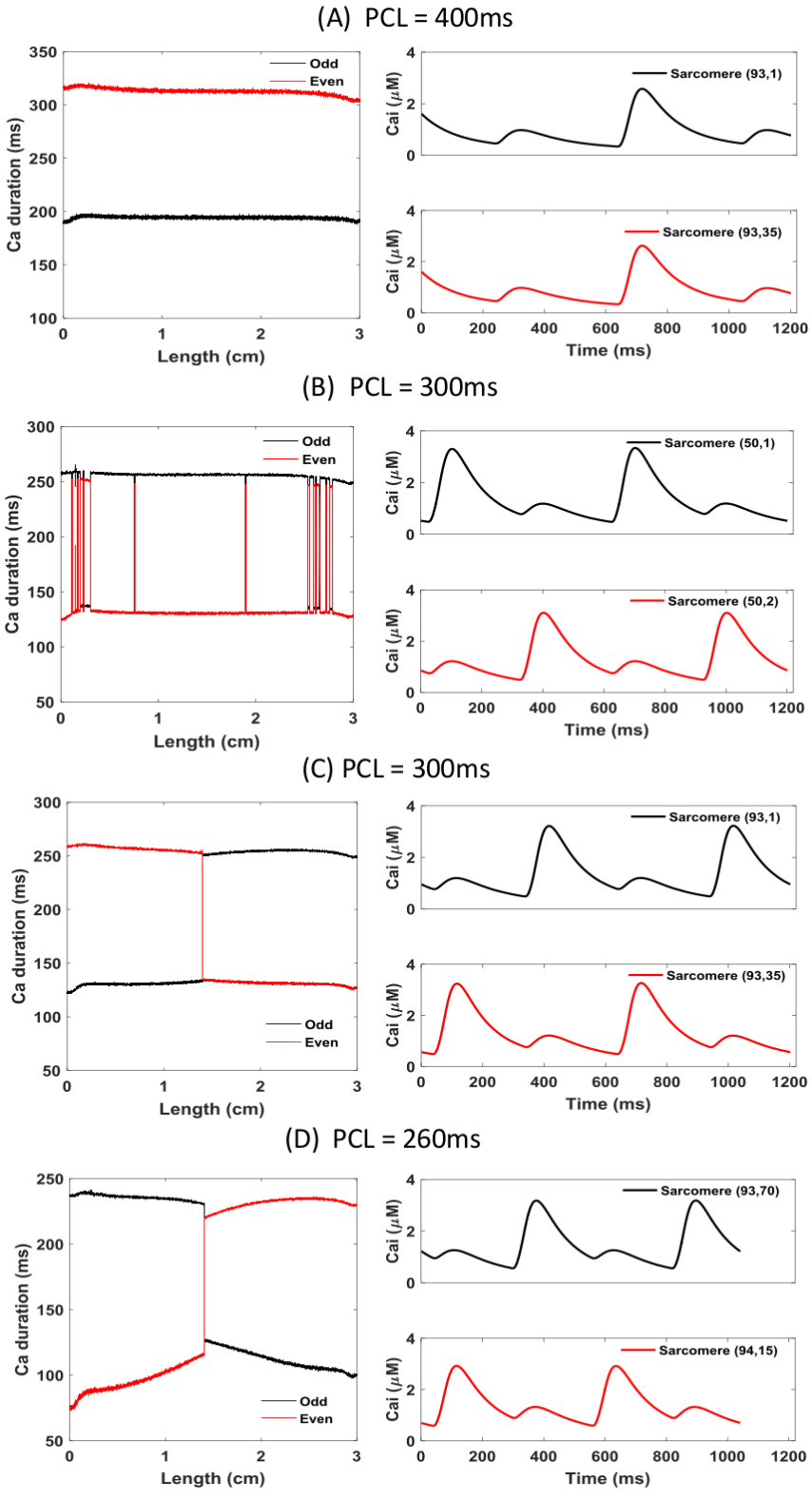

Figure 5.8: Calcium alternans in a 1D cable (L = 3cm, 200 cells, each cell consists of 75 sarcomeres). (A) PCL = 400 ms, (B) PCL=300 ms, (C) PCL=300 ms, and (D) PCL=260 ms. Left column: spatial profile of Ca duration for odd (black) and even (red) beats. Right column: Ca over time at two sarcomeres that are around the CaD nodal point where they are completely out of phase when discordant alternans is present.

Table 5.1: Steepness of APD and CaD nodal lines.

	PCL = 160ms	PCL = 150ms	PCL = 146ms	PCL = 140ms
Steepness of APD alternans nodal lines (ms/mm)	2.20±0.87	3.11±1.54	2.75±1.51	1.12±0.38
Steepness of CaD alternans nodal lines (ms/mm)	12.1±4.8	12.5±3.7	9.94±2.91	20.1±5.6

3 cm in length. Figure 5.7 illustrates APD as a function of length in the left column for even and odd beats at PCLs of 400, 300, and 260 ms. The right column shows the voltage signal for the corresponding PCL for two cells, one near the left end and one near the right end of the cable, so that if the cable exhibits discordant alternans, the voltage signal of the two cells should be out of phase. Figure 5.8 shows similar plots but for the calcium. The left column indicates CaD over the cable for even and odd beats for the same PCLs as in Figure 5.7. The right column of Figure 5.8 displays the calcium signal from two sarcomeres for corresponding PCLs, with the two sarcomeres chosen so that if there is discordant alternans in calcium, the two sarcomeres should be out of phase. Results for other PCLs (600, 500, 450, 350, 290, 280, and 270 ms) are presented in supplemental Figure E.1 for APD and Figure E.2 for CaD.

For large PCLs (>400ms), there is no alternans in either voltage or calcium (Supplementary Figure E.1A-C and E.2A-C). When the PCL drops to 400ms, concordant alternans appears (Figure 5.7A and Figure 5.8A). For PCLs 300ms or below, discordant alternans occurs (Figure 5.7C-D, Figure 5.8C-D and Supplementary Figure E.1E-G and Figure E.2E-G). In all these simulations, voltage and calcium alternans are ”synchronized”, meaning if there is no voltage alternans, there is no calcium alternans, and if there is discordant voltage alternans, there is discordant calcium alternans, with the exception of Figure 5.7B and Figure 5.8B. In Figure 5.7B and Figure 5.8B, where we used the second pacing protocol and the PCL is the same as Figure 5.7C, we obtained concordant voltage alternans,

whereas the calcium alternans is discordant with multiple nodes. By using different initial conditions, it is possible to obtain completely different dynamics for the same PCL. The Sato et al. model is very sensitive to initial conditions due to the random fluctuation term in the SERCA pump, and in this respect, it is similar to experiments, where it has been shown that small changes in initial conditions can result in very different alternans patterns [23]. In all the simulations presented in this thesis, the random noise was generated using the same seed.

One major difference between the experiments and the simulations is how sharp the calcium transition is between different alternans phases. In the experiments, both APD and CaD have relatively similar smooth transitions between the maximum and minimum values (Figure 5.4, Figure 5.5 and Figure 5.6), with calcium showing only a slightly faster transition, whereas in simulations, CaD has a significantly sharper transition than APD (Figure 5.7 and Figure 5.8). In addition, in experiments, as the PCL is decreased, CaD transitions from no alternans to concordant alternans and then to discordant alternans with the alternans amplitude increasing smoothly. In simulations, on the other hand, CaD changes drastically from no alternans to concordant alternans with an amplitude of 150 ms when the PCL decreases from 450 to 400 ms.

Figure 5.9 shows a bifurcation diagram for APD (left) and CaD (right) as a function of PCL calculated at one point from the numerical simulation of the 1D cable (top) and experimental data (bottom) where the alternans has the largest amplitude. As the PCL is decreased from 600 to 260 ms in the numerical simulations, the bifurcation appears simultaneously for both voltage and intracellular calcium just above a CL of 400 ms (PCL_c). The bifurcation amplitude for voltage grows is conjectured to be at a rate of the square root away from the bifurcation point ($\Delta APD \sim (PCL - PCL_c)^{1/2}$) [19]. The bifurcation amplitude in calcium experiences a sharp discontinuous jump (Figure 5.10 for the curve fitting). In contrast, the experimental bifurcations occur at much lower PCLs close to 250ms, and the amplitude of the alternans just beyond the bifurcation can be fit better into

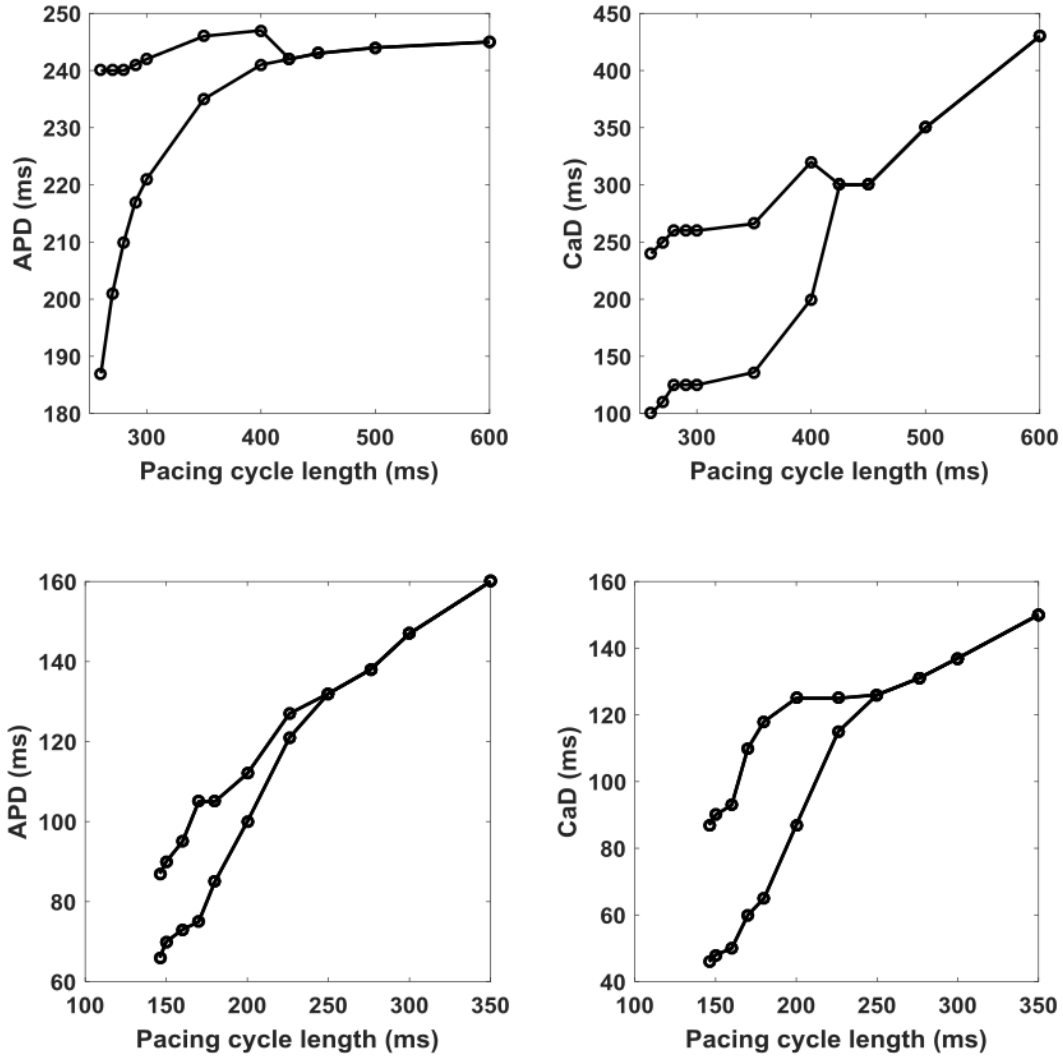

Figure 5.9: Bifurcation plots of APD (left) and CaD (right) as a function of PCL for simulations (top row) and experiments (bottom row).

a linear function with a smoother growth than in the simulations.

5.7 Discussion

Patients with LQTS have a higher risk of cardiac arrhythmias due to augmentation of the T-wave and increased spatial dispersion. For many years now, detection of LQTS and T-wave alternans in ECG has been used as a quantitative tool for predicting dangerous spatial variations in dispersion, which are dynamically induced at the cellular level and can induce arrhythmias. Since 2005, the FDA has required that new drugs be tested for QT prolongation and development of T-wave alternans and recently an FDA-sponsored consortium proposed an initiative to use mathematical action potential models in the aid of drug risk assessment. If models are indeed to be used to investigate pro-arrhythmic and anti-arrhythmic effects of drugs, they first need to be validated against experimental data in normal conditions. The main goal of this chapter is to create an in tissue experimental data set of simultaneous voltage and calcium optical mapping recordings from Langendorff-perfused rabbit hearts at high temporal and spatial resolution and in particular during alternans for use in validating the dynamics from numerical simulations from the most recent model of rabbit ventricular action potentials [132].

We found that alternans in voltage and calcium develops similarly in both experiments and simulations as the pacing cycle length is decreased; however, the model developed alternans much sooner at longer periods close to 420 ms compared to 240$\pm$10 ms in experiments. Likewise, the minimum period of stimulation before conduction block developed earlier at 260 ms in the model versus 140$\pm$5 ms in the experiments. Also, it is important to notice that in experiments, as in the models, the magnitude in variations of the APD were much smaller than the variations in CaD during alternans. However, the magnitudes in alternans were about twice as large in the model as in the experiments, with maximum values of 55 ms for APD and 150 ms for CaD in the model versus 25$\pm$4 ms and 65$\pm$5 ms respectively for the experiments.

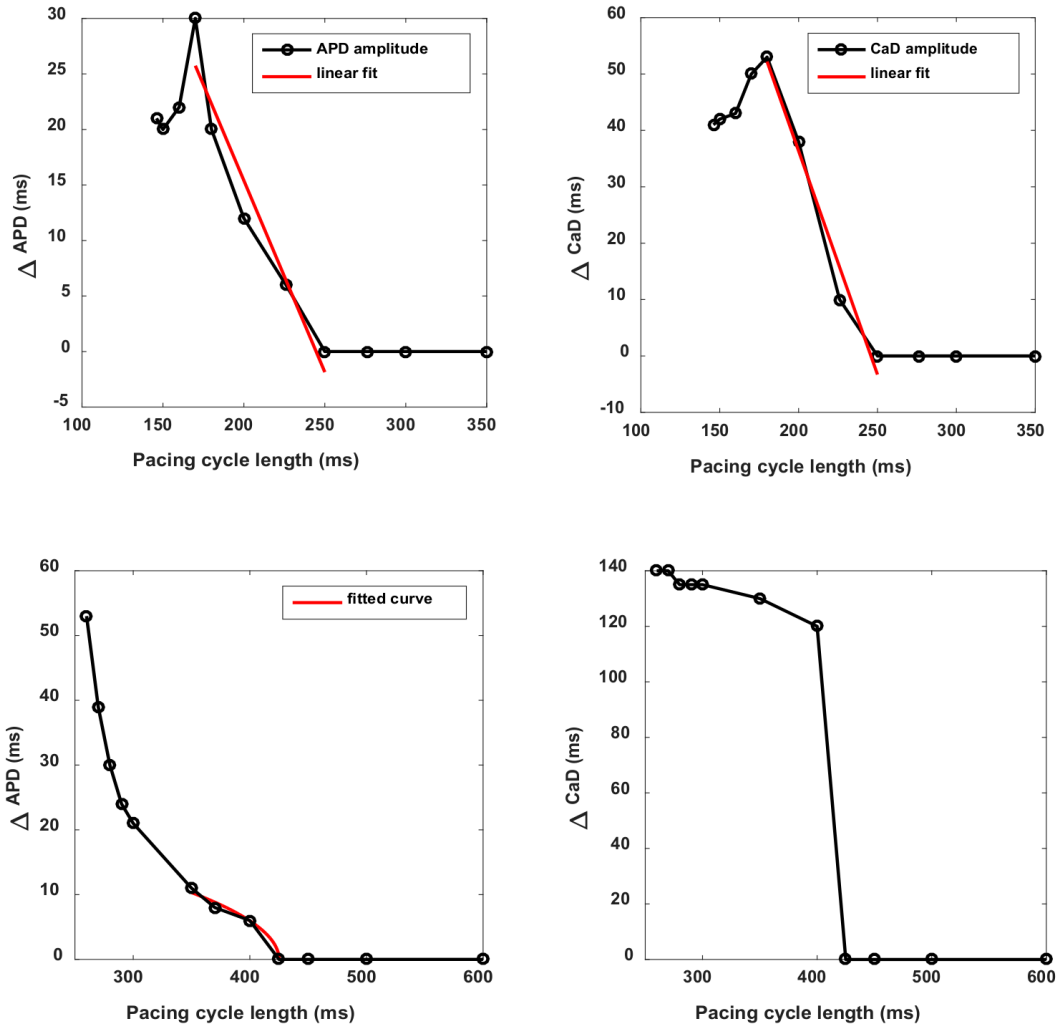

Figure 5.10: Bifurcation amplitude of APD (left) and CaD (right) of experiments (top row) and simulations (bottom row). We can fit the bifurcation amplitude beyond the bifurcation point in the experiment into a linear function (ΔAPD or $\Delta CaD \sim (PCL - PCL_c)$) with r^2 of 0.9306 and 0.9739 for voltage and calcium respectively. The voltage bifurcation amplitude in simulation can be fit into a function $\Delta APD \sim (PCL - PCL_c)^{1/2}$ with r^2 of 0.9802.

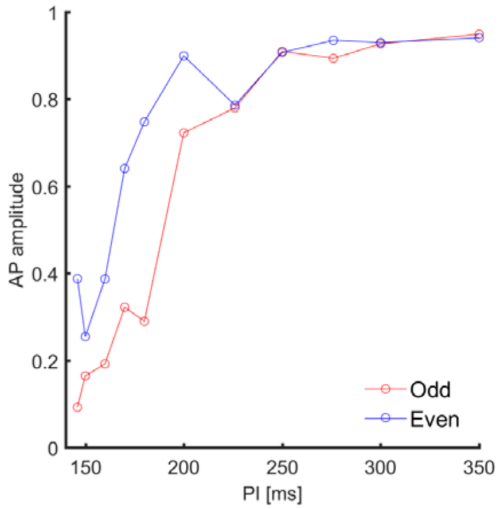

Figure 5.11: Action potential amplitude bifurcation from data in Figure 5.3A

More crucial differences arise from the way that the alternans develop. In experiments, alternans in voltage develops gradually, appearing to be more consistent with a border-collision bifurcation [14, 19, 138], where small changes in duration grow slowly and mostly linearly, whereas in the model alternans grows much faster, as with a pitchfork bifurcation [14]. Furthermore, the model does not yield action potential amplitude (APA) alternans as observed in the experiments when the tissue is paced at very short pacing cycle lengths (see Figure 5.11 from experiment), an important additional pro-arrhythmic mechanism recently described by Chen et al. [139] and Myles et al. [37]. On the other hand, while intracellular calcium does display amplitude alternans in both experiments and simulations, in experiments amplitude alternans develops slowly, while in the model a large difference in amplitude appears as soon as alternans develops and persists with a similar amplitude for all periods where alternans is present, as shown in Figure 5.10.

In regard to spatial distributions, in our experiments, we do not detect very sharp calcium duration transitions around nodal lines for most pacing cycle lengths; instead, we observe a smooth phase transition in both voltage and calcium, albeit with calcium appearing sharper, with more defined nodal lines than those in APD (Figure 5.4 and Table 5.1). This is contrary to simulations where CaD alternans transition can happen within a cell.

If the coupling between voltage and calcium is strong, calcium and voltage should have similar dynamics, i.e. the CaD alternans nodal line should follow that of the APD and vice versa. Therefore, we think the model, as it was published, lacks necessary coupling between voltage and calcium.

5.7.1 Shortcomings of the model

While the PCL at which the alternans appears is higher in the model than in the experiments by approximately 180ms, this difference could be fixed with a simple re-scaling of some of the time constants of the model. Similarly, the difference between the minimum PCL for propagation (around 260ms for the model compared to 140ms for experiments) could also be reduced by modifications to the recovery and inactivation time constants of the sodium gating variables. Previous publication [140] also showed that CaD alternans patterns can be smoothed by increasing voltage instability (and/or reducing Ca instability). However, there exist several other key physiological aspects that would require a more in-depth analysis and validation of the models equations.

(1) Type of bifurcation. The calcium dynamics should result in a border-collision bifurcation with slow linear growth.

(2) Development of alternans in calcium duration. In the model, as soon as alternans develops in calcium, its amplitude is almost at its maximum (Figure 5.8), whereas in the experiments, there is a very smooth transition in Ca alternans with decreasing cycle length (Figure 5.3).

(3) Development of alternans in amplitude. In the model, when alternans in the AP duration develops, at no point does alternans in AP amplitude appear (Figure 5.7). This is in contrast to experiments, where at very short cycle lengths alternans in amplitude is readily observed (Figure 5.3). Recent experiments and theory predict that the presence of amplitude alternans is key in the development of reentrant arrhythmias [139, 37].

(4) CV and nodal lines. In both simulations and experiments, concordant and discordant

alternans appears in tissues of similar size of about 3 cm. The conduction velocities are very different between simulations having a maximum velocity at about 47cm/s, versus experiments at around 100cm/s. Numerically, this means that if the diffusion coefficient was modified to fit the experimental CV values, it will result in tissues of more than twice the size needed experimentally to support discordant alternans.

5.7.2 Limitation

A major limitation of this study in this chapter is that we did not perform the simulations in 2D. The complexity of the calcium alternans will only be linearly rescaled when adding an extra dimension since calcium signal is local due to the low diffusion constant. However, the alternans patterns in voltage can be more complex and result in more nodes in each direction.

When comparing the Ca alternans, the resolution in the experiments is on the cell-level. However, in the simulations, we simulated the Ca signal on the sarcomere level. Proper averaging method should be used in order to compare the experiments and the simulations.

We did not consider when comparing the simulation results to the experiments is the error introduced by the optical mapping technique such as the scattering of the fluorescent photons. In the future, 2D simulations and scattering models should be used.

CHAPTER 6
SYNCHRONIZATION AS A MECHANISM FOR LOW ENERGY ANTI-FIBRILLATION PACING (LEAP)

In this Chapter, we performed both in vitro and in silico experiments to investigate the mechanism behind LEAP. We observed successful termination of both AF and VF using LEAP in simulations and ex vivo canine hearts and verified that synchronization from virtual electrodes is the key mechanism for LEAP. We further investigated the role of shock period and timing in the effectiveness of LEAP.

We induced VF using rapid pacing on canine LV (septum removed), then applied the LEAP protocol and recorded the voltage on the ventricular surface using optical mapping. Experimental protocols are described in Appendix F.

Computer simulations in this chapter were performed using a bidomain model (Eq. 3.2) subject to no-flux boundary conditions. Human atrial cell model was used [141]. The insulating plaque that typically forms between myocardial fibers in older hearts [142] were modeled by randomly removing gap junctions along short lines (average length 625 μm) oriented along the fiber direction (average spacing 2.5 mm). Spatial resolution was 250 μm. Time resolution was 0.05ms. Atrial simulations included the ACh-activated K^+ current [143]. Forward Euler was used to solve the reaction-diffusion equation and GMRes was used to solve the Poisson equation.

6.1 Termination of fibrillation by LEAP with reduced energy

Figure 6.1 shows an example of LEAP terminating VF in a canine LV (Movie 3) using a shock period of 95ms, 15ms below the dominant period of fibrillation (Figure 6.2). The figure consists of six rows. The top panel of each row is the optical mapping voltage. The top left row (indicated by blue) shows the time evolution of VF. The remaining five rows

(indicated by red) show the effects of the five shocks; the first 2-3 frames of each row show depolarization, the next 2-3 frames show repolarization. During the five shocks, an increasing area was captured by each additional pulse until all electrical activity was terminated. Standard defibrillation was performed on the same heart. For both LEAP and standard one-shock defibrillation, the electric field amplitude was gradually increased until the minimum energy to defibrillate was found. This procedure was performed on 7 ventricles (28 episodes). The energy of each LEAP pulse is 0.19 ± 0.14 (mean $\pm$ standard deviation) of one-shock defibrillation (Figure 6.3A). Similar energy reductions were observed in atria experiments (Movie 4). The energy of each LEAP pulse is 0.12 ± 0.11 of standard defibrillation (Figure 6.3B) in 5 atria (22 episodes). The total energy for LEAP (5 pulses) is comparable to the standard one-shock defibrillation, however, the energy reduction per pulse will lower the pain level for patients.

6.2 Synchronization as the key mechanism for arrhythmia termination by LEAP

To further explore the mechanism of LEAP termination arrhythmia, we performed phase analysis on the voltage data and displayed the dynamics using a modified Kuramoto plot. Kuramoto plots [144] are phase diagrams used to quantify synchronization of a system of oscillators, where the phase of all the oscillators is displayed on a unit circle. Figure 6.4 demonstrates how to make modified Kuramoto plots. From the optical mapping recordings, we can obtain for every pixel the voltage value of the action potential and assign to that pixel a phase. To define the phase, we first pick a threshold for the action potential. When the transmembrane voltage rises/drops across the threshold, we define the phase at that moment of that pixel to be $0/2\pi$ and the phase is evenly distributed from 0 to 2π for the time span in between. Then the phase of each pixel is presented by a dot on the circumference of a semi-circle. On the semi-circle, phase evenly increases from 0 to 2π from the left edge to the right edge of the circumference (we used semi-circle so phase 0 and 2π can be distinct). Then we repeat the previous two steps for all pixels and color the dots on the

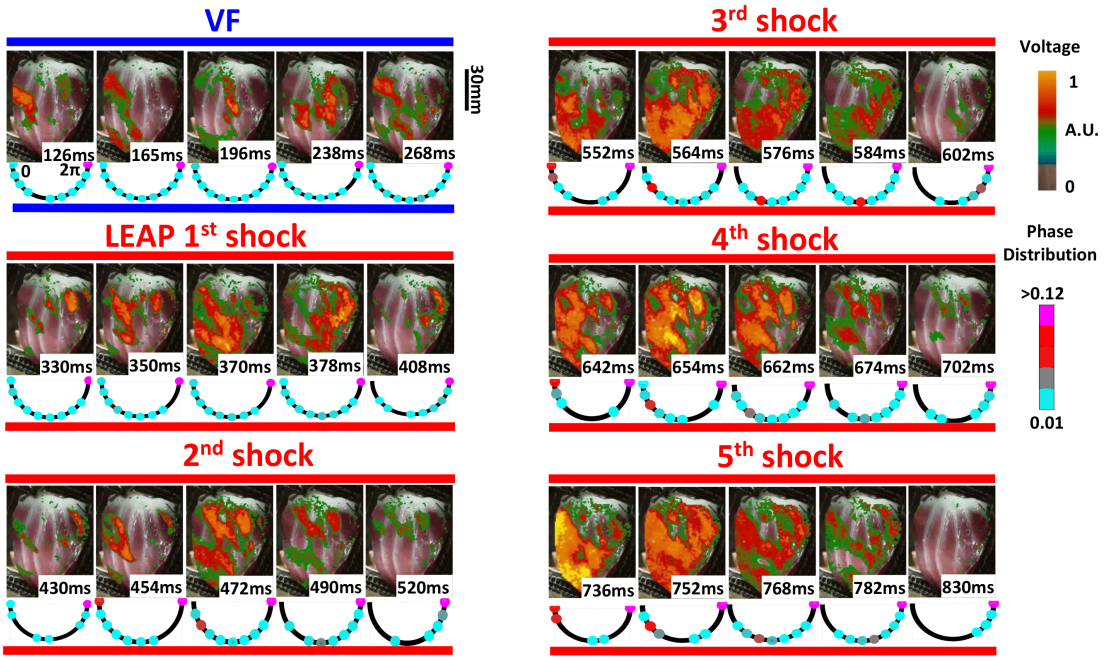

Figure 6.1: Termination of ventricular fibrillation. Each row (indicated by blue and red) consists of two panels. Top show voltage on canine LV from optical mapping. Bottom show modified Kuramoto plots corresponding to the voltage panels above them; colors indicate the percentage of pixels of the entire preparation in that phase at this time. Top left row (blue): fibrillation preceding LEAP. The rest rows (red): five electric pulses, 95ms apart (E=1.4V/cm).

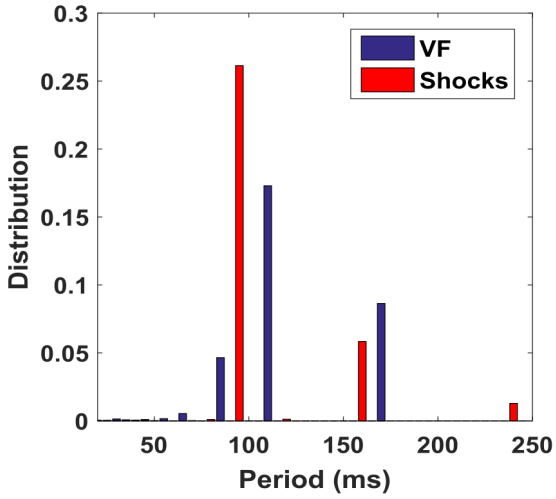

Figure 6.2: Dominant frequency of VF (110ms) and LEAP shocks (95ms). The frequency spectrum was calculated using the fast Fourier Transform function (fft) from MATLAB.

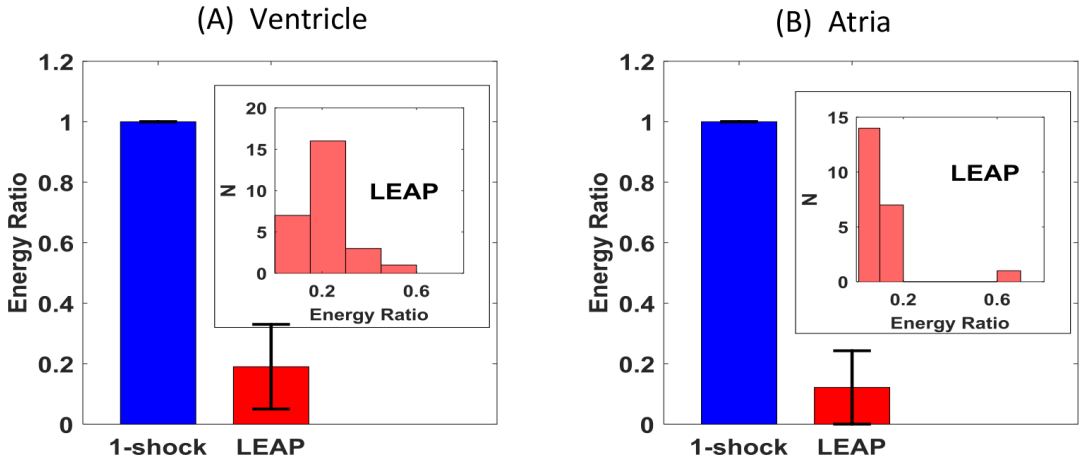

Figure 6.3: Ratio of energy used by LEAP compared to that used by standard 1-shock defibrillation. Error bar is standard deviation. (A) 7 ventricles (28 trials). (B) 5 atria (22 trials).

semi-circle (from cyan to magenta) to indicate (from low to high) the number of pixels in that phase. By using Kuramoto plots, the time evolution of the dynamics of the tissue can be better visualized. The red line indicates the threshold above which the tissue is considered excited.

Figure 6.1 shows the Kuramoto plot in the bottom panel of each row, corresponding to the voltage signal above it. During VF, the Kuramoto plots show that the phase was evenly distributed (blue row), indicating the de-coherence in the system. As the electric shocks were applied (E=1.4V/cm), the phases in all pixels were increasingly synchronized with each additional pulse until all elements were synchronized and the arrhythmia was terminated (Figure 6.1 red rows). In later shocks (3-5), both repolarization and depolarization were synchronized. The level of synchronization in repolarization was slightly less than depolarization. When LEAP failed, it was due to a lack of full synchronization, as shown in Movie 5, which has the same LEAP parameters as Figure 6.1 but a lower shock strength of 0.9V/cm. The phase plots show that less synchronization was achieved with each pulse compared with the successful case. Hence, after the last shock, the few regions not synchronized to the LEAP frequency restarted and perpetuated the arrhythmia.

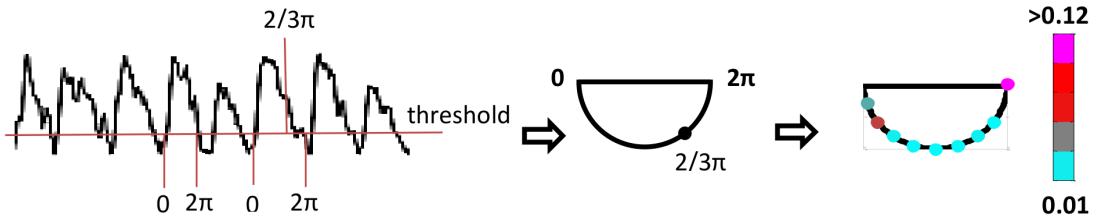

Figure 6.4: The modified Kuramoto plot.

To further verify the synchronization mechanism behind LEAP, we performed computer simulations using the Nygren et al. atrial cell model on a 7cm×7cm tissue with a fibrillating state driven by four spiral waves (Figure 6.5 and Movie 6) having a dominant period of T_0=201ms. Successful LEAP was simulated with four shocks delivered at the pacing cycle length of 190ms, with all spiral waves terminated after the fourth shock. Similarly, unsuccessful LEAP was simulated with a lower cycle length (164ms), which failed to terminate the arrhythmia even after ten shocks (Movie 7). Phase diagrams in the simulations, as in the experiments, indicate synchronization of the system resulted in successful termination, while unsuccessful defibrillation was due to a lack of full synchronization.

6.3 Comparing the arrhythmia-termination mechanisms of LEAP and one-shock defibrillation

To investigate how arrhythmia termination by LEAP differs from that of one-shock defibrillation, we calculated the fraction of tissue excited (FTE) as a function of time for both cases. We define FTE as the percentage of tissue with a voltage above a given threshold (40% of the amplitude of the AP). Figure 6.6 shows the voltage signal from one pixel and the FTE, both as a function of time, for successful LEAP (Figure 6.6A, E=1.4V/cm) and successful one-shock defibrillation (Figure 6.6B, E=4.67V/cm). During VF, the complex dynamics resulted in FTE oscillations (between 0.2 and 0.7) as different parts of the tissue continuously depolarized/repolarized, preventing FTE from reaching values close to 1.0/0.0. For both successful LEAP and one-shock defibrillation, FTE reached 1.0 once ar-

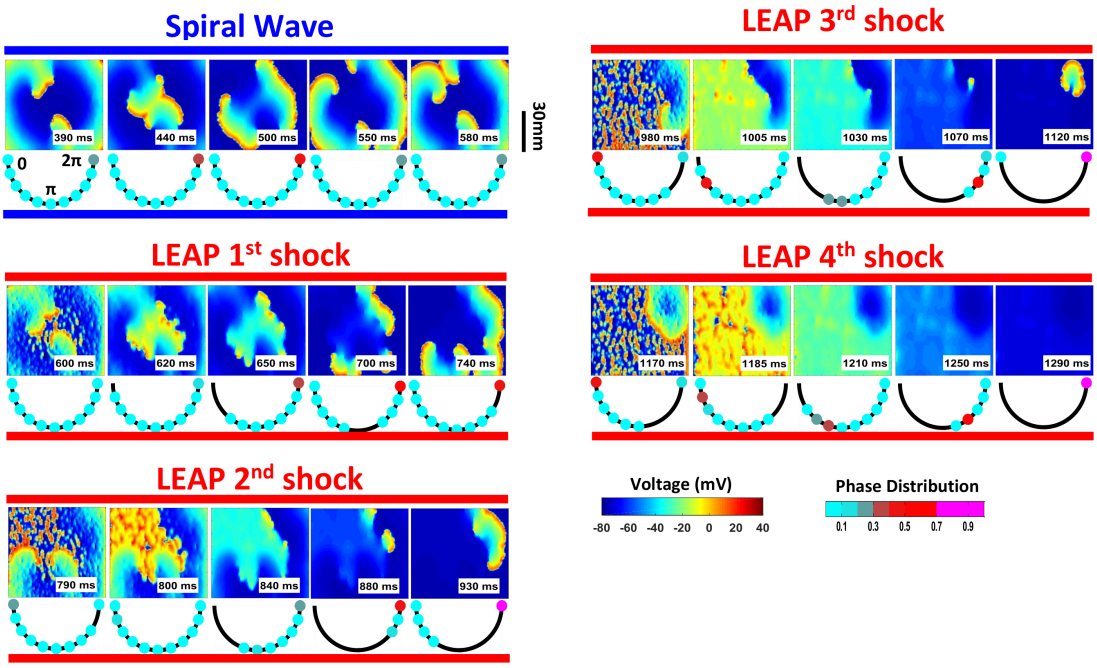

Figure 6.5: Termination of multiple spiral waves in simulations. Top rows: evolution of four spiral waves and application of four shocks (T=190ms); first frame of each row is 10ms after the most recent shock.

rhythmias were terminated. Statistical analysis on 26 LEAP trials (2 ventricles and 3 atria) show the average FTE gradually increased in five shocks during successful LEAP. Earlier shocks can present large variation in FTE whereas the last shock consistently induces high FTE values among all trials (Figure 6.7A).

The major difference between the successful LEAP and the standard one-shock defibrillation is how quickly they induce synchronization. We calculated in Figure 6.6 bottom panels the time derivative of FTE (dFTE/dt), which indicates how quickly the cells are excited. In successful LEAP (Figure 6.6), the peak of FTE gradually increased to 1.0 with the five pulses, but within each pulse, all cells were excited at the same time, revealed by the larger maximum values and narrow peaks of dFTE/dt. On the other hand, during the standard one-shock defibrillation (Figure 6.6B), the cells were not synchronized simultaneously, as shown by the lower dFTE/dt values associated with shock application. We performed the two-sample t-test to identify whether the peak dFTE/dt is significantly

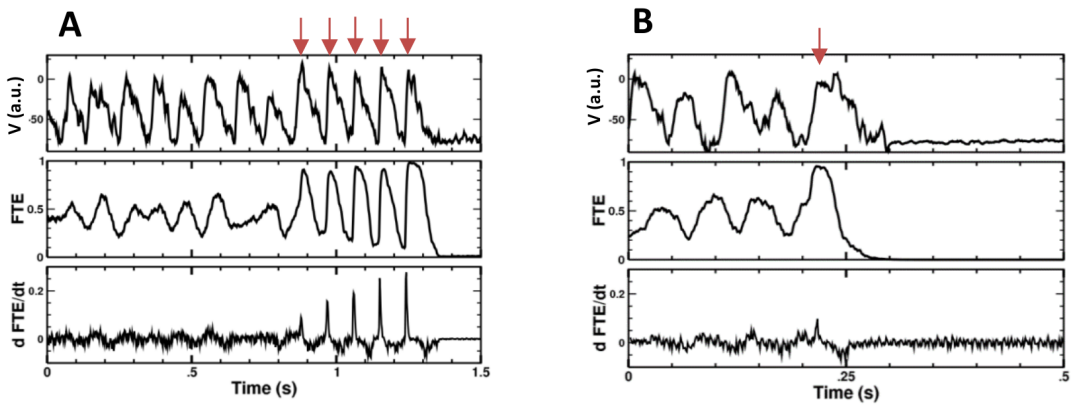

Figure 6.6: Voltage, fraction of tissue excited (FTE) and its time derivative (dFTE/dt) in experiments. (A) LEAP successfully terminate VF (E=1.4V/cm); (B) Standard one-shock defibrillation terminate VF (E=4.67V/cm). Red arrows indicate when shocks were applied.

different for LEAP and one-shock defibrillation. We found $p = 1 \times 10^{-7}$ (Figure 6.7B), which means the probability to find LEAP and one-shock defibrillation have the same mean dFTE/dt is very small. Therefore, it is statistical significant that LEAP has a larger dFTE/dt value than one-shock defibrillation. This confirmed LEAP synchronizes tissue faster than one-shock defibrillation.

6.4 Success rate of LEAP can be improved by adjusting period and timing of shocks

For both atrial and ventricular experiments, we found LEAP works not only for the pacing cycle length equal to the dominant frequency but also for frequencies that deviated up to approximately 15-25 percent from the dominant frequency (under- and over-pacing). Figure 6.8 shows two examples of LEAP termination using a slower period than the dominant frequency in ventricles (dominant period 120ms, LEAP cycle length 150ms) and atrium (dominant period 54ms, LEAP cycle length 62ms).

To further study the role of shock timing and LEAP period in relation to the dominant frequency, we performed numerical simulations using the same setting as Figure 6.5 where the amplitude and the duration of the shocks were fixed but the pacing cycle lengths were varied between 50% and 140% of the dominant period (T_0) with various timings of the

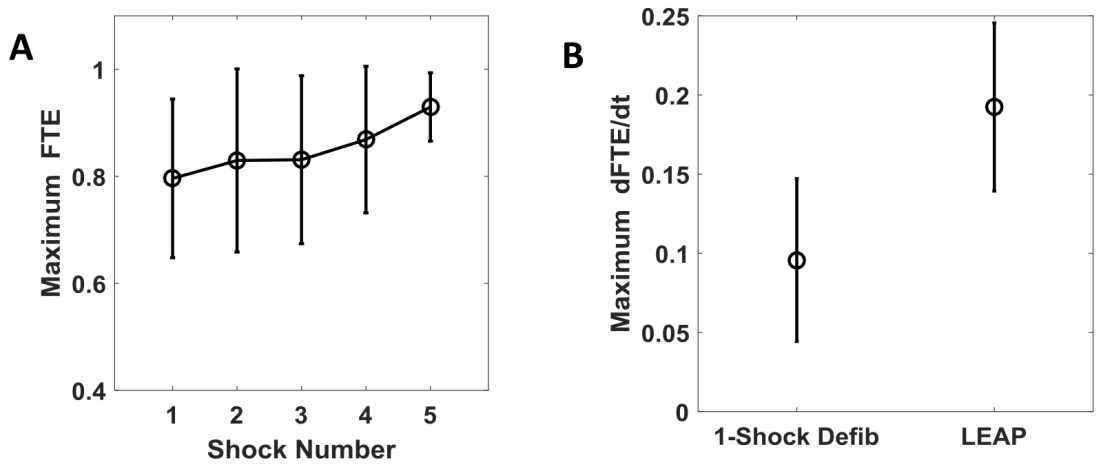

Figure 6.7: Statistical analysis for FTE. (A) Peak of FTE for each shock (from one to five) during LEAP, averaged among 26 trials (2 ventricles and 3 atria). (B) Peak of dFTE/dt for one-shock defibrillation (averaged among 19 trials) and LEAP (30 trials). Statistical significance level is $p = 1.0 \times 10^{-7}$.

first shock ranging from 500ms to 1000ms that covers roughly three rotations of the spiral waves. Movie 8 to Movie 11 show four examples that different combinations of shock periods and timings lead to various results. Figure 6.9 summarizes the results using different colors indicating the minimum number of shocks required to terminate the spiral waves for each period and timing (also see Table 6.1, 6.2). We found it more efficient for terminating the spiral waves when the shock period was close to the dominant period, in agreement with the experiments.

The simulations also showed that the influence of timing is more pronounced when the pacing cycle length is close to the dominant period. Far from T_0, such as $T = 0.5T_0$, ten shocks failed to terminate the spiral waves in all cases regardless of timing. For pacing cycle lengths close to the dominant period ($0.9T_0$ to $1.2T_0$), first shock's timings on the downslope of FTE in general were more successful than those on the upslope. Figure 6.10A uses different colors to indicate the correlation between FTE and the simulation results of different first shock timings for T=190ms. Defibrillation is harder to achieve if the first pulse is delivered when FTE is at a minimum, and it is best to defibrillate just after the FTE

Table 6.1: Simulation results of the influence of periods and timings on termination of spiral waves. Rows indicate the period of shocks. Columns indicate the timing of the first shock. T_0 is the period of the original spiral waves. N means spiral waves are not terminated after 10 shocks. Y means spiral waves are terminated after 10 shocks and the number in the prentice is the number of shocks that terminate the spiral waves. Shock strength (E=1.3V/cm) and duration (5ms) are fixed.

t_m (ms) / T (ms)	500	520	530	540	570	580	590	600	620	640	660	670	680	690	700	720	730	760
100 ($0.5T_0$)	N			N	N		N	N		N					N		N	
164 ($0.8T_0$)	N			N	N		N	N		Y (10)					N		N	
181 ($0.9T_0$)	N			N	Y (6)		Y (5)	Y (8)		N		N			Y (10)		Y (5)	
190 ($0.95T_0$)	N	Y (7)		Y (7)	Y (4)	Y (3)	Y (4)	Y (8)	Y (5)	N	N		Y (10)		Y (9)	Y (6)	Y (5)	Y (4)
201 (T_0)	Y (7)			Y (7)	Y (4)		Y (5)	Y (5)		Y (4)		Y (4)			Y (8)		Y (6)	
221 ($1.1T_0$)	Y (7)		Y (6)		Y (5)		Y (5)	Y (4)		Y (2)		Y (9)		Y (6)			Y (5)	Y (4)
241 ($1.2T_0$)	Y (5)			Y (5)	Y (3)		Y (4)	Y (3)		Y (9)		Y (6)			Y (5)		Y (5)	Y (4)
281 ($1.4T_0$)	N			N	N		N	Y (6)		N					N		Y (7)	

Table 6.2: Simulation results of the influence of periods and timings on termination of spiral waves (continue).

t_m (ms) / T (ms)	770	780	800	820	840	850	860	870	880	900	920	940	950	960	970	980	1000
100 ($0.5T_0$)			N			N				N			N				
164 ($0.8T_0$)		N				N				N			N				
181 ($0.9T_0$)	Y (3)		Y (5)	N		Y (3)		N		N			Y (6)				
190 ($0.95T_0$)		Y (10)	Y (5)	N	N	N	N		Y (10)	Y (6)	Y (6)	Y (5)	Y (4)	Y (4)		Y (5)	N
201 (T_0)	Y (6)		Y (5)	Y (5)		Y (7)		Y (7)		Y (5)			Y (3)				
221 ($1.1T_0$)			Y (4)	Y (3)		Y (4)		Y (7)		Y (7)			Y (5)				
241 ($1.2T_0$)		Y (4)	Y (10)		Y (8)		Y (10)			Y (5)			Y (2)				
281 ($1.4T_0$)			Y (10)			N				Y (10)					N		

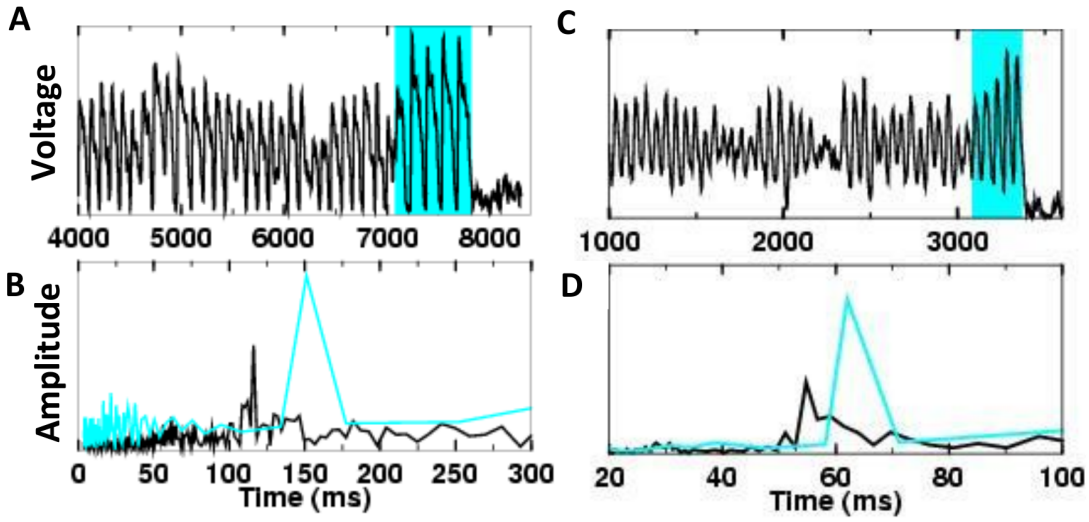

Figure 6.8: Underdrive pacing with LEAP can terminate arrhythmias. Voltage (top) and fast Fourier Transform amplitude after conversion of frequencies to periods (bottom) for VF (left) and AF (right).

maximum. Results from other pacing cycle lengths are shown in Figure 6.11. Figure 6.10B summarizes the results for the FTE upslope (dFTE/dt>0) and downslope (dFTE/dt<0), respectively, for all pacing cycle lengths. The percentage of trials that successfully terminated the spiral waves within five shocks (green) peaked around the dominant period, while the percentage that failed to terminate within ten shocks (red) dropped to minimum (Figure 6.10B and Figure 6.12a). First shocks applied during the FTE downslope had a higher percentage of arrhythmia termination within five shocks and a lower percentage of unsuccessful termination within ten shocks than those applied during the upslope, and the difference peaked around the dominant period (Figure 6.12b). Two-Sample t-tests on percentage of trials that successfully terminate arrhythmia within 5 shocks between the trials with their first shocks applied at the upslope on FTE and the trials with their first shocks applied at the downslope on FTE also confirmed the difference in efficiency between FTE upslope and downslope is statistically significant ($p = 0.005$, $n = 10$). This indicates that timing the shocks to coincide with the FTE downslope increases defibrillation efficacy, particularly as the pacing cycle length gets closer to the dominant period.

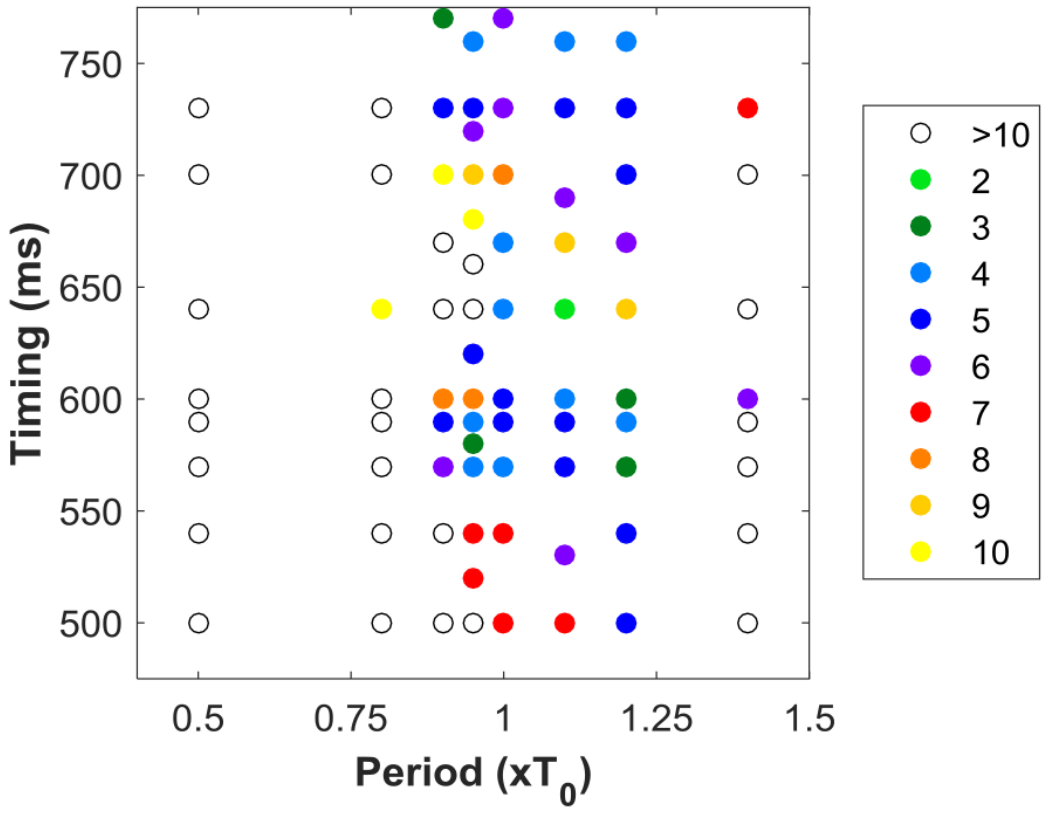

Figure 6.9: Numerical simulations testing different shock periods and timings. Shock periods vary between $0.5T_0$ and $1.4T_0$ (T_0 is the dominant period of the spiral waves) and timings of the first shock range between 500 ms and 1000 ms. Solid circles represent spiral waves terminated within 10 shocks; their colors indicate the minimum number of shocks required. Open circles represent LEAP fail to terminate spiral waves. All simulations start with the same initial conditions.

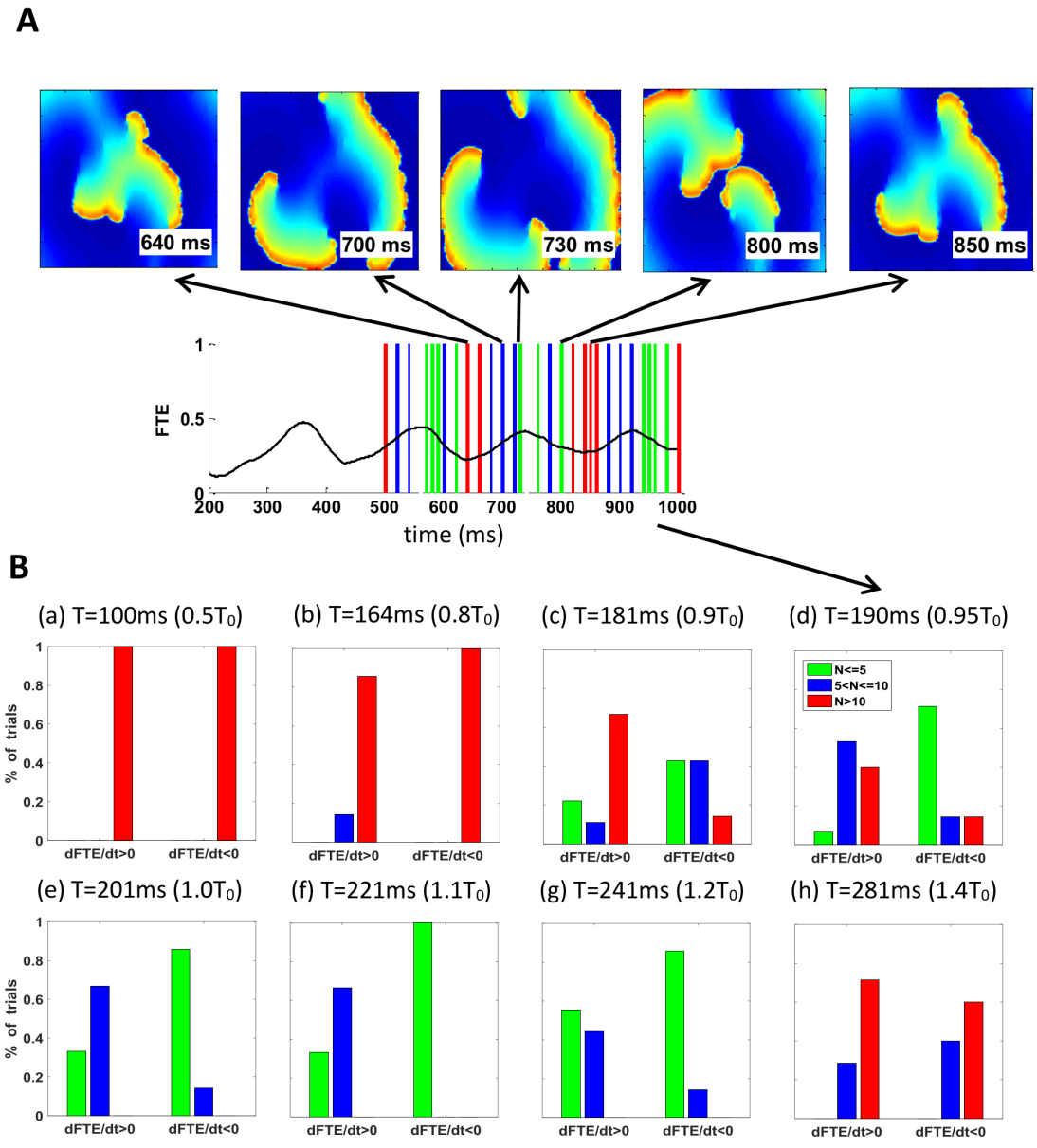

Figure 6.10: Role of shock period and timing in LEAP effectiveness. (A) Simulation results of different timings for T=190 ms. Fraction of tissue excited (FTE) for the spiral waves was plotted as a function of time (black line). Colored bars indicate timing of the first shock. Red indicates spirals were not terminated within 10 shocks; blue indicates spirals were terminated between 5 and 10 shocks; and green indicates spirals were terminated within 5 shocks. Top panel shows five example frames of the spiral waves. (B) Results for FTE upslope (dFTE/dt>0) and downslope (dFTE/dt<0) respectively for all the pacing cycle lengths. For example, for T=190 ms, 6.67% /71.4% trials on the FTE upslope/downslope terminated the spirals within five shocks (green bars in (d)).

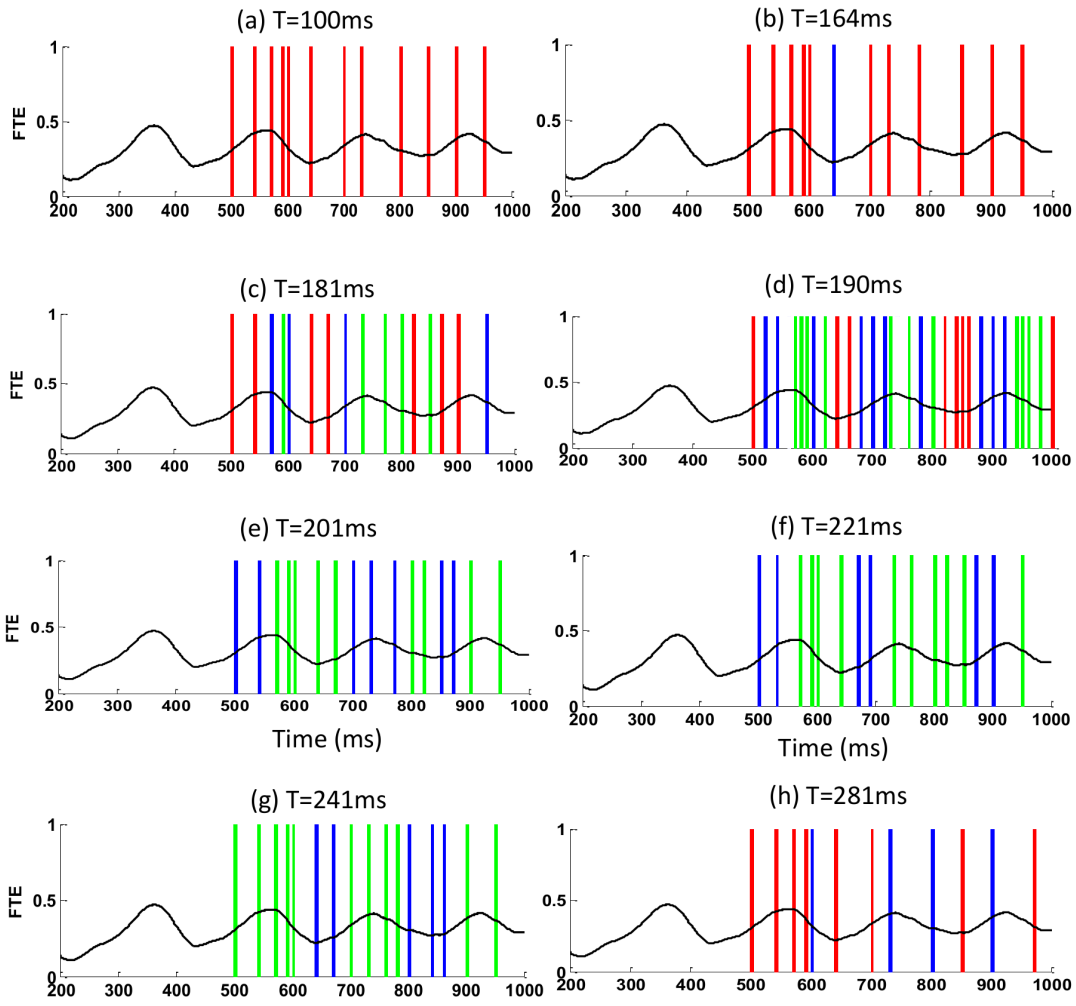

Figure 6.11: Graph demonstration of the results of the numerical experiment investigating the effects of shock periods and timings. In each trial, 10 shocks were delivered to the four spiral waves system. Fraction of tissue excited (FTE) for the spiral waves was plotted as the function of time (black line in each subfigure) for the first 1000 ms. In each subfigure, the pacing cycle length was fixed. Each bar indicates the timing of the first shock. Red indicates spirals were not terminated within 10 shocks for that period and timing; blue indicates spirals were terminated between 5 and 10 shocks and green means the spirals were terminated within 5 shocks.

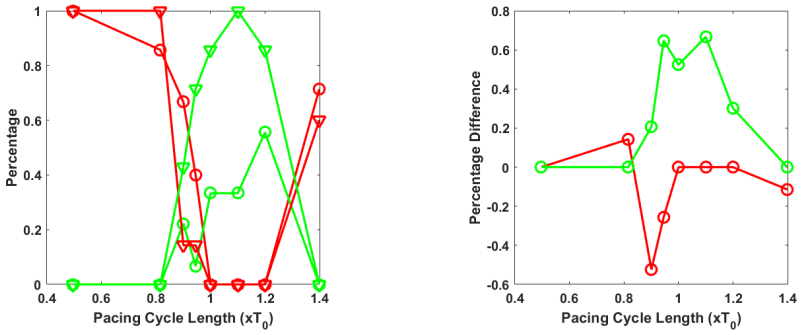

(a) Percentage for upslope and downslope trials

(b) Percentage difference for upslope and downslope trials

Figure 6.12: (a) Percentage of trials with timings in the upslope (circle) and downslope (triangle) of FTE that terminated the spiral waves within 5 shocks (green) and failed to terminate within 10 shocks (red), plotted against the pacing cycle length. The success (failed) percentage peaked (dipped) around the dominant period of the spiral waves. (b) The percentage difference between the upslope and the downslope (upslope-downslope) of terminating within 5 shocks (green) and failed to terminate within 10 shocks (red). The percentage difference peaked (dipped) around the dominant period and downslope work better than upslope in terminating the spiral waves.

6.5 Discussion

The main purpose of this chapter is to investigate how LEAP defibrillates differently than standard one-shock defibrillation. Both experiments and simulations (Figures 6.1, 6.3, 6.5) showed that LEAP works by gradually synchronizing the electric activity to the same frequency through each additional shock. Because the tissue is synchronized to the same frequency, both depolarization and repolarization are synchronized. There is no ununiform dispersion in refractoriness so additional shocks will not restart arrhythmia. Modified Kuramoto phase diagrams showed that, during arrhythmias, phase is relatively evenly distributed, and once LEAP is applied, the phase over the domain is increasingly focused with each shock. To further quantify this synchronicity, we calculated the fraction of tissue excited (FTE) as a function of time (Figure 6.6). The FTE peak progressively increases to one with each pulse for successful LEAP and its derivative indicates how fast the tissue synchronizes. In contrast, during one-shock defibrillation, the FTE upstroke is much slower compared to LEAP, indicating that all tissue is eventually excited but not at the same time.

The mechanism of LEAP is different from multi-stage electrotherapy [50], which consists of one to four low-energy biphasic shocks, six to ten ultralow-energy monophasic shocks, followed by anti-tachycardia pacing (ATP). The three stages of shocks are aimed to slowly decrease the complexity of the arrhythmia dynamics by first unpinning wave fronts that maintain the arrhythmia, then preventing the re-pinning of wave fronts to tissue heterogeneities, and finally annihilating the remaining wave fronts. In short, the method tries to first simplify the arrhythmia, then pace the arrhythmia driver out of the domain using ATP [50].

The field strength in LEAP is strong enough to produce AP propagation, hence it is clearly greater than those used in "sub-threshold" stimulation, which injects current stimuli that are too low to elicit a regenerative response of AP propagation in normal resting ventricle muscle. This could interrupt VF by increasing local conduction and/or improving the coupling between Purkinje and ventricular cells [145]. Sub-threshold effects could add an additional level of electrical synchronization to break up the arrhythmia thus may further contribute to the anti-fibrillation actions of LEAP, particularly in the ventricles where the endocardium contains an extensive network of Purkinje fibers.

LEAP is comparable to anti-tachycardia pacing (ATP) when terminating a single spiral with advantage over ATP when the spiral is pinned to a heterogeneity [146]. When multiple spiral waves are presented with higher frequency, some energy increase may be required for LEAP (Movies 12). Also with shock strength increases, the number of shocks required to terminate the arrhythmia will decrease (Figure 6.13).

Numerical simulations in this study suggested some ways to improve LEAP by adjusting the pacing period as well as the shock timings. The success rate is higher when the pacing cycle length is close to the dominant period of the arrhythmia. We found that when the pacing period is too short, most of the tissue is still refractory, which reduces the amount of tissue that can be captured by the shocks and hence lowers synchronization effectiveness. When the pacing period is too long, the influence of the previous shock has

dissipated before the next one, which weakens the collective effect of all shocks. Close to the dominant period, each pulse happens almost at the same phase of the spirals; thus, the influence of each pulse can be built on the previous ones, which would be more helpful in synchronizing the electrical activity. As long as the pacing period is close to the dominant period, both overdrive and underdrive pacing can terminate arrhythmias. Interestingly, the simulation shows an asymmetry between underdrive and overdrive: for underdrive pacing, the arrhythmias were terminated in all cases when the pacing cycle length was up to 20% above the dominant period, whereas for overdrive pacing, the spiral waves were not terminated in 28% cases when the pacing cycle length was only 5% below the dominant period. In simulations, spiral waves in rigid rotation mode tend to follow the highest possible frequency before conduction block, whereas in meander mode, the frequency can be lower [147]. Therefore, in our simulations where the spiral waves were in rigid rotation mode, it was harder to excite the tissue when the pacing frequency was higher, whereas in experiments, where the spiral waves were usually experienced a combination of rigid rotation and meander, the pacing cycle lengths had more freedom to vary.

The computer simulations also suggested a higher success rate when the first shock was applied at the downslope of the fraction of tissue excited (FTE) curve. Note, however, that this is only based on the correlation between FTE and the timing of the first shock. Nevertheless, our results seem to agree with those of Turner et al. [148], where termination of tachyarrhythmia in humans was most likely when delivered a few milliseconds after the ECG peak. A simulation study by Rantner et al. [149] proposed applying shocks at the times when tissue excitable volume is maximum (the excitable gap is largest) instead of at a fixed pacing cycle length. Although this protocol can effectively convert VF to VT, it does not always terminate it, and it therefore requires a second stage of low-voltage stimuli to terminate the arrhythmia. It also adds extra difficulty to experiments when the pacing cycle length is not fixed and each shock must happen when the least amount of tissue is excited. Our study only aimed to improve the success rate of LEAP based on its original

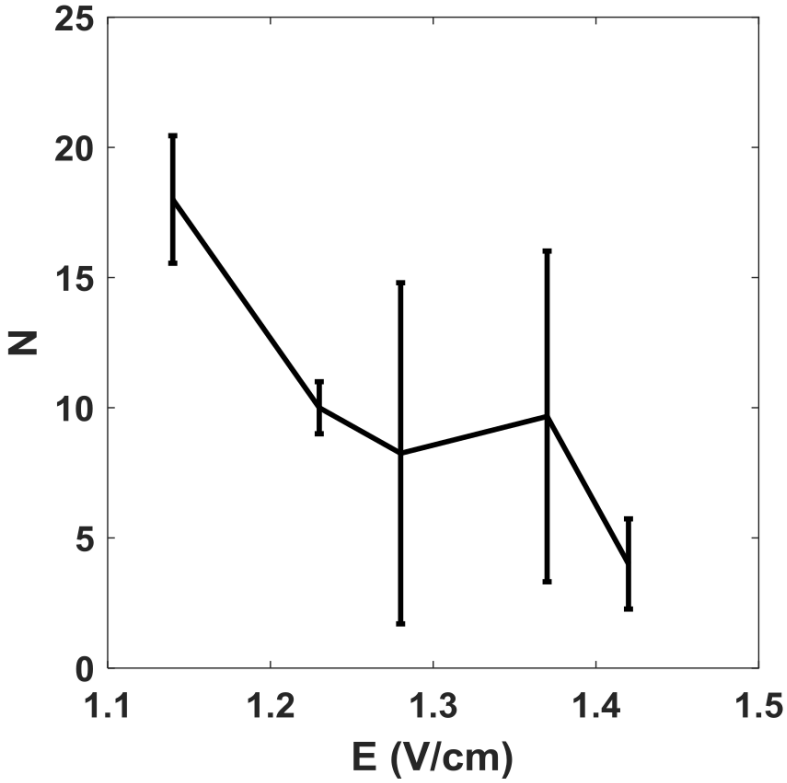

Figure 6.13: Average number of shocks as a function of shock strength to terminate the 4-sprial arrhythmia in simulations. Shock period is 221ms, 10% above the dominant period of the spirals. For each shock strength, 4 numerical simulations were performed, each with a different timing of the first shock. Then the number of shocks was averaged among the 4 trials. Error bar represents the standard deviation.

protocol instead of looking for optimal solution so that it can be easily implemented in future experiments.

6.6 Limitation

This chapter only tested arrhythmias in isolated atria and separated right and left ventricles (for better optical mapping visualization) but not in full hearts. We only performed 2D simulations because 2D shells can support complex dynamics and the atrial wall is usually only a few millimeters thick. However, we still need to test the shock timing hypothesis using more complicated models that display more complex breakup and different excitable

gaps. Only human atria model was simulated here. We also need to test the theories on ventricle models.

One major finding from this chapter is that synchronization is the main mechanism for LEAP to terminate arrhythmia. We used Kuramoto phase plot to demonstrate that. More rigorous analysis is needed for the future work. For example, we should calculate the standard deviation of phases before and during LEAP and LEAP should result in a smaller standard deviation.

CHAPTER 7

EFFECTS OF HETEROGENEITIES ON DEFIBRILLATION

In this Chapter, we explored how heterogeneities affect defibrillation results using WebGL accelerated simulations. The heterogeneities we are interested in are blood vessels. In 2D, we first compared the simulations with experiments, then we used the validated model to investigate factors affecting defibrillation success rates. In 3D, we verified the hypothesis that the low-energy shocks terminate fibrillation by detaching the vortex filaments from depolarization surface in realistic 3D structure.

7.1 Simulation setup

For defibrillation simulations in this chapter, we solved monodomain equations (Eq. 3.2) with boundary conditions as Eq. 3.4.

For the 2D situation, the simulation domain is a square with $D/C_m = 1.0\times10^{-3}\text{cm}^2/\text{ms}$. Non-conductive circles represent blood vessels on the tissue. Figure 7.2 shows an example of the 2D domain with 3% of the total areas being blood vessels. 5% and 8% of vessels are also being used. For each percentage, up to five structures with vessels located at different random positions are generated for simulations.

We used the Ten Tusscher model [75] and the Fenton-Karma-3V model [81] as ionic models (specified in each case). Explicit Euler and center difference schemes are used for the time and spatial integration and the resolutions are $\Delta t = 0.01ms$ and $\Delta x = 200\mu m$.

7.2 Validating virtual electrodes from blood vessels

The size distribution of the blood vessels follow the power law as the experiments [3]. In Figure 7.2, R is the vessel radius. There are more smaller vessels and fewer larger ones.

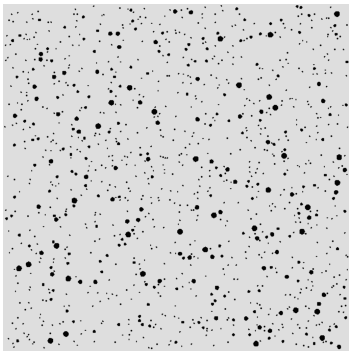

Figure 7.1: Example of 2D simulation domain. Grey areas are conductive tissue with $D/C_m = 1.0 \times 10^{-3}\text{cm}^2/\text{ms}$ and black circles represent non-conductive vessels with $D = 0$. The domain size is 20cm by 20cm.

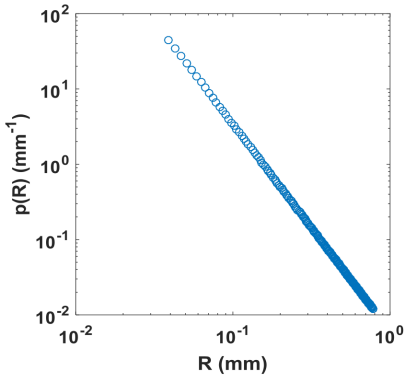

Figure 7.2: The size distribution of blood vessels following the same power law as experiments: $p \sim R^{-2.75}$.

The distribution density follows $p(R) \propto R^{-2.75}$.

In this section, we verified that two characteristics of virtual electrodes (minimum radius and excitation time) of our numerical simulations follow the power law close to the experimental results.

7.2.1 Minimum Radius

For a given electric field strength, there exists a minimum radius of the blood vessels to generate virtual electrodes. Figure 7.3 demonstrates this. The two blood vessels with different sizes are subjected to the same electric field strength. On the left, the vessel is smaller than the minimum radius so no excitations are generated while on the right, the

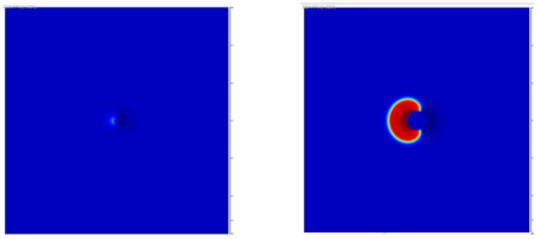

Figure 7.3: Vessel size affects the generation of virtual electrodes. The same electric field strength is applied to both vessels. The smaller vessel (R = 0.5mm) does not generate excitation while the larger one does (R = 1.7mm). The size of the tissue is 4cm×4cm

vessel is large enough to produce a propagation wave.

From theory, the minimum radius is inversely proportional to the electric field strength ($R_{min} \propto E^{-1}$) for large electric field[3]. We performed numerical experiment for the Ten Tusscher model. In the simulation, for a given electric field strength, we gradually increase the size of the vessel until an excitation wave is generated (Figure 7.3). We plot the minimum radius as a function of electric field strength and fit the curve into $log(R_{min}) = \alpha log(E) + \beta$ using MATLAB *polyfit* function and we get $\alpha = -1.0247$, $\beta = -3.5625$ with $r^2 = 0.9813$, which is close to the theoretical. However, there is a deviation. The theory for the power law breaks down when the electric field is small because there is a finite excitation threshold for a cell. It will also break down when the radius of the vessel is small because the resolution and the size of the cell is finite. These can both contribute to the discrepancy between the theory and the simulation.

7.2.2 Excitation Time

Next we verified the relation between the time for the excitations to propagate through the whole domain (τ) and the electric field strength (E).

We assume the number of virtual electrodes is proportional to the number of the blood vessels. By integrating the distribution density function of blood vessels we can get the

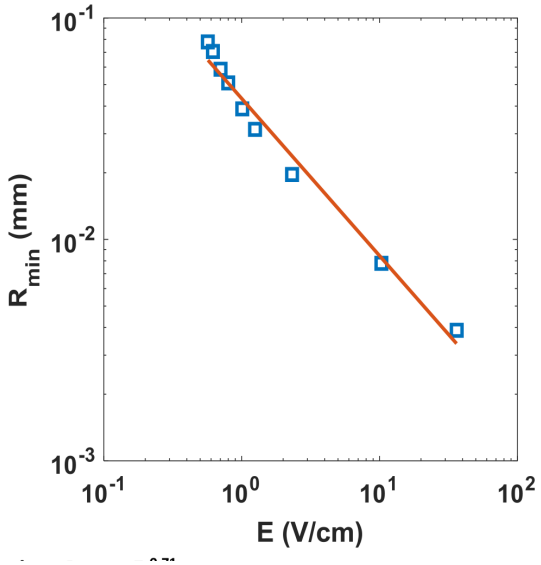

Figure 7.4: Fitting of the minimum radius to generate virtual electrode to a power law of the electric field strength. The power is -1.02, close to the theoretical value -1.

density of the virtual electrodes ρ:

$$\rho(E) = \int_{R_{min}(E)}^{R_{max}} p(R)dR \tag{7.1}$$

Then we assume the excitation from virtual electrodes propagate uniformly with a constant speed v, in time τ, it will occupy the volume of $V = \rho\frac{4}{3}\pi(v\tau)^3$, therefore we can calculate the excitation time τ from the total volume V of the heart based on the $p(R)$ acquired from experiments. This is the τ value in theory.

On the other hand, we can measure in experiments the total time it takes for the excitation to propagate through the surface from the optical mapping experiments. The theory and the experimental results agree with each other very well with $\tau \propto E^{-0.87}$ [3].

We verified the excitation time for the Ten Tusscher model with the domain size of 4 cm $\times$ 4 cm, which is similar to the tissue size in experiment [3]. The radii of the vessels range between 0.04 mm to 0.8 mm with spatial resolution of 0.04 mm. The results are shown in Figure 7.5

Circles are values from numerical experiments, averaged among 5 structures. Error

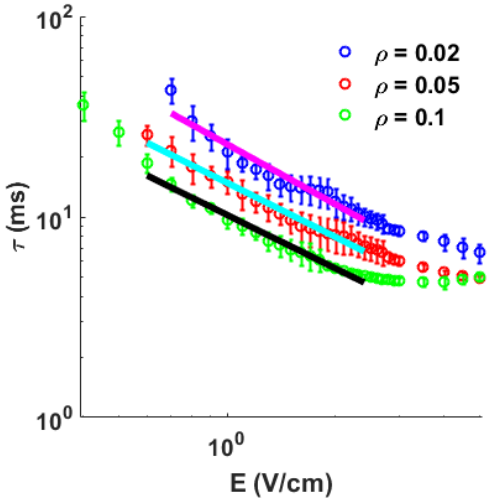

Figure 7.5: The fitting of the excitation time as a power law of the electric field strength for the Ten Tusscher model. The power of the fitting is close to the experimental value -0.87 for the three different numbers of vessels.

bars are standard deviations. Different colors (blue, red and green) are for different blood vessel numbers. The total area of blood vessels (ρ) is 2%, 5% and 10% of the total area of the square domain. The three curves do not fit into power law well if all the data points are included in the fitting. This is because when E keeps increasing beyond a threshold, an activation delay required to generate a propagating action potential thus τ reaches its nonzero lower bound.

However, if we only fit the curve within the experimental electric field range (magenta, cyan and black curves), which is between 0.5 and 2.5 mV [3], then the curves can be fit into $\tau = \beta E^{\alpha}$ with α being -1.0, -0.90 and -1.0 for $\rho = 0.02, 0.05, 0.1$, which are much closer to the theoretical value (Table 7.1). This means our simulations can reproduce the excitation time within the experimentally tested E range, and provide additional information in the range that is hard to test in experiments.

Table 7.1: Fitting the excitation time into a power law of the electric field strength $\tau \sim E^{\alpha}$.

ρ	α
0.02	-1.0
0.05	-0.90
0.1	-1.0
Experiment	-0.87

7.3 Comparison of the defibrillation success rate between LEAP and the one-shock defibrillation

We initialized the spiral waves using the S1-S2 protocol on a 20 cm $\times$ 20 cm domain and we induced the wave breaks by choosing ten random sites to excite. After sufficient wave breaks, we applied either the one-shock defibrillation or LEAP. Both LEAP and the one-shock defibrillation used biphasic shocks. For LEAP, pacing periods of $1.1T_0$, $1.5T_0$ and $2.0T_0$ were tested, T_0 being the dominant period of the fibrillation. For each shock strength, we calculated the defibrillation success rate for 40 trials with randomized initial conditions.

Figure 7.6 shows the comparison of the one-shock defibrillation and LEAP for two different structures. 3% of the total area is blood vessels in both structures but vessels are located at different random locations. In general, LEAP has a higher defibrillation success rate than the one-shock defibrillation. For example, for the first structure, to achieve 80% defibrillation success rate, the one-shock defibrillation needs electric field strength of at least 7.5 V/cm while LEAP with the period of $2T_0$ needs 4 V/cm, which is 72% of energy reduction per pulse.

The performance of LEAP depends on the period of the shocks. For both structures, the longer periods work better than the shorter ones. This can be explained by Figure 7.7, which shows the LEAP defibrillation success rate as a function of the number of shocks for pacing period of $1.5T_0$ (Figure 7.7a) and $2.0T_0$ (Figure 7.7b). Solid lines are for structure from Figure 7.6a and dotted lines are for structures from Figure 7.6b. Different colors indicate different electric shock strengths. For both structures, stronger shocks have higher

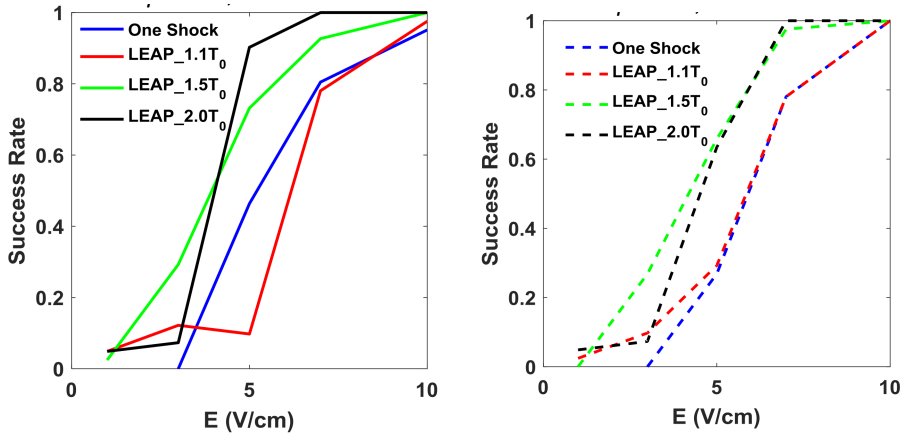

(a) Structure 1

(b) Structure 2

Figure 7.6: Comparison of defibrillation success rate between one-shock defibrillation and LEAP for two different structures with blood vessels located at different random locations. LEAP with longer pacing period has higher defibrillation success rate than the one with shorter pacing period and one-shock defibrillation.

defibrillation success rates. When the pacing period is $2.0T_0$, the success rate increases with each additional shock while when the period is $1.5T_0$, the success rate decreases at the third shock. This is because different regions on the domain has different frequencies. When the period is short, even though it is above the dominant period, there will be regions that have periods longer than the dominant period. In those regions, the wave front can catch up and interact with the wave back of the previous excitation, which can re-initiates wave breaks and make defibrillation harder. That's why in our simulations, LEAP works better with longer periods.

7.4 Factors affecting defibrillation success rate

First, we explored the effects of number of heterogeneities on one-shock defibrillation success rate. Five 20 cm $\times$ 20 cm domains with blood vessels located at random spots were generated for three different number of blood vessels each: 3%, 5% or 8%. We calculated the defibrillation success rate for each structure using the Ten Tusscher model and average among the five structures to get the averaged defibrillation success rate. Figure 7.8 shows the results. For a given structure, the defibrillation success rate increases to 1.0 when the

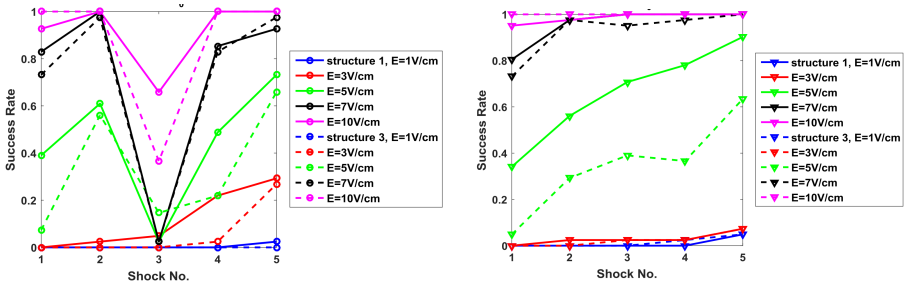

(a) T = $1.5T_0$ (b) T = $2.0T_0$

Figure 7.7: LEAP defibrillation success rate as a function of different number of shocks for pacing period of $1.5T_0$ and $2.0T_0$. For $T = 2.0T_0$, the defibrillation success rate increases when the number of shock increases. For $T = 1.0T_0$, however, the defibrillation success rate decreases at the third shock due to the re-initiation of spiral waves.

electric field strength increases. For the same electric field strength, domains with more blood vessels have higher defibrillation success rate. This is because more blood vessels and stronger electric field strength will produce more virtual electrodes and therefore higher success rate.

Next, we varied the size of the domain from 7.5 cm to 15.0 cm. Here the Fenton-Kamar-3V model is used. The choice of the model and the domain size is based on the feature of the fibrillation and the number of spiral waves we want to fit on the domain. We chose Fenton-Karma-3V model because its parameters have a highly-breakup regime that can fit 5 waves on the smallest domain we tested here and 20 waves on the largest domain. For each domain size, the area of blood vessel is fixed to be 3%. The maximum/minimum radius and the size distribution of the blood vessel is also the same for each domain size. Figure 7.9 shows the results. Figure 7.9a plots the success rate as a function of the electric field strength. Figure 7.9b plots the success rate as a function of the tissue size.

Similar to Figure 7.8, the defibrillation success rate increases to a plateau value when the electric field strength increases. However, the plateau values do not always equal to 1.0. With increasing tissue size, the plateau success rate decreases. This is because the model parameters are in a highly breakable regime. Even though the strong shocks can excite the whole domain, slight discrepancy in the excitability in different regions can cause re-

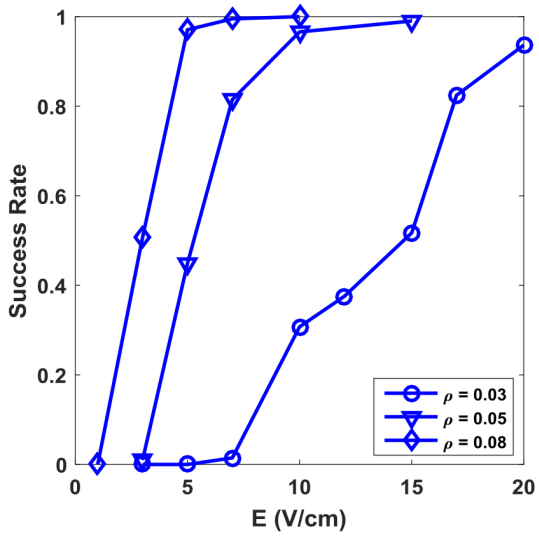

Figure 7.8: The effects of number of blood vessels on defibrillation success rate. When the number of heterogeneity increases, the defibrillation success rate increases. The Ten Tusscher model is used.

initiation of spiral waves.

For a given electric field strength, the defibrillation success rate decreases when the tissue size increases and the decreasing rate is almost linear. This is because for larger tissue, more waves can fit in the domain and the number of spiral waves is linearly increasing with respect to the tissue size 7.9c. More waves make it harder to defibrillate.

7.5 Electrode shapes affecting defibrillation results

All the defibrillation simulations we have done so far are with two plane electrodes so the electric field is uniform in between. In real life, defibrillators, especially the implantable ones, do not take form of plane electrodes. The implantable cardioverter defibrillator (ICD) usually applies the electric shocks between one or several electrodes that are implanted in the heart, usually 1 to 2 millimeters in diameter, and an oval shaped can, about 5 to 7 centimeters in length. In this section, we discuss how the shape of electrodes affect the defibrillation results.

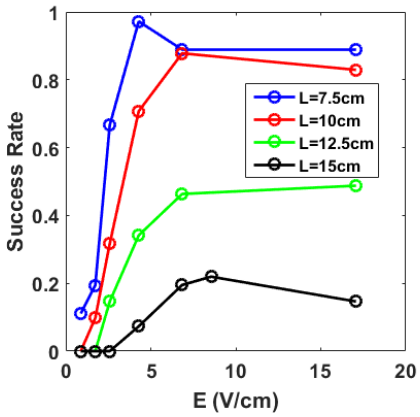

(a) S.R. as a function of E field

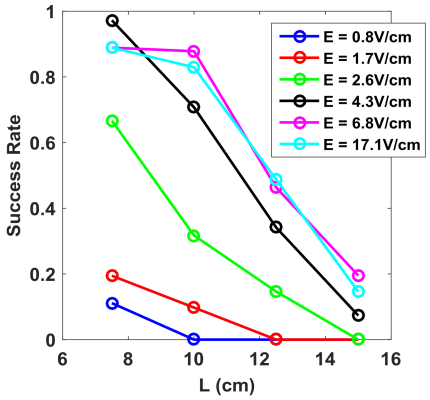

(b) S.R. as a function of the tissue size

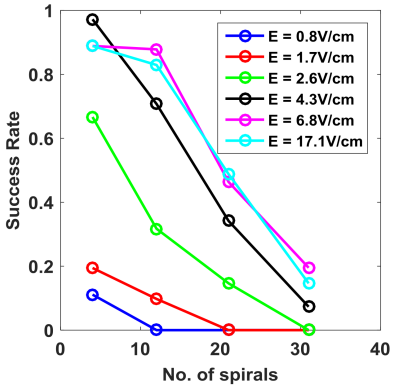

(c) S.R. as a function of the number of spiral waves

Figure 7.9: The effects of tissue size on defibrillation success rate. The defibrillation success rate decreases when domain size increases and the decreasing rate is linear for all electric field strength. Fenton-Karma 3V model is used.

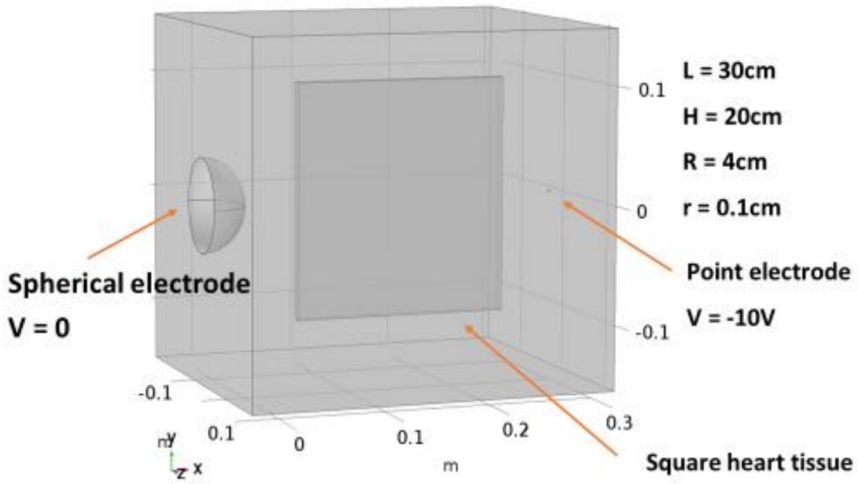

Figure 7.10: The setup of the electrodes

7.5.1 Electrodes setup

Inspired by the ICDs, we set one electrode to be a point electrode with a small radius of 1 mm and the other electrode takes a few different shapes: either a plane or a semi-sphere with a radius of 4cm that can be either concave or convex. The distance between the two electrodes is 30cm. The "heart tissue" is a 2D slab with the dimension of 20 cm $\times$ 20 cm, as in our previous Ten Tusscher simulations, located in the center between the two electrodes. We set the electric potential on the point electrode to be -10 V and the potential on the spherical electrode to be 0 V to create the electric field in between.

We built the electrodes setup in COMSOL. Figure 7.10 shows an example. In COMSOL, we used the Electric Current (ec) mode to solve the electric potential and the electric field in the 3D 30 cm $\times$ 30 cm $\times$ 30 cm space using the finite element method with an extremely fine mesh. A thin slab of heart tissue is placed in the center. The potential on the two electrodes are fixed to two constant values to create electric field in between. Boundary conditions everywhere else is zero-flux. Then we output the electric field in the heart tissue region and use that as the electric shocks in the 2D Ten Tusscher model simulation.

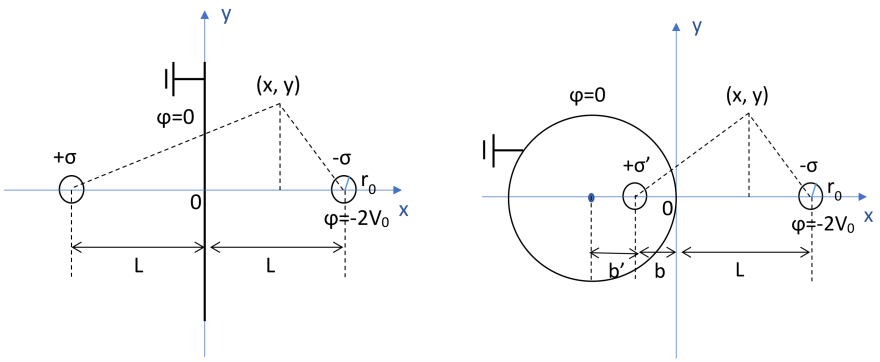

(a) Plane-Point electrodes

(b) Sphere-Point electrodes

Figure 7.11: Method of images for two electrodes configurations

7.5.2 Method of images

We also used the method of images to calculate the theoretical electric potential and electric field in two cases: (1) one point electrode and one infinite plane electrode (Figure 7.11a); (2) one point electrode and one convex spherical electrode (Figure 7.11b).

For the Plane-Point electrode setup, the infinite plane is grounded and the point electrode with $r_0 = 1mm$ has the electric potential of $-2V_0$. The distance between the plane and the point is L (Figure 7.11a). We make the approximation that charge is uniformly distributed on the point electrode and the charge density is $-\sigma$. We can make this approximation because $L >> r_0$. From the symmetry, we know this system is equivalent to an image point electrode located on the other side of the plane with charge density $+\sigma$ to make the potential equal to zero on the plane. Assuming the distance L is much larger than r_0, we can calculate the potential on the point electrode due to the charge on it and on the image point electrode:

$$\begin{aligned} -2V_0 = \phi(r_0) &= \frac{1}{4\pi\epsilon_0}\frac{-\sigma 4\pi r_0^2}{r_0} + \frac{1}{4\pi\epsilon_0}\frac{\sigma 4\pi r_0^2}{2L} \\ &= \frac{\sigma}{\epsilon_0}(-r_0 + \frac{r_0^2}{2L}) \end{aligned} \tag{7.2}$$

Therefore,

$$\sigma = \sigma_0 = \frac{-2\epsilon_0 V_0}{r_0} \frac{1}{-1 + \frac{r_0}{2L}} \tag{7.3}$$

$$q_0 = \sigma_0 4\pi r_0^2 \tag{7.4}$$

Treat both the point electrode and the image point electrode as point charges. The electric field at location (x,y) produced by $+\sigma$ and $-\sigma$ are:

$$\vec{E}_+ = \frac{q_0}{4\pi\epsilon_0} \left(\frac{L+x}{((L+x)^2+y^2)^{3/2}} \hat{i} + \frac{y}{((L+x)^2+y^2)^{3/2}} \hat{j} \right) \tag{7.5}$$

$$\vec{E}_- = \frac{q_0}{4\pi\epsilon_0} \left(\frac{L-x}{((L-x)^2+y^2)^{3/2}} \hat{i} - \frac{y}{((L-x)^2+y^2)^{3/2}} \hat{j} \right) \tag{7.6}$$

The net electric field is $\vec{E} = \vec{E}_+ + \vec{E}_-$.

Similarly, for the Sphere-Point electrode setup, the sphere is grounded and the point electrode has an electric potential of $-2V_0$ (Figure 7.11b). Assume a uniform charge distribution on the point electrode with the charge density of σ. An image electrode with charge density of σ' is located inside the sphere at a distance of b' from the center. $b' = \frac{R^2}{R+L} = \alpha R$ and $\sigma' = \frac{R}{R+L}\sigma = \alpha\sigma$, R being the radius of the sphere. To maintain the potential on the point electrode to be $-2V_0$, $\sigma = -\frac{2\epsilon_0 V_0}{r_0} \frac{1}{-1+\frac{r_0}{2L}\frac{1}{1+L/(2R)}} = \sigma_0\beta < \sigma_0$.

Let $q = \sigma 4\pi r_0^2 = \beta\sigma_0 4\pi r_0^2 = \beta q_0$,

$$\begin{aligned} \vec{E} = \vec{E}_+ + \vec{E}_- = \frac{\beta q_0}{4\pi\epsilon_0} \Bigg(& \left[\frac{\alpha(\alpha L + x)}{((\alpha L + x)^2 + y^2)^{3/2}} + \frac{L-x}{((L-x)^2+y^2)^{3/2}} \right] \hat{i} \\ & + y \left[\frac{\alpha}{((\alpha L + x)^2 + y^2)^{3/2}} - \frac{1}{((L-x)^2+y^2)^{3/2}} \right] \hat{j} \Bigg) \end{aligned} \tag{7.7}$$

7.5.3 Compare the results between COMSOL and the method of images

We set $V_0 = 5V$ in both COMSOL and the method of images and calculated the electric potential between the two electrodes. Figure 7.12 shows the results. The potential distribu-

tion follows the same trend. There is a discrepancy between COMSOL and the method of images and the difference is less than 10%.

Then we output the electric field in the region where the heart tissue is supposed to be and we rescaled it so that the mean value of the magnitude of the electric field on the tissue domain is the field strength that we tested in simulations in the previous section. We tested the defibrillation success rate for the one-shock defibrillation and plotted it as a function of average E field strength for different electrode configurations. The Ten Tusscher model is used with 5% blood vessels.

Figure 7.13 shows the results. The blue line is the defibrillation result for two infinite plane electrodes (same as in Figure 7.8). The red and the green lines with triangle markers used the electric field strength from the Plane-Point and the Sphere-Point electrode configurations from COMSOL. The red and the green lines with circles used the electric field from the method of images.

The Plane-Plane configuration has the highest defibrillation success rate. It is because the electric field in between is uniform. It is easier to get more excitations for a given E field strength. The Plane-Point works better than the Sphere-Point configuration, but the difference is not much. There is a clear discrepancy between COMSOL and the method of images. In order to understand this, I plotted in Figure 7.14 the distribution of the magnitude of the E field strength for (i) Plane-Point configuration in COMSOL (top left), (ii) Plane-Point configuration in the method of images (top right), (iii) Sphere-Point configuration in COMSOL (bottom left), and (iv) Sphere-Point configuration in the method of images (bottom right). In all cases, the average E field magnitude is the same. Within the same configuration, the COMSOL distribution is more narrow than the method of images. This means the E field is more uniformly distributed, similar to the Plane-Plane configuration. If the distribution is wide, when part of the domain is applied by a strong E field, the other part is under a weak field strength. This will cause excitations of only a part of the domain, therefore failed termination of fibrillations.

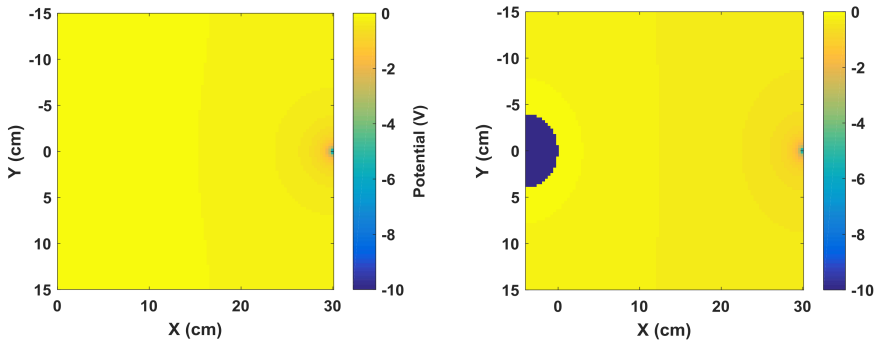

(a) COMSOL: Plane-Point

(b) COMSOL: Sphere-Point

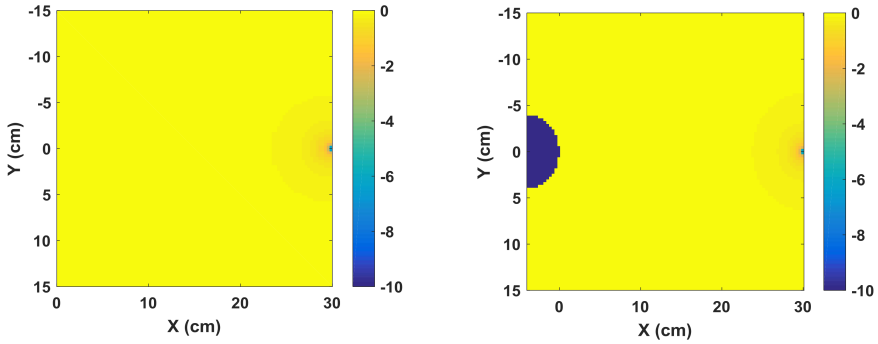

(c) Method of image: Plane-Point

(d) Method of image: Sphere-Point

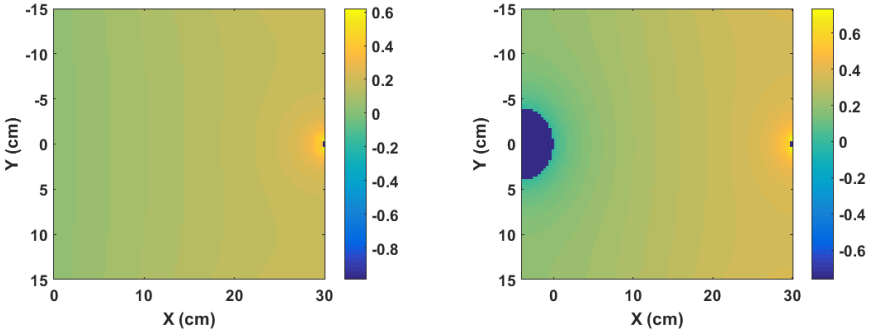

(e) Difference: Plane-Point

(f) Difference: Sphere-Point

Figure 7.12: The electric potential of Plane-Point and Sphere-Point electrode configuration solved using COMSOL and the method of images and compare the difference between the two methods. The difference is less than 10%

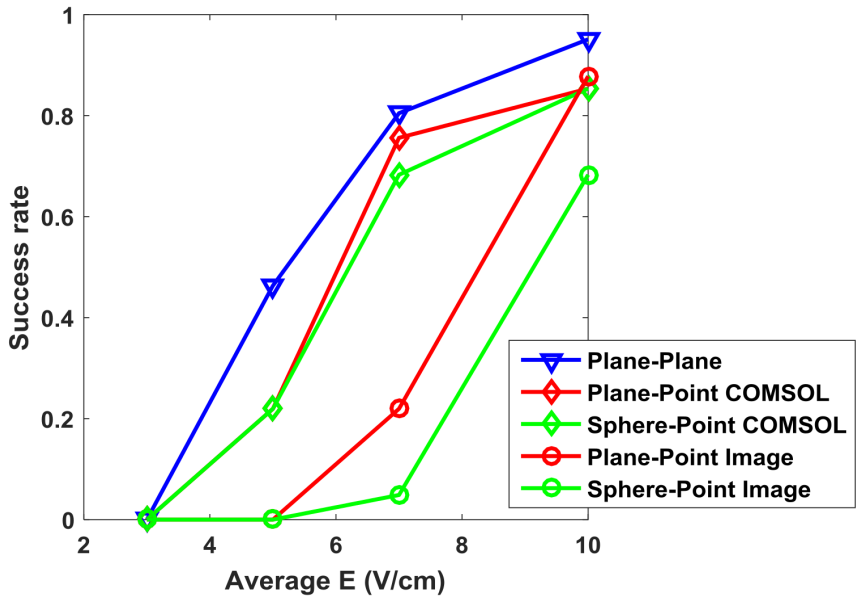

Figure 7.13: The defibrillation success rate for different electrode configurations. The Plane-Plane configuration has the best defibrillation results. Within COMSOL/method of images, there are not much difference between the Plane-Point and Sphere-Point electrode configuration but there's a clear difference between COMSOL and the method of images.

7.6 Low energy shocks terminate arrhythmia by detaching vortices's filaments from depolarized surface

One hypothesis for the low-energy shocks to terminate fibrillation is that the shocks detach the vortices filaments from the depolarized surface [150]. Previous simulations have shown this in simplified geometries such as cylinders and hemispheres that represent heart tissue. Here we demonstrate it in a realistic 3D structure.

A canine left ventricle structure was extracted from micro-CT scans. Blood vessels imbedded in the tissue was treated as inexcitable medium. The size of the 3D structure is $3.7 \times 2.15 \times 4.76$ cm^3 (x-y-z) and the grid size is $256 \times 128 \times 128$. Figure 7.15 shows the structure. Note that the resolutions in the x and the y directions are comparable and they are much higher than the z direction due to the resolution of the original CT scans. Time resolution is 2.0×10^{-2} ms. Fenton-Karma 3V model with none-breakup parameters was

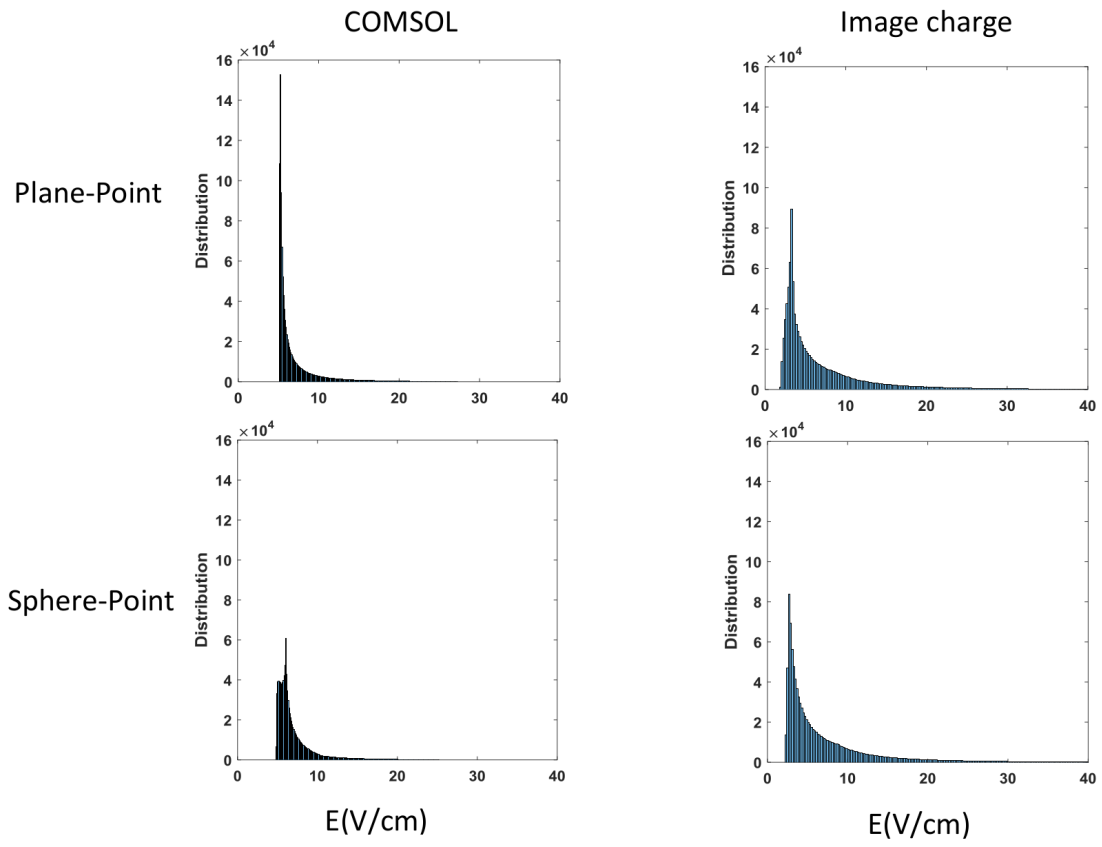

Figure 7.14: The magnitude of E field distribution for Plane-Point (top) and Sphere-Point (bottom) electrode configurations in COMSOL (left) and the method of images (right). The E field strength is more homogeneous in the COMSOL simulation than in the method of images.

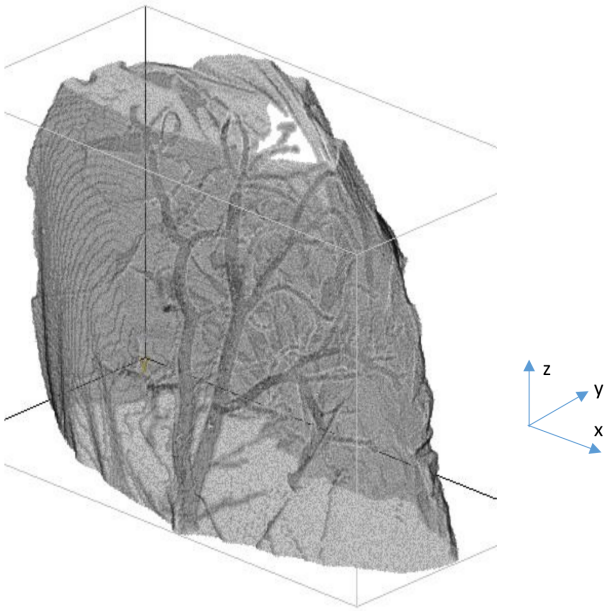

Figure 7.15: 3D canine left ventricle structure with blood vessels.

used.

Figure 7.16 shows the evolution of the scroll waves (left panels) and their filaments (right panels) before and after the shock.

One spiral wave was initiated and it broke into two counter-rotating scroll waves. The two filaments run in parallel connecting epicardium (front surface) and endocardium (back surface) (Figure 7.16a). Then a monophasic shock with the strength of 1 V/cm and the duration of 5 ms is applied. During the shock, the epicardium is depolarized. Figure 7.16b shows 2 ms after the end of the shock. Figure 7.16c and Figure 7.16d shows 15 ms and 40 ms after the shock. The end of the filament formerly connected to the epicardium is detached and connected to the top/bottom surface. This demonstrates the ability of the shock to disconnect filaments from the surface depolarized by the shock. Then the two filaments shrink and disappear (Figure 7.16e). This confirmed Otani's theory that low energy shocks can transform all filaments into shapes that tend to shrink and disappear thereby terminating all the vortices and associated turbulence.

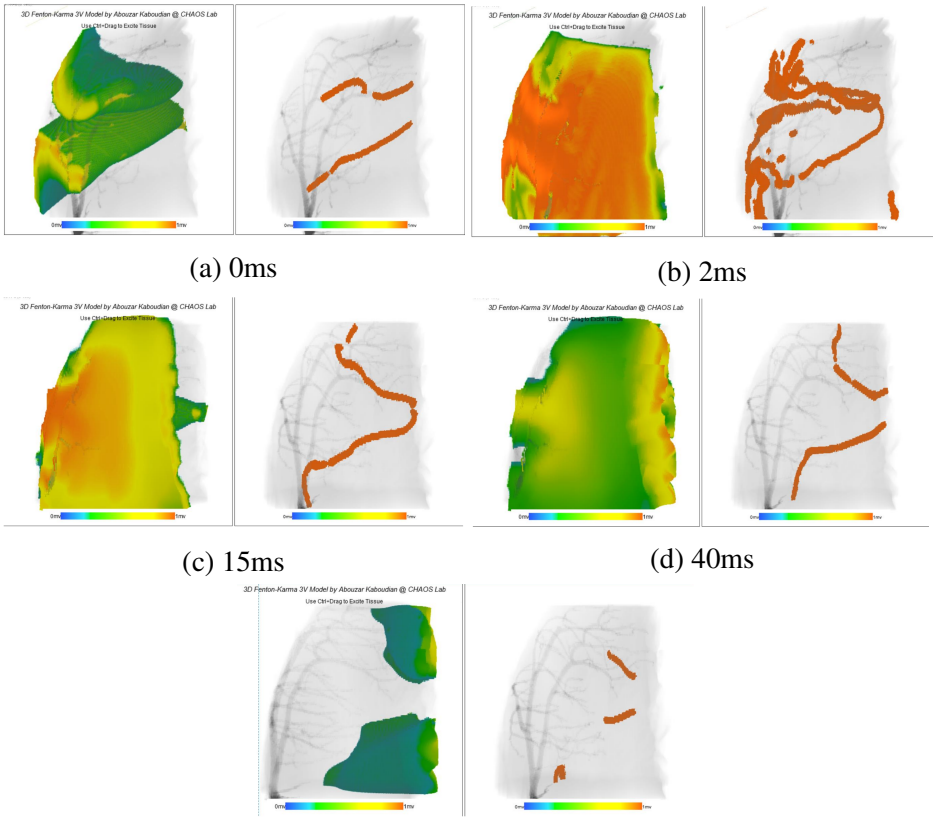

(a) 0ms

(b) 2ms

(c) 15ms

(d) 40ms

(e) 65ms

Figure 7.16: Effects of the electric shocks on vortices's filaments. The time in each figure is the time after the shock. The shock disconnected the filaments from the depolarized surface (epicardium, the front surface) and annihilate the filaments.

7.7 Conclusion and limitation

The main purpose of this chapter is to use WebGL-accelerated simulations to investigate how heterogeneity affects defibrillation results. We first verified that the simulations can reproduce two important characteristics associated with virtual electrode: the minimum radius of the heterogeneity to generate virtual electrode and the excitation time for the wave to propagate through the whole domain as a function of electric field strength. Then we showed that LEAP works better in simulations with longer pacing period. This is because longer period shocks are less likely to re-initialize spiral waves when the spirals are in a highly-breakable regime. Furthermore we demonstrated that larger domains with more waves fit in them are harder to defibrillate. Then using COMSOL simulations and the method of images, we showed that the uniform electric field have the best defibrillation results and except for Plane-Plane electrode configurations, other shapes of electrodes do not change the defibrillation results much. Finally, we conducted 3D simulations to demonstrate the termination of fibrillation by detaching the vortices's filaments from the depolarized surface.

From these results, we suggest a few tests for future LEAP simulations and experiments:

(1) The pacing period should depend on what kind of spiral waves the system has. If the spiral is in steady rotation mode or the system has a narrow frequency spectrum, the pacing period should be close to the dominant period. If such shocks re-initiate fibrillation, long pacing period should be considered.

(2) Reducing the number of spiral waves could be the first stage of LEAP before terminating them all. Other pacing protocols such as ATP could be combined to LEAP for this purpose.

(3) When design and test the shape and the position of electrodes for delivering shocks, the ones that ensure a uniform electric field distribution (such as large plane electrodes)

should have better defibrillation results.

Limitations and future work:

(1) In this chapter, we only considered blood vessels as the heterogeneity. Caldwell et al. used 3D optical mapping showed that virtual electrodes are generated due to the lateral cell uncoupling in the direction of the electric field instead of at large blood vessels when the shock strength is so low that it doesn't produce an activation wave [151]. We should consider the effects of not only the tissue level heterogeneity such as blood vessels and fiber rotations, but also cellular level heterogeneity such as cellular uncoupling.

(2) There is a noticeable difference in the results between COMSOL and the method of images. One possible reason could be the setup of the COMSOL simulation is not comparable to the method of images. For example, the computation domain in COMSOL could be set to be larger to reduce the boundary effects. More careful verification is needed.

(3) When we tried to fit the "minimum radius" and the "excitation time" into power laws, we observed a difference between the simulation and the theory. We provided some explanation why the theory breaks down. Rigorous algorithms could be used for testing whether the simulation data is truly a power law [152].

CHAPTER 8
CONCLUSION

The main goal of this thesis is to investigate the mechanism of low-energy defibrillation and to improve it. The thesis can be divided into three parts. The first part is background, literature review and problem description. The second part is validation of two aspects of numerical models: contraction and calcium dynamics. The third part focus on the mechanism of LEAP and the effect of heterogeneities on defibrillation results.

In Chapter 4, we developed a systematic methodology to implement contraction into electrophysiology models. We found that EP models with dynamic calcium troponin buffers are better candidates to implement contraction. The inclusion of contraction does not disturb properties in the original models and the contraction behavior of post-extrasystolic potentiation fits experiments better.

In Chapter 5, we characterized with high spatio-temporal resolution the development of discordant alternans patterns in transmembrane voltage (V_m) and intracellular calcium concentration ($[Ca_i^{2+}]$) as a function of pacing period in rabbit hearts. Then we compared the dynamics to that of Sato et al. model. We found that in experiments, the nodal lines of CaD alternans have a steeper slope than those of APD alternans, but not as steep as predicted by numerical simulations in rabbit models. Alternans in CaD have nodal lines that are about an order of magnitude steeper compared to those of APD alternans. Current action potential models lack the necessary coupling between voltage and calcium compared to experiments and fail to reproduce some key dynamics such as, voltage amplitude alternans, smooth development of calcium alternans in time, conduction velocity and the steepness of the nodal lines of APD and CaD.

In Chapter 6, we investigated the mechanism of LEAP with both ex vivo experiments and simulations. We induced atrial and ventricular fibrillation in isolated canine hearts and

applied LEAP and standard one-shock defibrillation to terminate the arrhythmia. We simulated the arrhythmia and LEAP using a 2D bidomain human atrial model. Both experiments and simulations verified synchronization from virtual electrodes is the key mechanism for termination of arrhythmia by LEAP using modified Kuramoto phase plots and fraction of tissue excited (FTE) plots. We also observed in simulations that LEAP is more effective when the shock period is close to the dominant period and the first shock is delivered when FTE is decreasing.

In Chapter 7, we investigated the effect of multiple factors on defibrillation. We showed that LEAP works better in simulations with longer period. We demonstrated that larger domains with more waves fit in them are harder to defibrillate. Then using COMSOL simulations and the image charge method, we showed that the uniform electric field have the best defibrillation results and except for Plane-Plane electrode configurations, other shapes of electrodes do not change the defibrillation results much. Finally, we conducted 3D simulations to demonstrate the termination of fibrillation by detaching the vortices's filaments from the depolarized surface.

Appendices

APPENDIX A

IMPLEMENTATION OF NL96

A.1 Step 0: Handling models that already have contractions.

If the model has NL96 contraction then we only need to take that out. For example, Matsuoka_etal_2003 has NL96 contraction. We eliminate the four troponin states in NL96 and replace them with the single-state dynamic equation for CaTRPN like Eq. 4.3 and set K_{on} and K_{off} to the values of Y_1 and Z_1.

If the model has contraction but not the NL96 one, we first take out the original contraction then implement NL96. For example, Iribe_etal_2006 model has Rice1999 contraction. Rice mechanics model has six tropomyosin/cross-bridge states. The transform rates among these six states are related to CaTRPN. Their CaTRPN is expressed by a single-state dynamic equation like Eq. 4.3 with a dynamic K_{off} dependent on force. To take out contraction from Iribe_etal_2006, we eliminate the six tropomyosin/cross-bridge states and set K_{off} for CaTRPN to a constant value by fixing the force in the K_{off} expression to half of its maximum value. After taking out Rice1999 contraction, follow Step 3 in the NL96 contraction implementation flowchart to implement NL96.

A.2 Step 1: Add instantaneous CaTRPN buffer

If the model has one general Ca^{2+} buffer (referred as General) representing the average effect of all intracellular Ca^{2+} buffers (e.g. TenTusscher_etal_2006 and Fink_etal_2008), we split the general buffer into two parts: CaTRPN and Other. We keep $K_{d,TRPN}$ and $K_{d,Other}$ to be the same as $K_{d,General}$ in the original model so that the Ca affinity of the instantaneous buffer will be retained. $B_{max,TRPN}$ was set to be 0.07mM, which is a standard value in most models. $B_{max,Other} = B_{max,General} - B_{max,TRPN}$ so that the concentration of the

total intracellular Ca^{2+} buffer is the same as in the original model. If the model has other Ca^{2+} buffers (such as CMDN) but no CaTRPN (e.g. Fox_etal_2002), we keep the other buffers unchanged and add a CaTRPN buffer. For the new CaTRPN buffer we also set $B_{max,TRPN} = 0.07mM$ and $K_{d,TRPN} = 0.6\mu M$, which are both common values in many models.

A.3 Step 2: Change the instantaneous intracellular CaTRPN into a dynamic buffer.

Keep all other buffers instantaneous.

A.3.1 Equations

Original

$$\frac{d[Ca^{2+}]_i}{dt} = \beta I_{total}^{Ca} \tag{A.1a}$$

$$\beta = 1/(1 + \sum_j \frac{B_{max,j} K_{d,j}}{([Ca^{2+}]_i + K_{d,j})^2}) \tag{A.1b}$$

(A.1c)

I_{total}^{Ca} is the total intracellular Ca^{2+} current; β is the instantaneous buffer factor; index j represents each type of intracellular Ca^{2+} buffer; $B_{max,j}$ and $K_{d,j}$ are the total concentration and the affinity constant for buffer j.

Modified

$$\frac{d[Ca^{2+}]_i}{dt} = \beta'(I^{Ca}_{total} - I_{CaTRPN} \tag{A.2a}$$

$$\beta = 1/(1 + \sum_{j}^{'} \frac{B_{max,j'} K_{d,j'}}{([Ca^{2+}]_i + K_{d,j'})^2}) \tag{A.2b}$$

$$I_{CaTRPN} = \frac{d[CaTRPN]}{dt} = K_{on}[Ca^{2+}]_i(B_{max,trop} - [CaTRPN]) - K_{off}[CaTRPN] \tag{A.2c}$$

in which J' goes through all Ca^{2+} buffers except for CaTRPN.

To change instantaneous CaTRPN into a dynamic buffer, we delete the term corresponding to troponin in the instantaneous buffer factor β and subtract the CaTRPN current from the total intracellular Ca^{2+} current. The dynamic equation for CaTRPN represents the simple chemical reaction:

$$\mathrm{Ca}^{2+} + \mathrm{TRPN} \underset{K_{off}}{\overset{K_{on}}{\leftrightarrows}} \mathrm{CaTRPN} \tag{A.3}$$

The way to choose K_{on} and K_{off} here is not unique as long as $\frac{K_{off}}{K_{on}} = K_d$ in the original model. We choose $K_{off} = \sqrt{\sigma} K_{off,s}$ and $K_{on} = 1/\sqrt{\sigma} K_{on,s}$, where s indicates the values from the Shannon_etal_2004 model and $\sigma = \frac{K_d}{K_{d,s}}$.

A.3.2 Initial condition

$[Ca^{2+}]_i$(t=0) and other variable values are quiescent values of the original model.

[CaTRPN]$_i$(t=0) is the value that makes $\frac{d[CaTRPN]_i}{dt} = 0$, namely, $[CaTRPN]_i(t = 0) = \frac{B_{max,tropnin}[Ca^{2+}]_i}{[Ca^{2+}]_i + K_{d,troponin}}$.

A.4 Step 3: Split the single state dynamic CaTRPN in Step 2 (or original model) into 2 states: with (TCa*) or without (TCa) cross-bridges.

Keep all the other buffers unchanged.

A.4.1 Equations

$$\frac{d[Ca^{2+}]_i}{dt} = \beta'(I^{Ca}_{total} - I_{CaTRPN} \tag{A.4a}$$

$$\beta = 1/(1 + \sum_{j}^{'} \frac{B_{max,j'} K_{d,j'}}{([Ca^{2+}]_i + K_{d,j'})^2}) \tag{A.4b}$$

$$I_{CaTRPN} = \frac{d[CaTRPN]}{dt} = \frac{dTCa}{dt} + \frac{dTCa^*}{dt} \tag{A.4c}$$

$$\frac{d[T^*]}{dt} = (Y_3[TCa^*] - Z_3[T^*][Ca^{2+}]_i) - Y_4[T^*] - Y_d(dX/dt)^2[T^*] \tag{A.4d}$$

$$\frac{d[TCa]}{dt} = (Y_1[Ca^{2+}]_i[T] - Z_1[TCa]) - (Y_2[TCa]_{eff} - Z_2[TCa^*]) \tag{A.4e}$$

$$\frac{d[TCa^*]}{dt} = -(Y_3[TCa^*] - Z_3[T^*][Ca^{2+}]_i) + (Y_2[TCa]_{eff} - Z_2[TCa^*]) - Y_d(dX/dt)^2[TCa^*] \tag{A.4f}$$

$$[T] = [Troponin]_{total} - [T^*] - [TCa] - [TCa^*] \tag{A.4g}$$

If the original model has dynamic equation for all buffers then there will be no instantaneous buffer factor β so simply ignore it in the implementation steps for this kind of model.

A.4.2 Initial conditions

$[Ca^{2+}]_i$(t=0) and other variable values are quiescent values of the original model.

$[T^*]$(t=0), $[TCa]$(t=0), $[TCa^*]$(t=0) are determined by solving $\frac{d[T^*]}{dt} = 0$, $\frac{d[TCa]}{dt} = 0$, $\frac{d[TCa^*]}{dt} = 0$.

[CaTRPN](t=0) = $[TCa]$(t=0) + $[TCa^*]$(t=0), calculated from the above step, approximately equal to the value of [CaTRPN] in quiescent state if the original model has [CaTRPN].

There are multiple K_{on} and K_{off}. They are kept the same as original NL96 paper [106]

except for Y_1 and Z_1, which are chosen to match the values of K_{on} and K_{off} from the original model (if the original model has dynamic CaTRPN) or from Step 2.

A.5 Implementation of instantaneous NL96 into models with instantaneous CaTRPN

The original NL96 model can be written as $\frac{dS_j}{dt} = f_j$. $S_j = [T], [T^*], [TCa], [TCa*]$ for j = 1,...,4. The equation for $[T]$ can be replaced with the conservation of total troponin concentration: $[T] + [T^*] + [TCa] + [TCa^*] = [Troponin]_{tot}$.

For the instantaneous NL96, we set $dS_j = 0$ and solve for $[T], [T^*], [TCa], [TCa^*]$.

The matrix form is $Ax = b$, in which $x = ([T],\ [T^*],\ [TCa],\ [TCa^*])^T$,
$b = (0,\ 0,\ 0,\ [Tropnin]_{tot})^T$ and

$$A = \begin{bmatrix} Y_1[Ca^{2+}]_i & 0 & -(Z_1 + Y_2 expo) & Z_2 \\ 0 & Z_3[Ca^{2+}]_i & Y_2 expo & -\left(Z_2 + Y_3 + Y_d\left(\frac{dX}{dt}\right)^2\right) \\ 0 & -\left(Y_4 + Z_3[Ca^{2+}]_i + Y_d\left(\frac{dX}{dt}\right)^2\right) & 0 & Y_3 \\ 1 & 1 & 1 & 1 \end{bmatrix}$$

$expo = exp(-R(L - L_a)^2)$. At each time step, solve $x = A^{-1}b$ to get $[T]$, $[T^*]$, $[TCa]$, $[TCa^*]$.

To implement this instantaneous NL96 into EP models with instantaneous CaTRPN, we modify the original equations:

$$\frac{d[Ca^{2+}]_i}{dt} = \beta I^{Ca}_{total}$$
$$\beta = 1/(1 + \sum_j \frac{B_{max,j} K_{d,j}}{([Ca^{2+}]_i + K_{d,j})^2})$$

into:

$$\frac{d[Ca^{2+}]_i}{dt} = \beta' I^{Ca}_{total}$$
$$\beta' = 1/\left(1 + \sum_j \frac{B_{max,j} K_{d,j}}{([Ca^{2+}]_i + K_{d,j})^2} + \frac{B_{TCa} K_{d,TCa}}{([Ca^{2+}]_i + K_{d,TCa})^2} + \frac{B_{TCa^*} K_{d,TCa^*}}{([Ca^{2+}]_i + K_{d,TCa^*})^2}\right)$$

$$B_{TCa} = [T] + [TCa],\ B_{TCa^*} = [T^*] + [TCa^*],\ K_{d,TCa} = Z_1/Y_1,\ K_{d,TCa^*} = Y_3/Z_3$$

APPENDIX B

CA^{2+} AND CONTRACTION RESULTS FOR ALL 14 EP MODELS

B.1 Priming Ca^{2+} transients for all models.

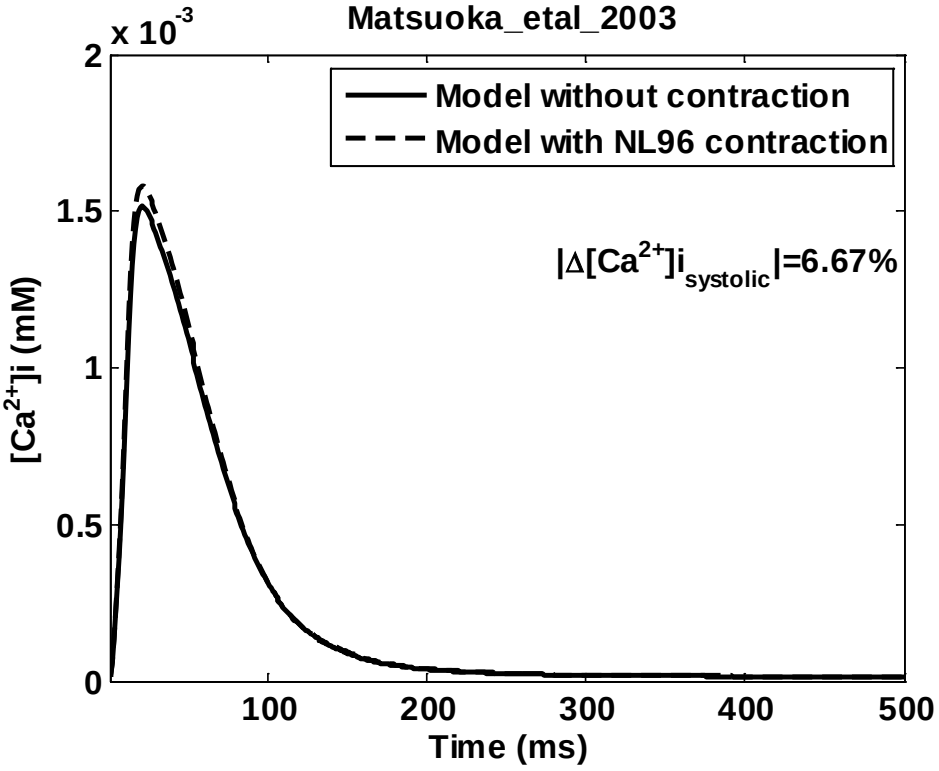
Matsuoka_etal_2003
x 10^-3
2
1.5
1
0.5
0
Model without contraction
Model with NL96 contraction
|Δ[Ca2+]i systolic|=6.67%
[Ca2+]i (mM)
100
200
300
400
500
Time (ms)

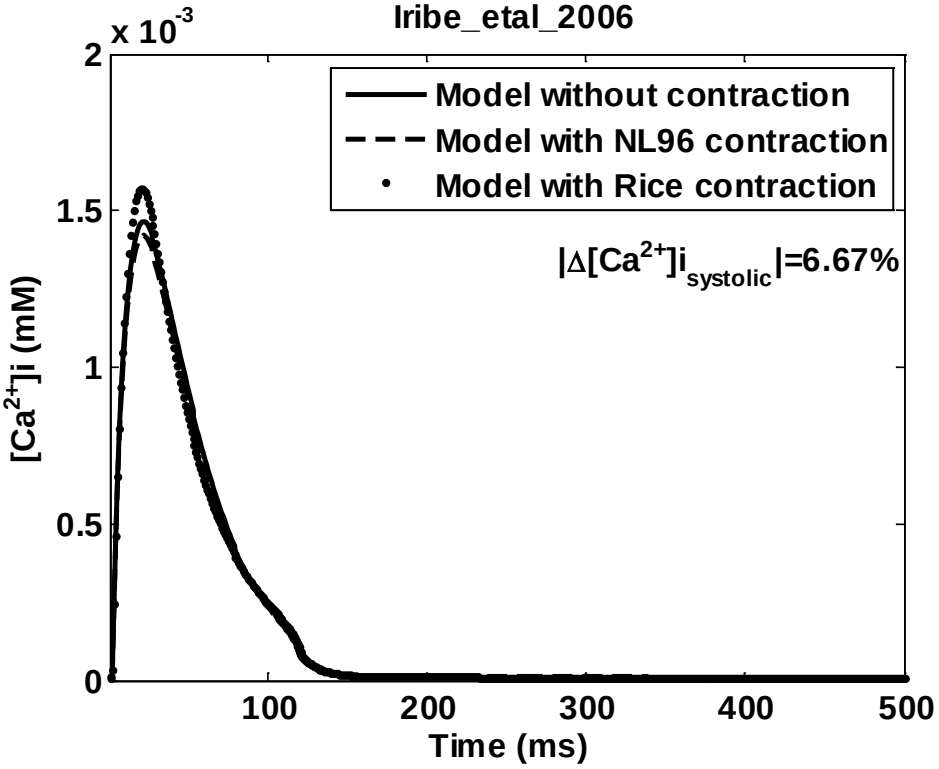
Iribe_etal_2006
x 10^-3
2
1.5
1
0.5
0
Model without contraction
Model with NL96 contraction
Model with Rice contraction
|Δ[Ca2+]i systolic|=6.67%
[Ca2+]i (mM)
100
200
300
400
500
Time (ms)

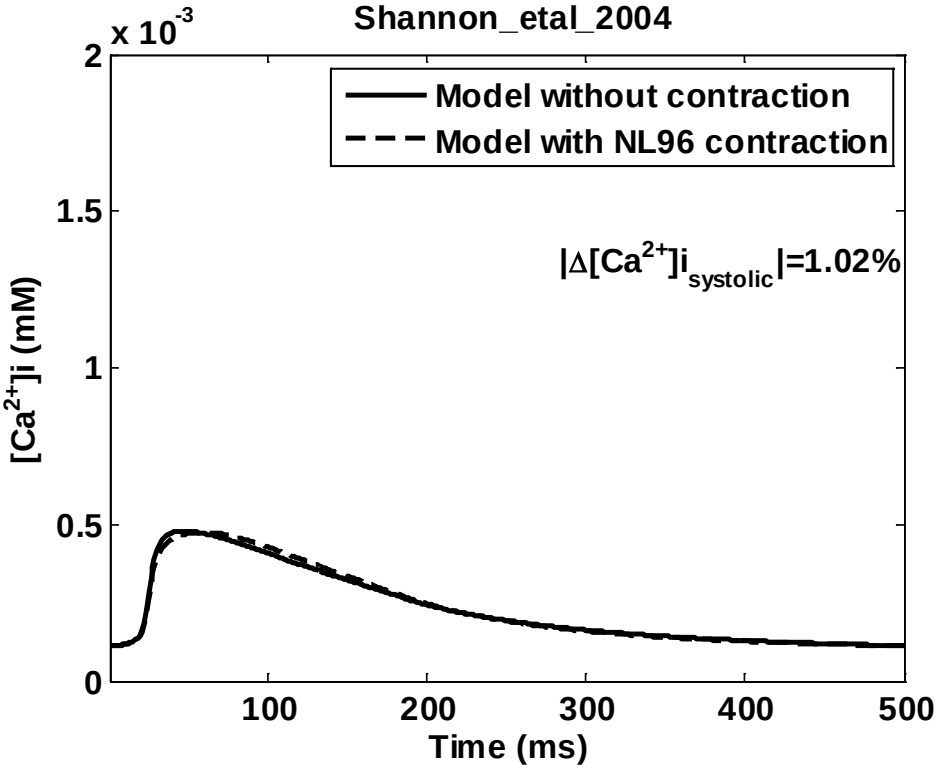
Shannon_etal_2004
x 10^-3
Model without contraction
Model with NL96 contraction
|Δ[Ca2+]i systolic|=1.02%
[Ca2+]i (mM)
Time (ms)
0
0.5
1
1.5
2
100
200
300
400
500

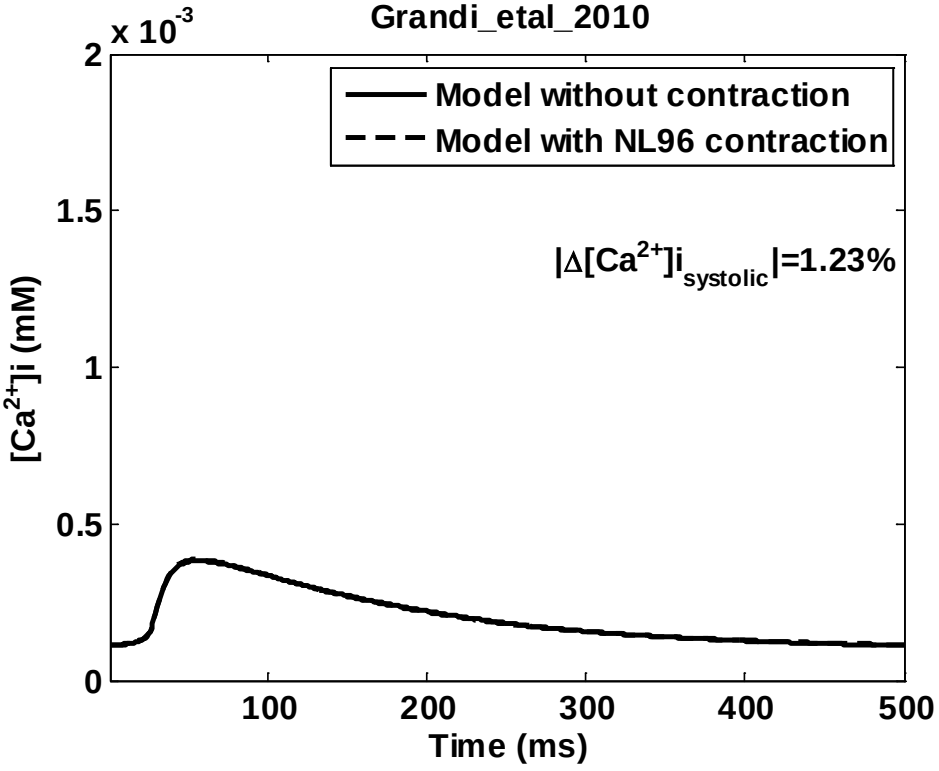
Grandi_etal_2010
x 10^-3
Model without contraction
Model with NL96 contraction
|Δ[Ca2+]i systolic|=1.23%
[Ca2+]i (mM)
Time (ms)
0
0.5
1
1.5
2
100
200
300
400
500

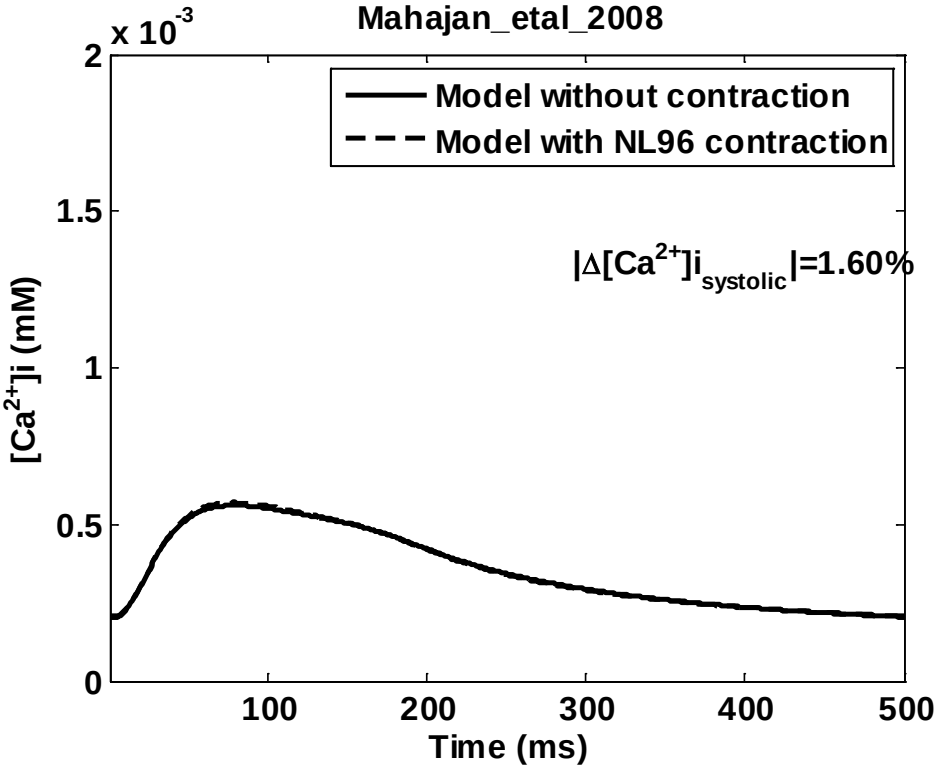
Mahajan_etal_2008
x 10^-3
Model without contraction
Model with NL96 contraction
|Δ[Ca2+]i systolic|=1.60%
[Ca2+]i (mM)
Time (ms)
0
0.5
1
1.5
2
100
200
300
400
500

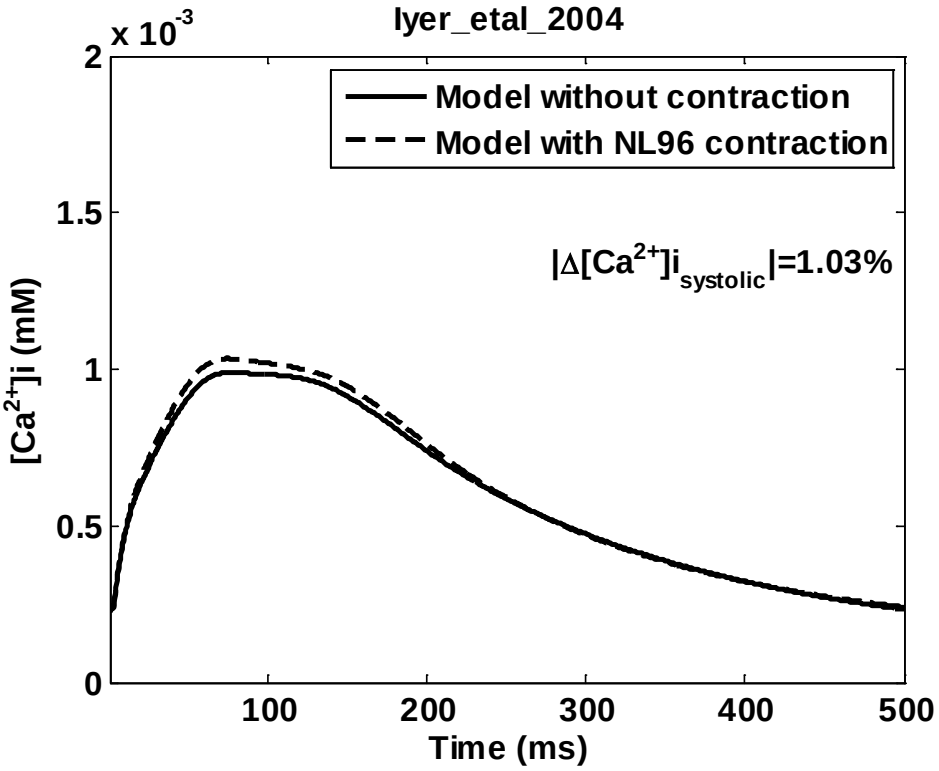
Iyer_etal_2004
x 10^-3
Model without contraction
Model with NL96 contraction
|Δ[Ca2+]i systolic|=1.03%
[Ca2+]i (mM)
Time (ms)
0
0.5
1
1.5
2
100
200
300
400
500

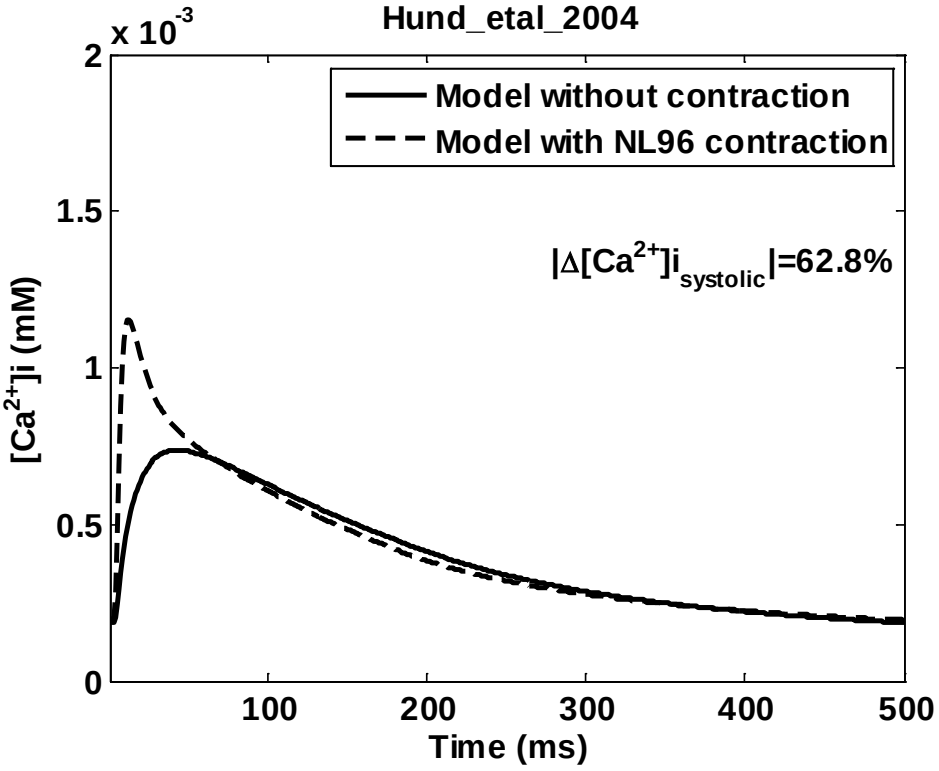
Hund_etal_2004
x 10^-3
Model without contraction
Model with NL96 contraction
|Δ[Ca2+]i systolic|=62.8%
[Ca2+]i (mM)
Time (ms)

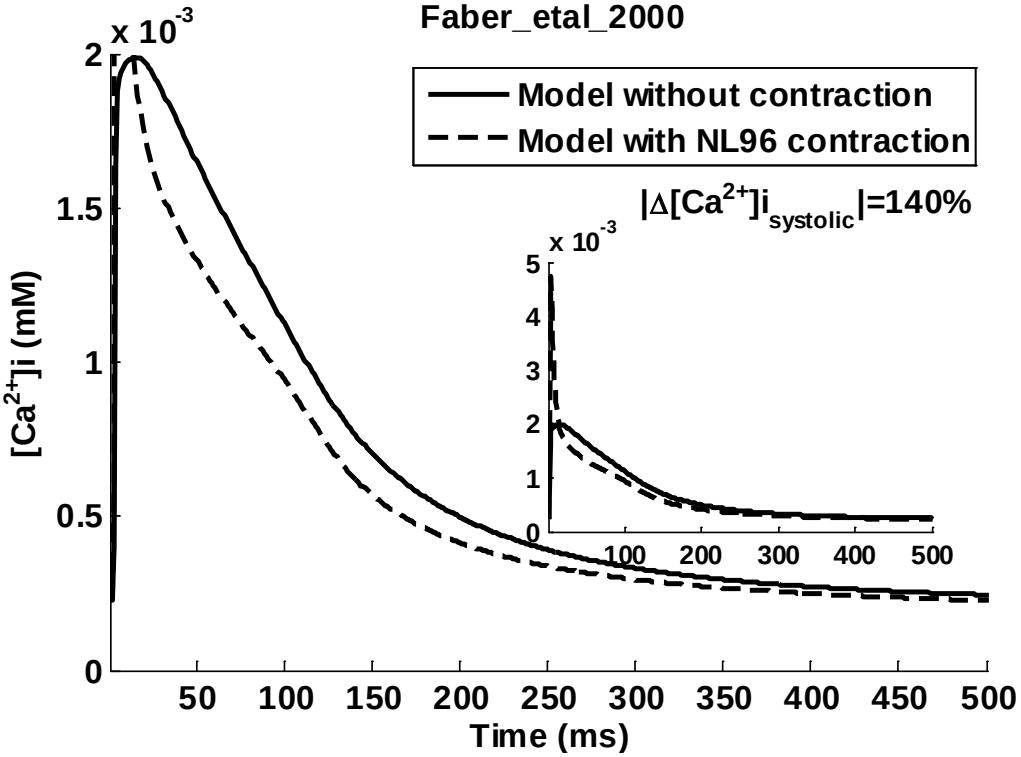
Faber_etal_2000
x 10^-3
Model without contraction
Model with NL96 contraction
|Δ[Ca2+]i systolic|=140%
[Ca2+]i (mM)
Time (ms)

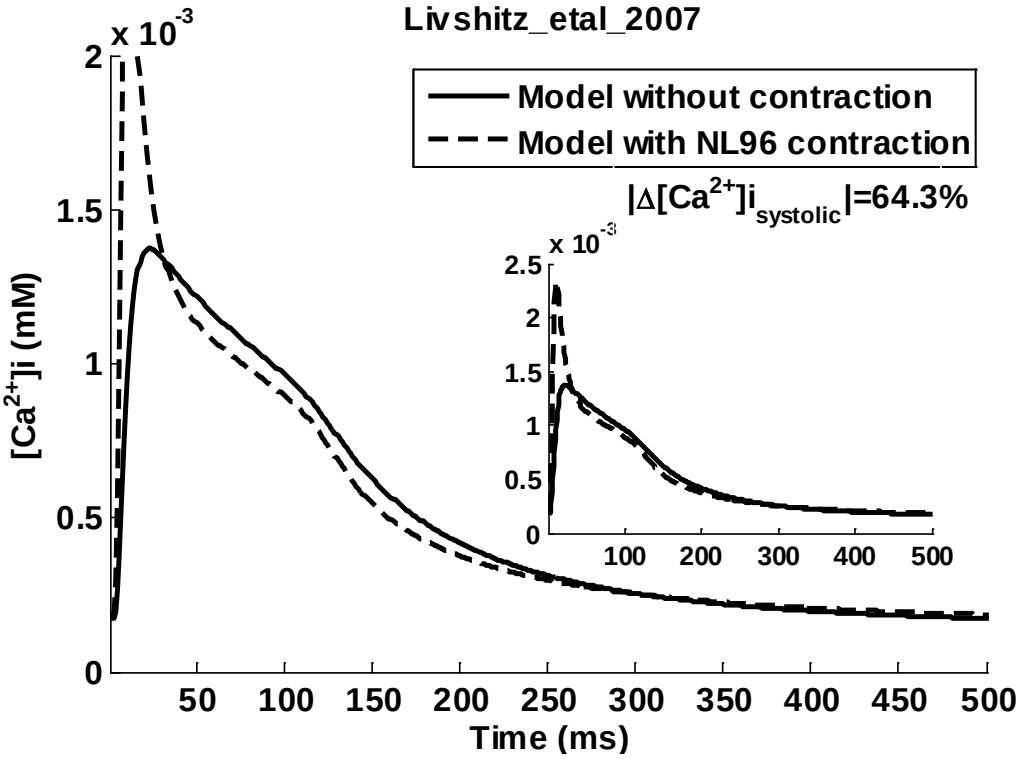
Livshitz_etal_2007
x 10^-3
Model without contraction
Model with NL96 contraction
|Δ[Ca2+]i systolic|=64.3%
[Ca2+]i (mM)
Time (ms)

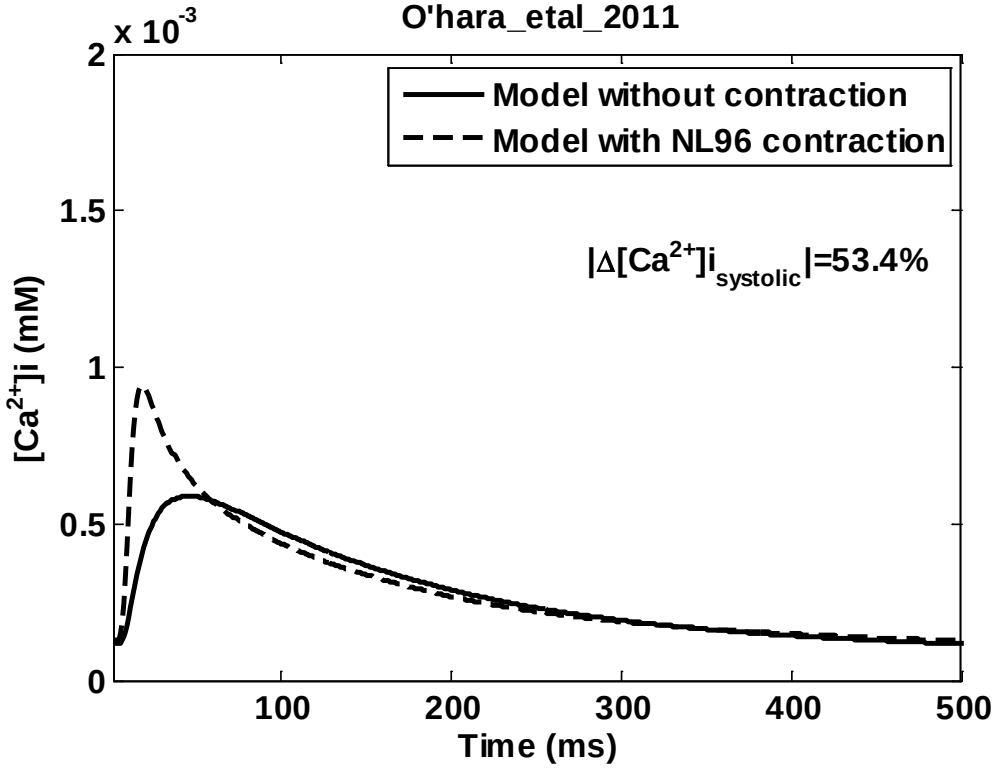
O'hara_etal_2011
x 10^-3
Model without contraction
Model with NL96 contraction
|Δ[Ca2+]i systolic|=53.4%
[Ca2+]i (mM)
Time (ms)

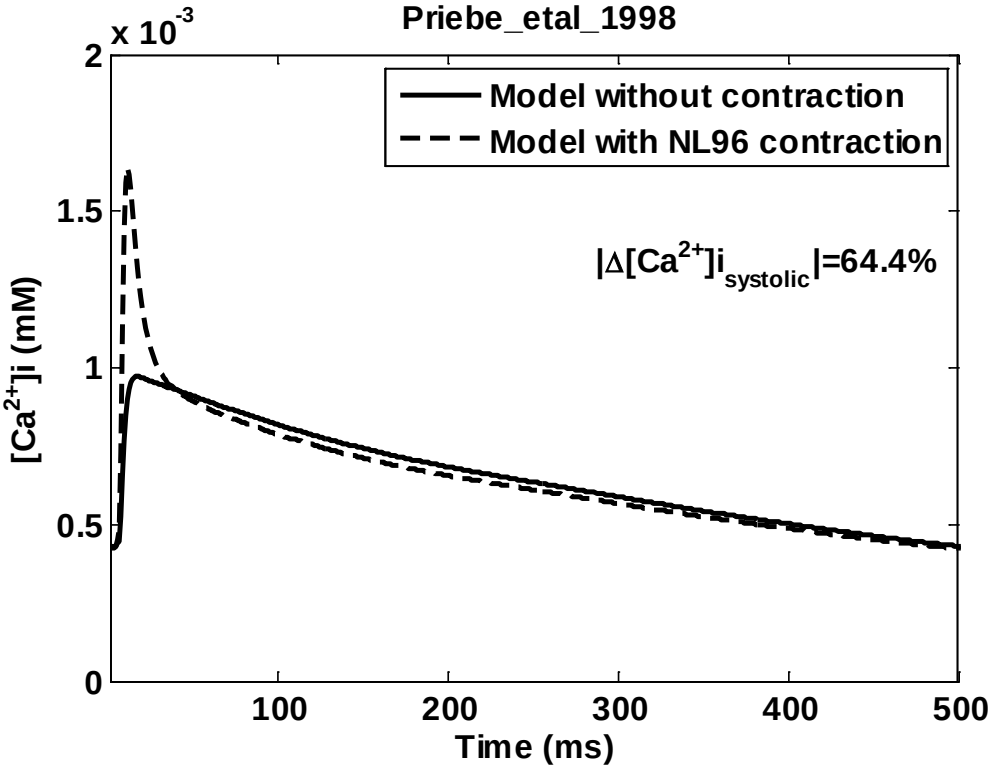
Priebe_etal_1998
x 10^-3
Model without contraction
Model with NL96 contraction
|Δ[Ca2+]i systolic|=64.4%
[Ca2+]i (mM)
Time (ms)
0
0.5
1
1.5
2
100
200
300
400
500

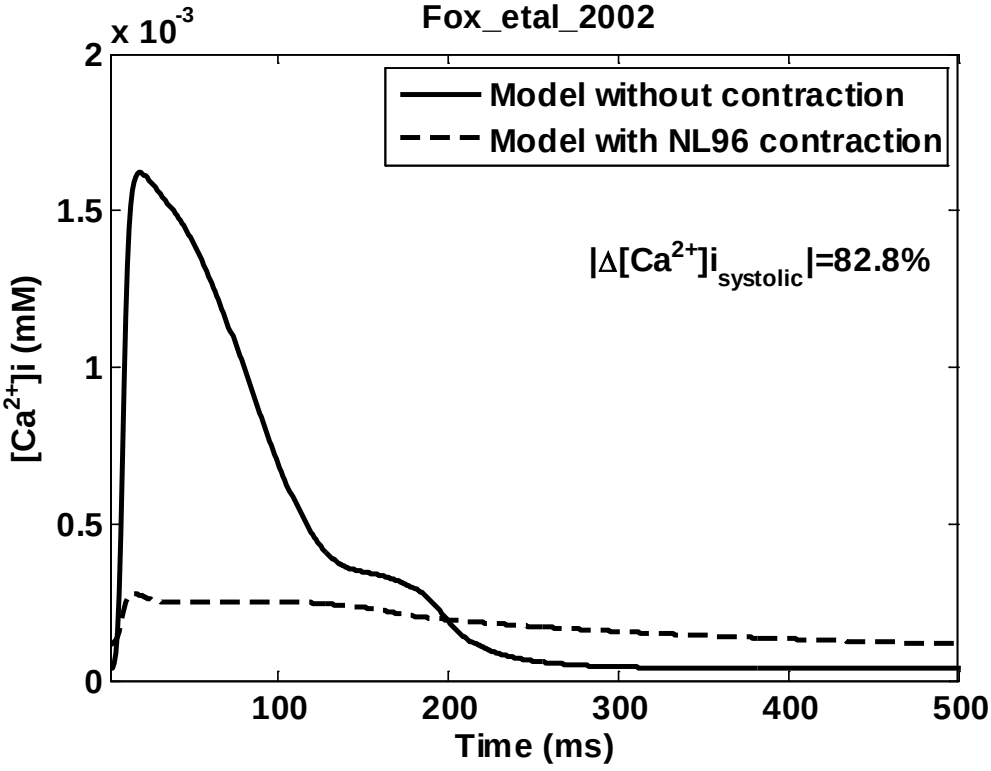
Fox_etal_2002
x 10^-3
Model without contraction
Model with NL96 contraction
|Δ[Ca2+]i systolic|=82.8%
[Ca2+]i (mM)
Time (ms)
0
0.5
1
1.5
2
100
200
300
400
500

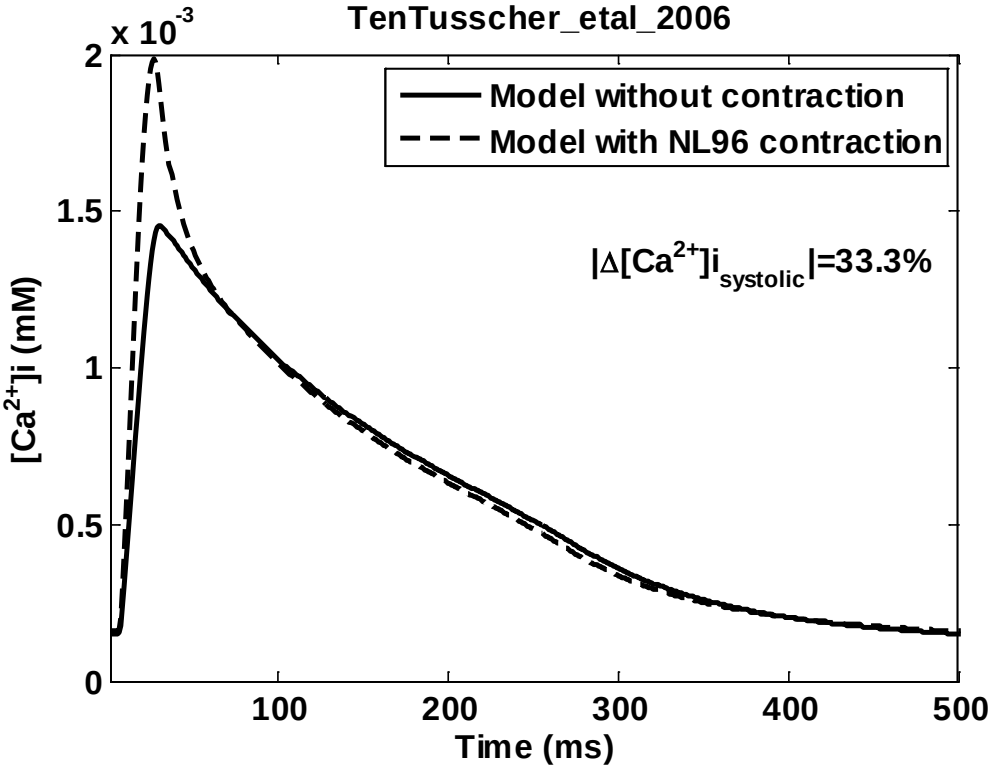
TenTusscher_etal_2006
x 10^-3
Model without contraction
Model with NL96 contraction
|Δ[Ca2+]i systolic|=33.3%
[Ca2+]i (mM)
Time (ms)
0
0.5
1
1.5
2
100
200
300
400
500

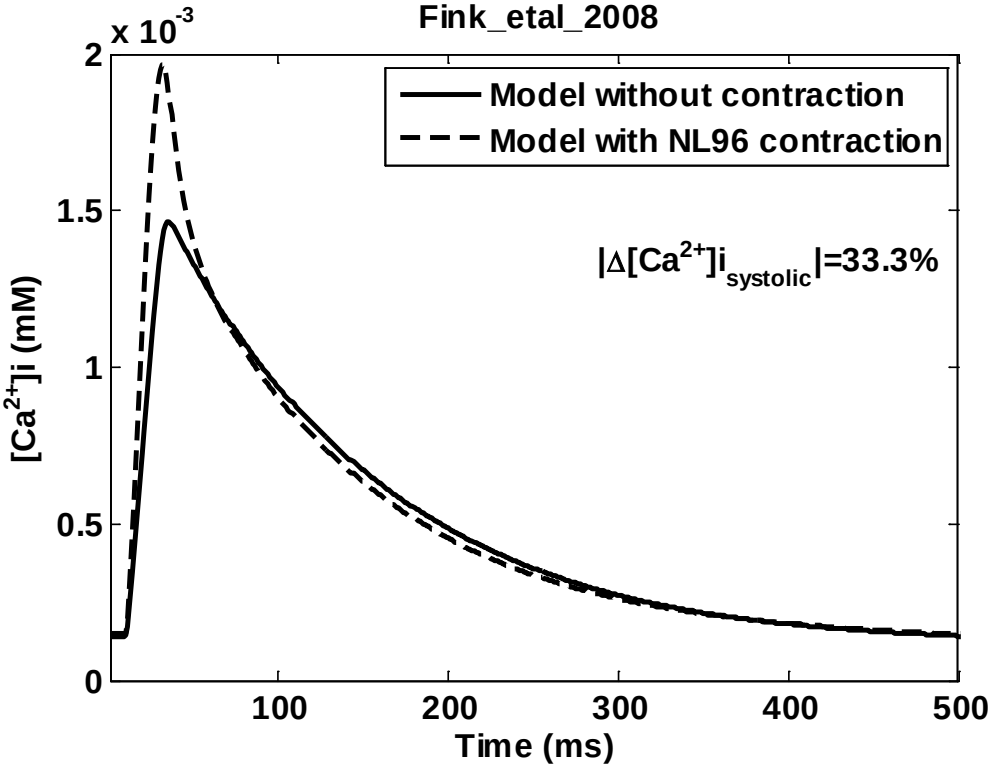
Fink_etal_2008
x 10^-3
Model without contraction
Model with NL96 contraction
|Δ[Ca2+]i systolic|=33.3%
[Ca2+]i (mM)
Time (ms)
0
0.5
1
1.5
2
100
200
300
400
500

B.2 Postextrasystolic potentiation in Ca^{2+} for all models.

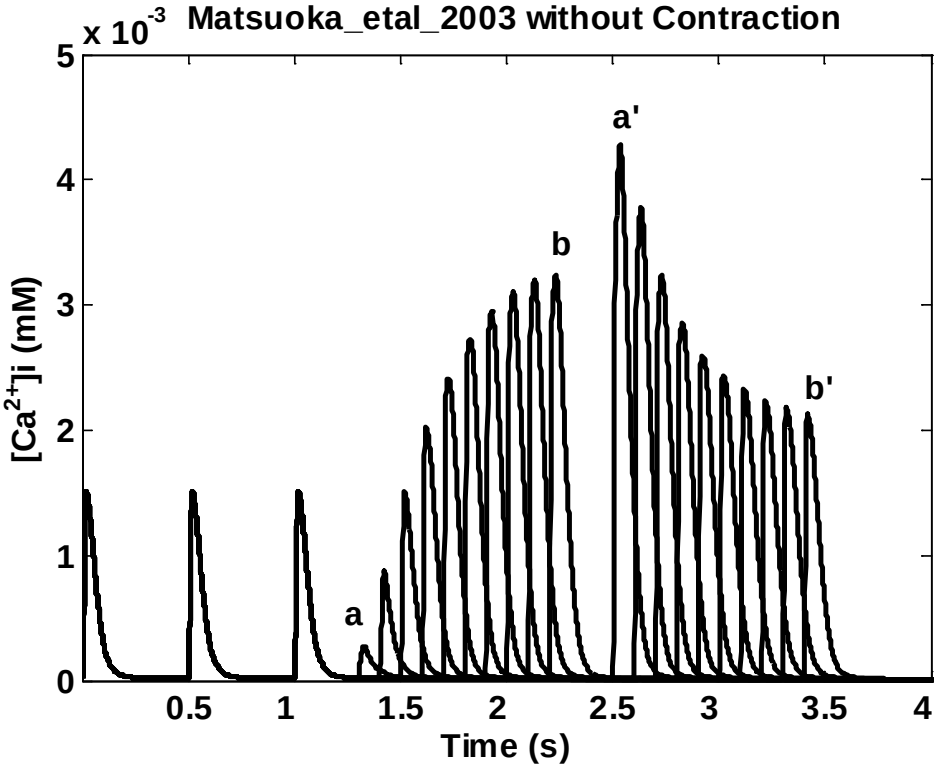
x 10^-3
Matsuoka_etal_2003 without Contraction
[Ca2+]i (mM)
Time (s)
a
b
a'
b'

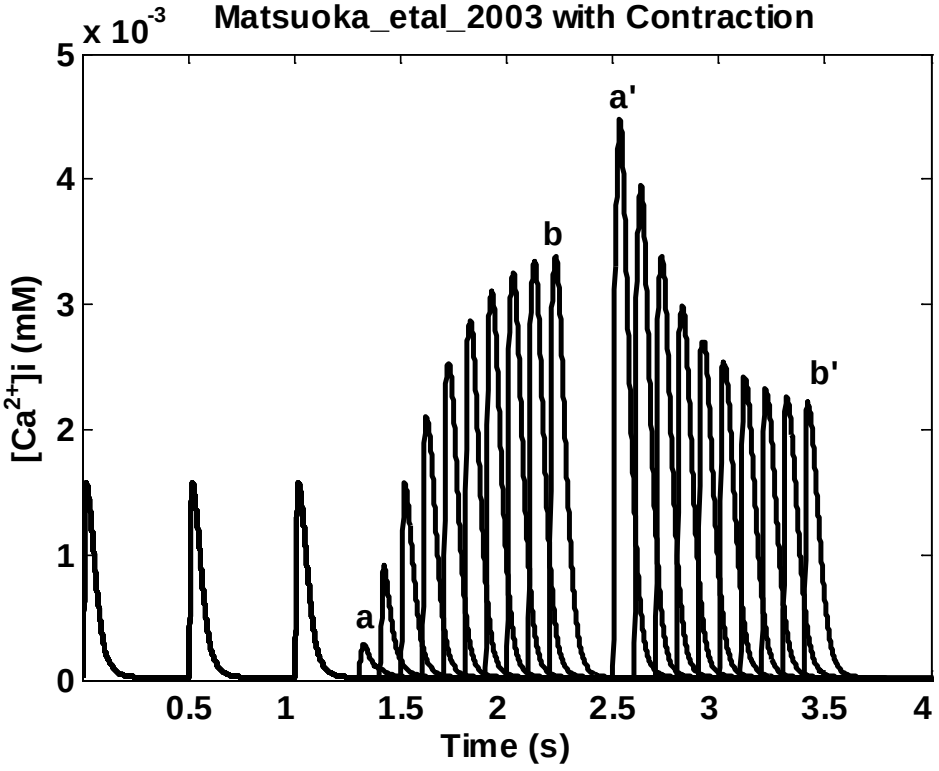
x 10^-3
Matsuoka_etal_2003 with Contraction
[Ca2+]i (mM)
Time (s)
a
b
a'
b'

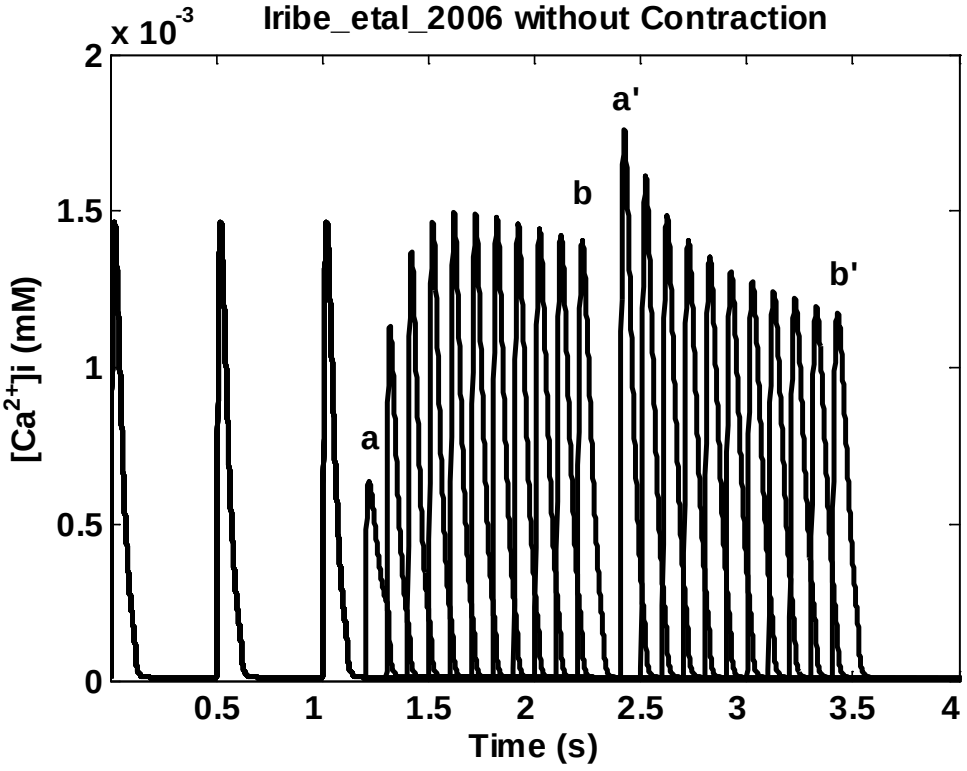
Iribe_etal_2006 without Contraction
x 10^-3
[Ca2+]i (mM)
Time (s)
a
b
a'
b'

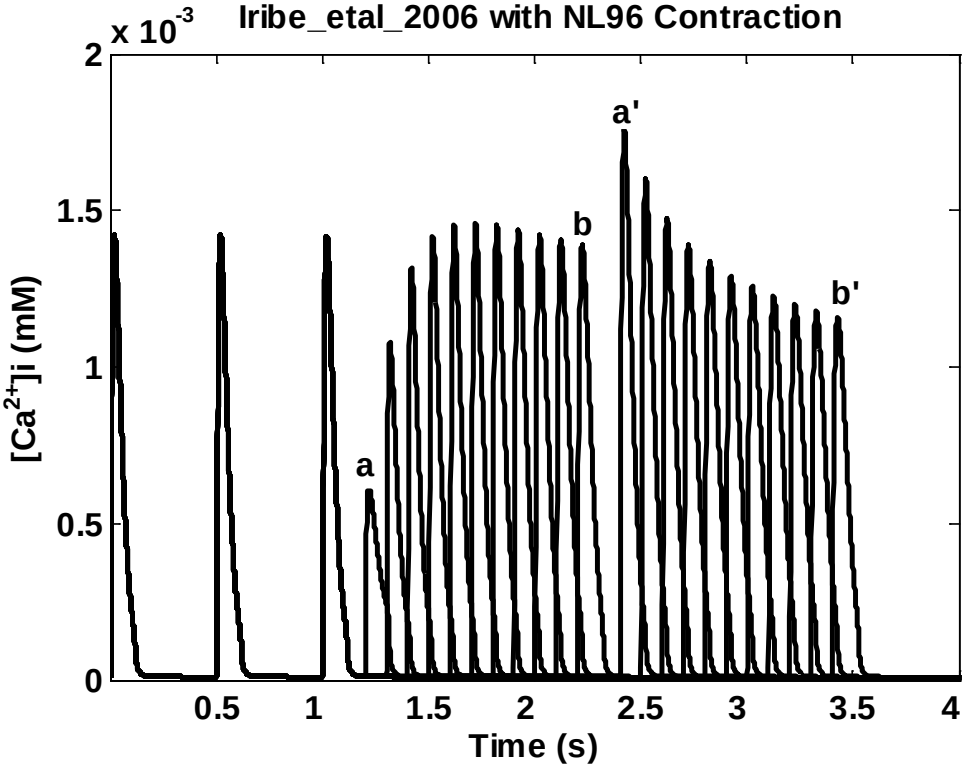
Iribe_etal_2006 with NL96 Contraction
x 10^-3
[Ca2+]i (mM)
Time (s)
a
b
a'
b'

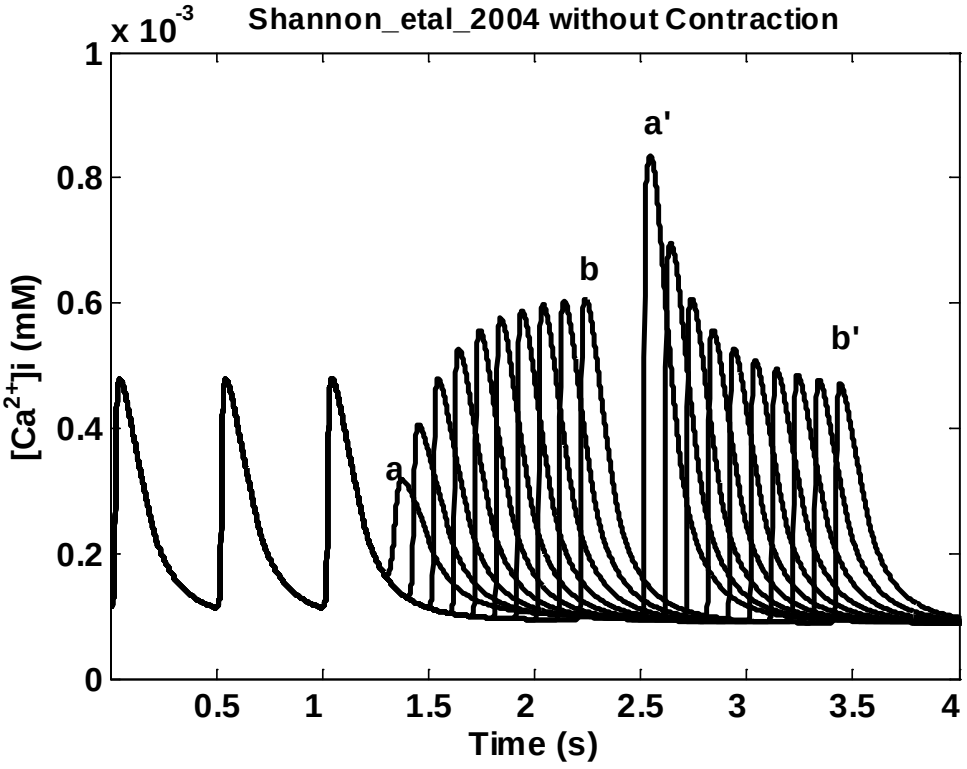
Shannon_etal_2004 without Contraction
x 10^-3
[Ca2+]i (mM)
Time (s)
a
b
a'
b'

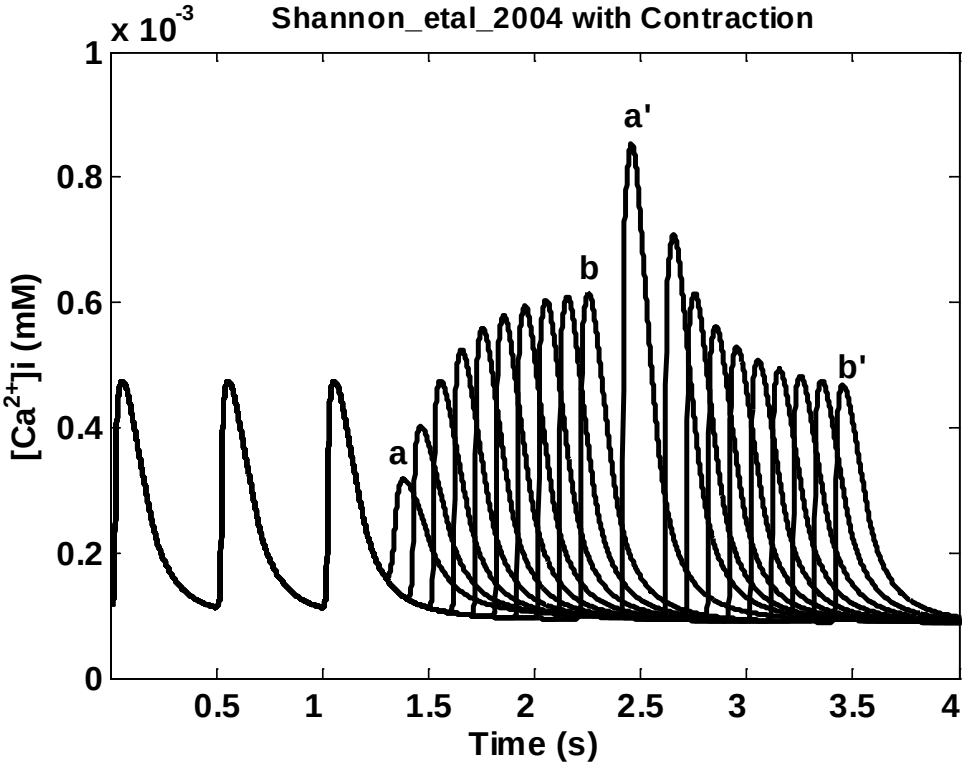
Shannon_etal_2004 with Contraction
x 10^-3
[Ca2+]i (mM)
Time (s)
a
b
a'
b'

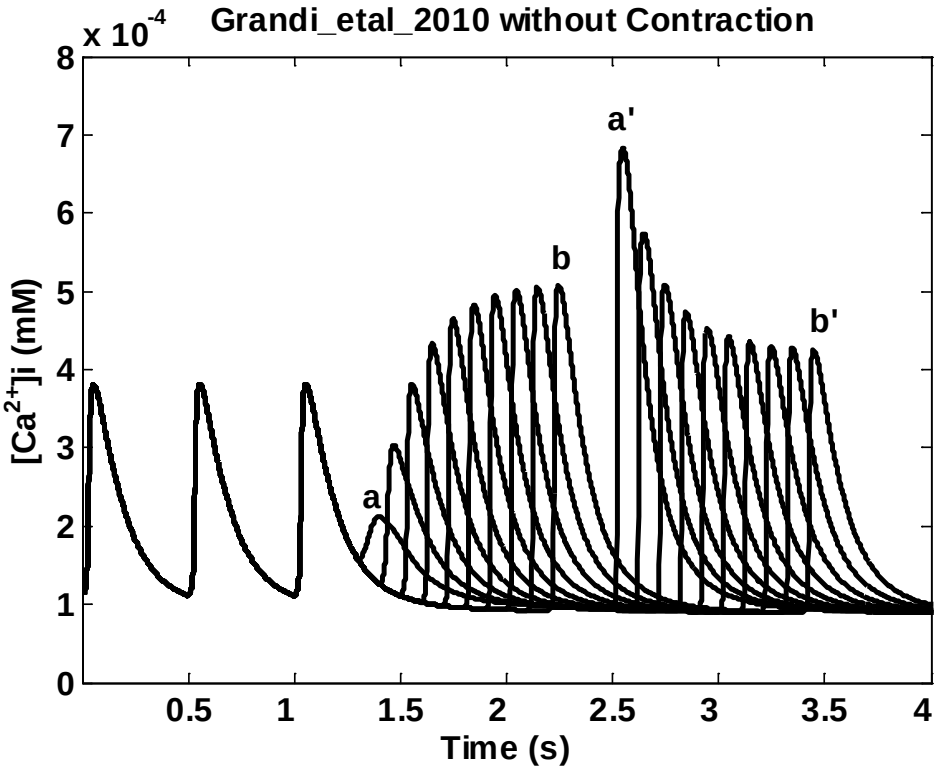
Grandi_etal_2010 without Contraction
x 10^-4
[Ca2+]i (mM)
Time (s)
a
a'
b
b'

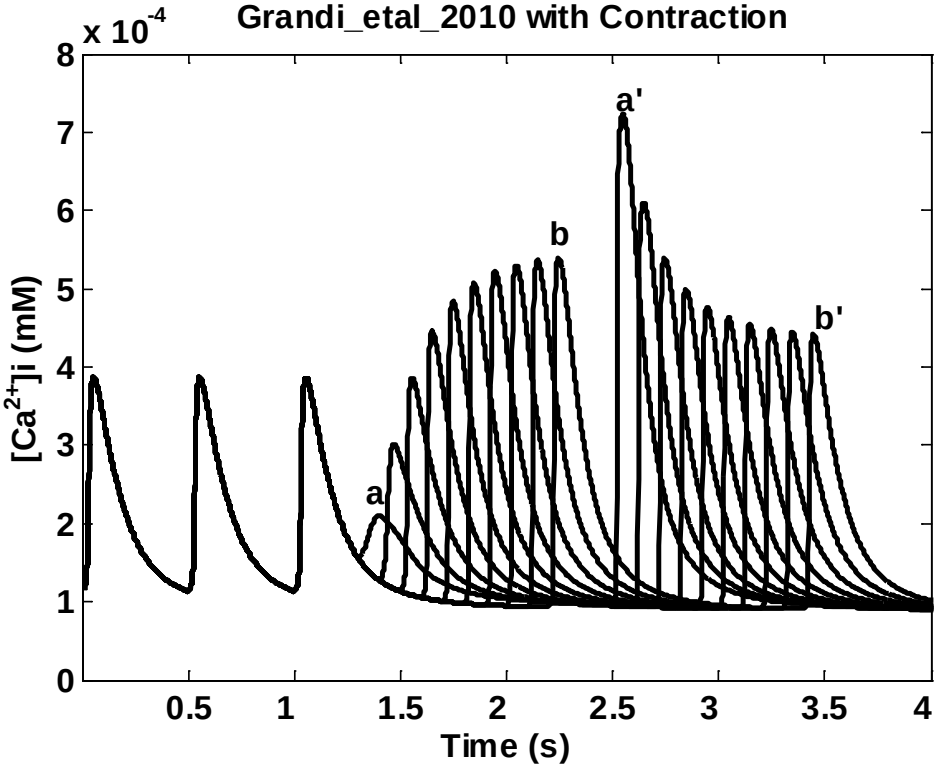
Grandi_etal_2010 with Contraction
x 10^-4
[Ca2+]i (mM)
Time (s)
a
a'
b
b'

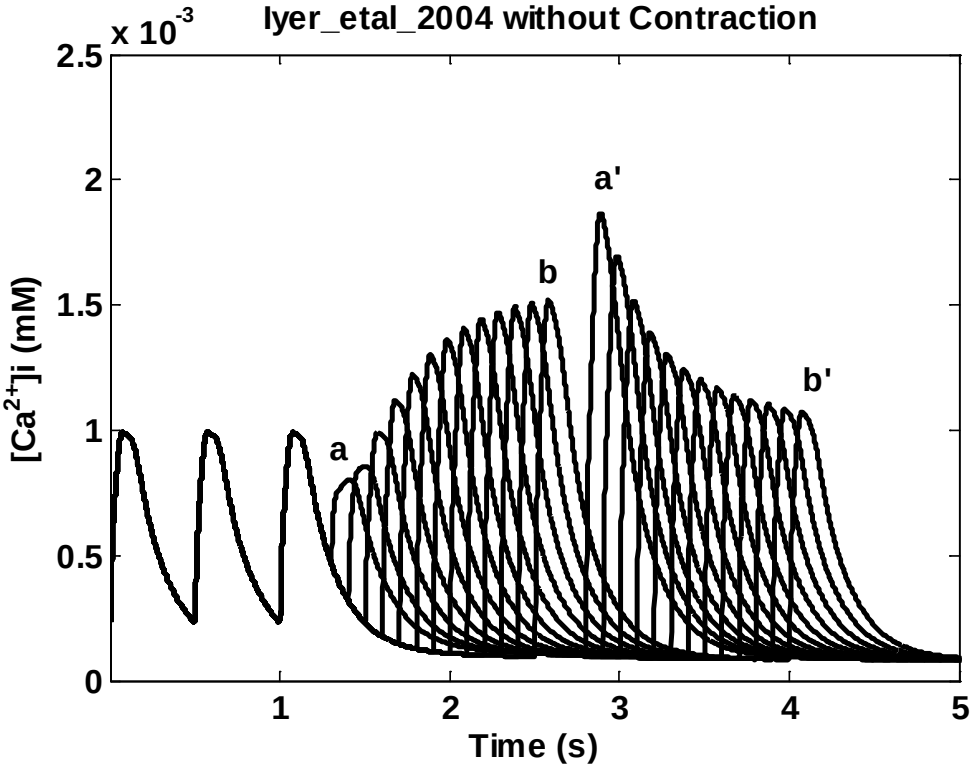
Iyer_etal_2004 without Contraction
x 10^-3
2.5
2
1.5
1
0.5
0
[Ca2+]i (mM)
a
b
a'
b'
1
2
3
4
5
Time (s)

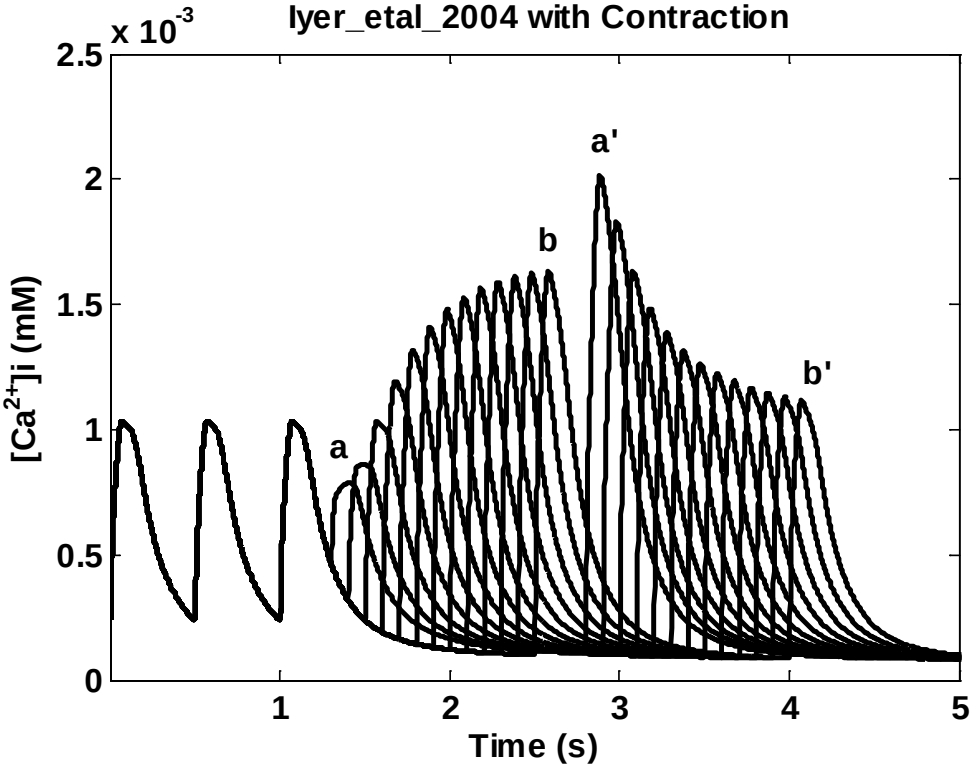
Iyer_etal_2004 with Contraction
x 10^-3
2.5
2
1.5
1
0.5
0
[Ca2+]i (mM)
a
b
a'
b'
1
2
3
4
5
Time (s)

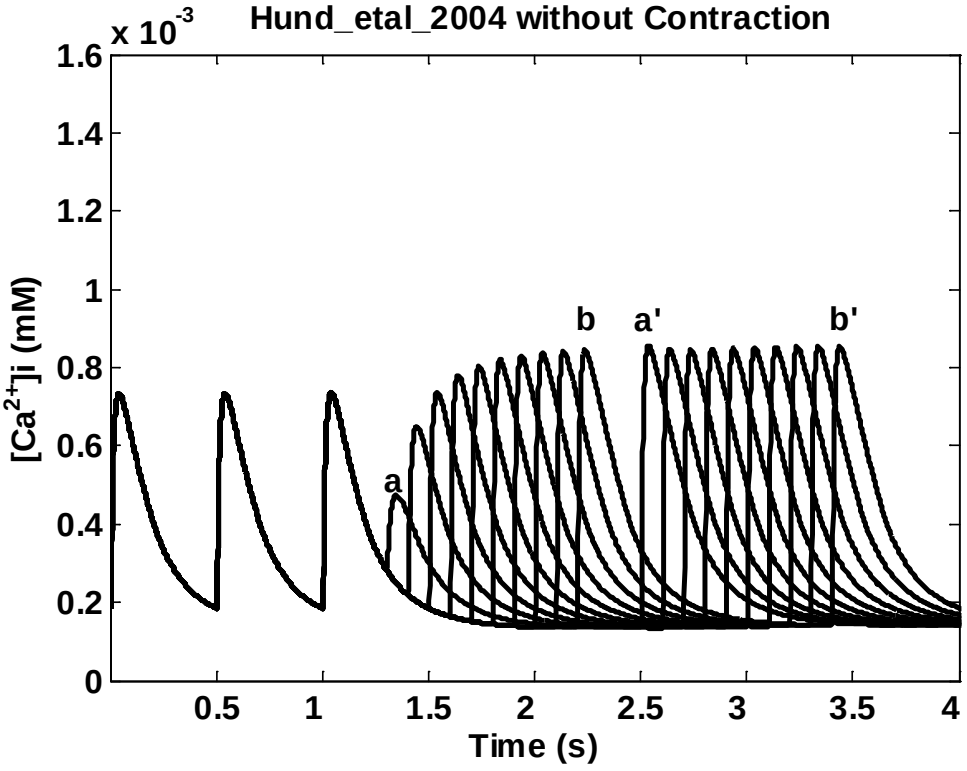
Hund_etal_2004 without Contraction
x 10^-3
[Ca2+]i (mM)
Time (s)
a
b
a'
b'

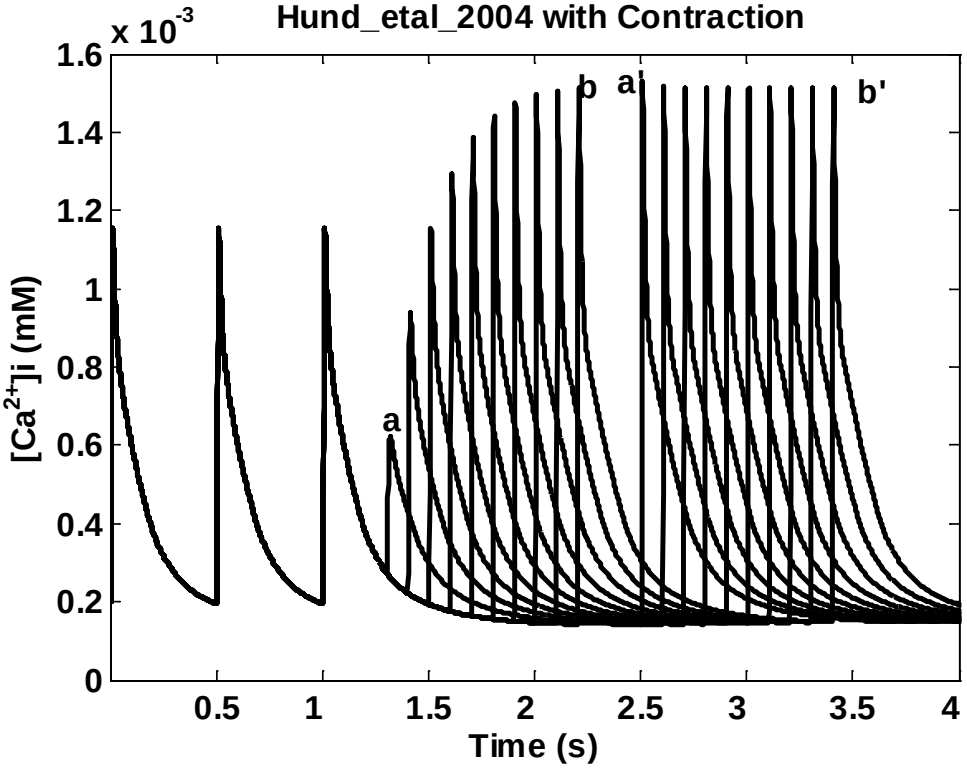
Hund_etal_2004 with Contraction
x 10^-3
[Ca2+]i (mM)
Time (s)
a
b
a'
b'

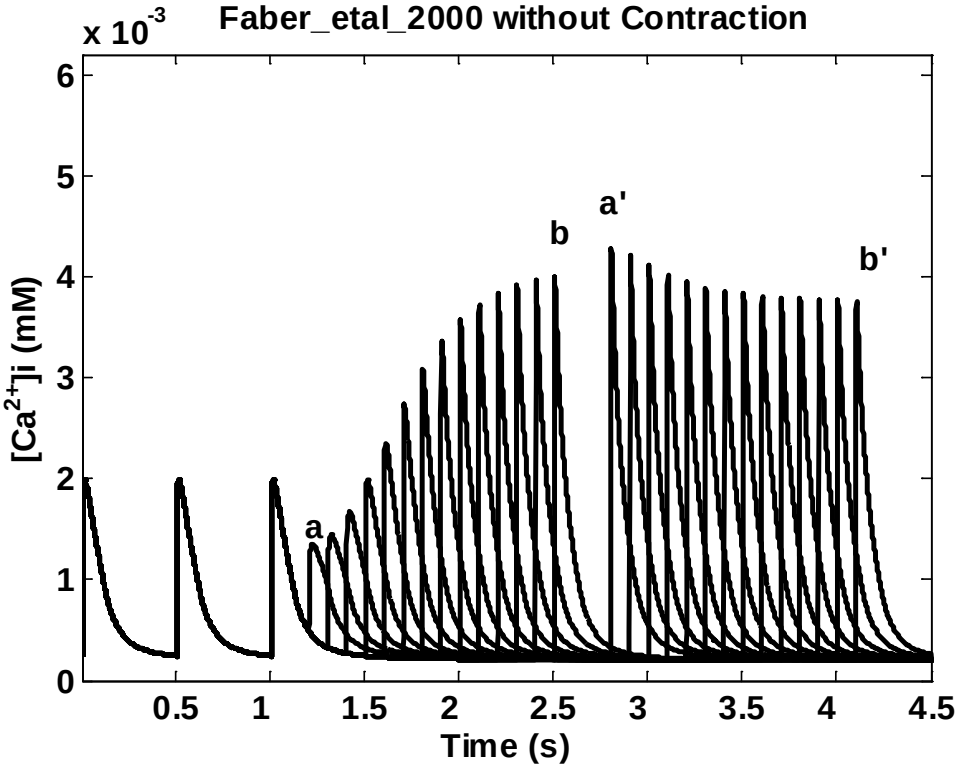
Faber_etal_2000 without Contraction
x 10^-3
[Ca2+]i (mM)
Time (s)
a
b
a'
b'

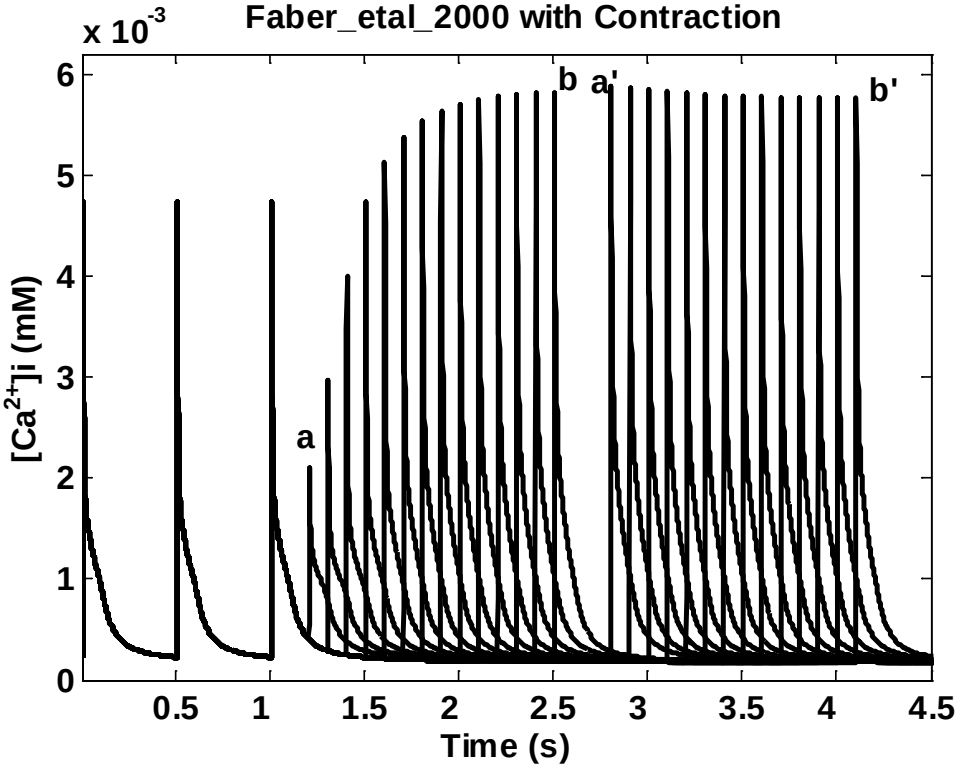
Faber_etal_2000 with Contraction
x 10^-3
[Ca2+]i (mM)
Time (s)
a
b
a'
b'

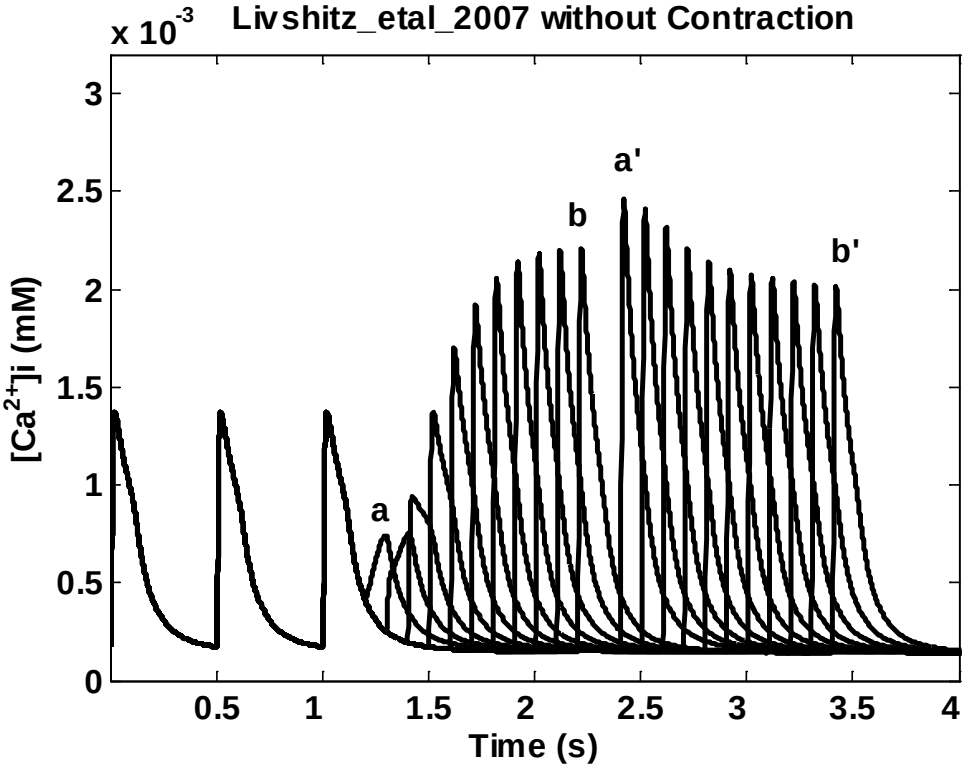
x 10^-3
Livshitz_etal_2007 without Contraction
[Ca2+]i (mM)
Time (s)
a
b
a'
b'

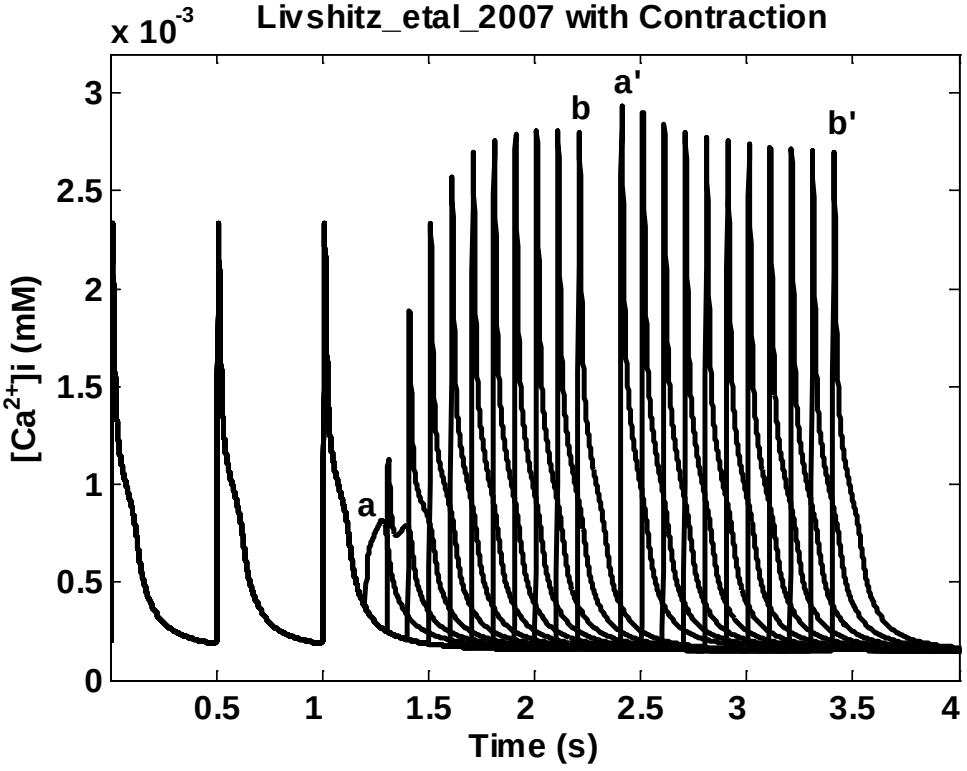
x 10^-3
Livshitz_etal_2007 with Contraction
[Ca2+]i (mM)
Time (s)
a
b
a'
b'

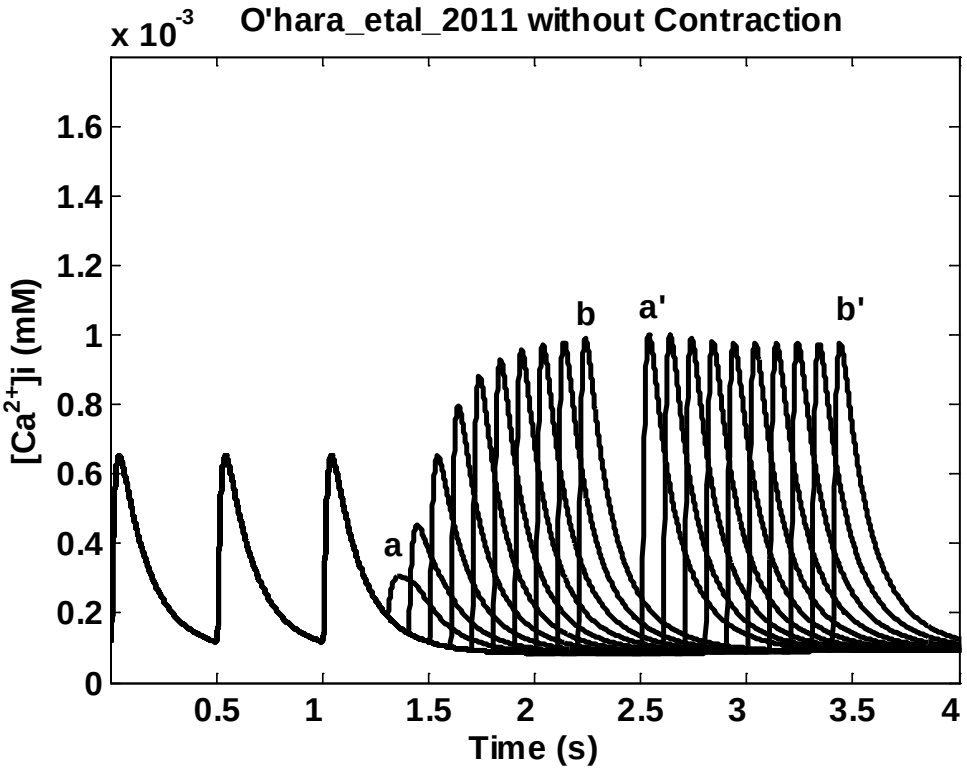
x 10^-3
O'hara_etal_2011 without Contraction
[Ca2+]i (mM)
Time (s)
a
b
a'
b'

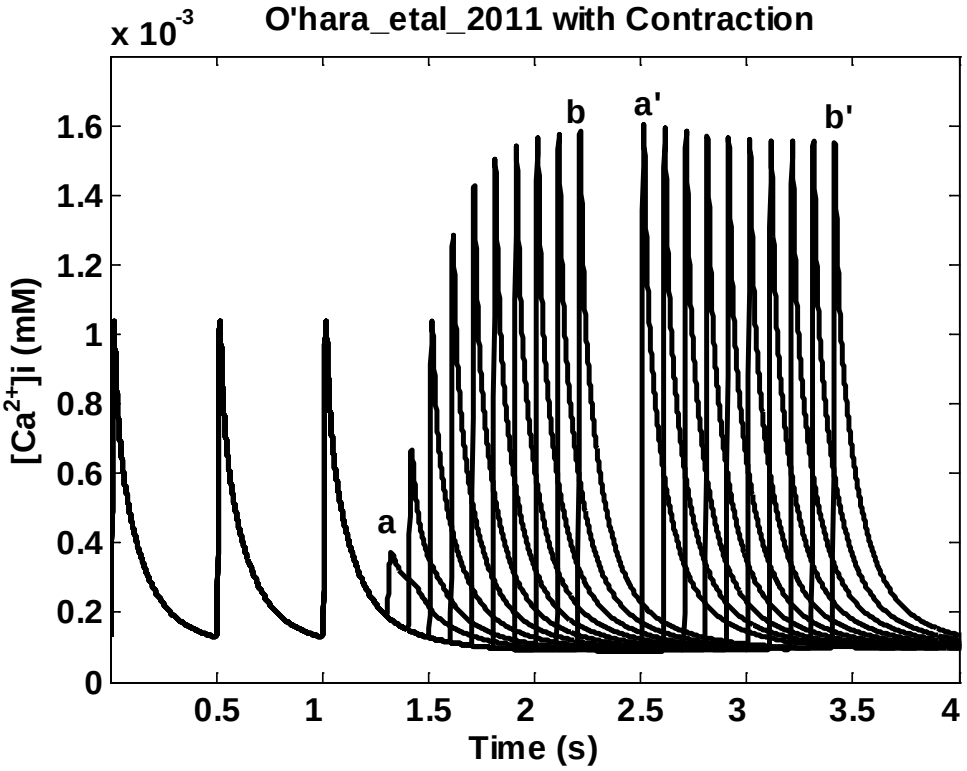
x 10^-3
O'hara_etal_2011 with Contraction
[Ca2+]i (mM)
Time (s)
a
b
a'
b'

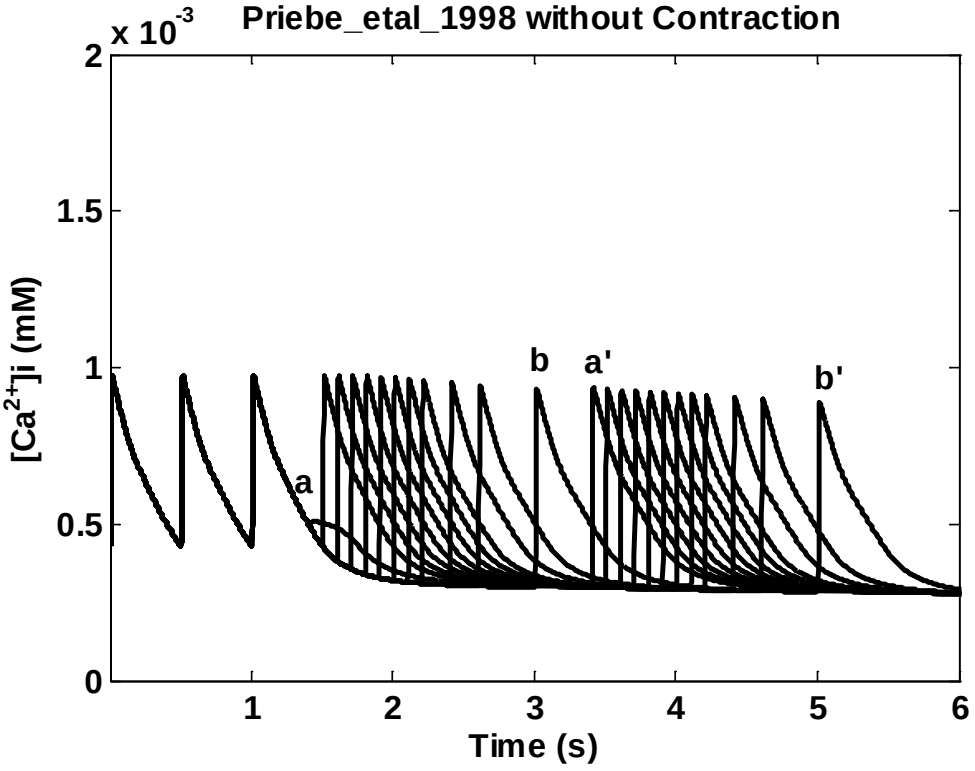
Priebe_etal_1998 without Contraction
x 10^-3
[Ca2+]i (mM)
Time (s)
a
b
a'
b'

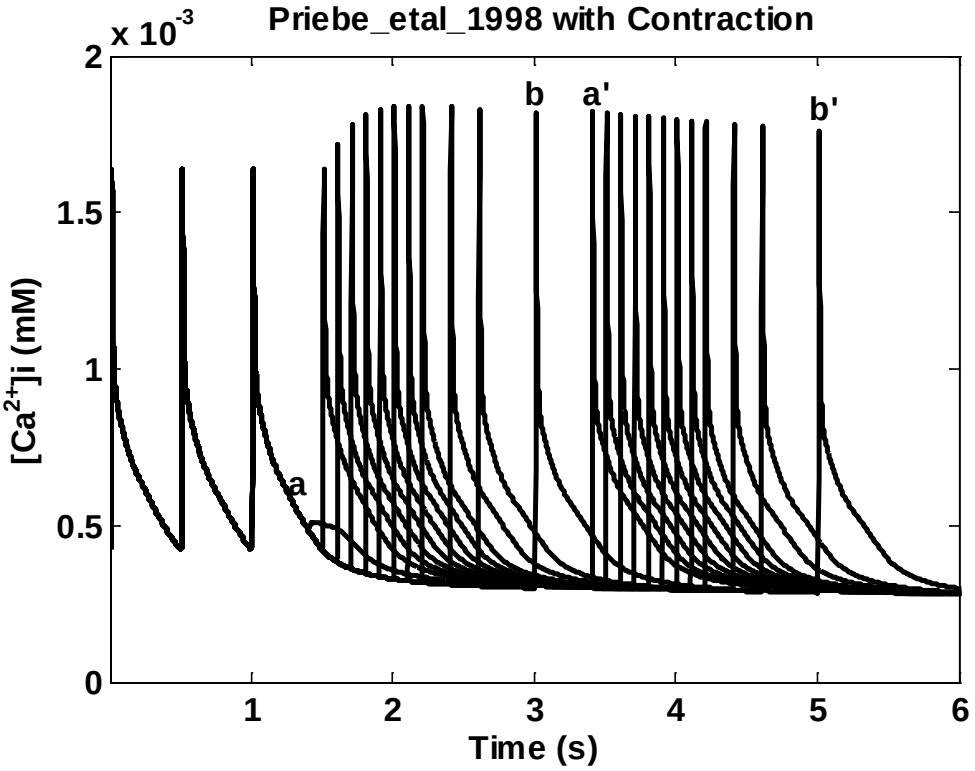
Priebe_etal_1998 with Contraction
x 10^-3
[Ca2+]i (mM)
Time (s)
a
b
a'
b'

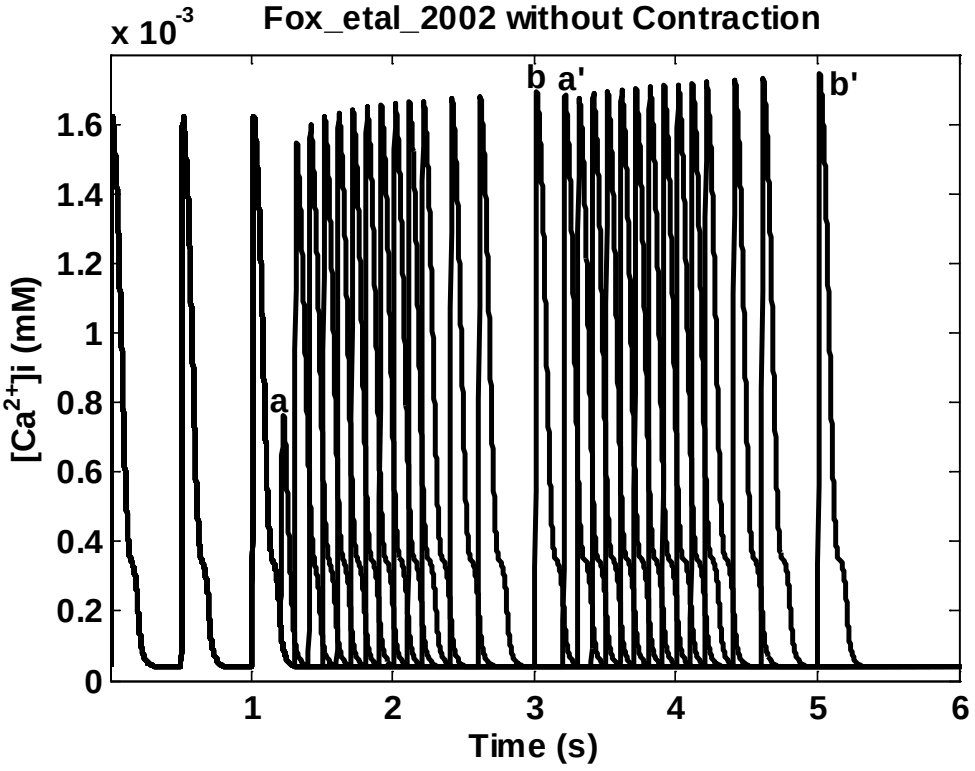
Fox_etal_2002 without Contraction
x 10^-3
[Ca2+]i (mM)
Time (s)
a
b a'
b'

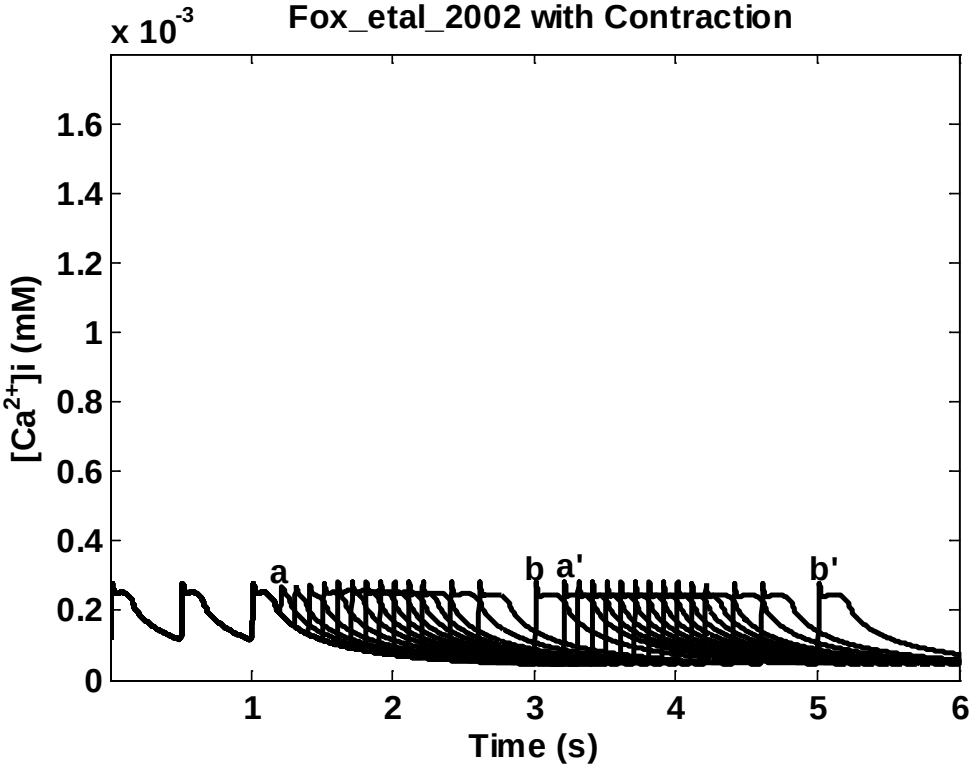
Fox_etal_2002 with Contraction
x 10^-3
[Ca2+]i (mM)
Time (s)
a
b a'
b'

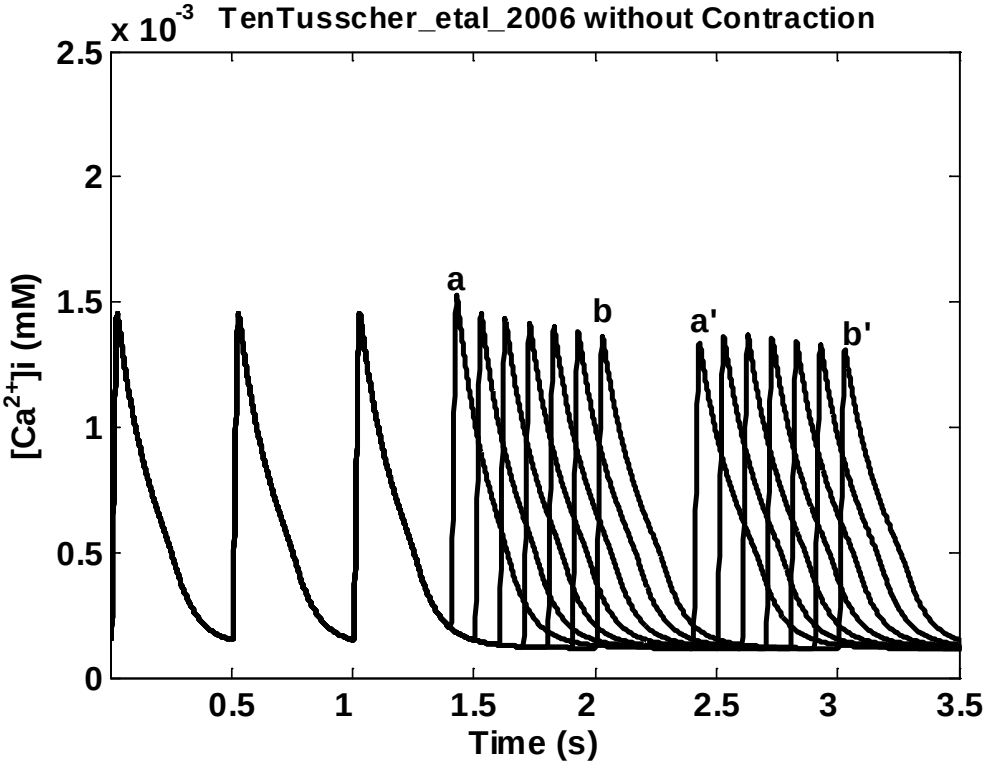
x 10^-3
TenTusscher_etal_2006 without Contraction
[Ca2+]i (mM)
Time (s)
a
b
a'
b'

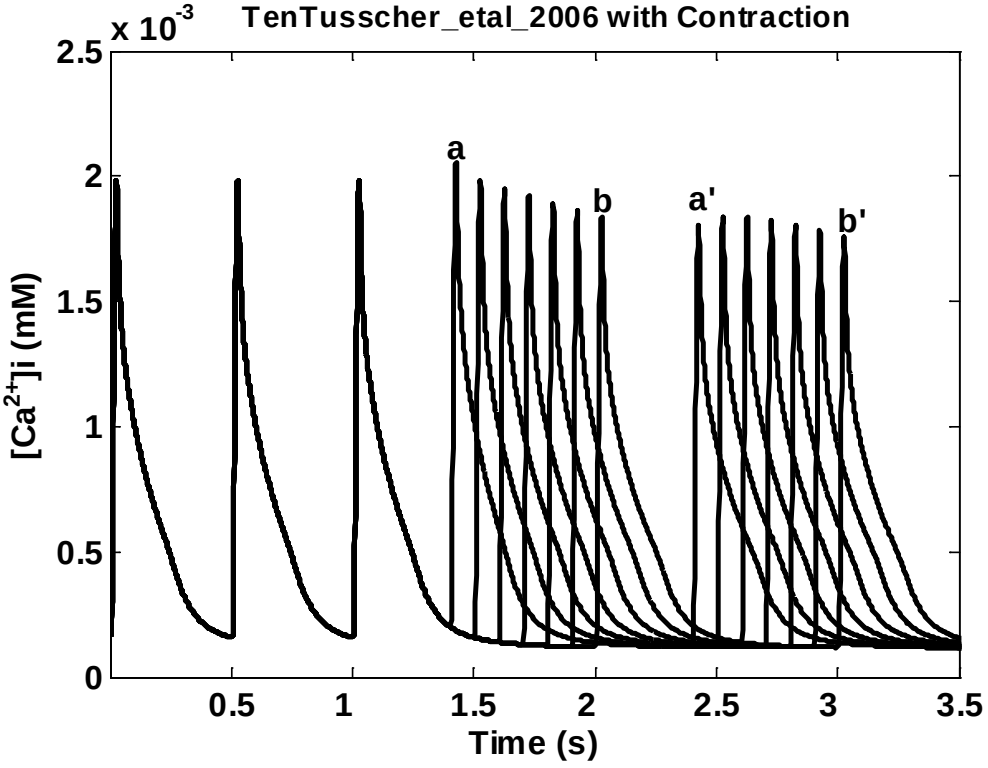
x 10^-3
TenTusscher_etal_2006 with Contraction
[Ca2+]i (mM)
Time (s)
a
b
a'
b'

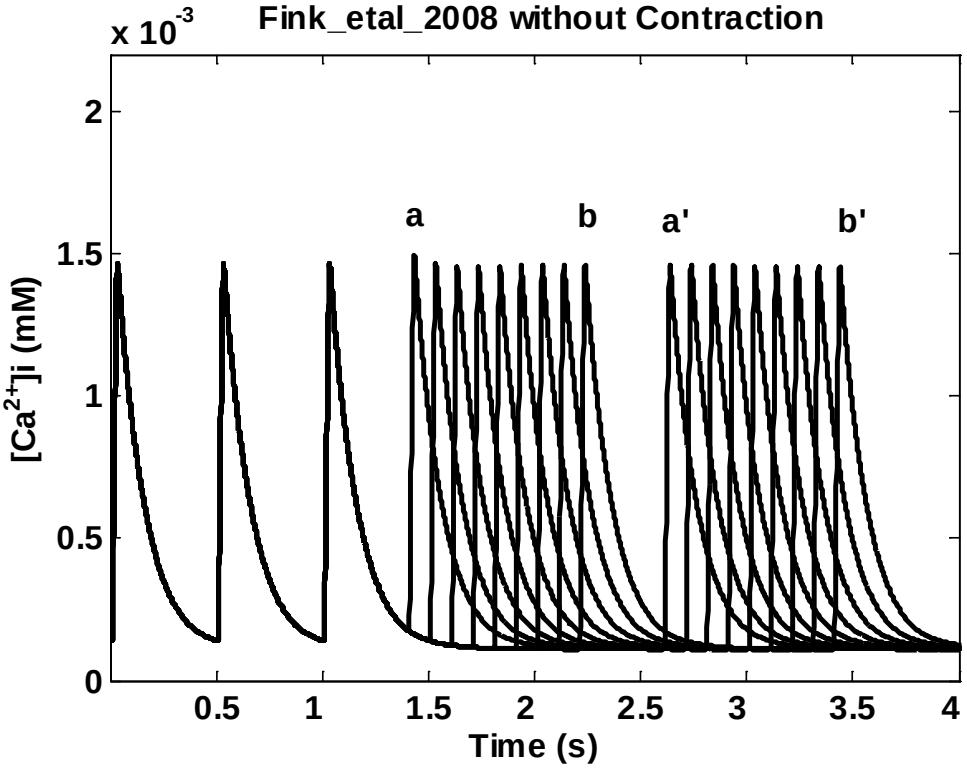
Fink_etal_2008 without Contraction
x 10^-3
[Ca2+]i (mM)
Time (s)
a
b
a'
b'
0
0.5
1
1.5
2
0.5
1
1.5
2
2.5
3
3.5
4

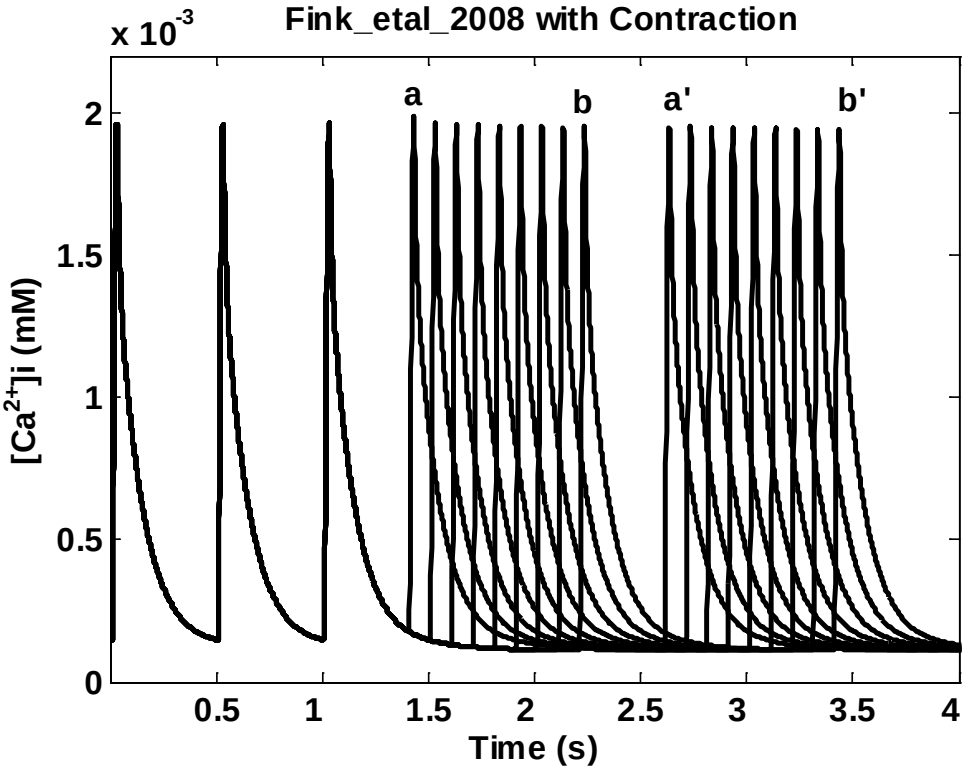
Fink_etal_2008 with Contraction
x 10^-3
[Ca2+]i (mM)
Time (s)
a
b
a'
b'
0
0.5
1
1.5
2
0.5
1
1.5
2
2.5
3
3.5
4

B.3 Postextrasystolic mechanical restitution curves (MRC_{pes}) for all models.

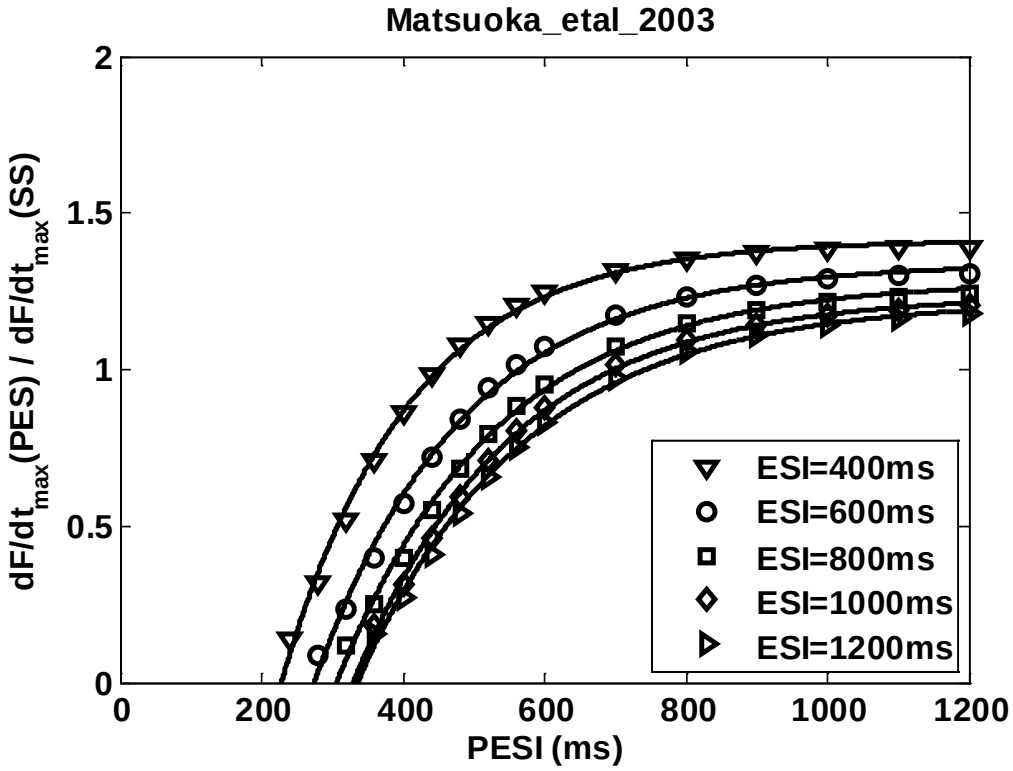
Matsuoka_etal_2003
dF/dt_max(PES) / dF/dt_max(SS)
PESI (ms)
ESI=400ms
ESI=600ms
ESI=800ms
ESI=1000ms
ESI=1200ms

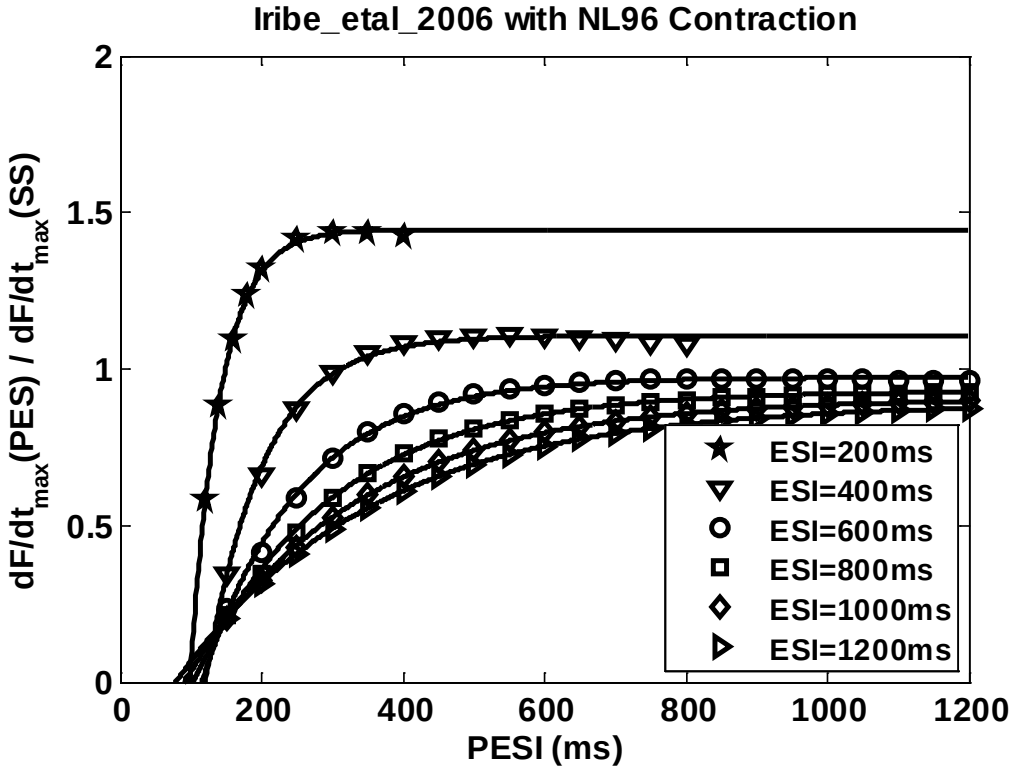
Iribe_etal_2006 with NL96 Contraction
dF/dt_max(PES) / dF/dt_max(SS)
PESI (ms)
ESI=200ms
ESI=400ms
ESI=600ms
ESI=800ms
ESI=1000ms
ESI=1200ms

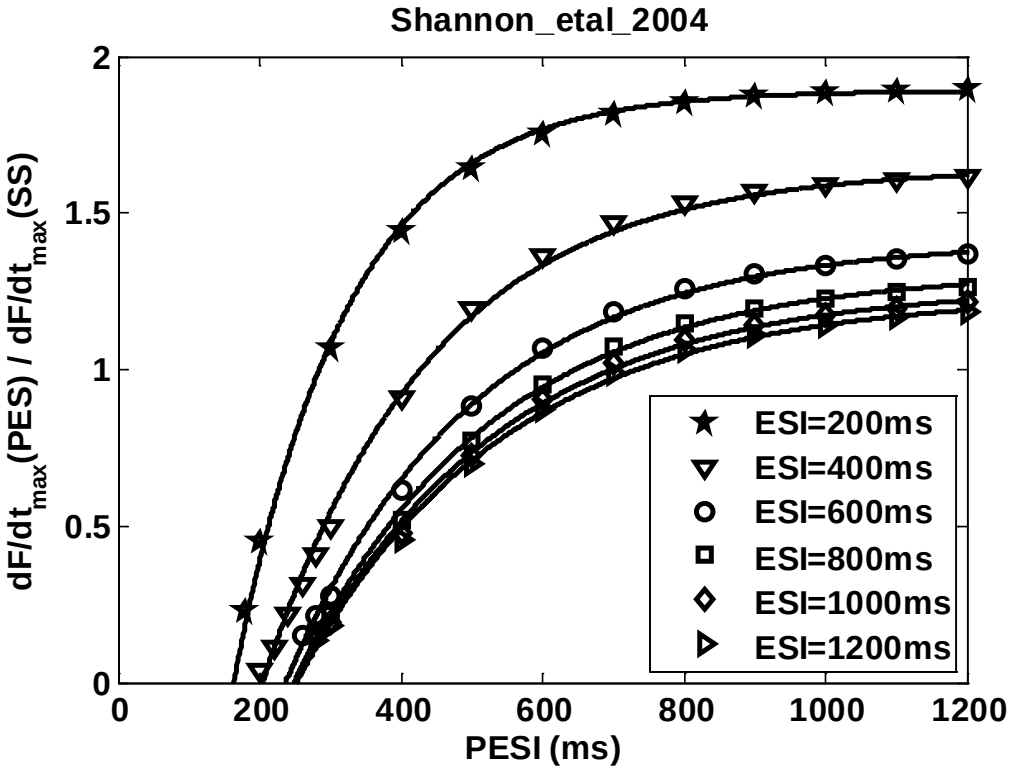
Shannon_etal_2004
dF/dt_max(PES) / dF/dt_max(SS)
PESI (ms)
ESI=200ms
ESI=400ms
ESI=600ms
ESI=800ms
ESI=1000ms
ESI=1200ms

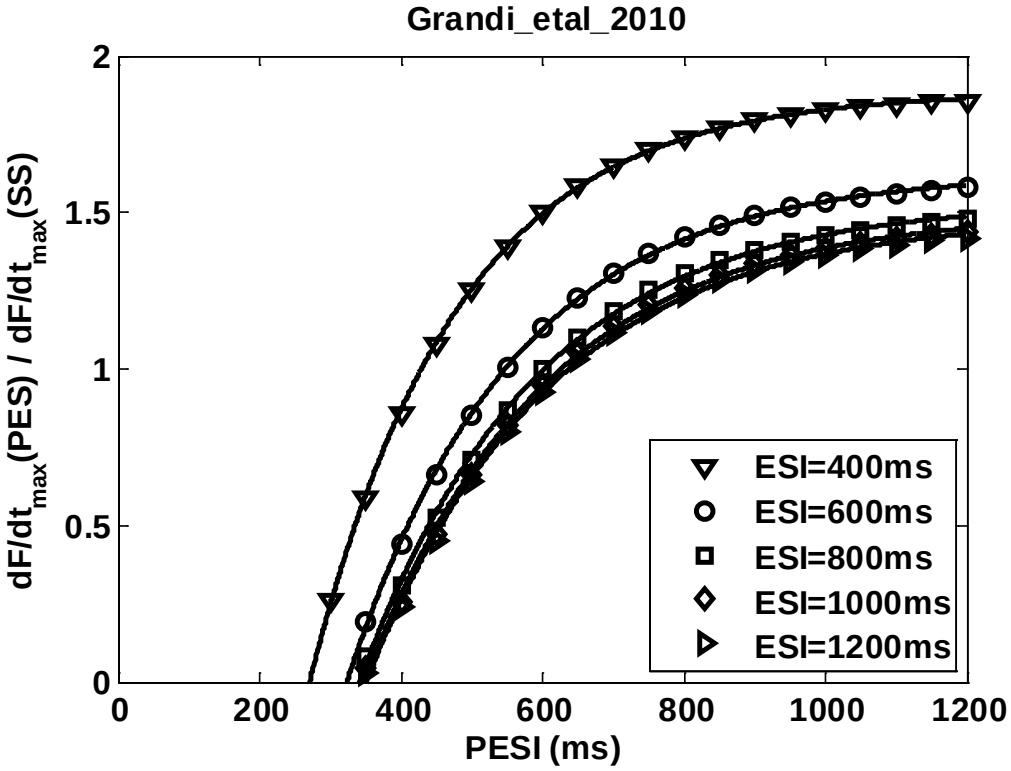
Grandi_etal_2010
dF/dt_max(PES) / dF/dt_max(SS)
PESI (ms)
ESI=400ms
ESI=600ms
ESI=800ms
ESI=1000ms
ESI=1200ms

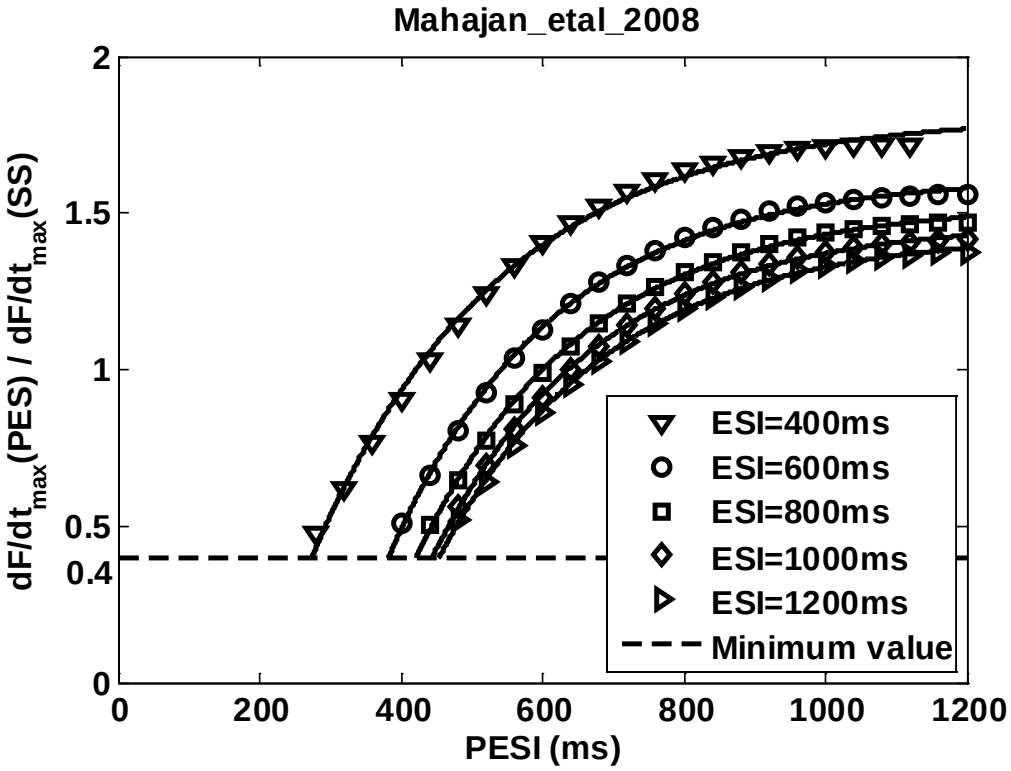
Mahajan_etal_2008
dF/dt_max(PES) / dF/dt_max(SS)
PESI (ms)
ESI=400ms
ESI=600ms
ESI=800ms
ESI=1000ms
ESI=1200ms
Minimum value

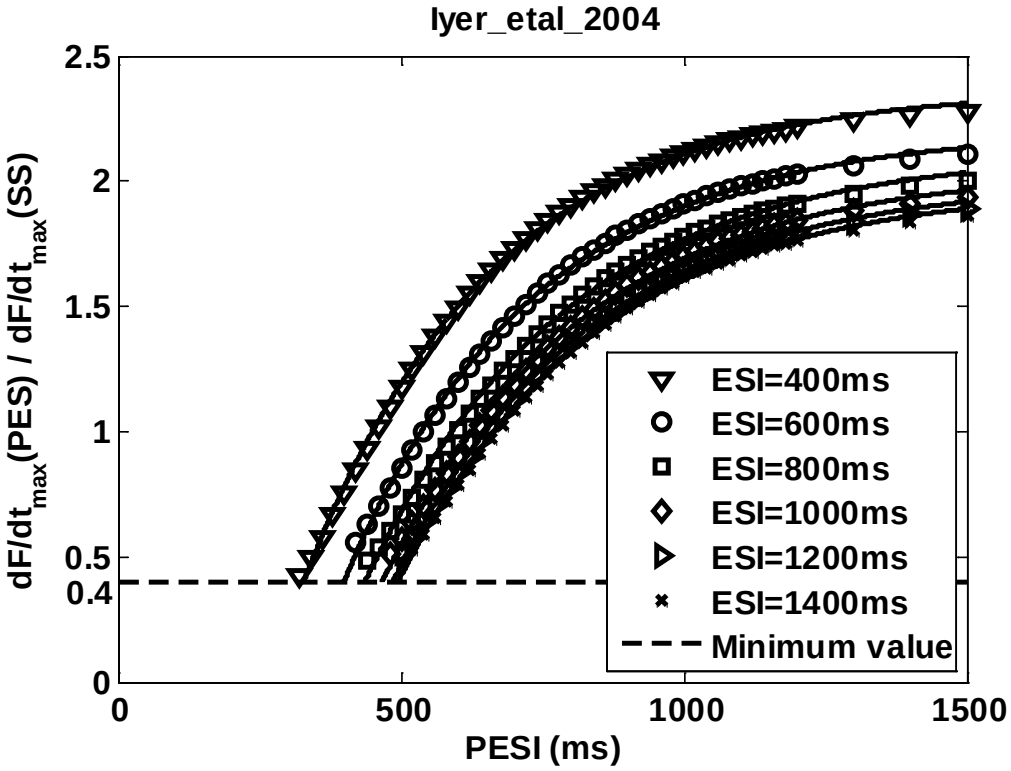
Iyer_etal_2004
dF/dt_max(PES) / dF/dt_max(SS)
PESI (ms)
ESI=400ms
ESI=600ms
ESI=800ms
ESI=1000ms
ESI=1200ms
ESI=1400ms
Minimum value

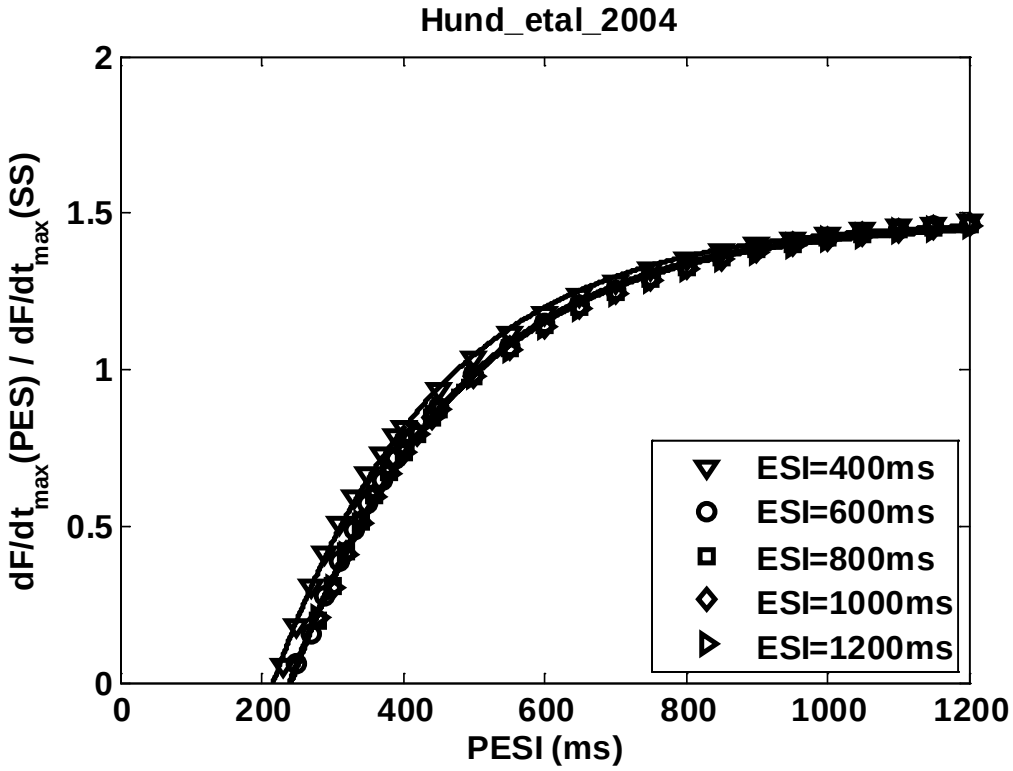
Hund_etal_2004
dF/dt_max(PES) / dF/dt_max(SS)
PESI (ms)
ESI=400ms
ESI=600ms
ESI=800ms
ESI=1000ms
ESI=1200ms

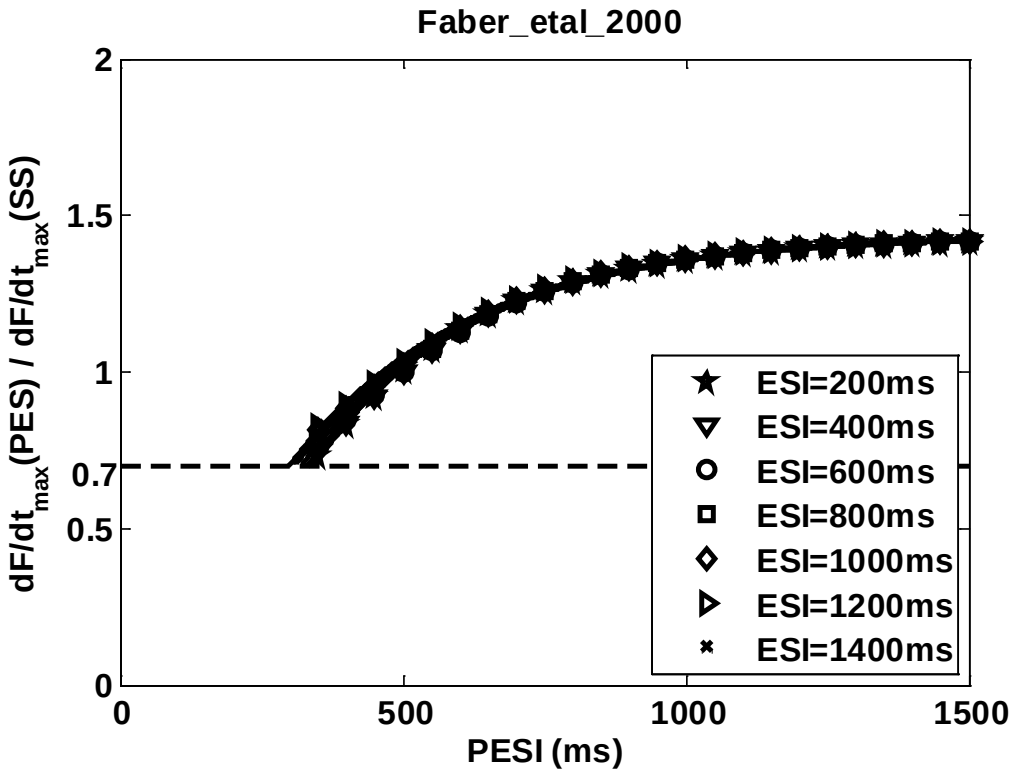
Faber_etal_2000
dF/dt_max(PES) / dF/dt_max(SS)
PESI (ms)
ESI=200ms
ESI=400ms
ESI=600ms
ESI=800ms
ESI=1000ms
ESI=1200ms
ESI=1400ms

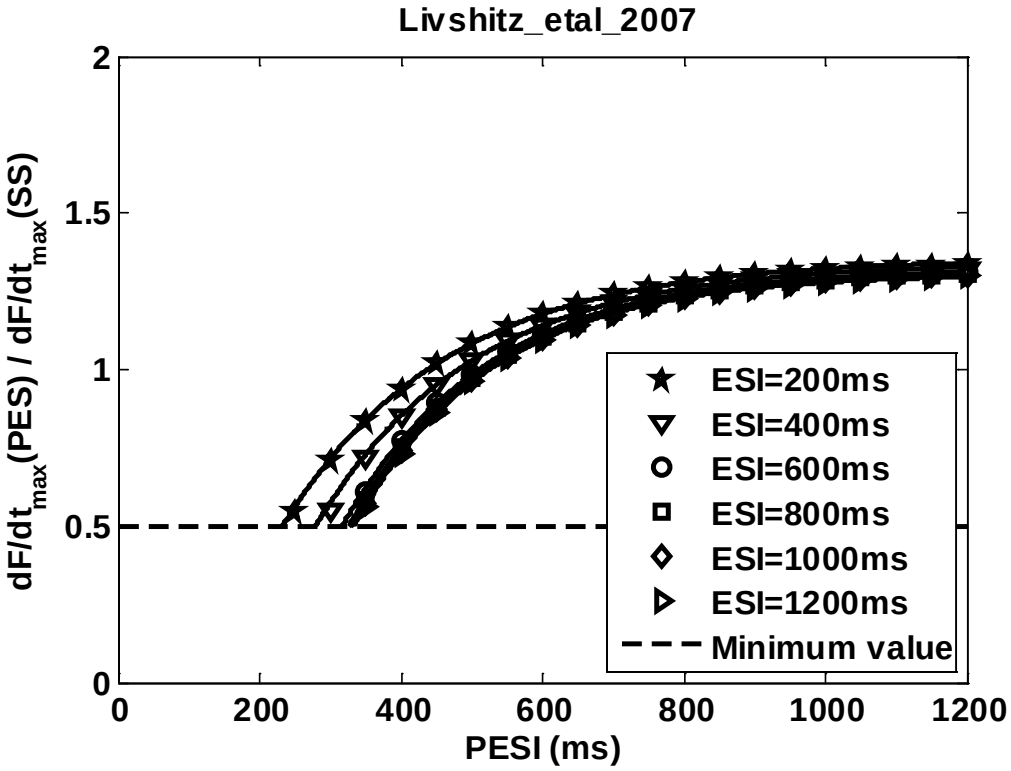
Livshitz_etal_2007
dF/dt_max(PES) / dF/dt_max(SS)
PESI (ms)
ESI=200ms
ESI=400ms
ESI=600ms
ESI=800ms
ESI=1000ms
ESI=1200ms
Minimum value

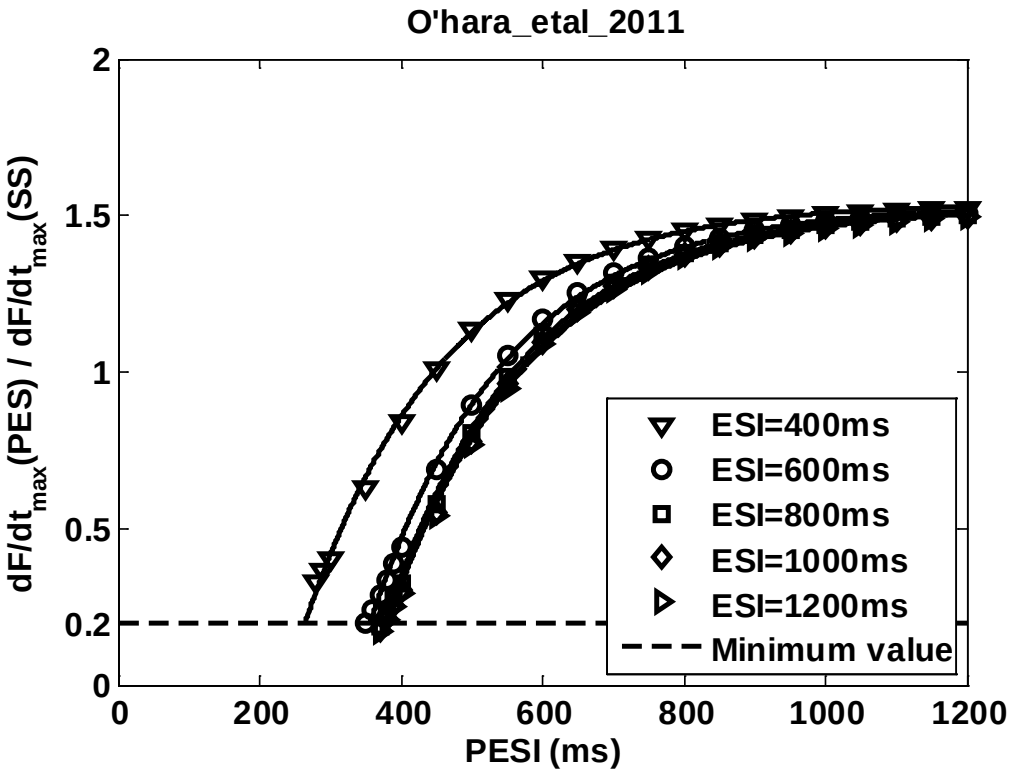
O'hara_etal_2011
dF/dt_max(PES) / dF/dt_max(SS)
PESI (ms)
ESI=400ms
ESI=600ms
ESI=800ms
ESI=1000ms
ESI=1200ms
Minimum value

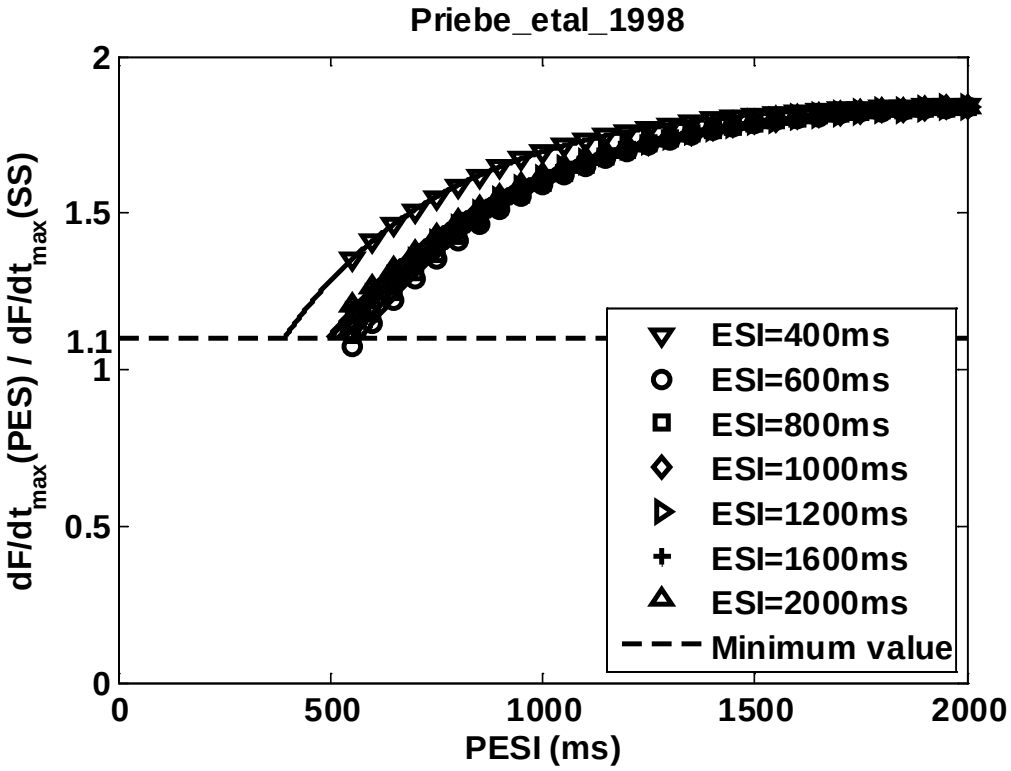
Priebe_etal_1998
dF/dt_max(PES) / dF/dt_max(SS)
PESI (ms)
ESI=400ms
ESI=600ms
ESI=800ms
ESI=1000ms
ESI=1200ms
ESI=1600ms
ESI=2000ms
Minimum value

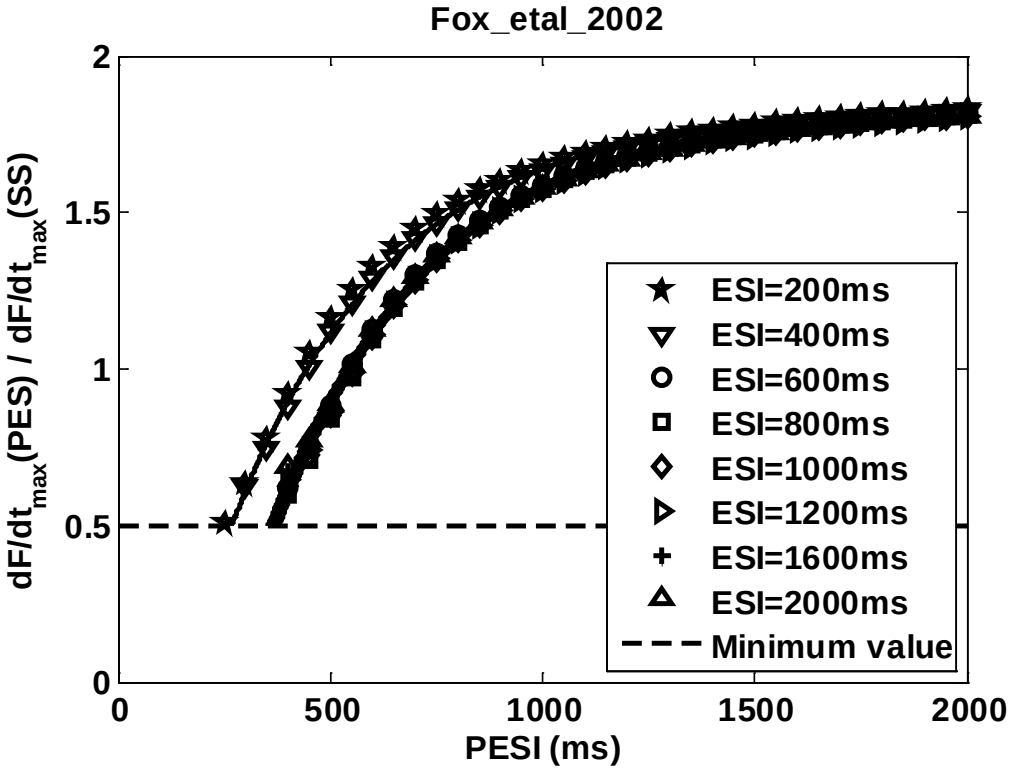
Fox_etal_2002
dF/dt_max(PES) / dF/dt_max(SS)
PESI (ms)
ESI=200ms
ESI=400ms
ESI=600ms
ESI=800ms
ESI=1000ms
ESI=1200ms
ESI=1600ms
ESI=2000ms
Minimum value

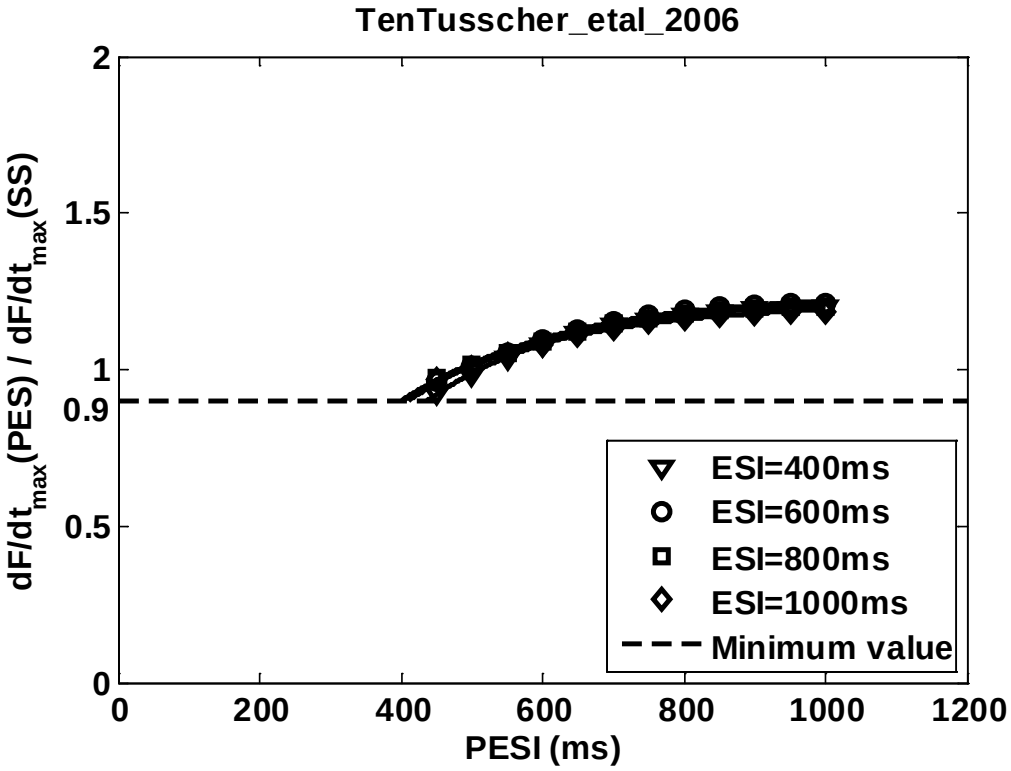
TenTusscher_etal_2006
dF/dt_max(PES) / dF/dt_max(SS)
PESI (ms)
ESI=400ms
ESI=600ms
ESI=800ms
ESI=1000ms
Minimum value

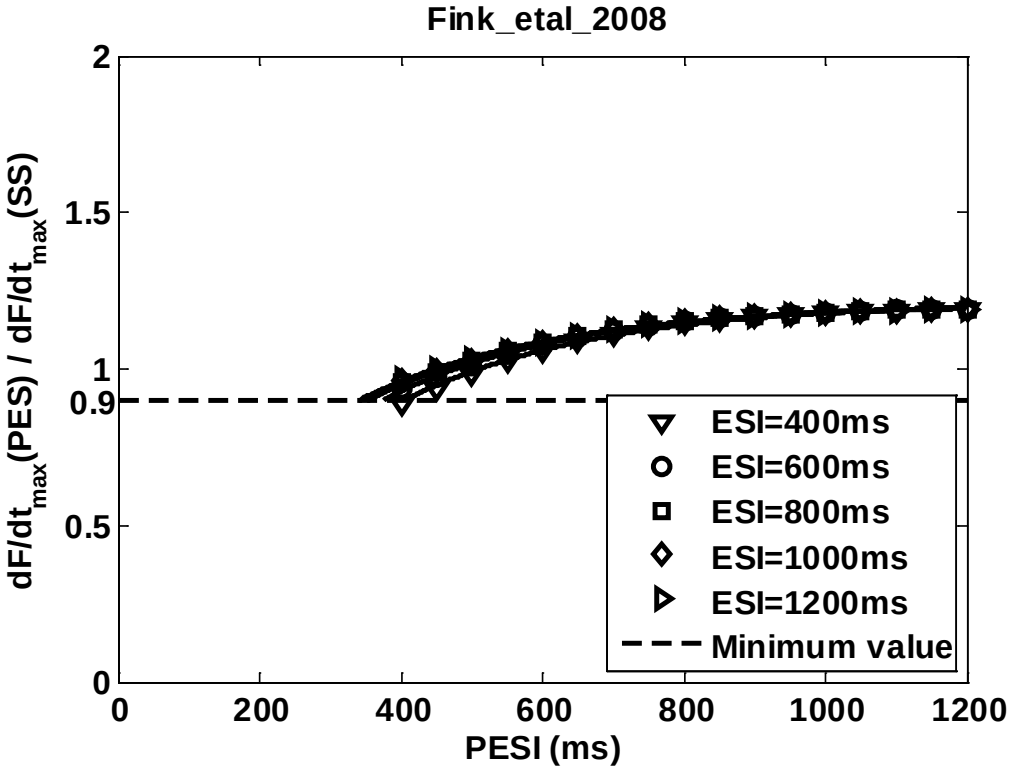
Fink_etal_2008
dF/dt_max(PES) / dF/dt_max(SS)
PESI (ms)
ESI=400ms
ESI=600ms
ESI=800ms
ESI=1000ms
ESI=1200ms
Minimum value

B.4 Postextrasystolic potnetiation curve (PESPC, circles o) and extrasystolic mechanical restitution curve (MRC_{es}, stars *) for all models.

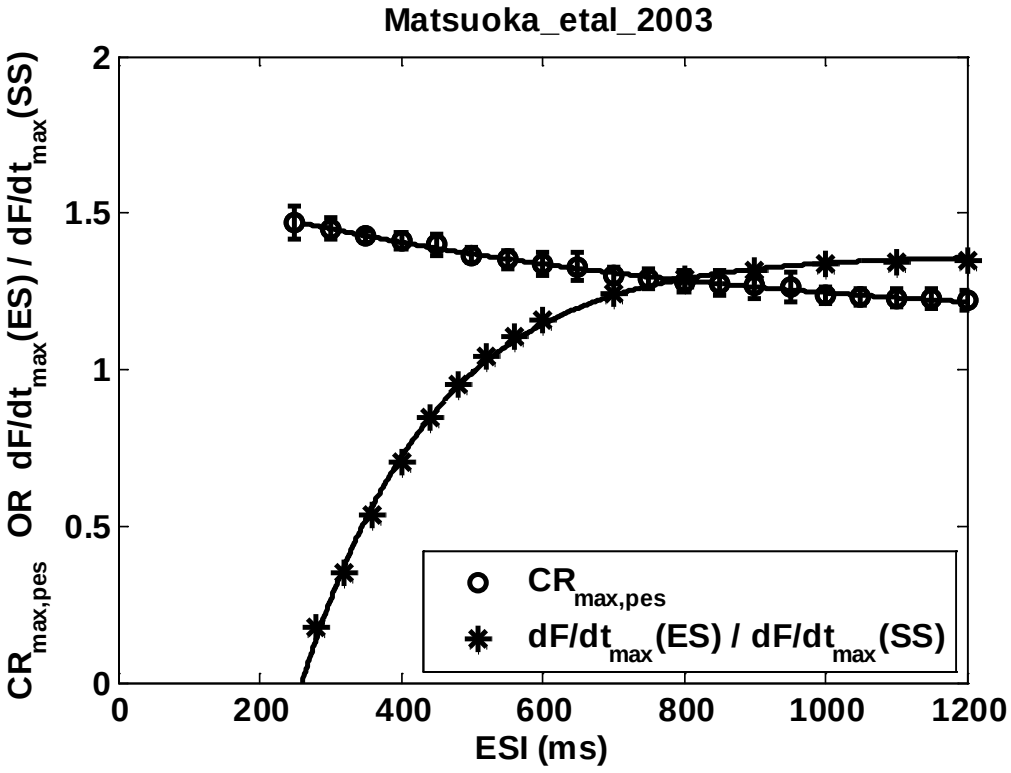
Matsuoka_etal_2003
CR_max,pes OR dF/dt_max(ES) / dF/dt_max(SS)
ESI (ms)
CR_max,pes
dF/dt_max(ES) / dF/dt_max(SS)

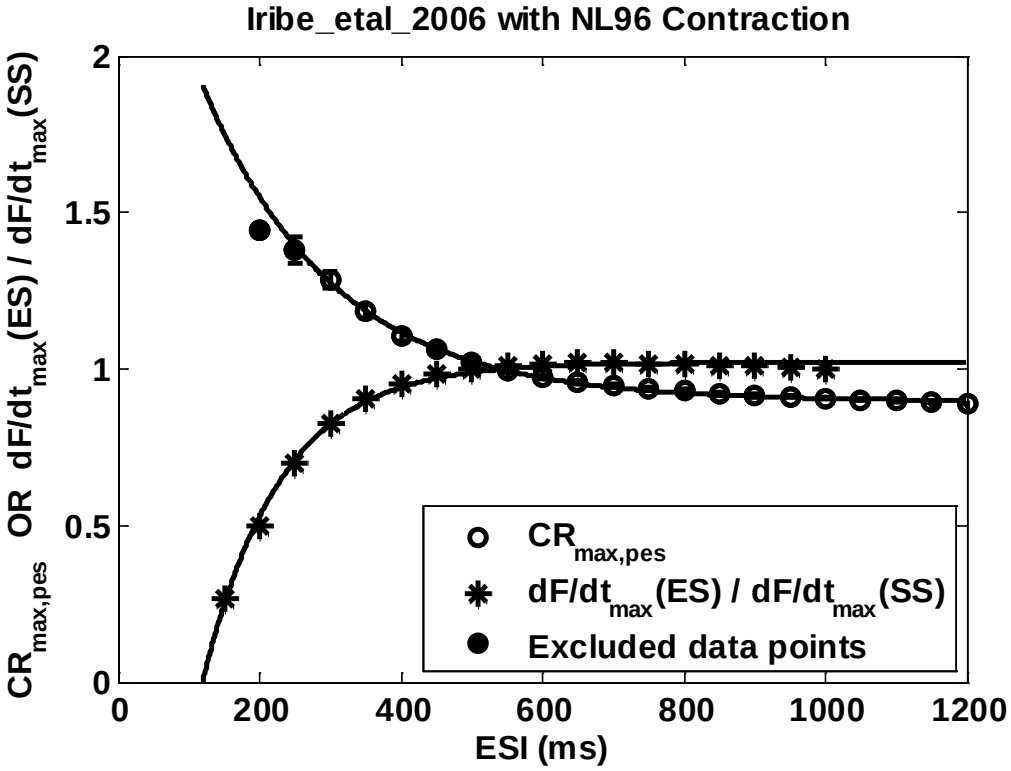
Iribe_etal_2006 with NL96 Contraction
CR_max,pes OR dF/dt_max(ES) / dF/dt_max(SS)
ESI (ms)
CR_max,pes
dF/dt_max(ES) / dF/dt_max(SS)
Excluded data points

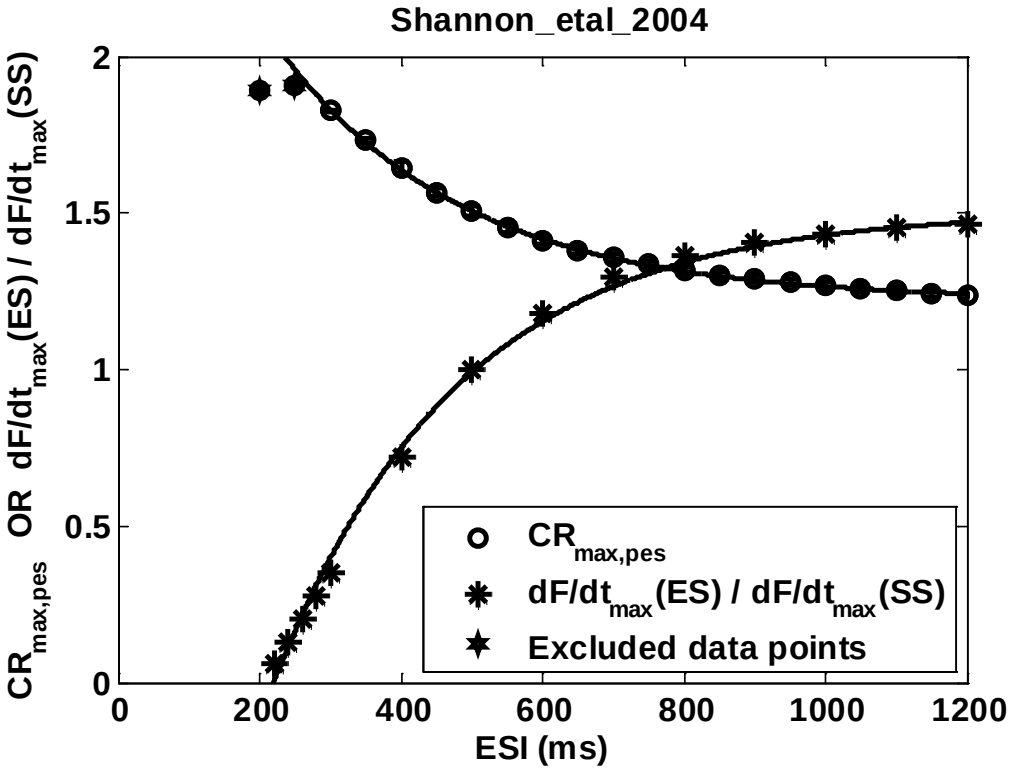
Shannon_etal_2004
CR_max,pes OR dF/dt_max(ES) / dF/dt_max(SS)
ESI (ms)
CR_max,pes
dF/dt_max(ES) / dF/dt_max(SS)
Excluded data points

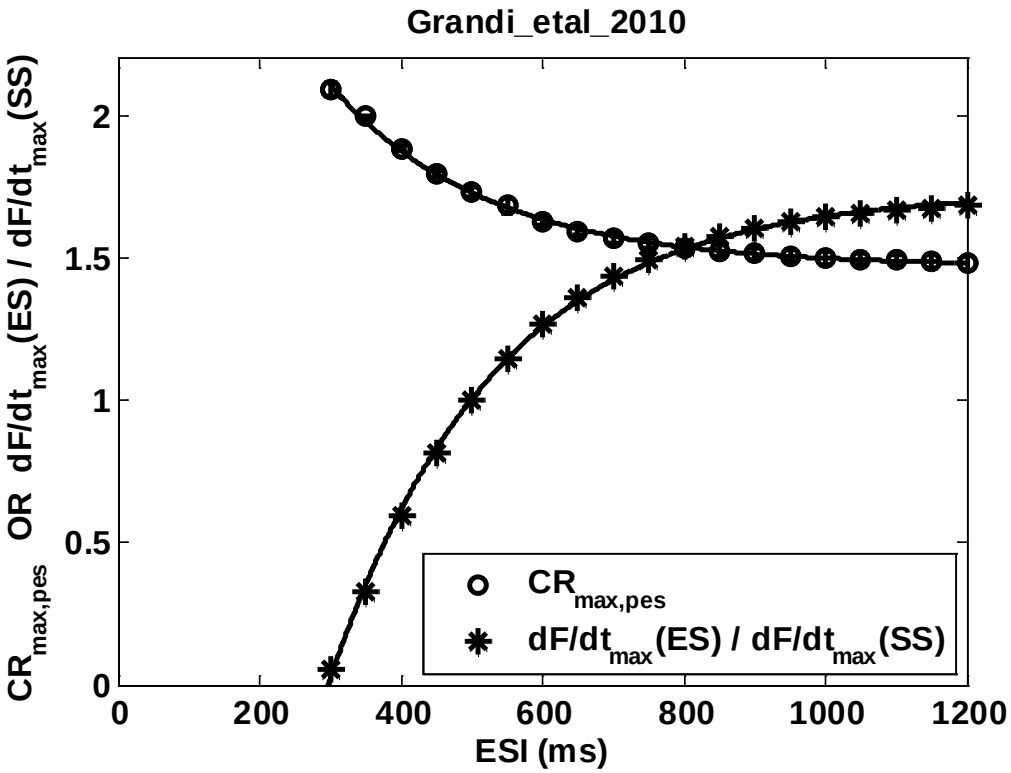
Grandi_etal_2010
CR_max,pes OR dF/dt_max(ES) / dF/dt_max(SS)
ESI (ms)
CR_max,pes
dF/dt_max(ES) / dF/dt_max(SS)

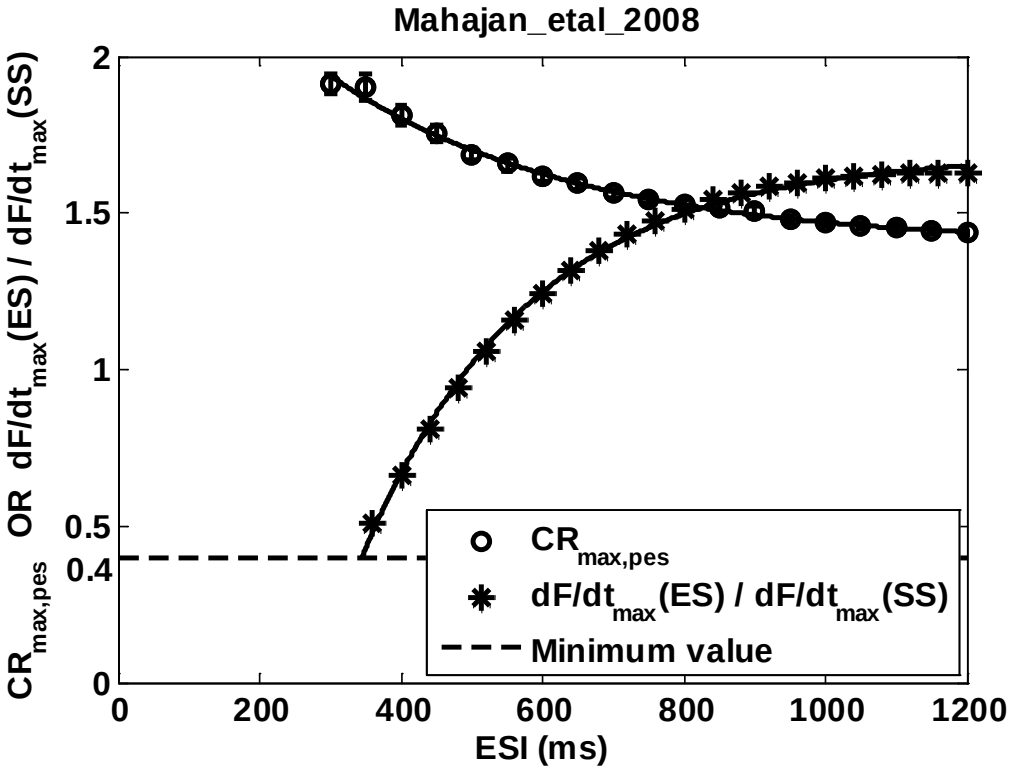
Mahajan_etal_2008
CR_max,pes OR dF/dt_max(ES) / dF/dt_max(SS)
ESI (ms)
CR_max,pes
dF/dt_max(ES) / dF/dt_max(SS)
Minimum value

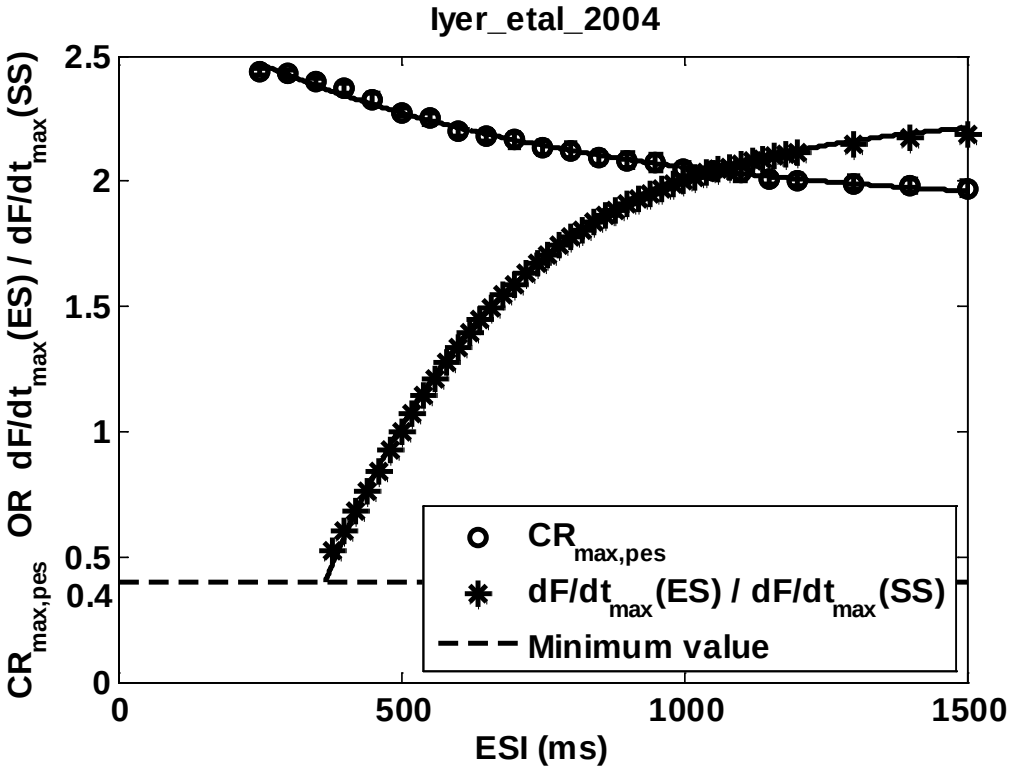
Iyer_etal_2004
CR_max,pes OR dF/dt_max(ES) / dF/dt_max(SS)
ESI (ms)
CR_max,pes
dF/dt_max(ES) / dF/dt_max(SS)
Minimum value

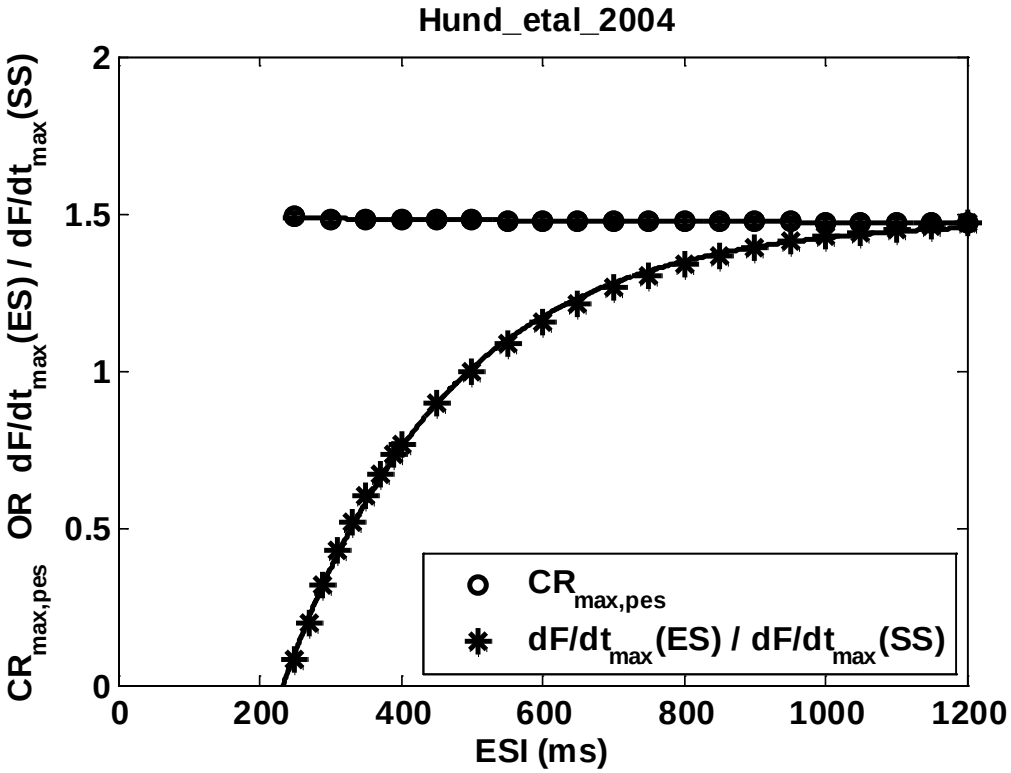
Hund_etal_2004
CR_max,pes OR dF/dt_max(ES) / dF/dt_max(SS)
ESI (ms)
CR_max,pes
dF/dt_max(ES) / dF/dt_max(SS)

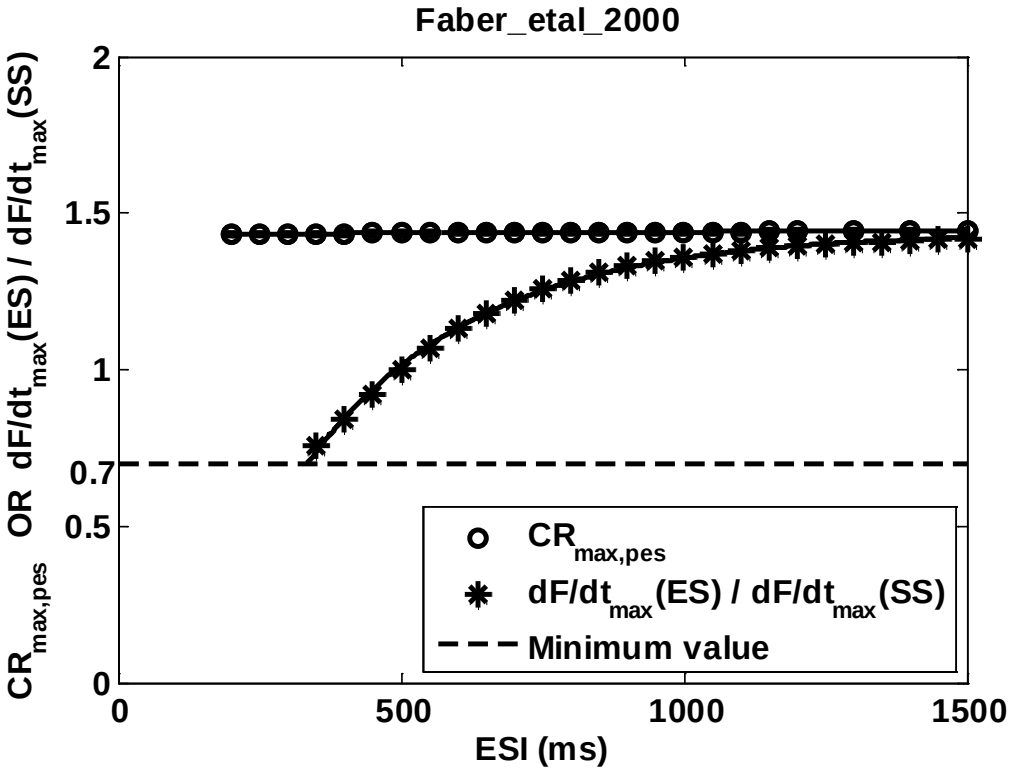
Faber_etal_2000
CR_max,pes OR dF/dt_max(ES) / dF/dt_max(SS)
ESI (ms)
CR_max,pes
dF/dt_max(ES) / dF/dt_max(SS)
Minimum value

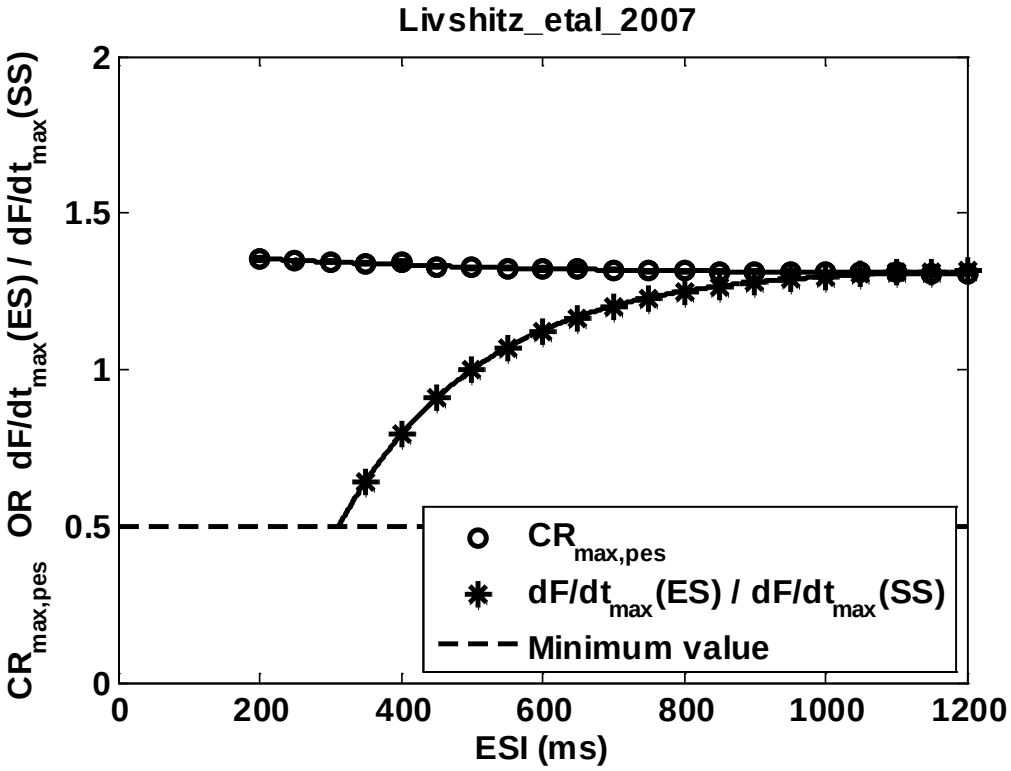
Livshitz_etal_2007
CR_max,pes OR dF/dt_max(ES) / dF/dt_max(SS)
ESI (ms)
CR_max,pes
dF/dt_max(ES) / dF/dt_max(SS)
Minimum value

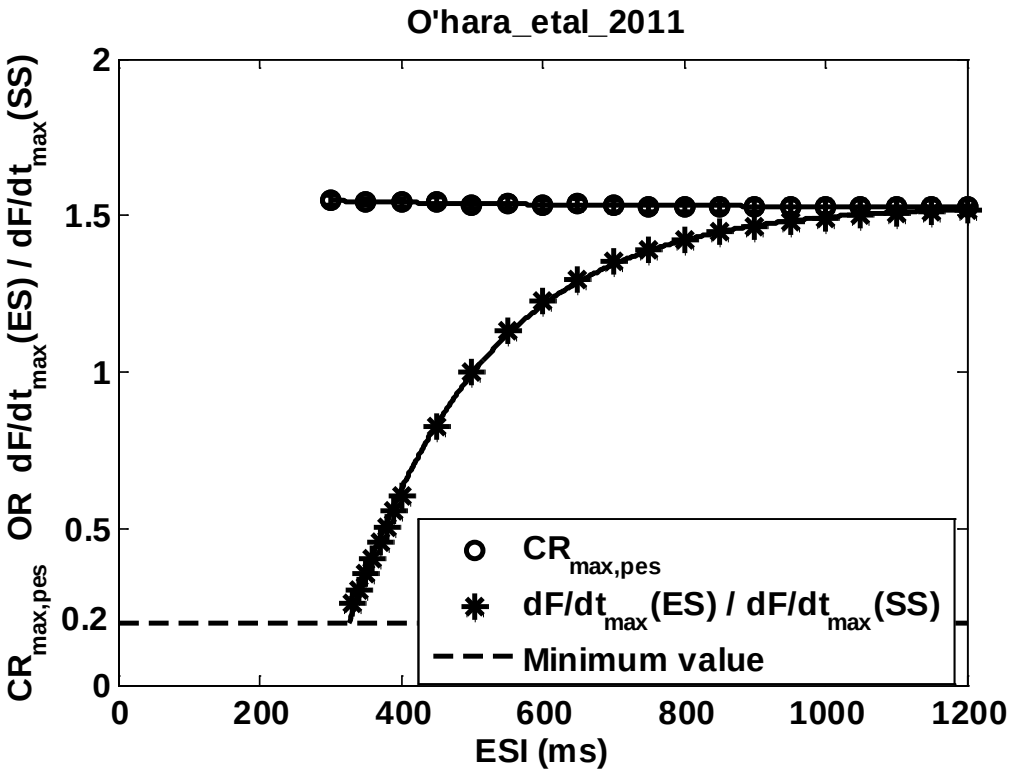
O'hara_etal_2011
CR_max,pes OR dF/dt_max(ES) / dF/dt_max(SS)
ESI (ms)
CR_max,pes
dF/dt_max(ES) / dF/dt_max(SS)
Minimum value

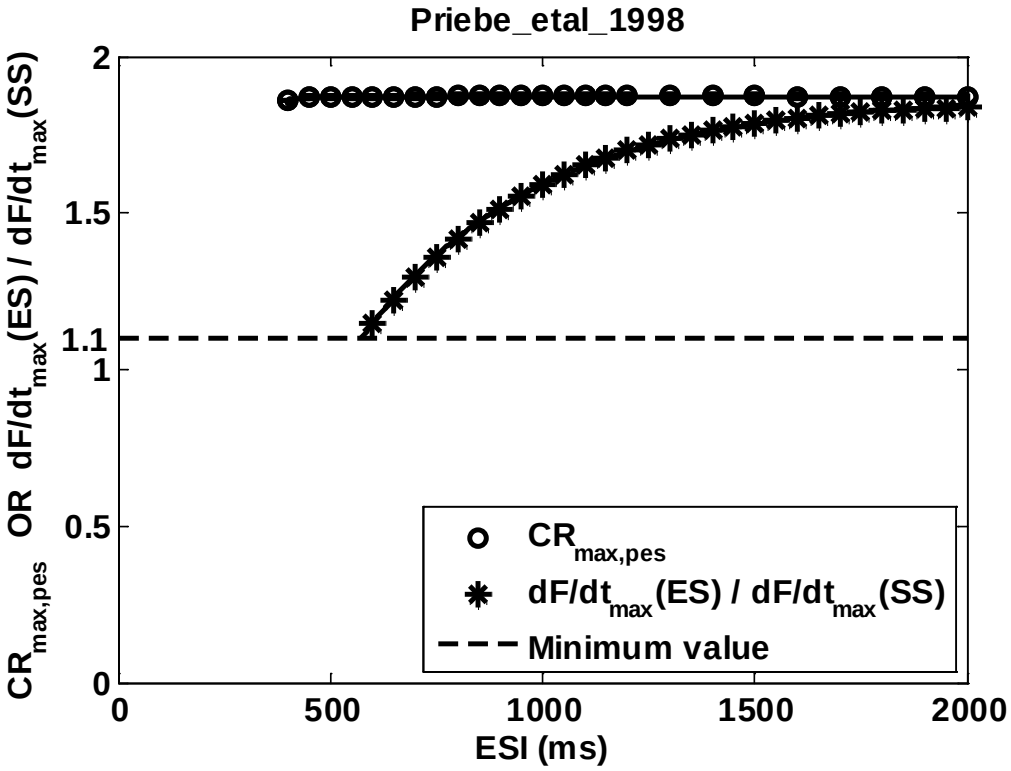
Priebe_etal_1998
CR_max,pes OR dF/dt_max(ES) / dF/dt_max(SS)
ESI (ms)
CR_max,pes
dF/dt_max(ES) / dF/dt_max(SS)
Minimum value

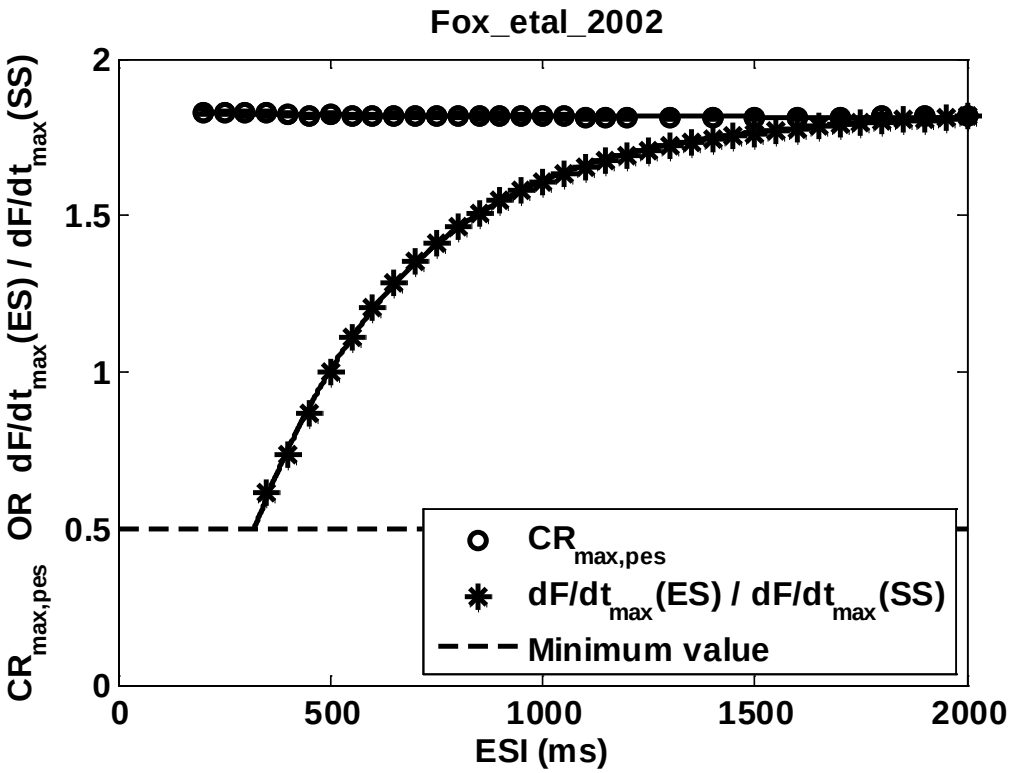
Fox_etal_2002
CR_max,pes OR dF/dt_max(ES) / dF/dt_max(SS)
ESI (ms)
CR_max,pes
dF/dt_max(ES) / dF/dt_max(SS)
Minimum value

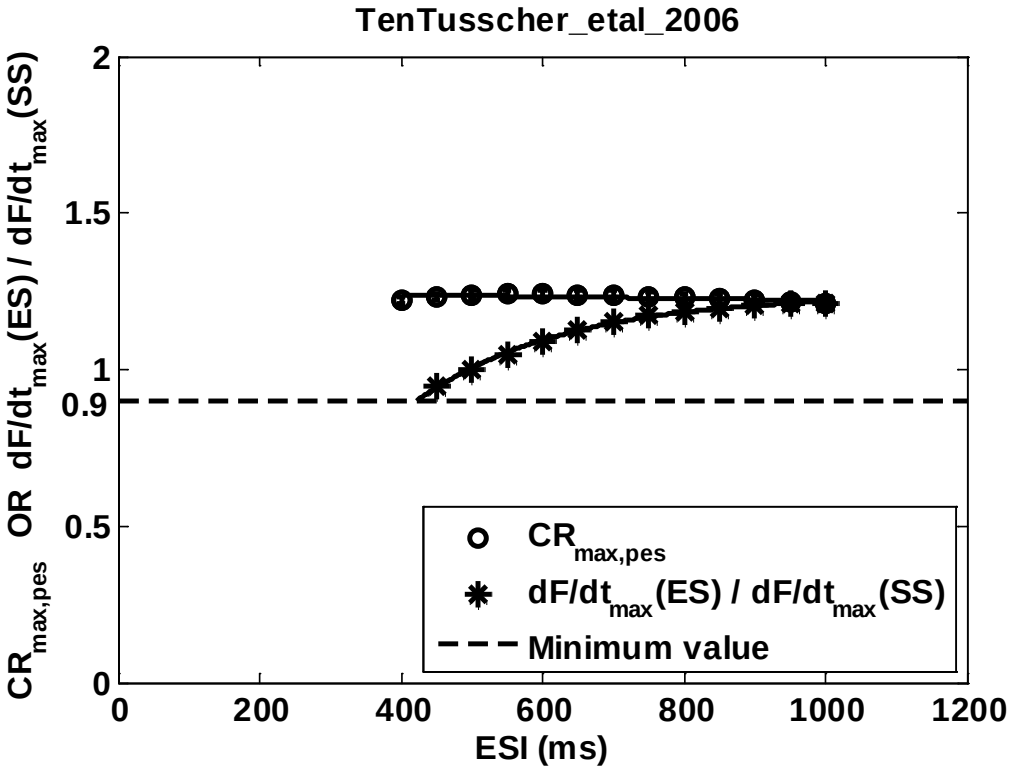
TenTusscher_etal_2006
CR_max,pes OR dF/dt_max(ES) / dF/dt_max(SS)
ESI (ms)
CR_max,pes
dF/dt_max(ES) / dF/dt_max(SS)
Minimum value

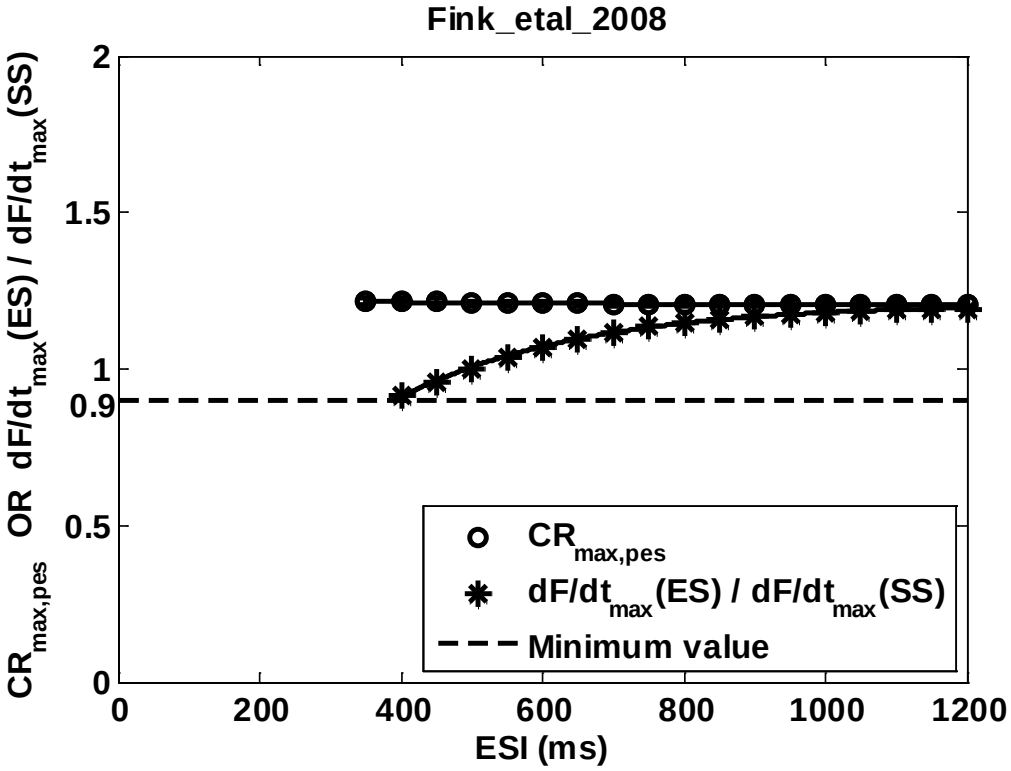
Fink_etal_2008
CR_max,pes OR dF/dt_max(ES) / dF/dt_max(SS)
ESI (ms)
CR_max,pes
dF/dt_max(ES) / dF/dt_max(SS)
Minimum value

B.5 Minimum-value axis intercept curve ($t_{o,pes}$) for all models.

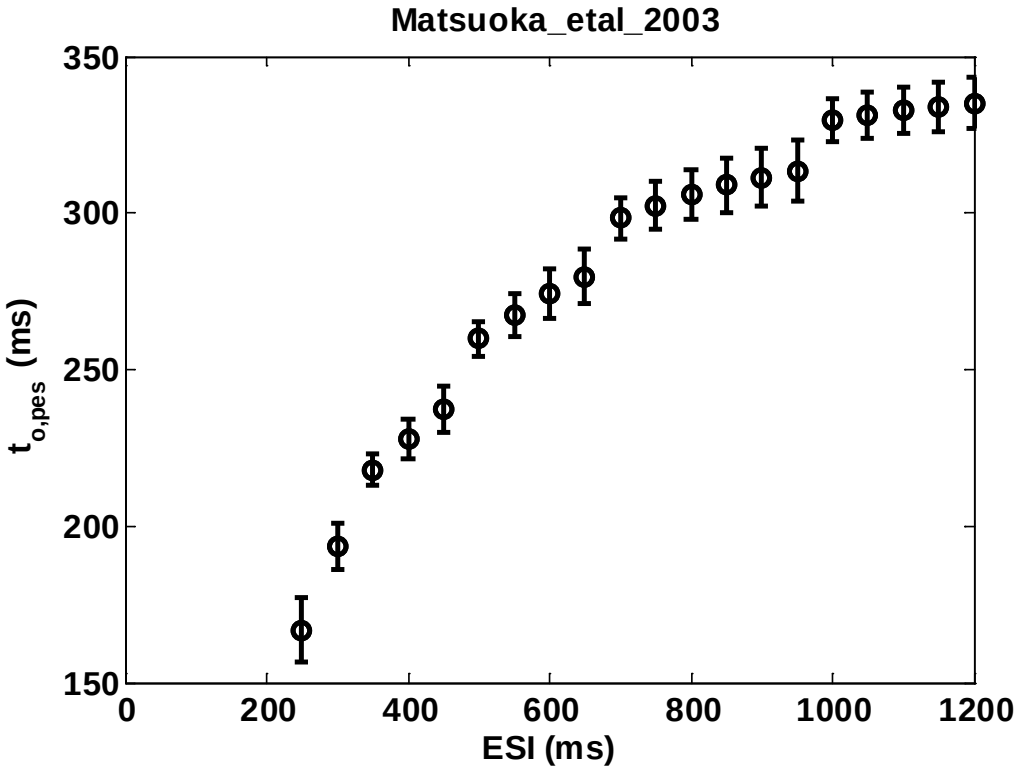
Matsuoka_etal_2003
350
300
250
200
150
$t_{o,pes}$ (ms)
0
200
400
600
800
1000
1200
ESI (ms)

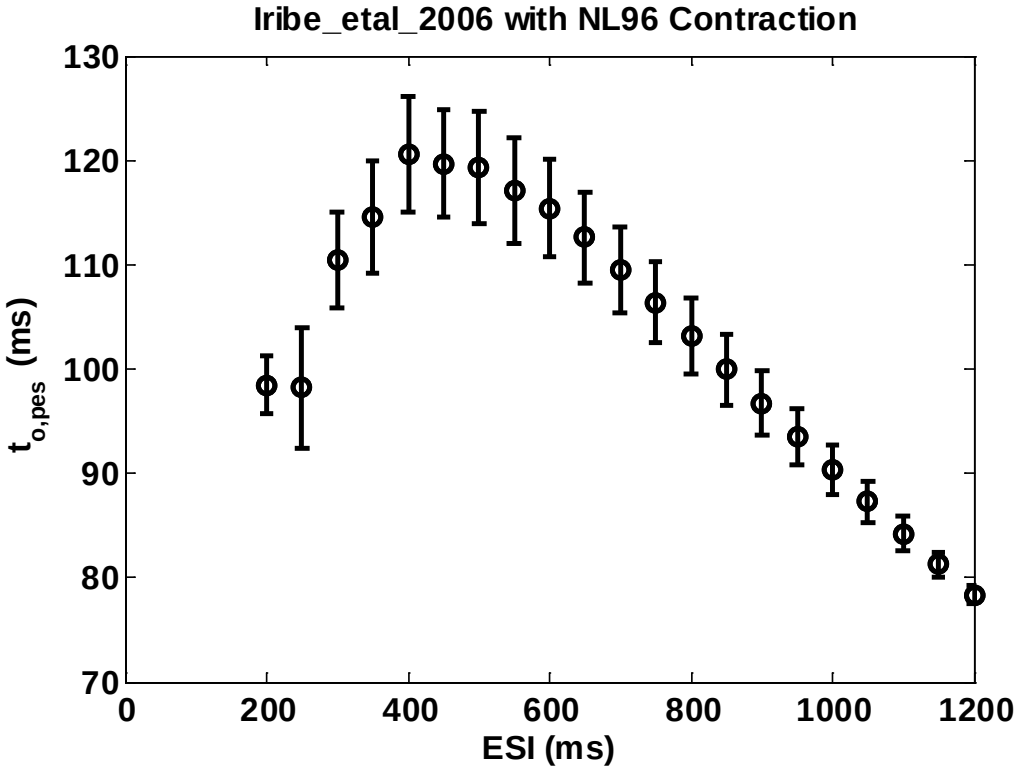
Iribe_etal_2006 with NL96 Contraction
130
120
110
100
90
80
70
$t_{o,pes}$ (ms)
0
200
400
600
800
1000
1200
ESI (ms)

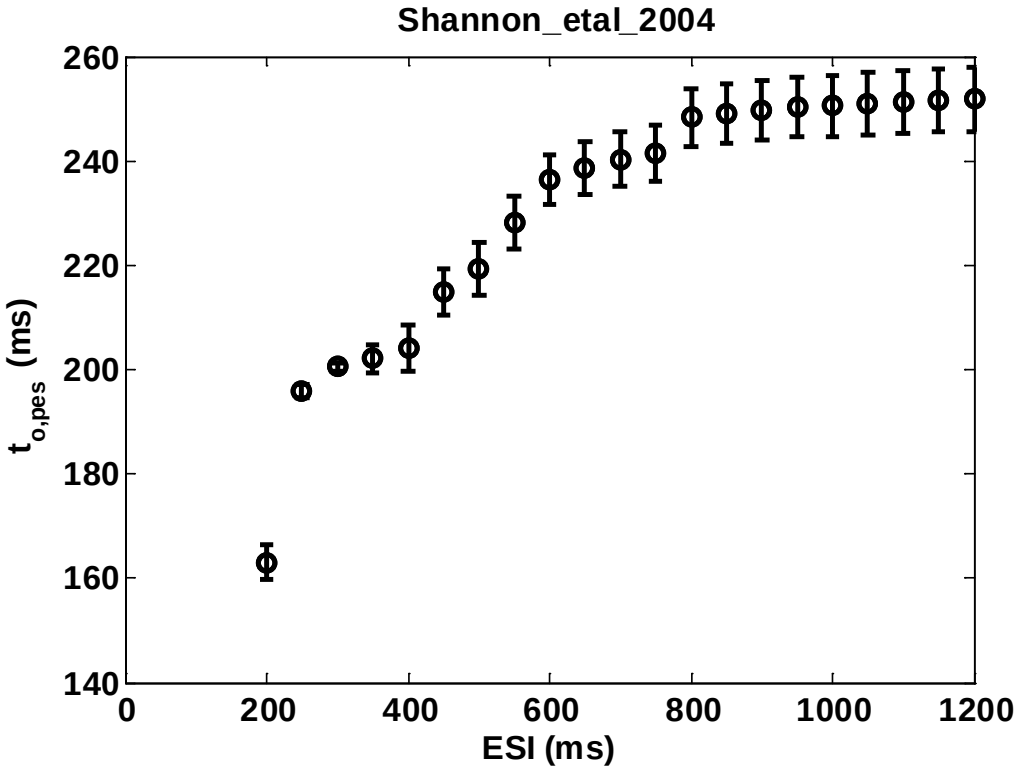
Shannon_etal_2004
260
240
220
200
180
160
140
$t_{o,pes}$ (ms)
0
200
400
600
800
1000
1200
ESI (ms)

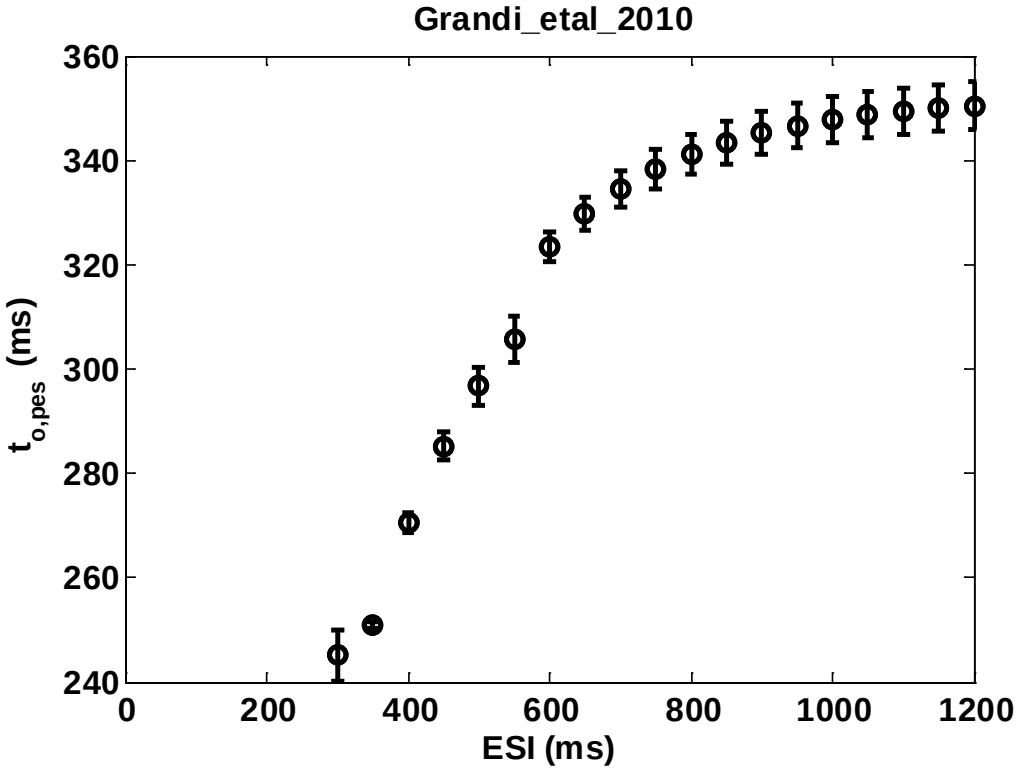
Grandi_etal_2010
360
340
320
300
280
260
240
$t_{o,pes}$ (ms)
0
200
400
600
800
1000
1200
ESI (ms)

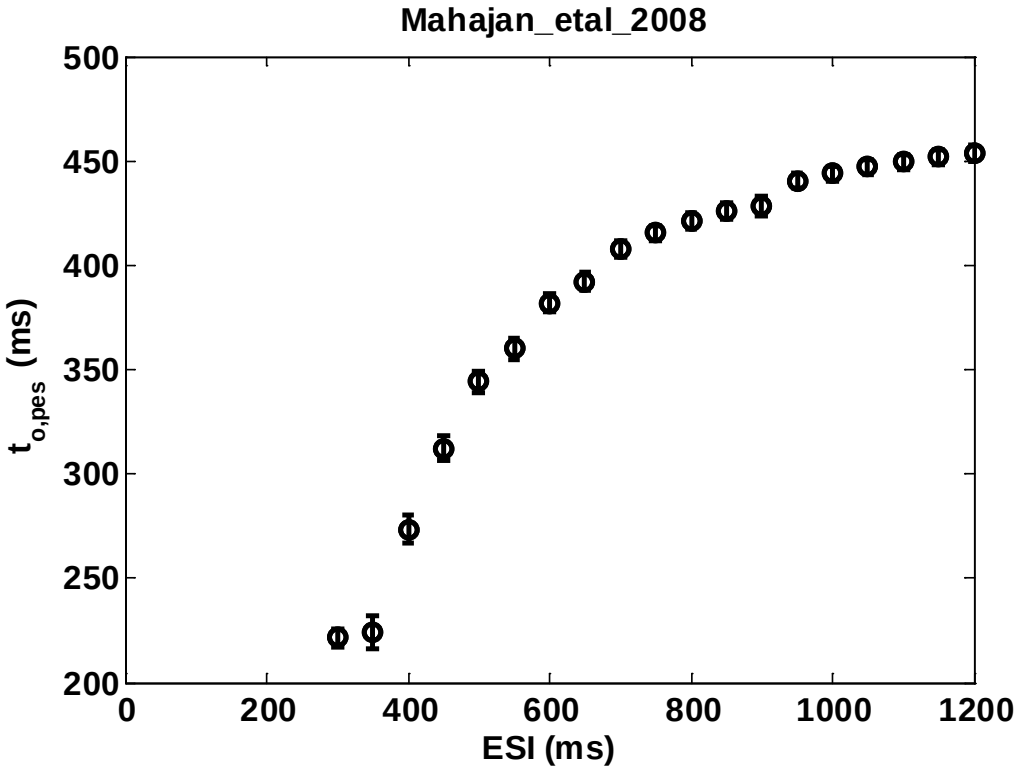
Mahajan_etal_2008
500
450
400
350
300
250
200
$t_{o,pes}$ (ms)
0
200
400
600
800
1000
1200
ESI (ms)

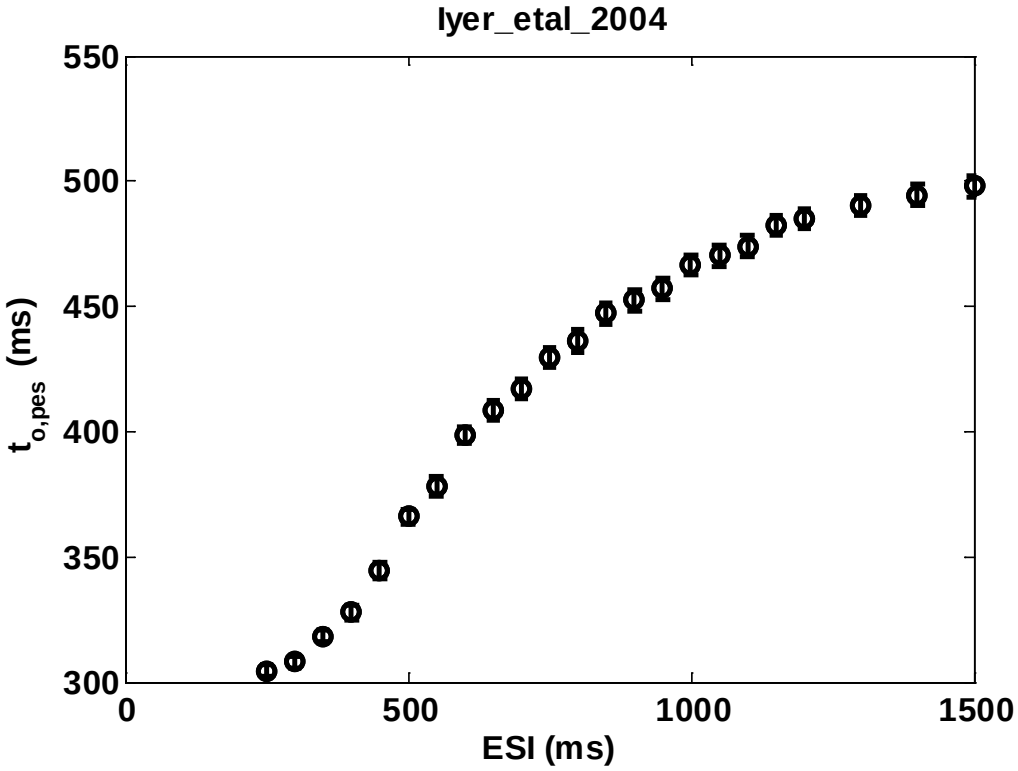
Iyer_etal_2004
550
500
450
400
350
300
$t_{o,pes}$ (ms)
0
500
1000
1500
ESI (ms)

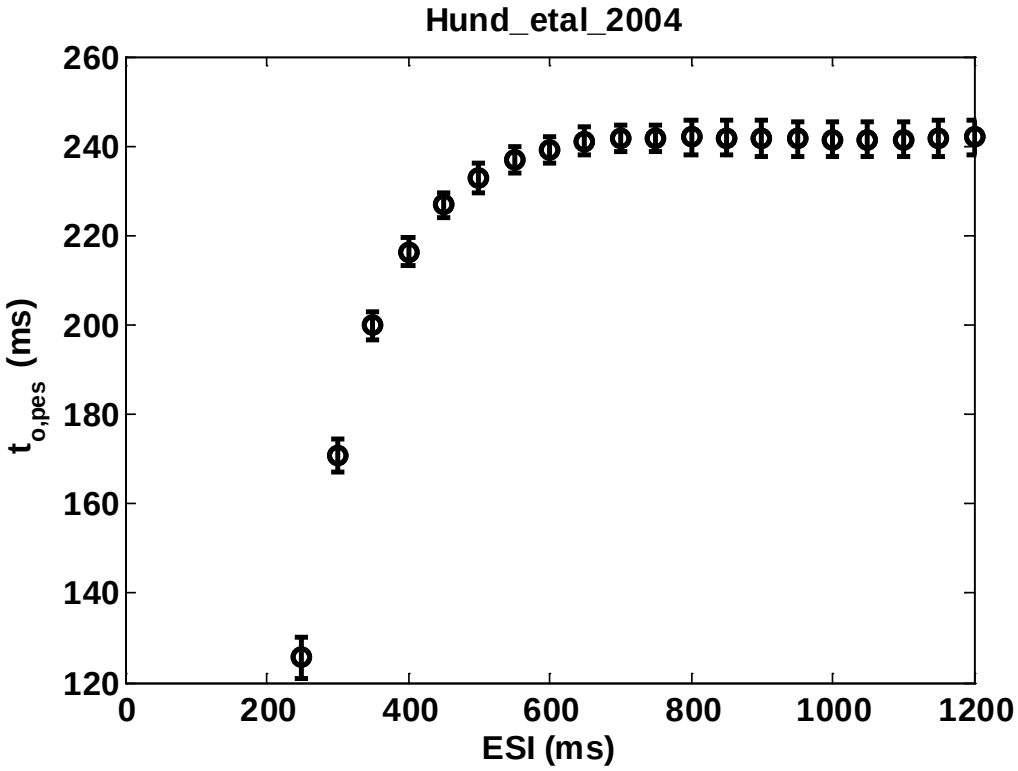
Hund_etal_2004
260
240
220
200
180
160
140
120
0
200
400
600
800
1000
1200
ESI (ms)
$t_{o,pes}$ (ms)

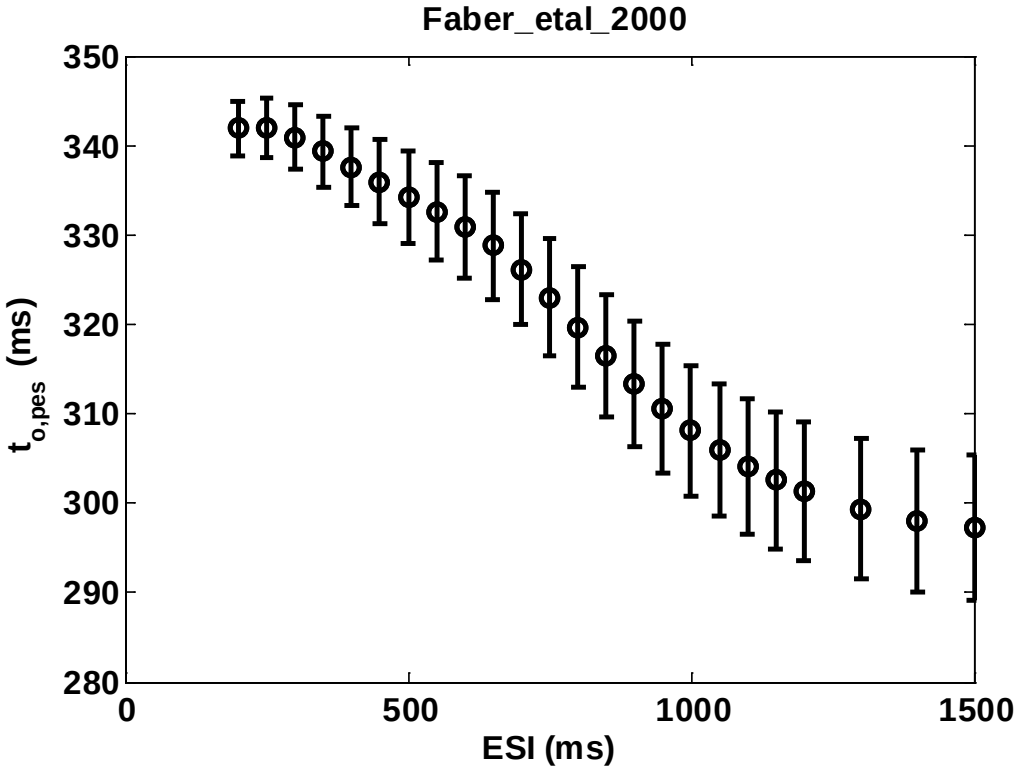
Faber_etal_2000
350
340
330
320
310
300
290
280
0
500
1000
1500
ESI (ms)
$t_{o,pes}$ (ms)

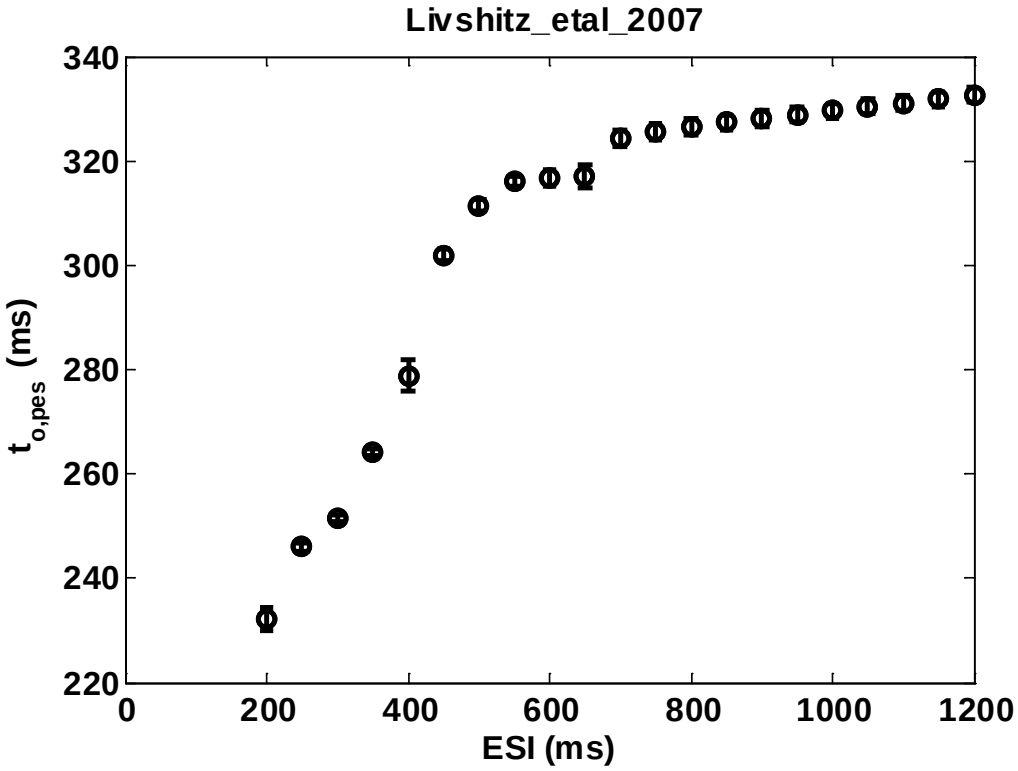
Livshitz_etal_2007
340
320
300
280
260
240
220
$t_{o,pes}$ (ms)
0
200
400
600
800
1000
1200
ESI (ms)

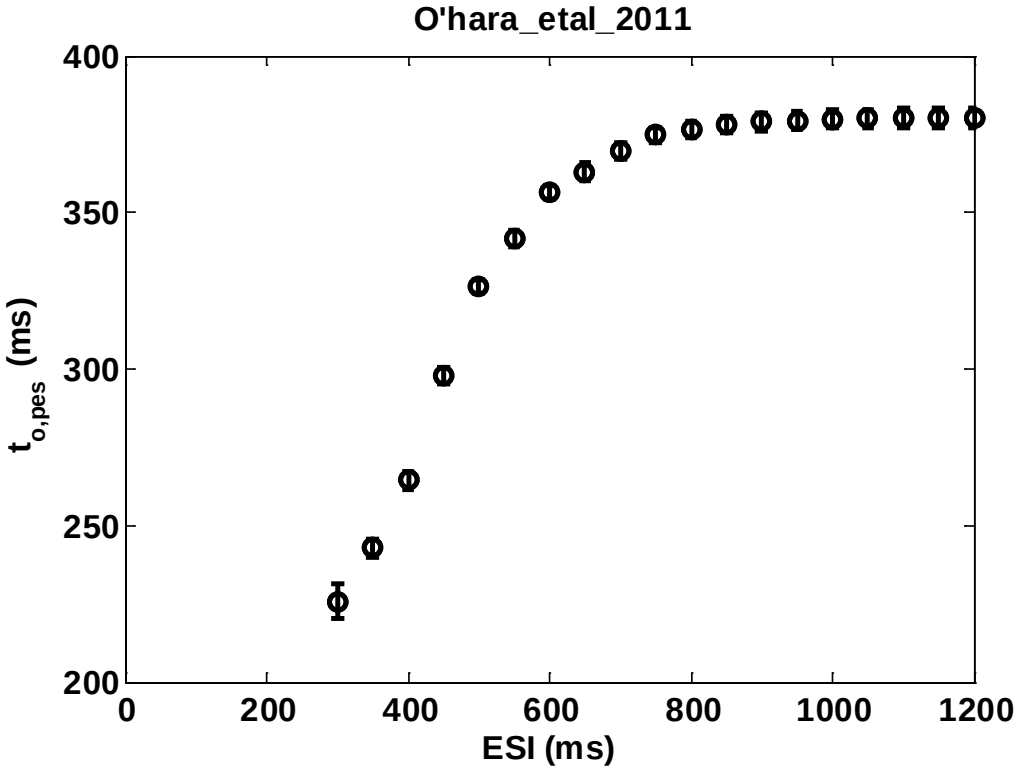
O'hara_etal_2011
400
350
300
250
200
$t_{o,pes}$ (ms)
0
200
400
600
800
1000
1200
ESI (ms)

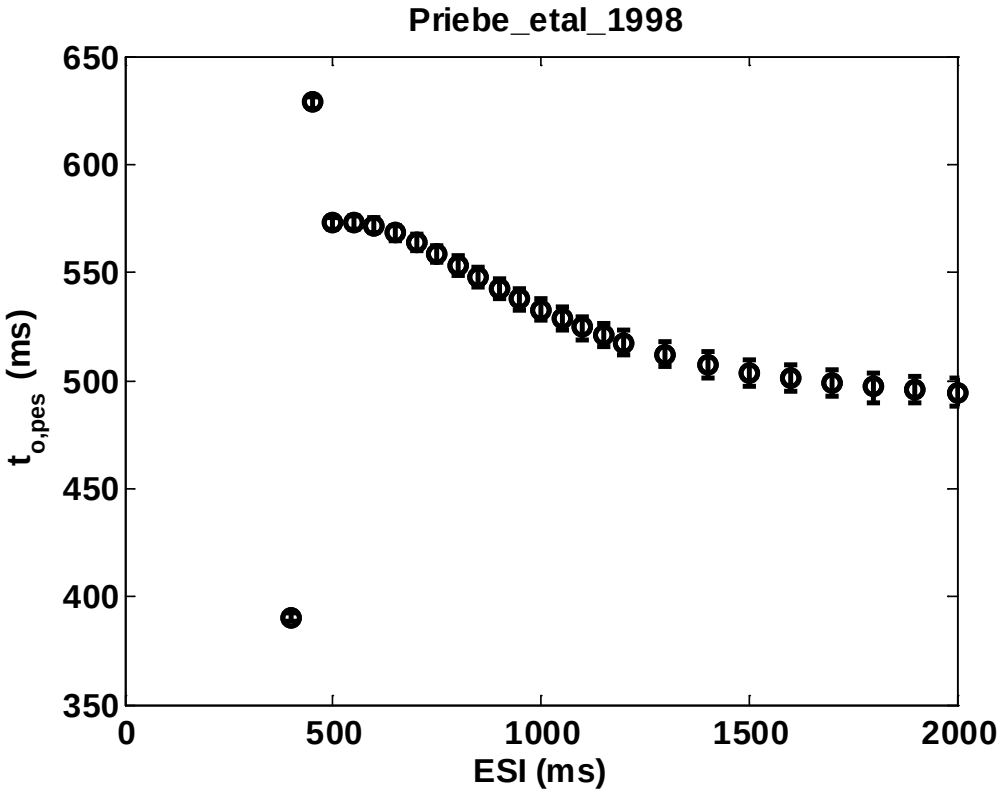
Priebe_etal_1998
650
600
550
500
450
400
350
0
500
1000
1500
2000
ESI (ms)
$t_{o,pes}$ (ms)

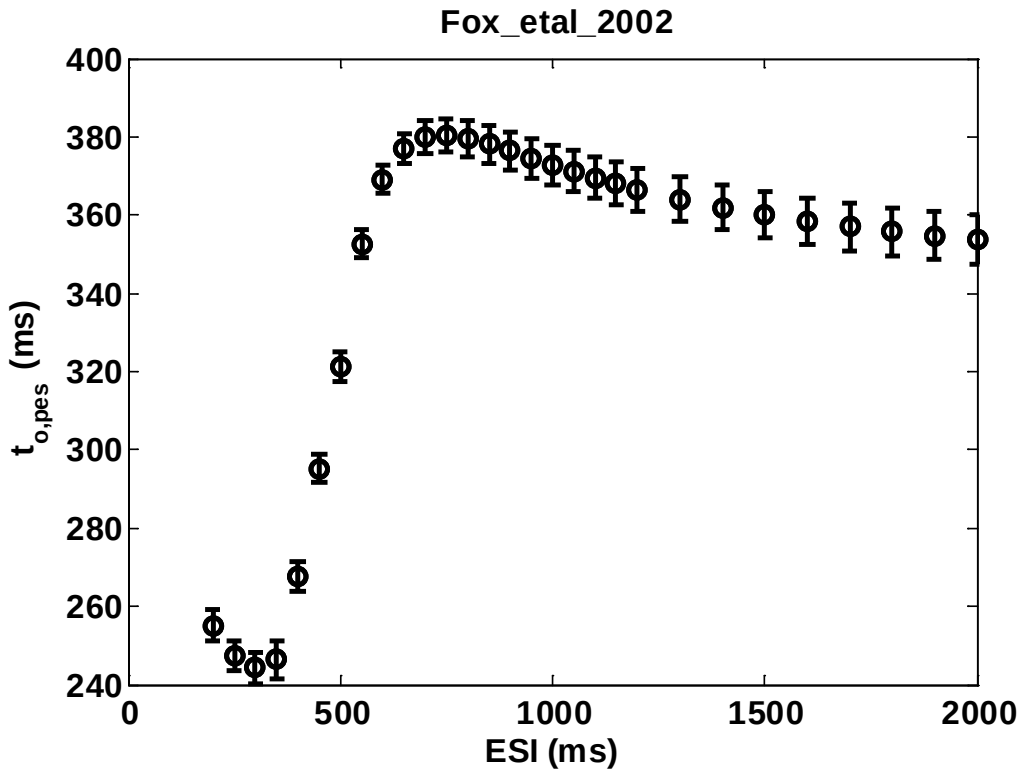
Fox_etal_2002
400
380
360
340
320
300
280
260
240
0
500
1000
1500
2000
ESI (ms)
$t_{o,pes}$ (ms)

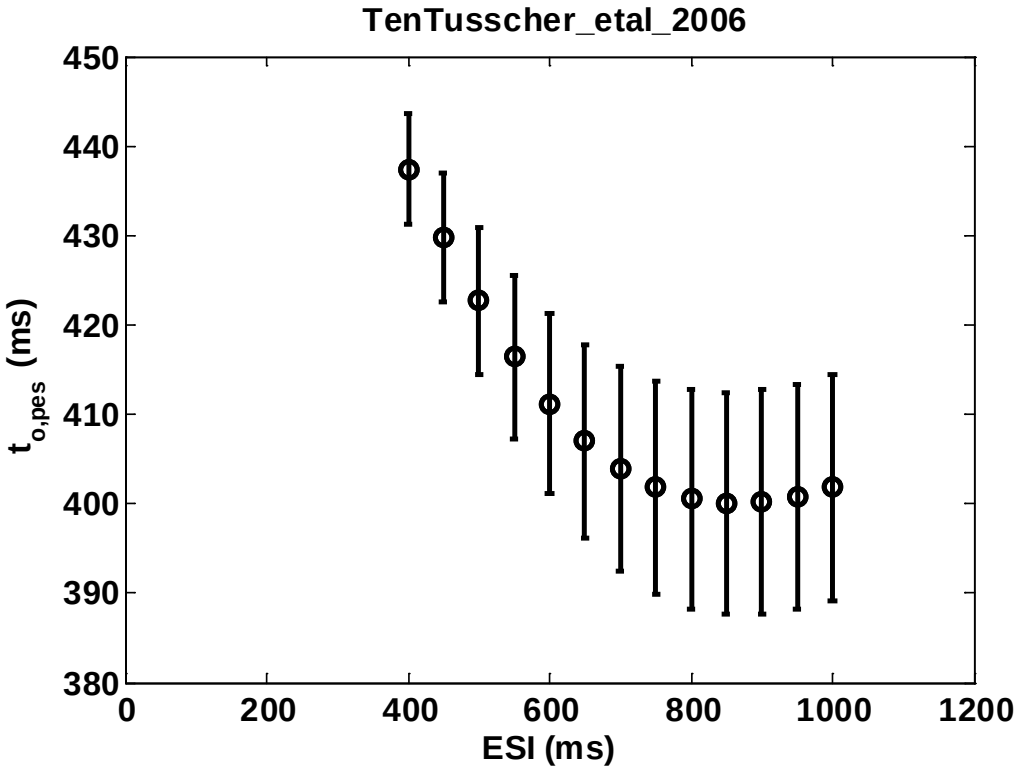
TenTusscher_etal_2006
450
440
430
420
410
400
390
380
$t_{o,pes}$ (ms)
0
200
400
600
800
1000
1200
ESI (ms)

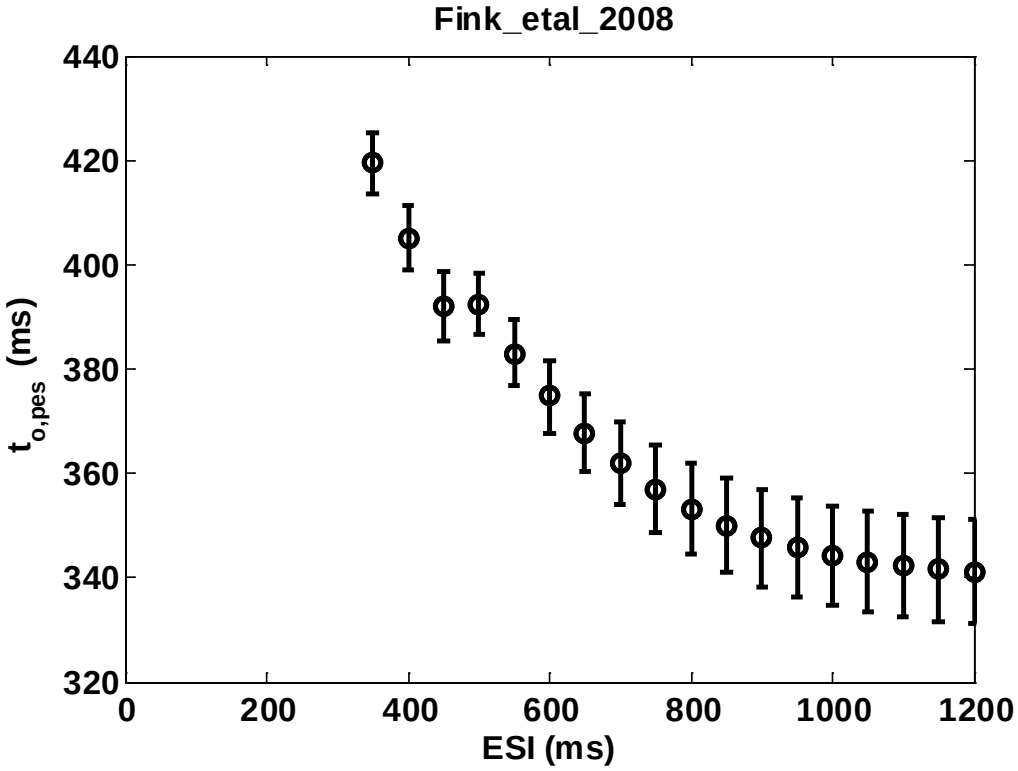
Fink_etal_2008
440
420
400
380
360
340
320
$t_{o,pes}$ (ms)
0
200
400
600
800
1000
1200
ESI (ms)

B.6 Time constant of MRC_{pes} curve ($T_{mrc,pes}$) for all models.

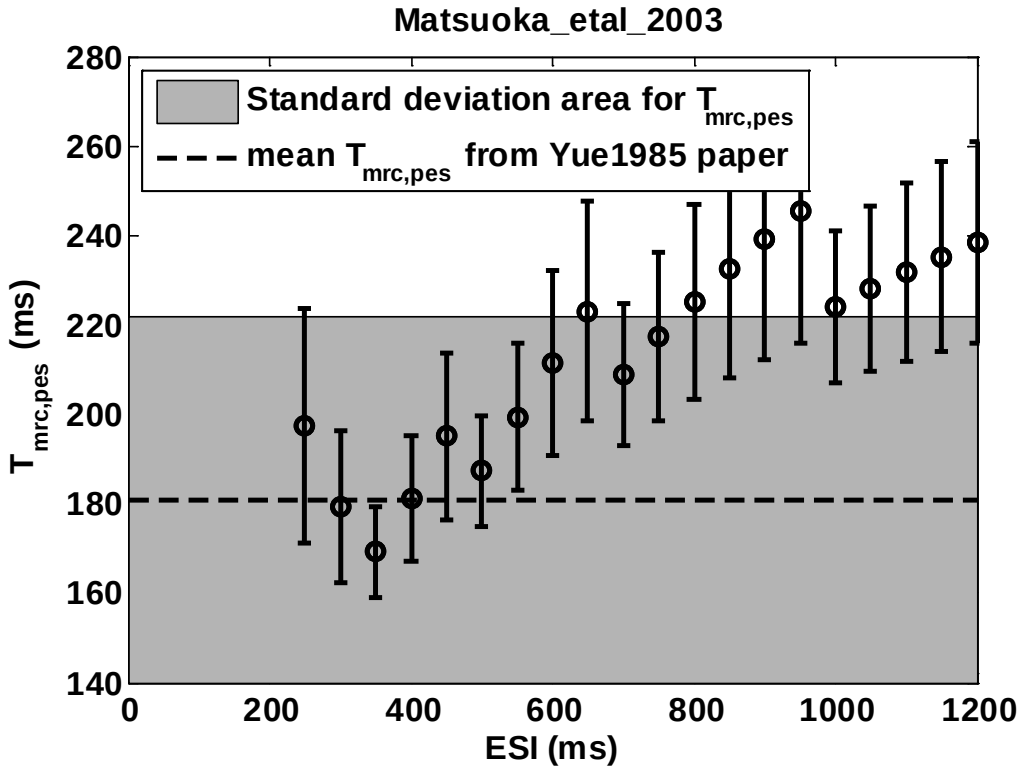
Matsuoka_etal_2003
Standard deviation area for T mrc,pes
mean T mrc,pes from Yue1985 paper
T mrc,pes (ms)
ESI (ms)
280
260
240
220
200
180
160
140
0
200
400
600
800
1000
1200

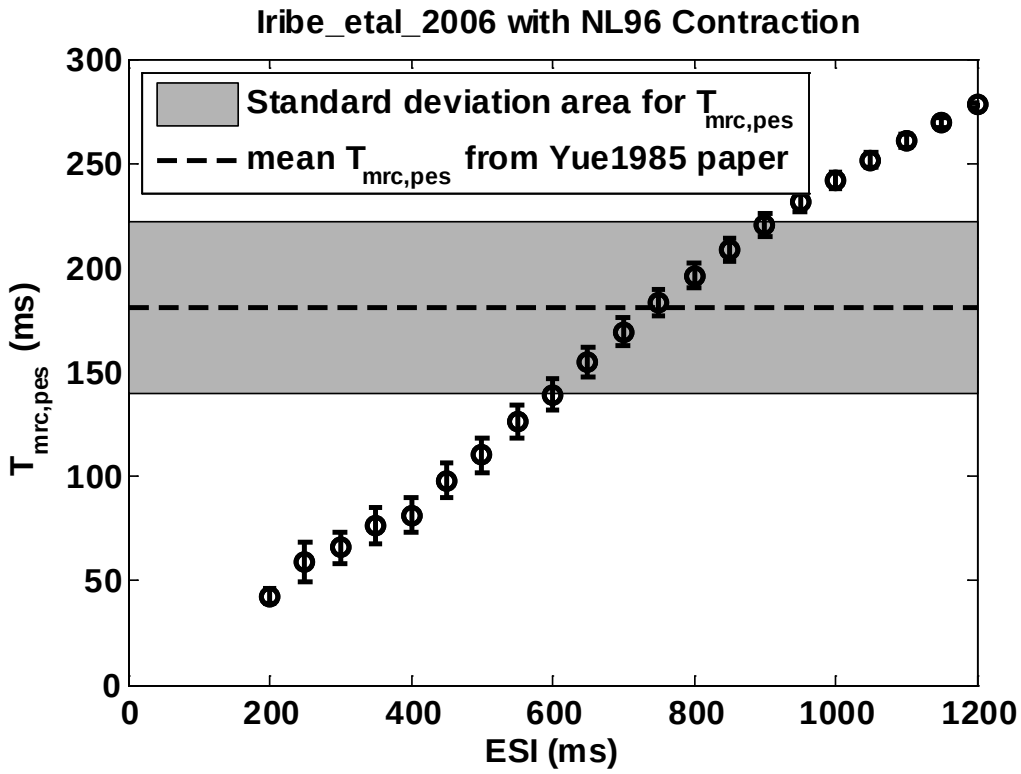
Iribe_etal_2006 with NL96 Contraction
Standard deviation area for T mrc,pes
mean T mrc,pes from Yue1985 paper
T mrc,pes (ms)
ESI (ms)
300
250
200
150
100
50
0
0
200
400
600
800
1000
1200

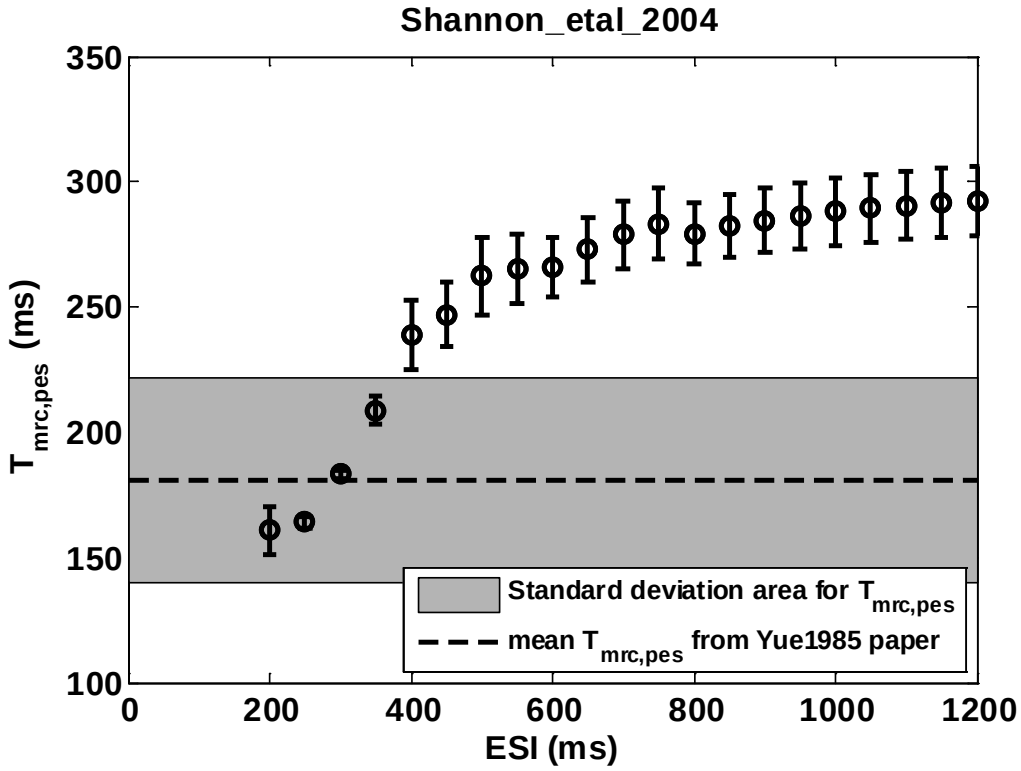
Shannon_etal_2004
350
300
250
200
150
100
0
200
400
600
800
1000
1200
T mrc,pes (ms)
ESI (ms)
Standard deviation area for T mrc,pes
mean T mrc,pes from Yue1985 paper

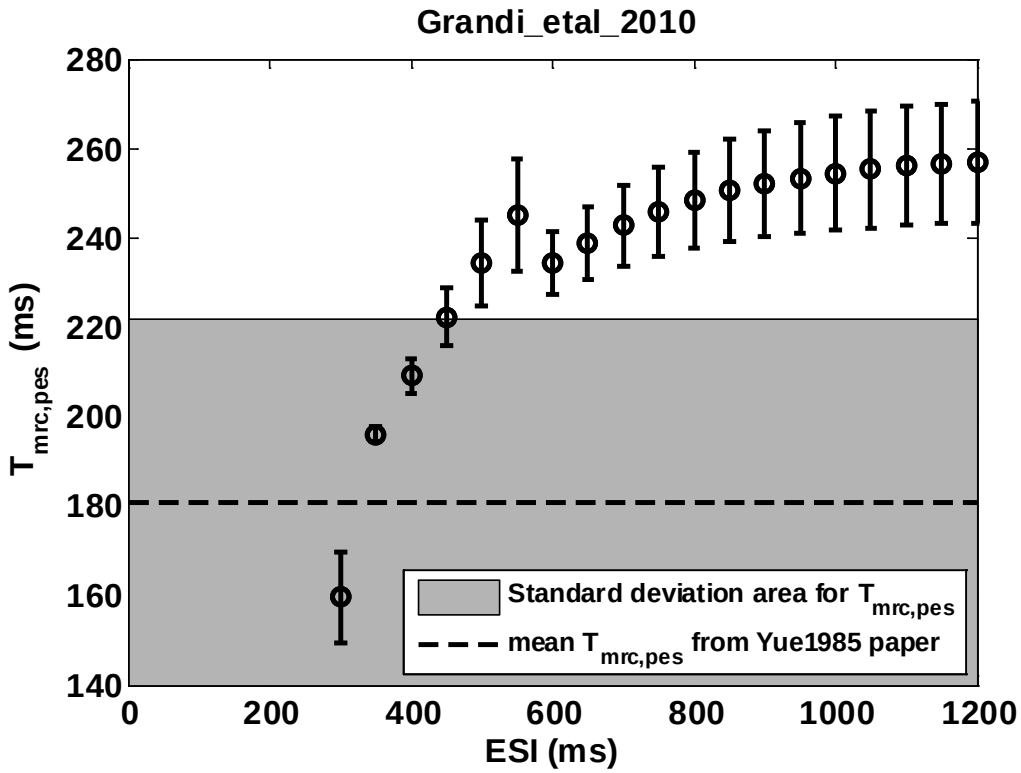
Grandi_etal_2010
280
260
240
220
200
180
160
140
0
200
400
600
800
1000
1200
T mrc,pes (ms)
ESI (ms)
Standard deviation area for T mrc,pes
mean T mrc,pes from Yue1985 paper

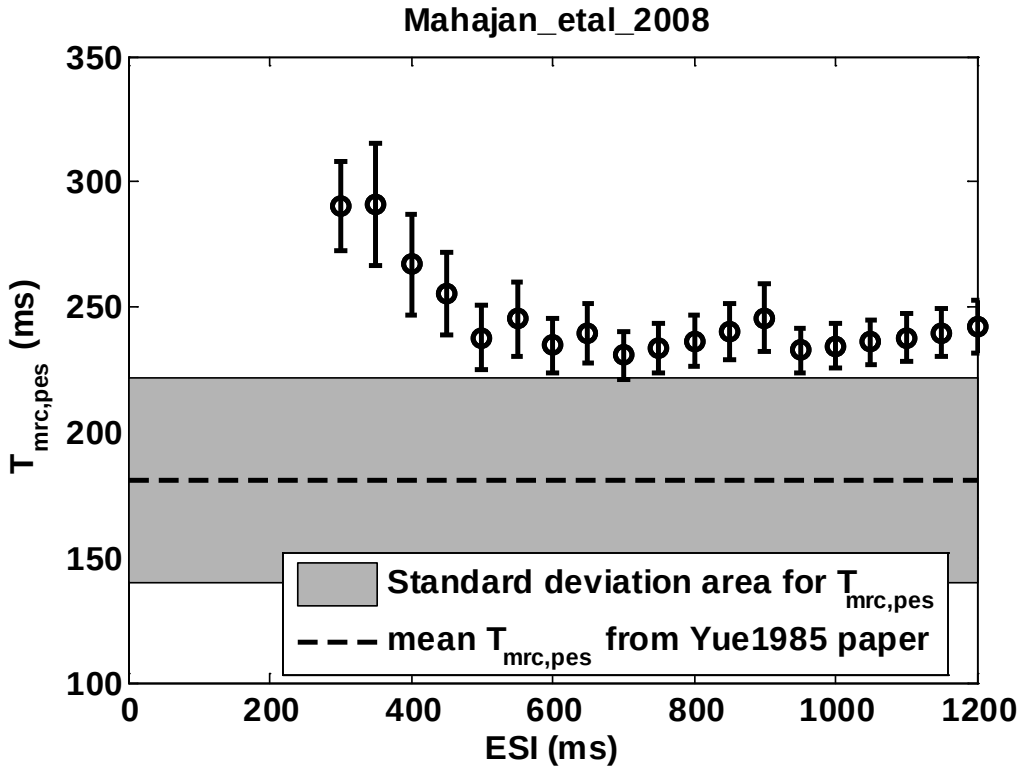
Mahajan_etal_2008
350
300
250
200
150
100
0
200
400
600
800
1000
1200
T mrc,pes (ms)
ESI (ms)
Standard deviation area for T mrc,pes
mean T mrc,pes from Yue1985 paper

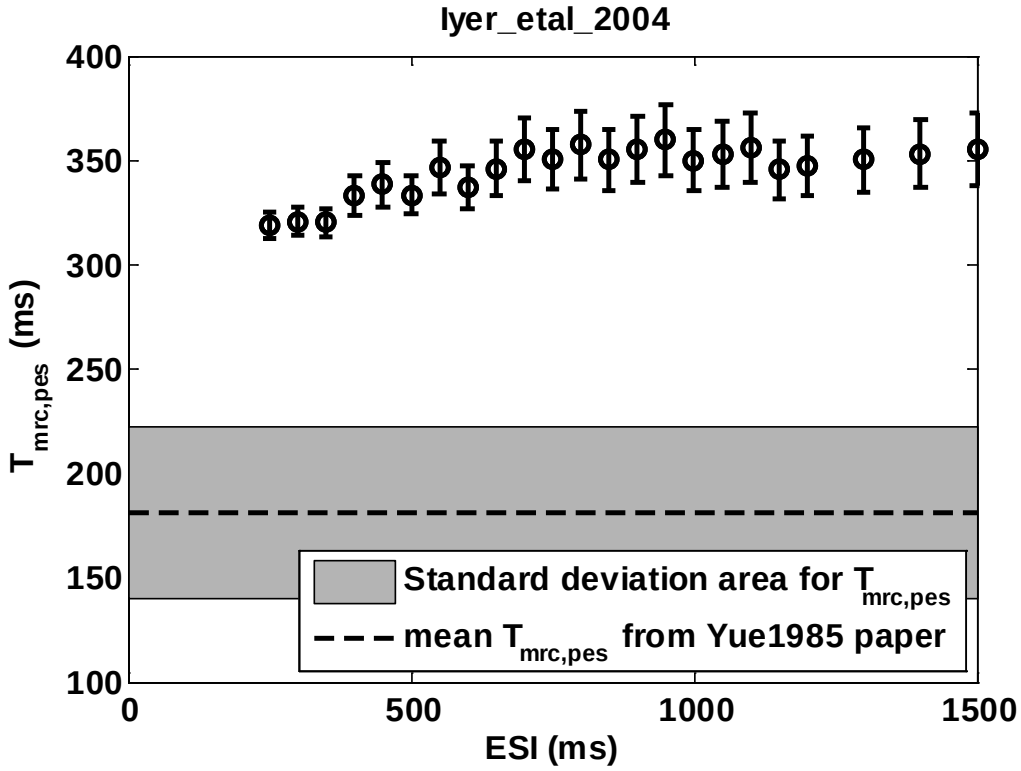
Iyer_etal_2004
400
350
300
250
200
150
100
0
500
1000
1500
T mrc,pes (ms)
ESI (ms)
Standard deviation area for T mrc,pes
mean T mrc,pes from Yue1985 paper

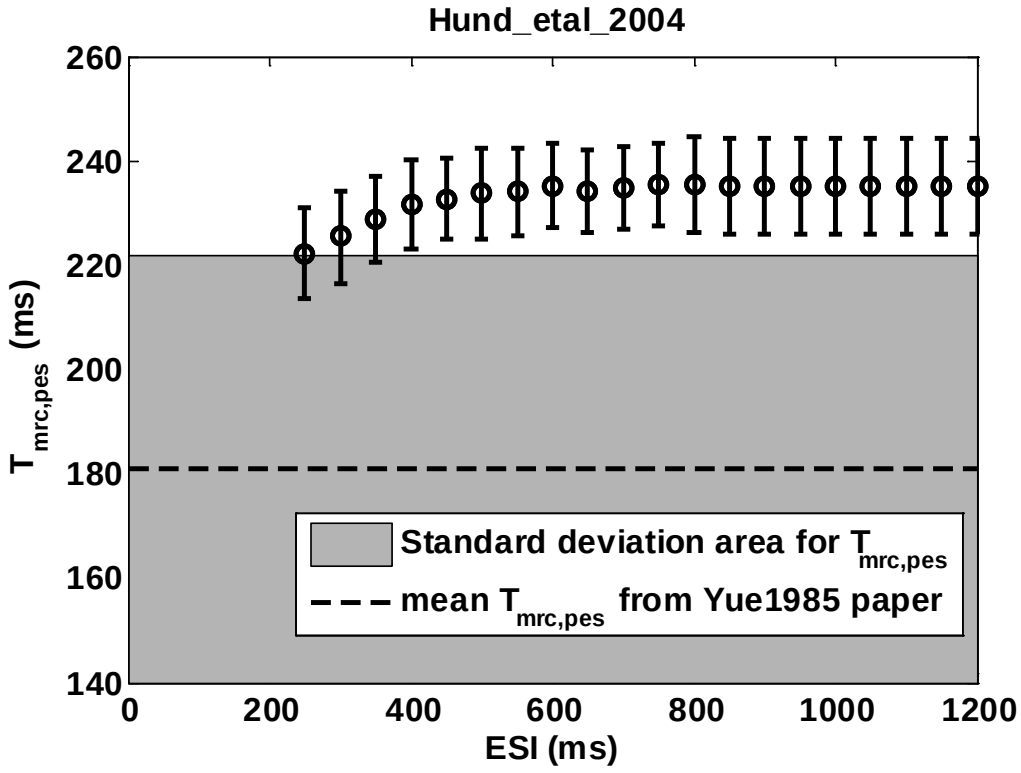
Hund_etal_2004
260
240
220
200
180
160
140
0
200
400
600
800
1000
1200
ESI (ms)
T mrc,pes (ms)
Standard deviation area for T mrc,pes
mean T mrc,pes from Yue1985 paper

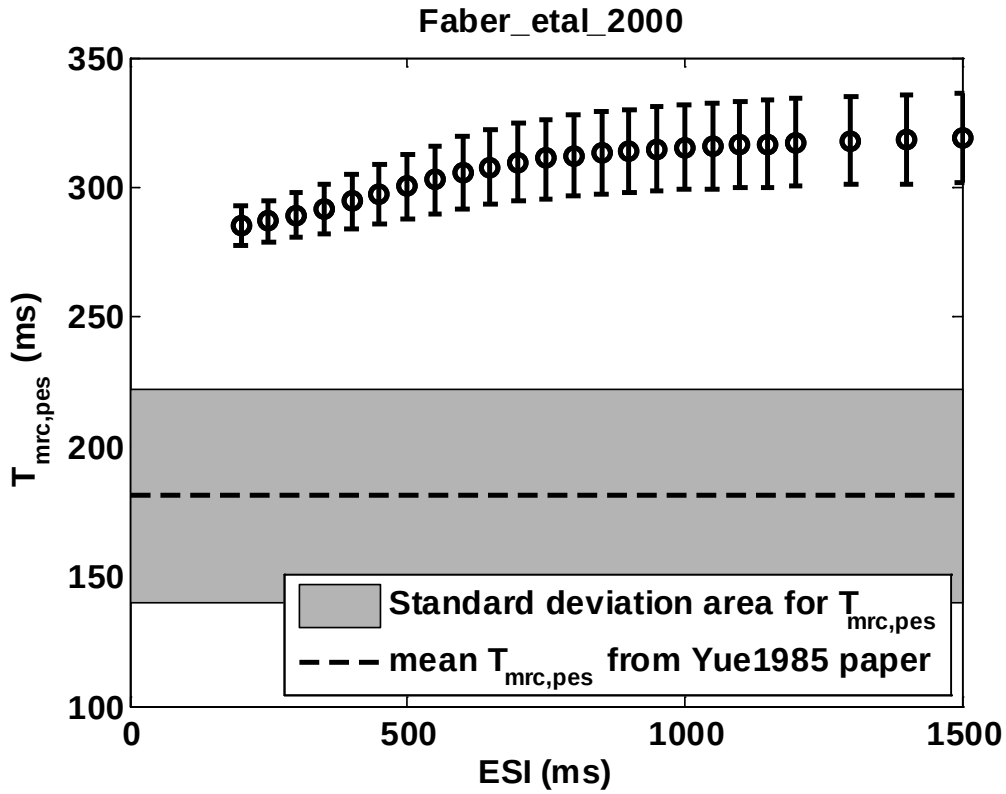
Faber_etal_2000
350
300
250
200
150
100
0
500
1000
1500
ESI (ms)
T mrc,pes (ms)
Standard deviation area for T mrc,pes
mean T mrc,pes from Yue1985 paper

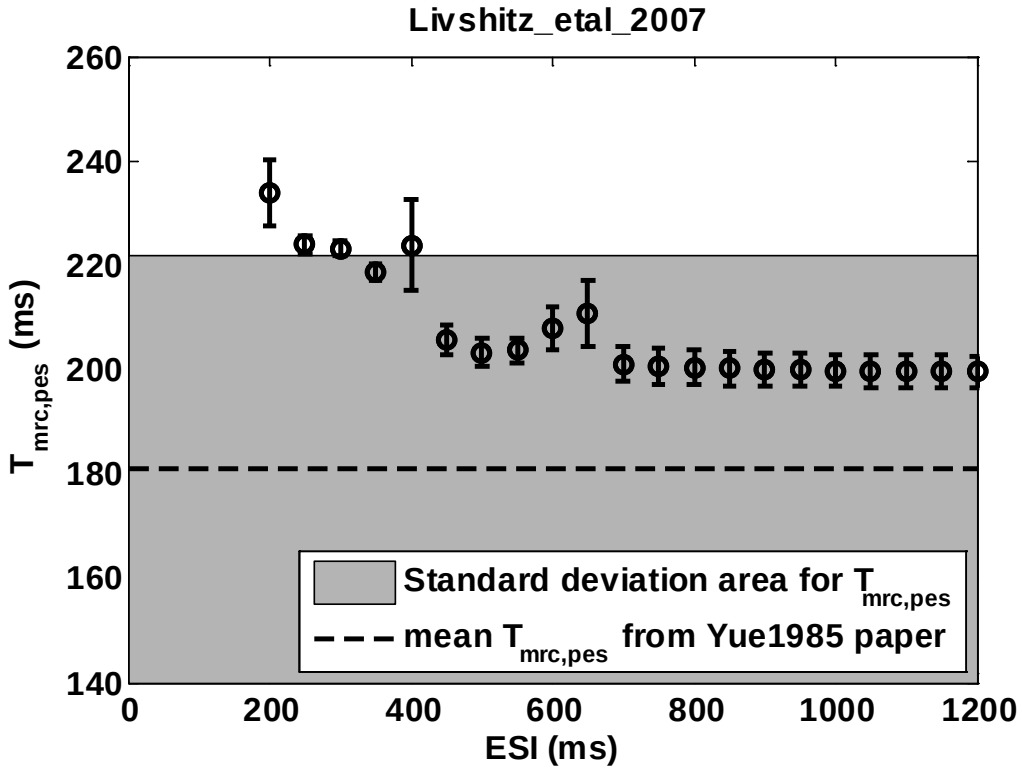
Livshitz_etal_2007
260
240
220
200
180
160
140
0
200
400
600
800
1000
1200
ESI (ms)
T mrc,pes (ms)
Standard deviation area for T mrc,pes
mean T mrc,pes from Yue1985 paper

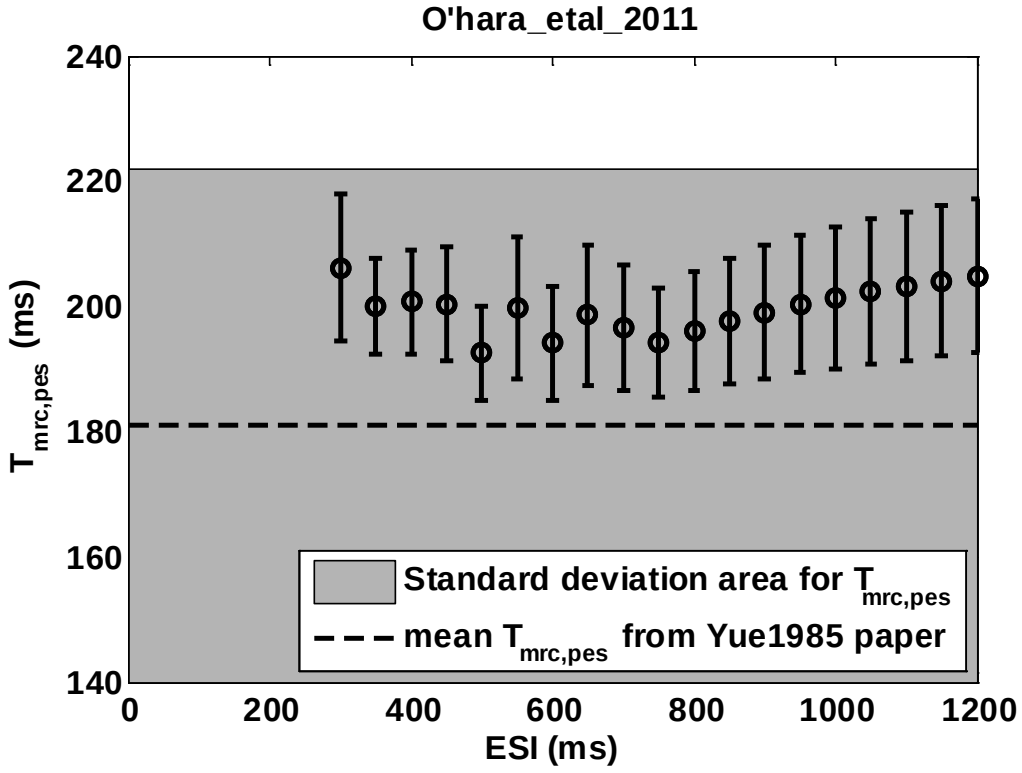
O'hara_etal_2011
240
220
200
180
160
140
0
200
400
600
800
1000
1200
ESI (ms)
T mrc,pes (ms)
Standard deviation area for T mrc,pes
mean T mrc,pes from Yue1985 paper

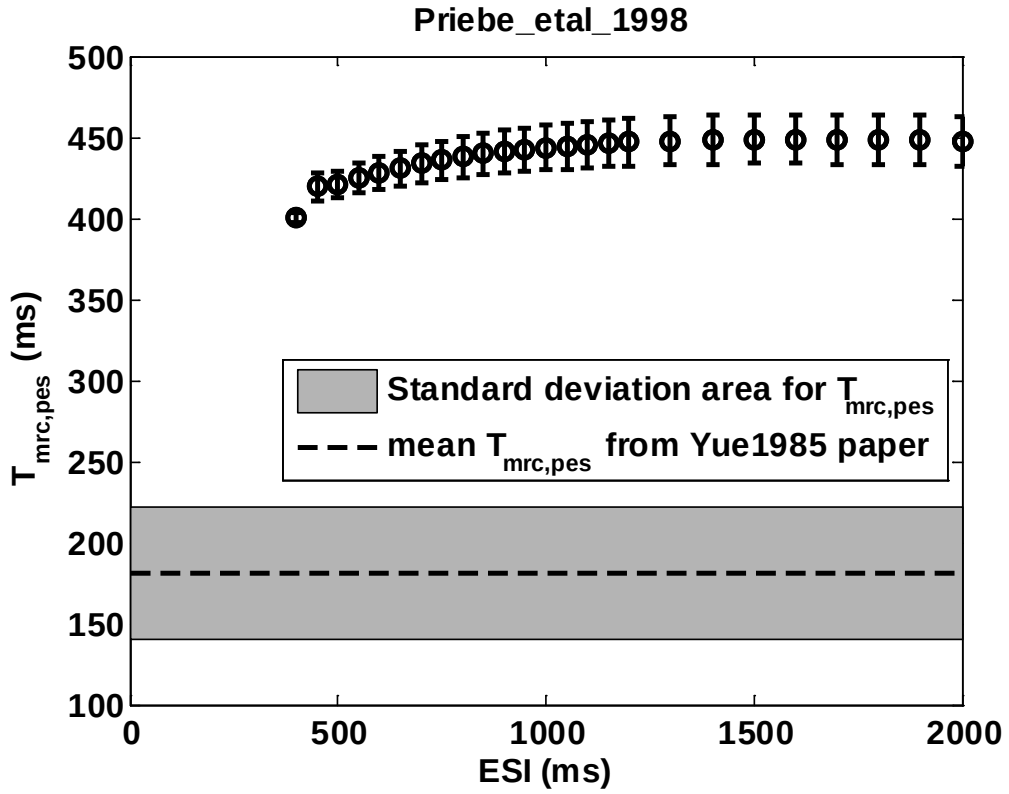
Priebe_etal_1998
500
450
400
350
300
250
200
150
100
0
500
1000
1500
2000
ESI (ms)
T mrc,pes (ms)
Standard deviation area for T mrc,pes
mean T mrc,pes from Yue1985 paper

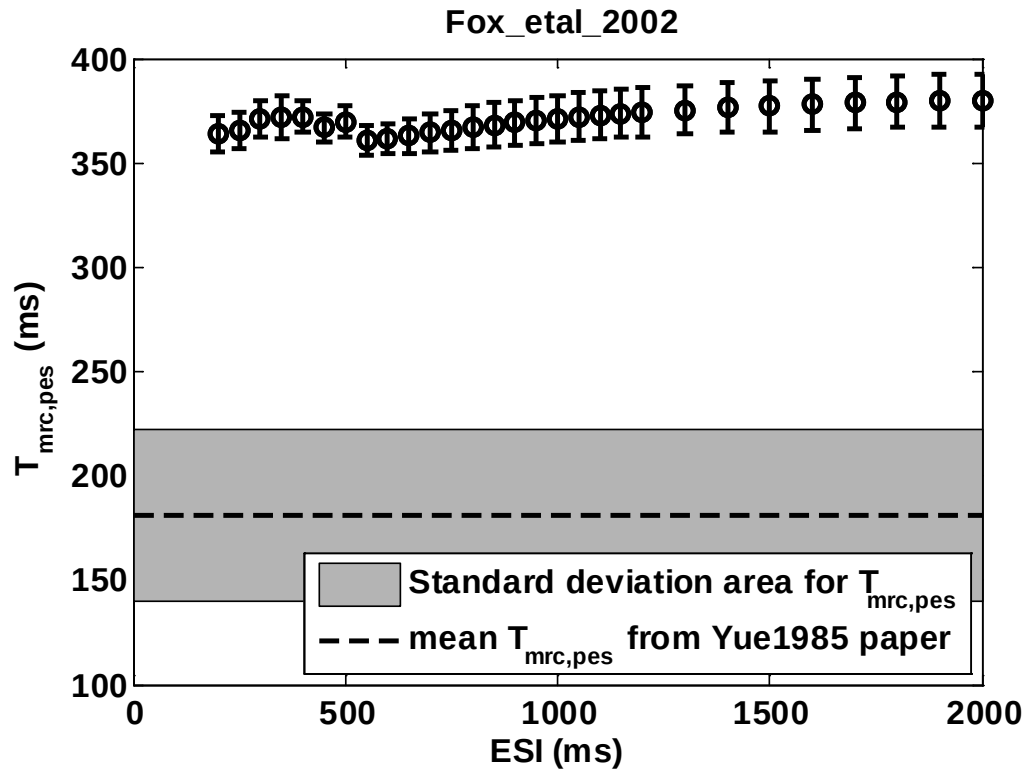
Fox_etal_2002
400
350
300
250
200
150
100
0
500
1000
1500
2000
ESI (ms)
T mrc,pes (ms)
Standard deviation area for T mrc,pes
mean T mrc,pes from Yue1985 paper

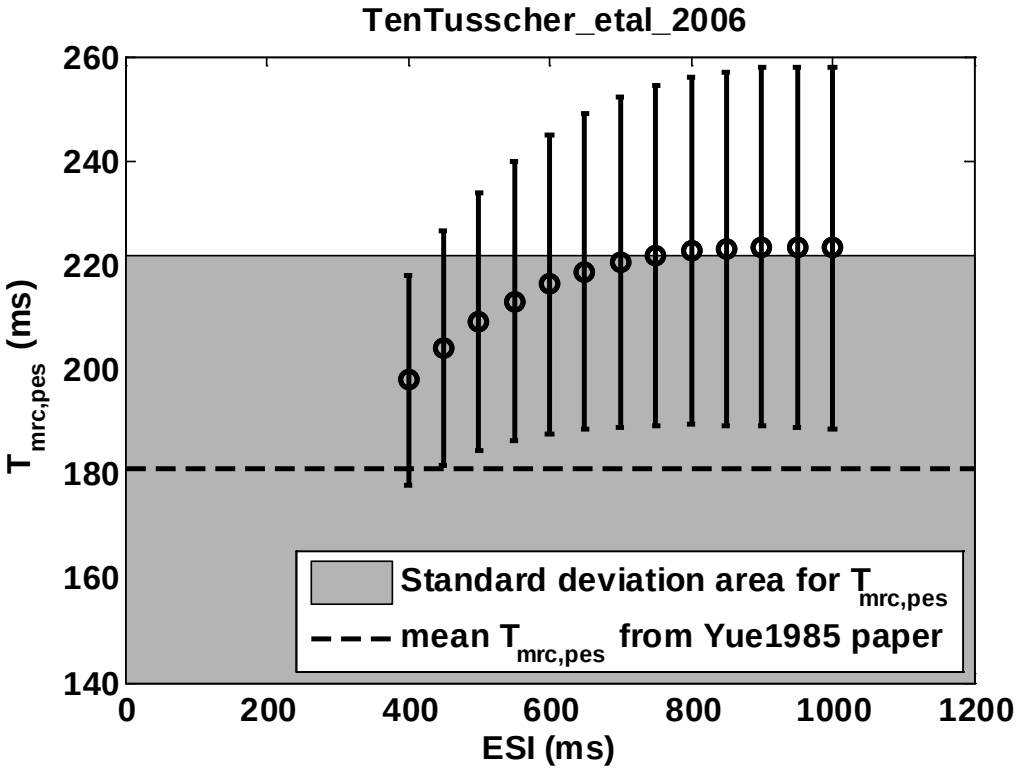
TenTusscher_etal_2006
260
240
220
200
180
160
140
0
200
400
600
800
1000
1200
ESI (ms)
T mrc,pes (ms)
Standard deviation area for T mrc,pes
mean T mrc,pes from Yue1985 paper

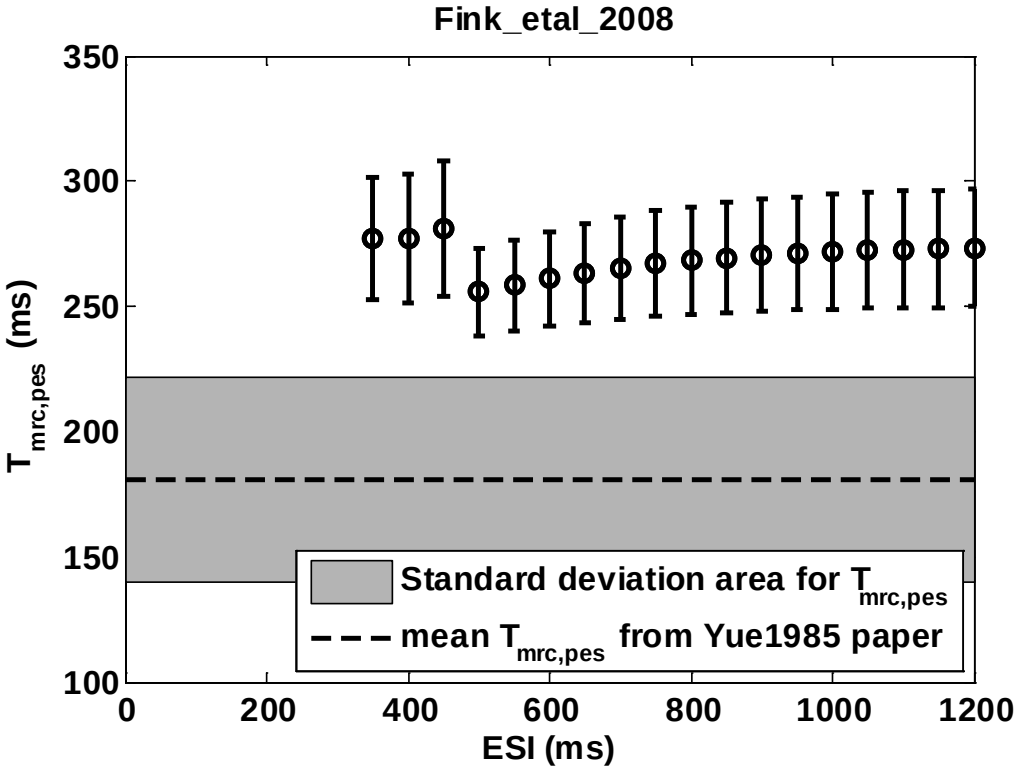
Fink_etal_2008
350
300
250
200
150
100
0
200
400
600
800
1000
1200
ESI (ms)
T mrc,pes (ms)
Standard deviation area for T mrc,pes
mean T mrc,pes from Yue1985 paper

APPENDIX C
COMPARISONS BETWEEN NL96 AND TWO OTHER CONTRACTION MODELS

C.1 Comparison between NL96 and RWH99

Since Iribe_etal_2006 has RWH99 in the original version, we compare the contraction dynamics between Iribe_etal_2006 with NL96 and with RWH99. Results of Iribe_etal_2006 with NL96 have been presented in previous figures while the results for Iribe_etal_2006 with RWH99 are in Fig. C.1. The two models show very similar characteristics except for two parameters: $t_{o,pes}$ and $T_{mrc,pes}$.

The PESI-axis interception $t_{o,pes}$ increases monotonically with respect to ESI for Iribe_etal_2006 with RWH99 while it is not monotonic for NL96, therefore MRC_{pes} curves cross each other at low PESI values. In addition, the $t_{o,pes}$ value range for NL96 is much lower than RWH99, whose value is closer to Yues experiment.

However, Iribe_etal_2006 with NL96 is more consistent with the experimental values of $T_{mrc,pes}$ compared to the corresponding RWH99 model. The deviation in $T_{mrc,pes}$ is smaller for NL96 and more data points fall into Yues mean$\pm$SD range than RWH99.

Therefore, under the isometric conditions, we observed no significant differences between NL96 and RWH99 under the scope of this study in the sense that each model matches some parameters with experiments better than the other in this study.

C.2 Comparison between NL96 and instantaneous NL96

Including NL96 contraction into EP models with instantaneous or no CaTRPN (Type Four and Five) changes the original Ca^{2+} shape. To provide evidence that the deformed Ca^{2+} transients are not the direct cause for the poor contraction behavior of this type of model,

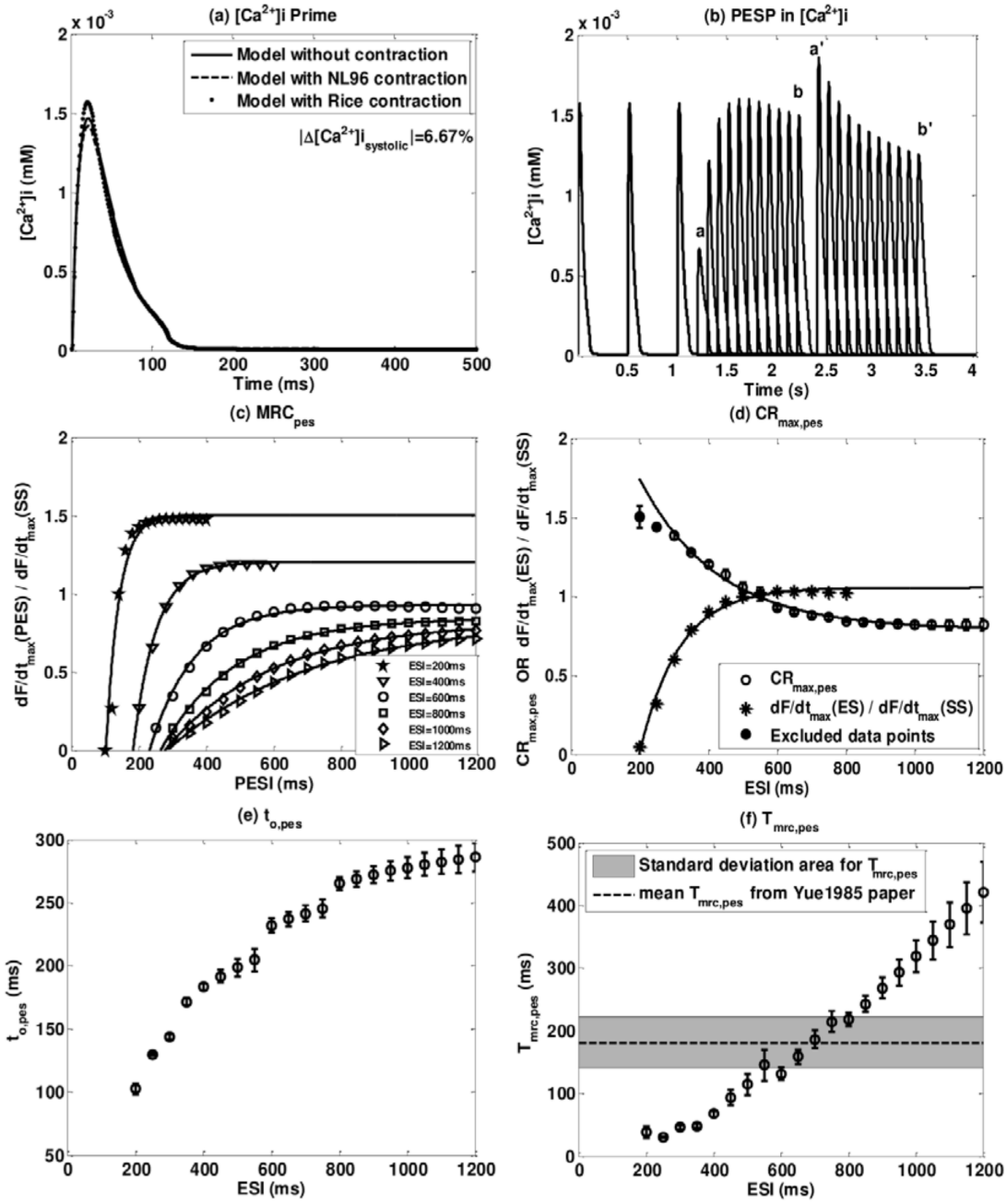

Figure C.1: Dynamics of the Iribe_etal_2006 with RWH99 contraction: (a) Priming ; (b) postextrasystolic potentiation in Ca^{2+}; (c) postextrasystolic mechanical restitution curves (MRC_{pes}); (d) postextrasystolic potnetiation curve (PESPC); (e) minimum-value axis intercept curve ($t_{o,pes}$); (f) Time constant for curve MRC_{pes} ($T_{mrc,pes}$).

we introduce the instantaneous NL96 contraction model by setting the dynamic equations in the NL96 model to be instantaneous, i.e. to set the right side of ODEs (Eq. 4.2) to be zero. In this way, all four states associated with the CaTRPN are instantaneous variables expressed by algebraic functions. Therefore we can easily incorporate them into EP models with instantaneous or no CaTRPN (Type Four and Five). Detailed steps are shown in A. In this models construction, the time delay between Ca^{2+} and the four states of troponin buffer disappears. Figure shows results after implementing the instantaneous NL96 into Ohara_etal_2011. They are similar to those of the Ohara_etal_2011 model with NL96 implemented except that MRC_{pes} and PESPC are shifted upward and $t_{o,pes}$ is shifted rightward due to the elevation of systolic $[Ca^{2+}]_i$. In a word, after the implementation of the instantaneous NL96, the Ca^{2+} transient is hardly altered from the original model yet the contraction results are still not consistent with Yues experiment in multiple parameters.

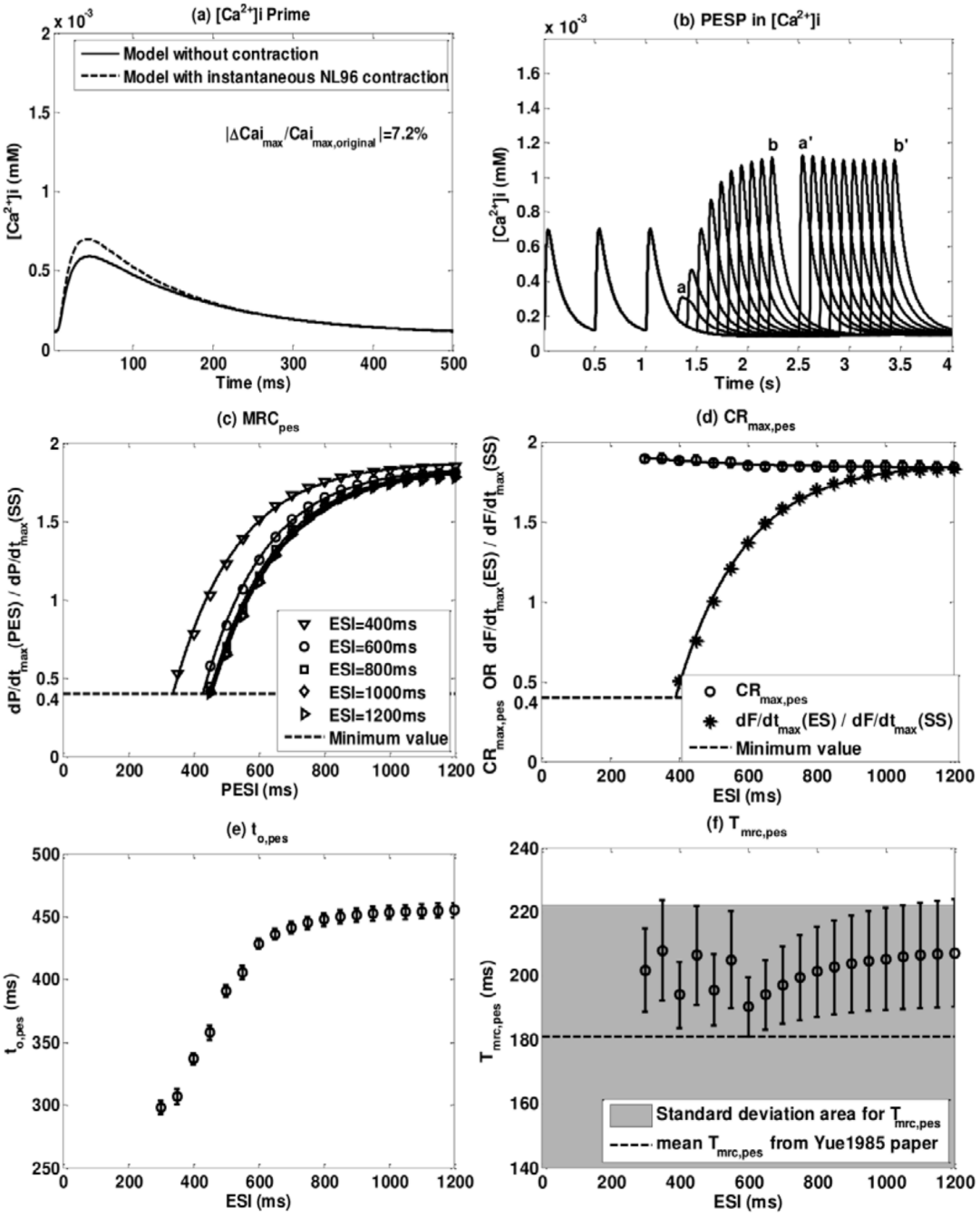

Figure C.2: Dynamics of the Ohara_etal_2011 with instantaneous NL96: (a) Priming Ca^{2+}; (b) postextrasystolic potentiation in Ca^{2+}; (c) postextrasystolic mechanical restitution curves (MRC_{pes}); (d) postextrasystolic potentiation curve (PESPC); (e) minimum-value axis intercept curve ($t_{o,pes}$); (f) Time constant for curve MRC_{pes} ($T_{mrc,pes}$)

APPENDIX D
VARYING PHYSIOLOGICAL PARAMETERS IN CONTRACTION IMPLEMENTATION

D.1 Pacing frequency

In our studies we used 500ms as the priming pacing cycle length for all the models for two reasons. First, its close to the pacing period in Yues experiment [], with which we compared our simulation results. Second, we wanted to compare all the models uniformly with one prime period (PP) and 500ms is close to the physiological heart rate of dogs and its between that of guinea pigs and humans. Nevertheless, to check and verify the validation of our results at 500 ms, we performed additional simulations on the Grandi_etal_2010 (human) model using 850ms as the priming period. Figure D.1 compares the MRC_{pes}, PESPC, $t_{o,pes}$, $T_{mrc,pes}$ and the PESP in Ca^{2+} of the Grandi_etal_2010 model when using a pp=500ms (left panels) and 850ms (right panels). The Grandi_etal_2010 model shows qualitatively similar behaviors for 850ms comparing with 500ms and the difference in the amplitude of MRC_{pes} and PESPC is directly related to the change in the normalization. Therefore we believe that our results using uniform priming period of 500 ms for all models is a good compromise and does not change quantitatively the PESP behaviors when comparing with physiological pacing cycle length for different species.

(a)

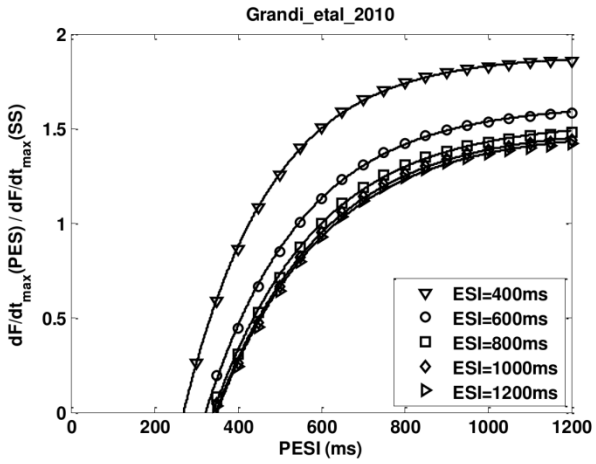
Grandi_etal_2010
dF/dt_max(PES) / dF/dt_max(SS)
PESI (ms)
ESI=400ms
ESI=600ms
ESI=800ms
ESI=1000ms
ESI=1200ms

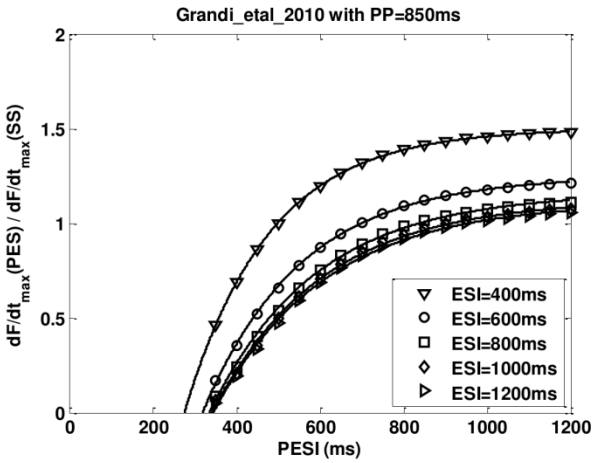
Grandi_etal_2010 with PP=850ms
dF/dt_max(PES) / dF/dt_max(SS)
PESI (ms)
ESI=400ms
ESI=600ms
ESI=800ms
ESI=1000ms
ESI=1200ms

(b)

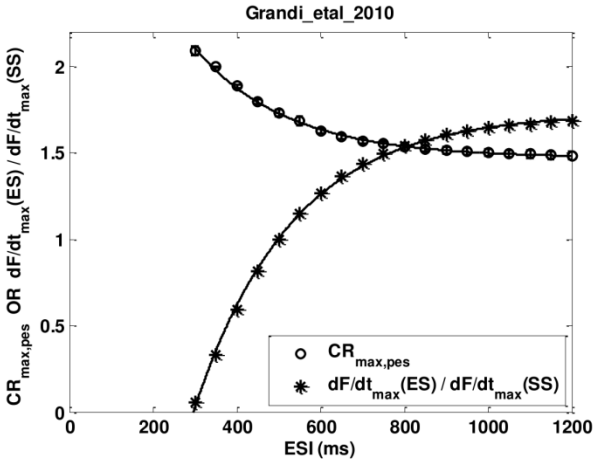
Grandi_etal_2010
CR_max,pes OR dF/dt_max(ES) / dF/dt_max(SS)
ESI (ms)
CR_max,pes
dF/dt_max(ES) / dF/dt_max(SS)

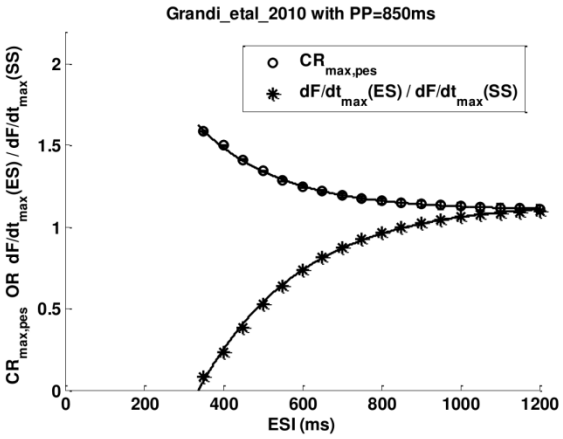
Grandi_etal_2010 with PP=850ms
CR_max,pes OR dF/dt_max(ES) / dF/dt_max(SS)
ESI (ms)
CR_max,pes
dF/dt_max(ES) / dF/dt_max(SS)

(c)

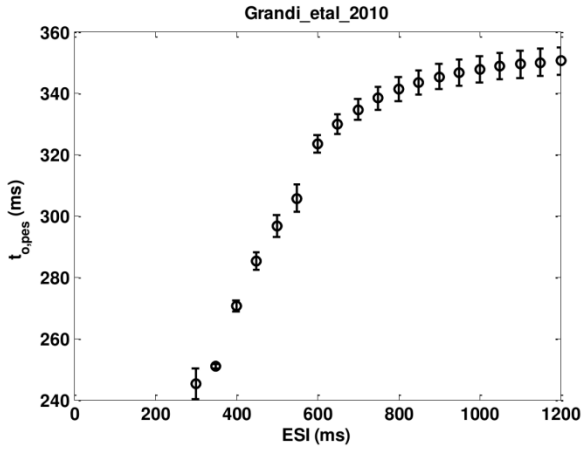
Grandi_etal_2010
t_o,pes (ms)
ESI (ms)

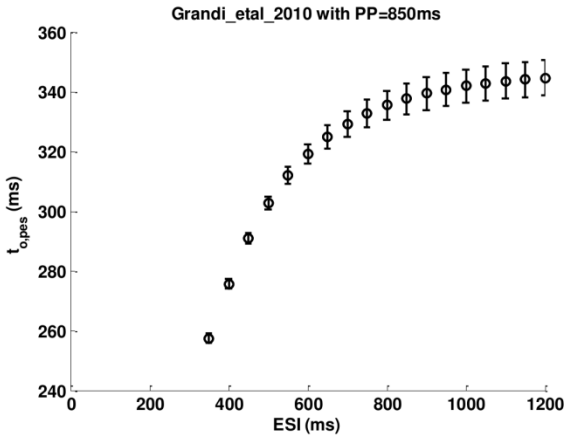
Grandi_etal_2010 with PP=850ms
t_o,pes (ms)
ESI (ms)

(d)

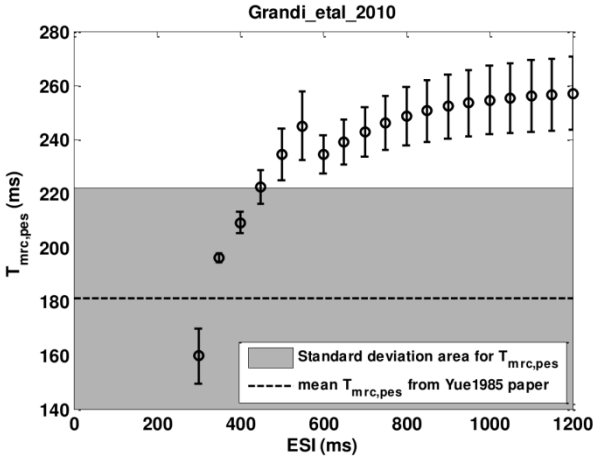
Grandi_etal_2010
$T_{mrc,pes}$ (ms)
ESI (ms)
Standard deviation area for $T_{mrc,pes}$
mean $T_{mrc,pes}$ from Yue1985 paper

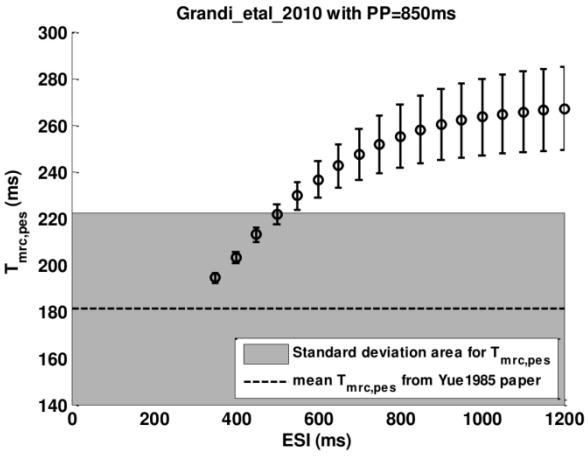
Grandi_etal_2010 with PP=850ms
$T_{mrc,pes}$ (ms)
ESI (ms)
Standard deviation area for $T_{mrc,pes}$
mean $T_{mrc,pes}$ from Yue1985 paper

(e)

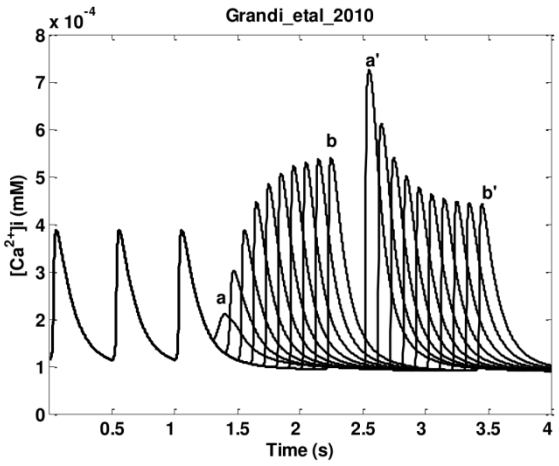
Grandi_etal_2010
x 10^-4
$[Ca^{2+}]i$ (mM)
Time (s)
a
b
a'
b'

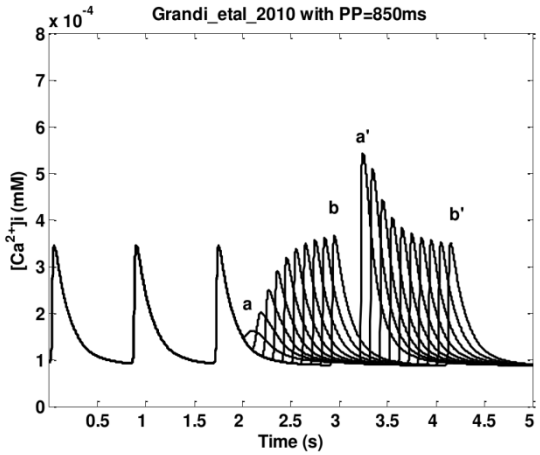
Grandi_etal_2010 with PP=850ms
x 10^-4
$[Ca^{2+}]i$ (mM)
Time (s)
a
b
a'
b'

D.2 Temperature

It has been shown that changes in temperature can produce large effects in the dynamics of cardiac tissue [153, 154, 155, 156]. Because we are combining a room temperature contraction model (NL96) with body temperature (37C) EP models, we wanted to investigate how temperature could influence our results. For this we reversed the approach of Matusoka_etal_2003, where they modified the NL96 to physiological temperatures by multiplying the rate constants (Y_2, Z_2, Y_4, Y_d) by three [76]. We proceeded to change the rate constants in Matsuoka_etal_2003 back to the original values in NL96 and compare their dynamics. Figure D.2 shows MRC_{pes}, PESPC, $t_{o,pes}$, $T_{mrc,pes}$ and the PESP in Ca^{2+} for the Matsuoka_etal_2003 model with physiological temperature (left panels) and with room temperature (right panels). We observed that changing the rate constants back to room temperature values did not change any of the four contraction characteristic curves or the Ca^{2+}. This shows that combining room temperature NL96 contraction to body temperature EP models should not affect the results obtained in this study. However it is important to notice that most cell models do not produce large changes when temperatures are modified [157] and thus models need to be tuned to experimental data [155, 156].

(a)

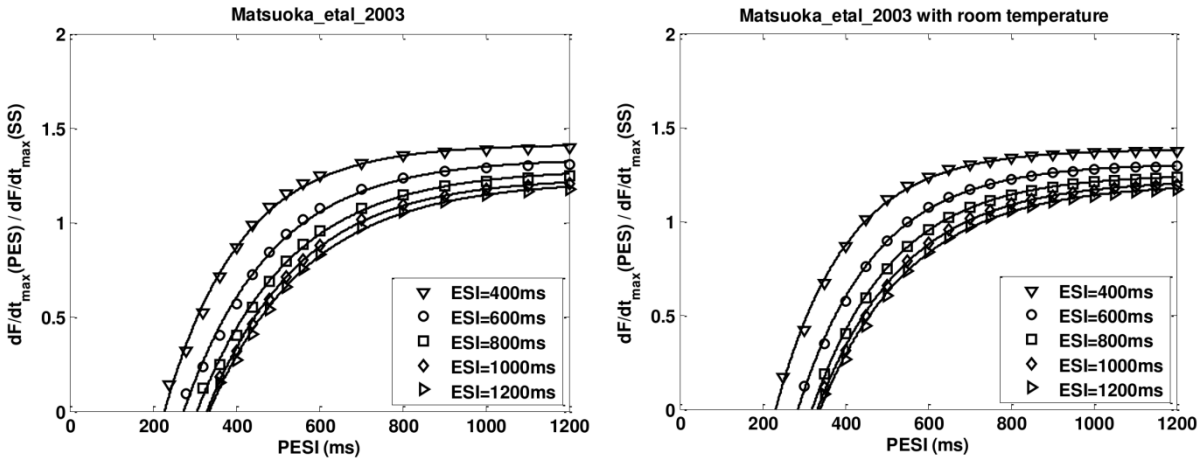
Matsuoka_etal_2003
Matsuoka_etal_2003 with room temperature
dF/dt_max(PES) / dF/dt_max(SS)
PESI (ms)
ESI=400ms
ESI=600ms
ESI=800ms
ESI=1000ms
ESI=1200ms

(b)

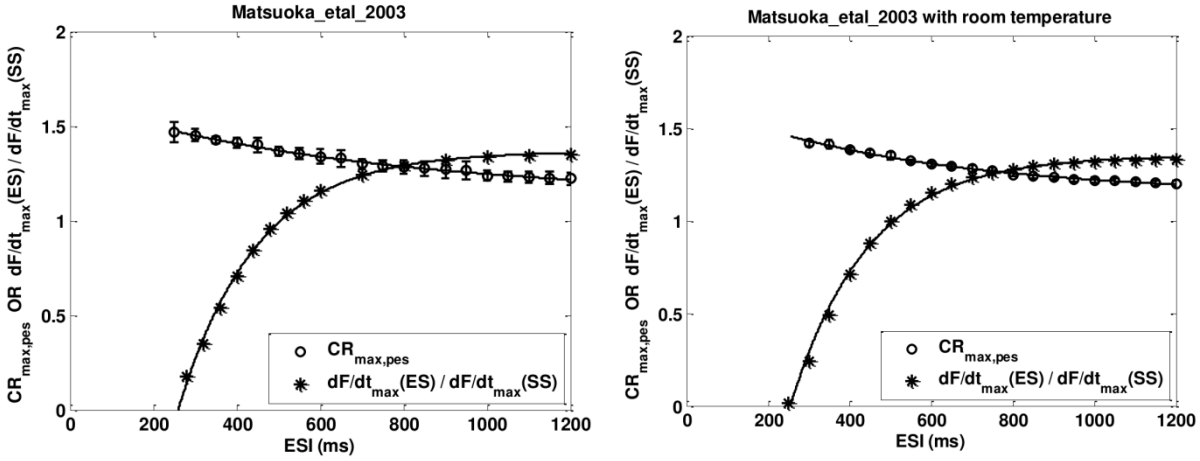
Matsuoka_etal_2003
Matsuoka_etal_2003 with room temperature
CR_max,pes OR dF/dt_max(ES) / dF/dt_max(SS)
ESI (ms)
CR_max,pes
dF/dt_max(ES) / dF/dt_max(SS)

(c)

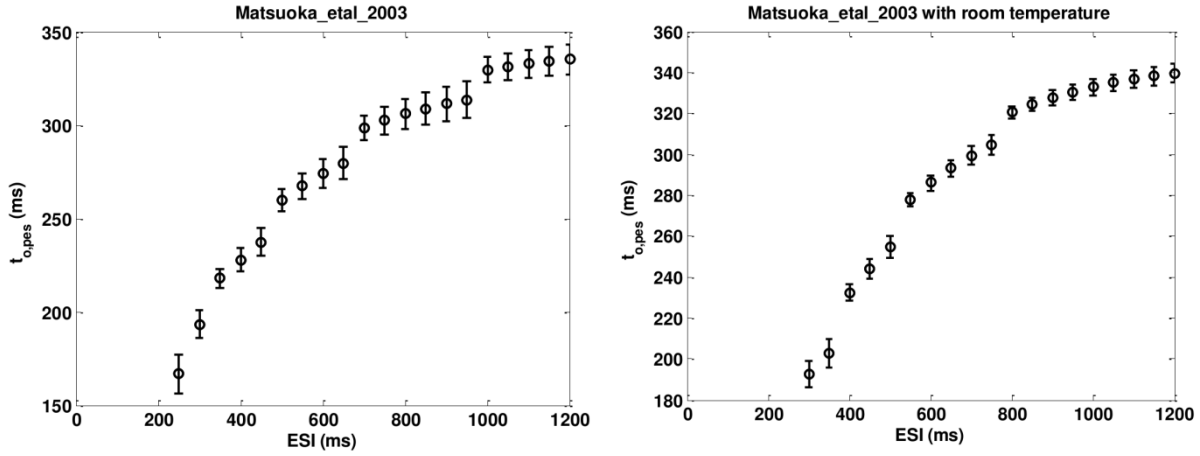
Matsuoka_etal_2003
Matsuoka_etal_2003 with room temperature
t_o,pes (ms)
ESI (ms)

(d)

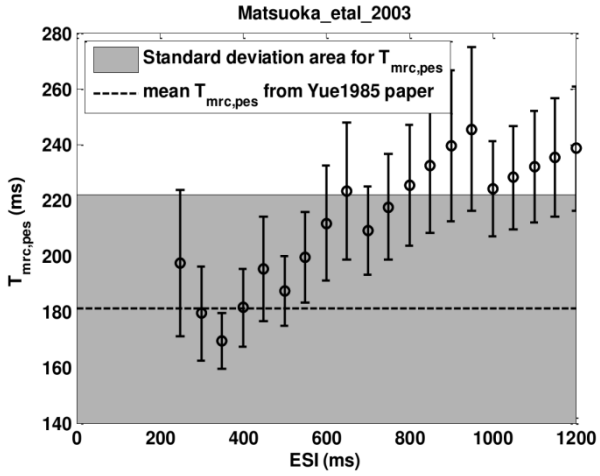
Matsuoka_etal_2003
Standard deviation area for T mrc,pes
----- mean T mrc,pes from Yue1985 paper
T mrc,pes (ms)
ESI (ms)

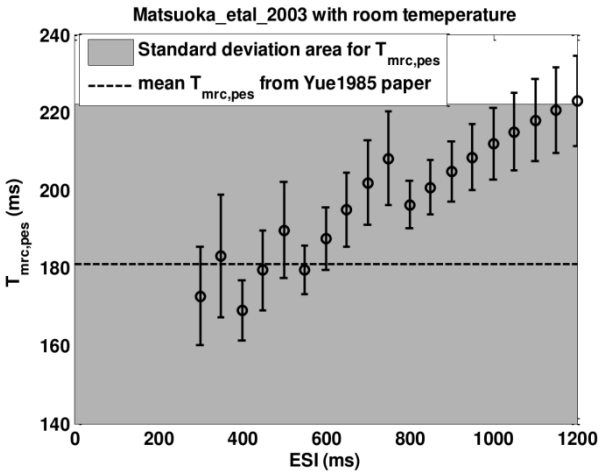
Matsuoka_etal_2003 with room temeperature
Standard deviation area for T mrc,pes
----- mean T mrc,pes from Yue1985 paper
T mrc,pes (ms)
ESI (ms)

(e)

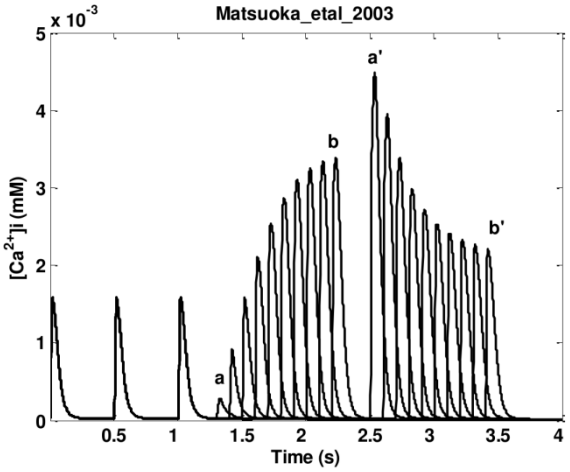
x 10-3
Matsuoka_etal_2003
a
b
a'
b'
[Ca2+]i (mM)
Time (s)

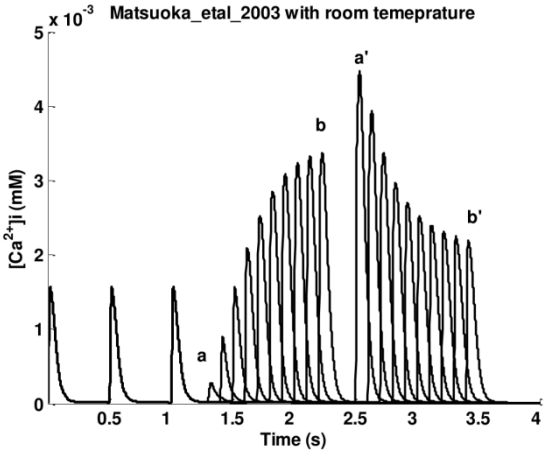
x 10-3
Matsuoka_etal_2003 with room temeprature
a
b
a'
b'
[Ca2+]i (mM)
Time (s)

D.3 Cooperativity

The NL96 has limited cooperativity as the Hill coefficient used in simulations is 1.3 which is lower than reported in experiments (between 2 and 6) [158, 159]. Negroni and Lascano published a newer version of their contraction model NL08 [160], with two major changes. First they used a troponin system (TS), which consists of three adjacent troponin-tropomyosin regulatory units as the basic unit; second, the cross-bridges have two possible conformations: strong and weak, which results in six total states for the troponin system instead of four. The newer model could reproduce better cooperative effect required for force- relationships and force response to length steps. The Hill coefficient is calculated to be from 4.15 to 4.00, corresponding to L=0.9 to 1.1m [160]. To investigate the influence of the Hill coefficient, we implemented NL08 into Matsuoka_etal_2003 and compared it with the original Matsuoka model (with NL06). Results are shown in Fig. D.3. We found no notable difference in the four contractile characteristic curves. The postextrasystolic potentiation in Ca^{2+} is also retained except for the reduced maximum value of $[Ca^{2+}]_i$. The Hill coefficient mainly determines the absolute value of force as a function of Calcium concentration. Since the MRC_{pes} and PESPC are normalized (to the prime beat) force changing rate, the contraction characteristic curves are maintained after the alteration of Hill coefficient.

(a)

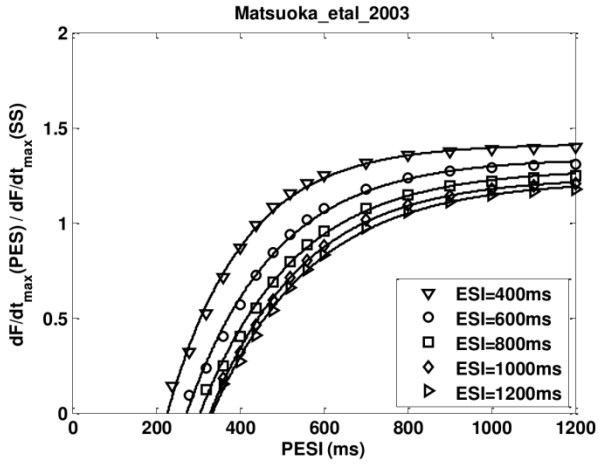
Matsuoka_etal_2003
dF/dt_max(PES) / dF/dt_max(SS)
PESI (ms)
ESI=400ms
ESI=600ms
ESI=800ms
ESI=1000ms
ESI=1200ms

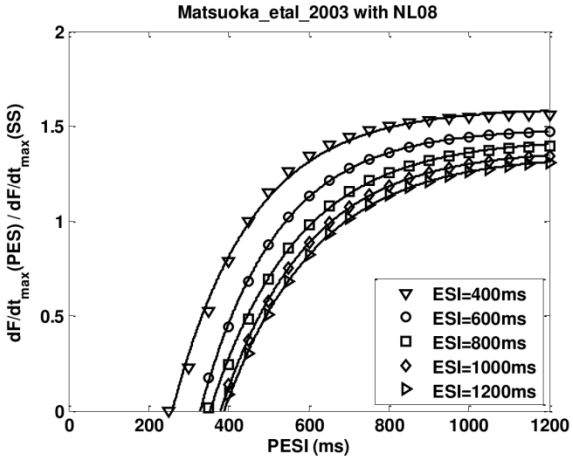
Matsuoka_etal_2003 with NL08
dF/dt_max(PES) / dF/dt_max(SS)
PESI (ms)
ESI=400ms
ESI=600ms
ESI=800ms
ESI=1000ms
ESI=1200ms

(b)

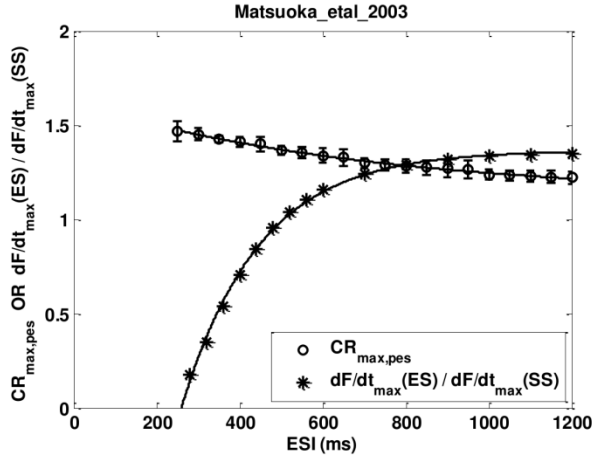
Matsuoka_etal_2003
CR_max,pes OR dF/dt_max(ES) / dF/dt_max(SS)
ESI (ms)
CR_max,pes
dF/dt_max(ES) / dF/dt_max(SS)

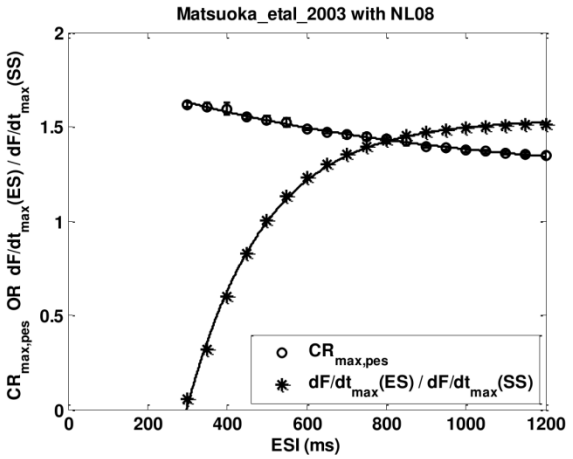
Matsuoka_etal_2003 with NL08
CR_max,pes OR dF/dt_max(ES) / dF/dt_max(SS)
ESI (ms)
CR_max,pes
dF/dt_max(ES) / dF/dt_max(SS)

(c)

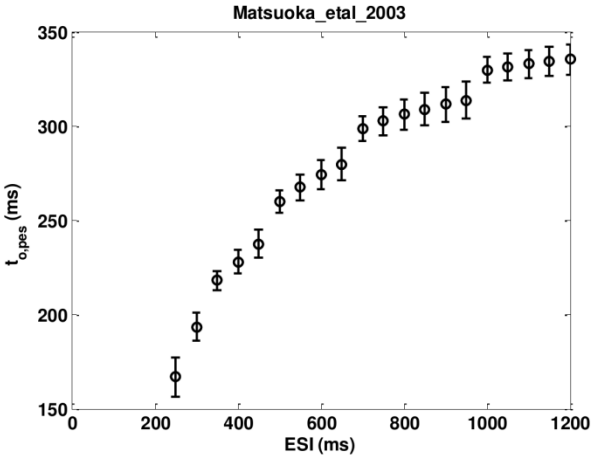
Matsuoka_etal_2003
t_o,pes (ms)
ESI (ms)

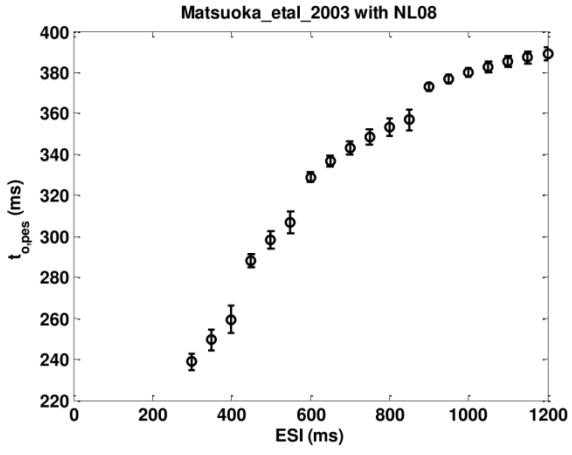
Matsuoka_etal_2003 with NL08
t_o,pes (ms)
ESI (ms)

(d)

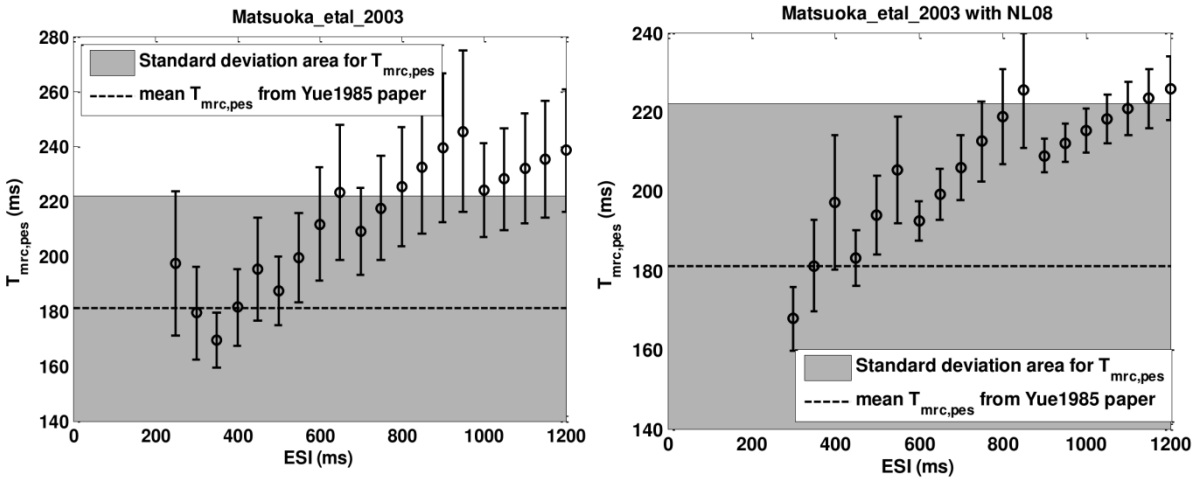
Matsuoka_etal_2003
Standard deviation area for T_mrc,pes
mean T_mrc,pes from Yue1985 paper
T_mrc,pes (ms)
ESI (ms)
Matsuoka_etal_2003 with NL08
Standard deviation area for T_mrc,pes
mean T_mrc,pes from Yue1985 paper
T_mrc,pes (ms)
ESI (ms)

(e)

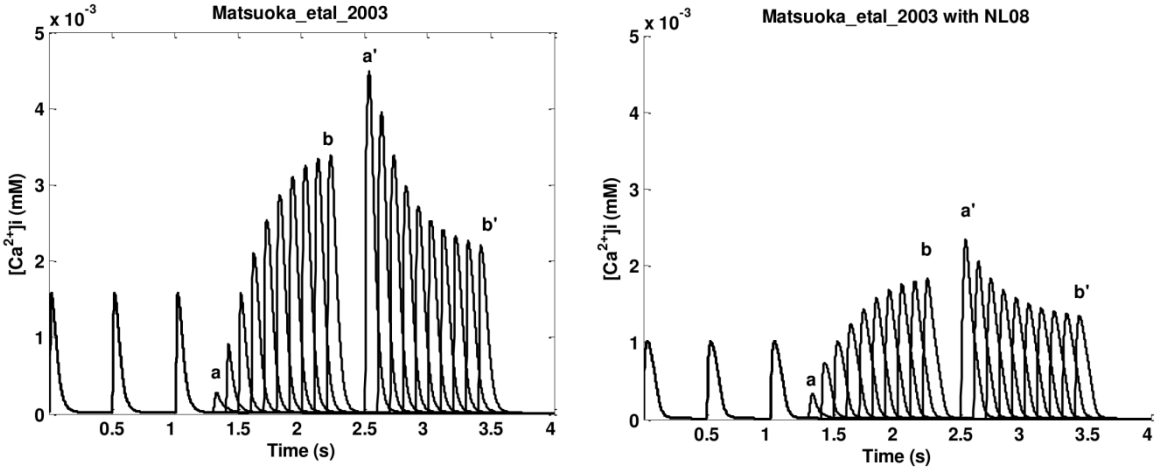
Matsuoka_etal_2003
x 10^-3
[Ca2+]i (mM)
a
b
a'
b'
Time (s)
Matsuoka_etal_2003 with NL08
x 10^-3
[Ca2+]i (mM)
a
b
a'
b'
Time (s)

APPENDIX E

CALCIUM ALTERNANS

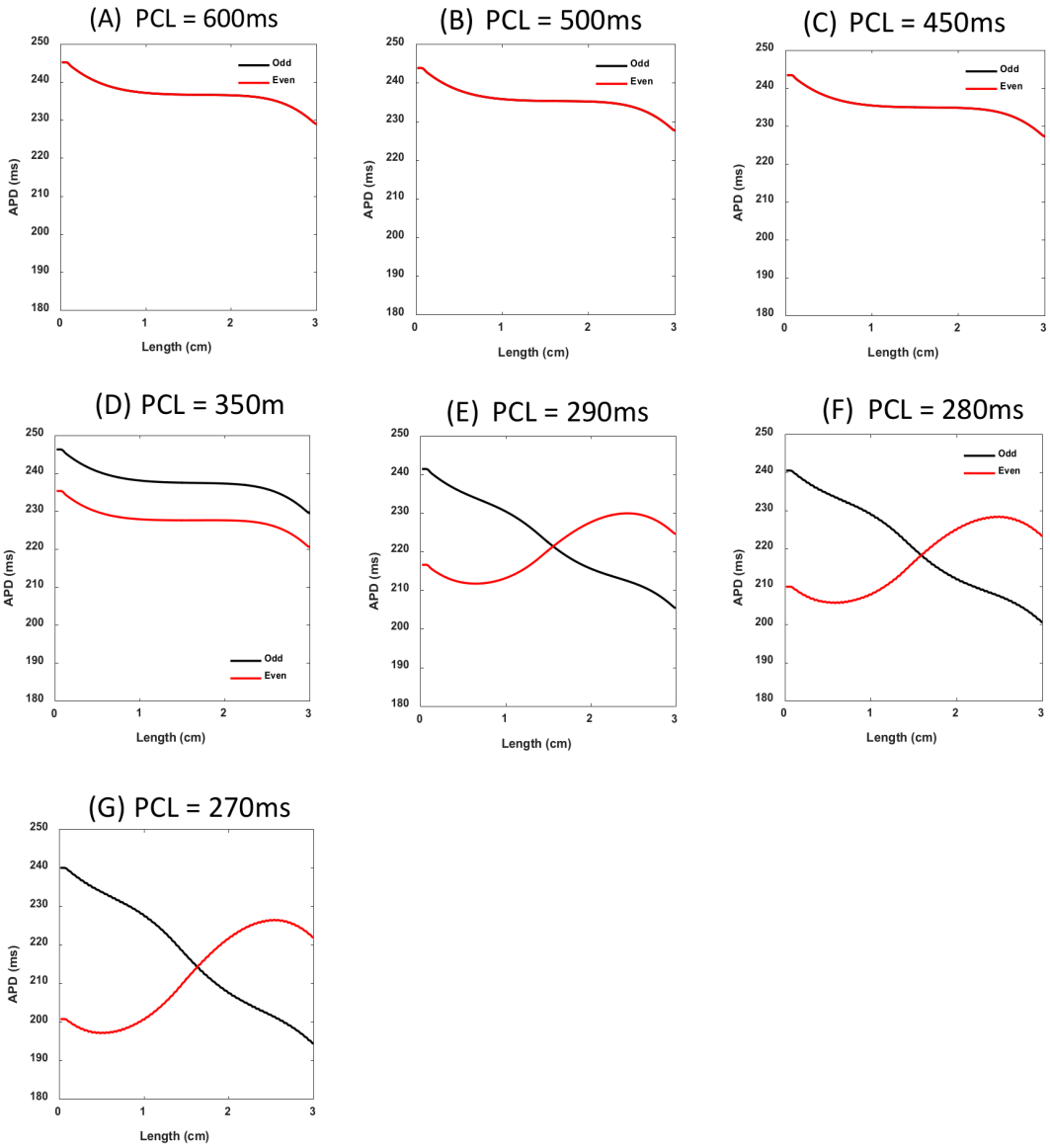

Figure E.1: APD for different pacing cycle lengths.

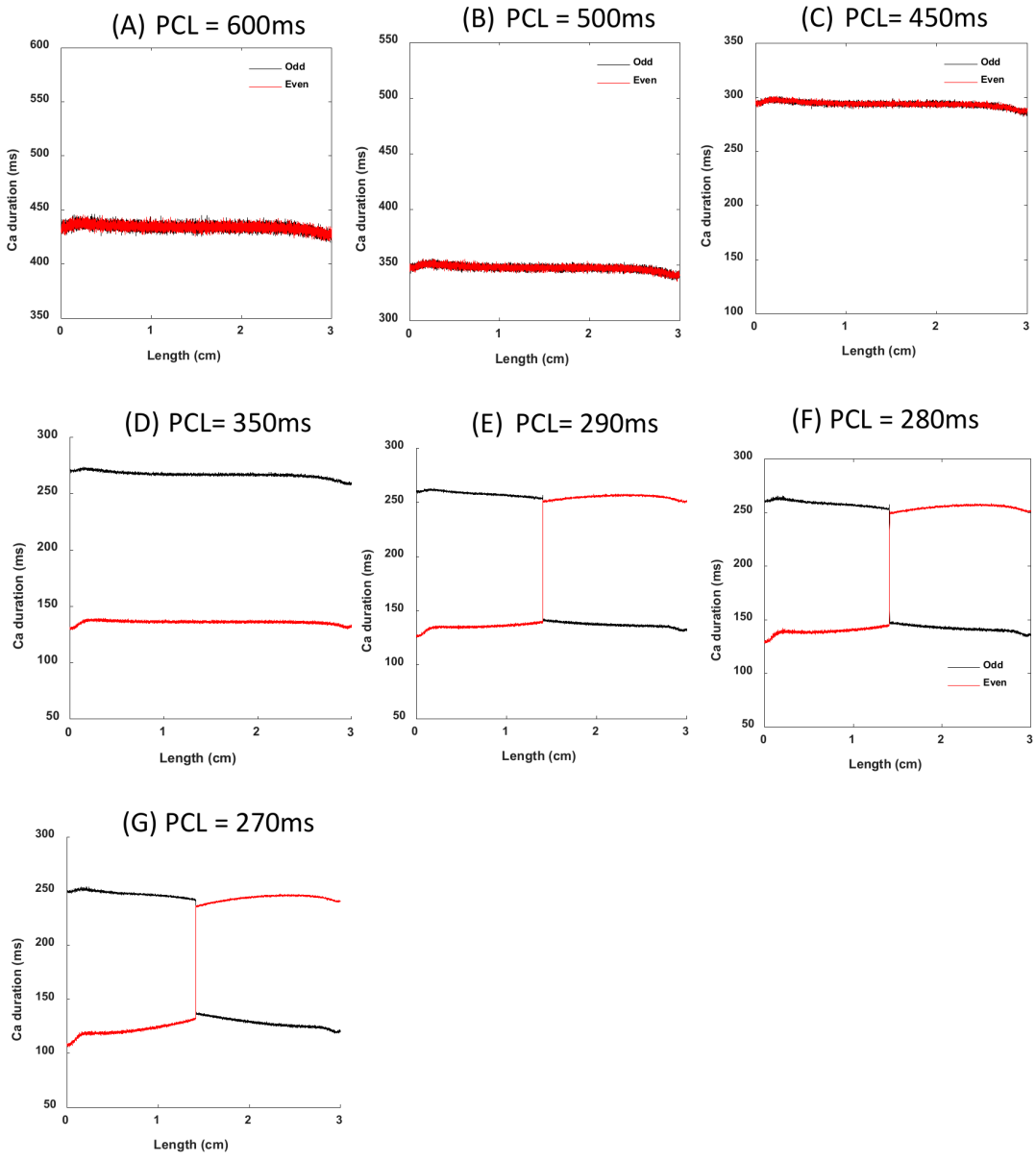

Figure E.2: CaD for different pacing cycle lengths.

APPENDIX F

LEAP EXPERIMENTAL PROTOCOL

F.1 Tissue preparation

Studies were performed using hearts obtained from adult mongrel dogs of either sex weighing 10 to 30 kg (n=7). The dogs were anesthetized with Fatal-Plus (390 mg/mL pentobarbital sodium; Vortex Pharmaceuticals; 86 mg/kg IV) and their hearts were excised rapidly. Both coronary arteries were cannulated with polyethylene tubing, and the whole atrial myocardium (both right and left) or the left ventricular myocardium (without the septum) were excised and suspended in a heated (37°C) bath where they were continuously both perfused and superfused with normal Tyrodes solution. Oxygen level, action potential morphology and speed were monitored throughout the experiments. No ischemia was found in the tissue. After 15 to 30 minutes of equilibration, voltage-sensitive dye Di_4_ANEPPS (10 μM/L bolus) and Blebbistatin (10 μM/L) were then added to stain the preparation and prevent motion artifact respectively. Arrhythmias in ventricles were induced by fast pacing. The dominant period of VF was varied between 60ms and 150ms. Arrhythmias in atria were induced by applying acetylcholine (ACh) (1-4 μM) before pacing. By adjusting the concentration of Ach, the dominant period of arrhythmia was varied between 30 and 65ms, which provided an opportunity to create arrhythmias that simulated atrial tachycardia, atrial flutter, and AF in an intact heart. Both VF and AF are presented by multiple coupled spiral waves. If shocks were not applied, fibrillation was persistent (maximum time tracked was 2 hours, minimum time 5 minutes). Figure F.1A shows the experimental setup, which consists of a CCD camera, LED lights, bath with pumping system that can circulate perfusion solution and control temperature. Figure F.1B zooms in to the bath where the tissue is place in the center with four electrodes on the side. In experiments, only two electrodes at a time

will be connected to stimulus isolator. Figure F.1C shows the thin atria tissue.

F.2 Electrodes and pacing

Field stimulating electrodes consisted of 1 cm $\times$ 5 cm platinum plates embedded in epoxy and were place on either side of the preparation, 10cm apart (Figure F.1B). The electrodes were perpendicular to the surface of the ventricle (and atria). With the slab electrodes thicker than the preparation, we expect activations at all parallel surfaces to be similar to the top visualized one. Pacing and far-field stimuli consisted of rectangular pulses delivered, respectively, with a bipolar electrode and stimulus isolator (World Precision Instruments) and a function generator (Agilent 33220A) coupled to a power amplifier (Kepco BOB 100 to 4 mol/L) capable of delivering field strengths from 0.01 to 4.6 V/cm at cycle lengths as short as 30 ms. The field strength between the electrodes was measured using two Teflon-coated silver wires 5-7 cm apart and immersed in the bath. The electric field is calculated by E=ΔV/L with ΔV being the potential difference between the two sides of the electrode and L being the distance in between.

F.3 Optical mapping

Excitation light was produced by 16 high-performance light-emitting diodes (Luxeon III star, LXHL-FM3C, wavelength 530 $\pm$ 20 nm) driven by a low-noise constant-current source. The illumination efficiency was significantly enhanced by collimator lenses (Luxeon, LXHL-NX05). The fluorescence emission light was collected by a Navitar lens (DO-2595, focal length 25 mm, F/# 0.95), passed through a long-pass filter ($<$610 nm), and imaged by a 128$\times$128 back-illuminated EMCCD array (electron-multiplied charge coupled device, Photometrics Cascade 128+). The signal was digitized with a 16bit A/D converter at a frame rate of 511 Hz. The PCI interface provided high-bandwidth uninterrupted data transfer to the host computer. The instantaneous dominant frequency of an arrhythmia was obtained in real time by calculating the fast Fourier transformation (FFT) of the signal

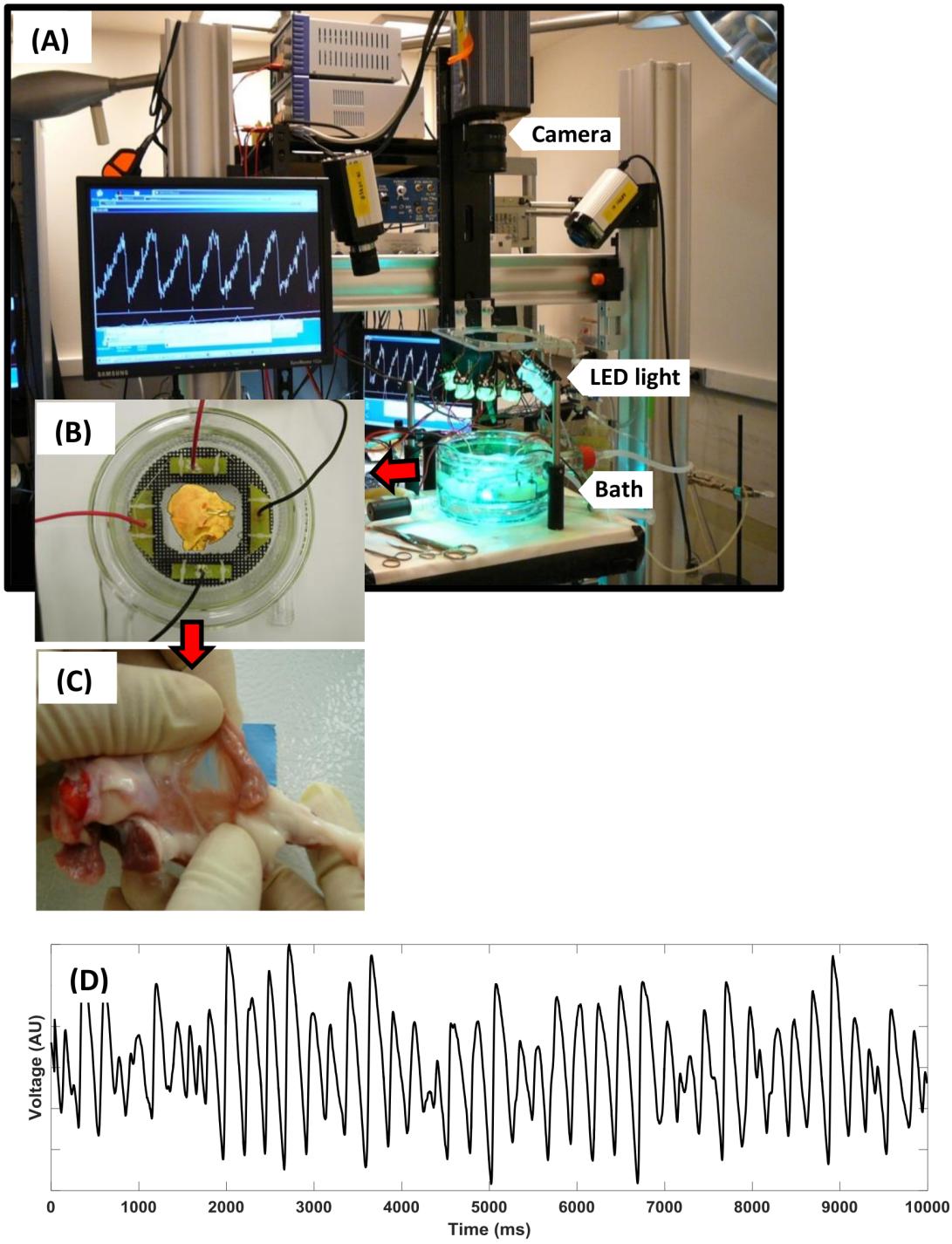

Figure F.1: Ex vivo experiment setup. (A) Optical mapping setup. (B) Defibrillation setup for either the 1 shock or LEAP. Picture shows tissue preparation (center) and four electrodes on the side. Defibrillation was performed using only one of the two pair of parallel electrodes. (C) Picture showing right canine atria with very thin regions of tissue. (D) Extended time signal from one pixel during VF.

recorded from 1 pixel in the center of the preparation in real time.

F.4 LEAP and one-shock defibrillation protocol

For the LEAP experiments, a sequence of either 5 or 10 pulses was applied after the induction of arrhythmia with a 5 ms pulse duration and a cycle length 5-10 ms below or above the dominant cycle length of the arrhythmia. A series of recordings was made in each experiment with each recording lasting up to 15 seconds in duration. Field strength was varied and applied from the threshold level of activation (0.25 V/cm), as determined prior to arrhythmia induction, until arrhythmia termination was achieved or the maximal deliverable field strength was reached ($\sim$ 4.6V/cm). After the arrhythmia termination was achieved, the arrhythmia was re-induced and standard one shock defibrillation was performed on the same hearts and the minimum energy required to terminate fibrillation was compared with LEAP.

F.5 Data Analysis

After masking out the area that either no heart tissue is presented (bath etc.) or the tissue that is not well perfused by the voltage-sensitive dye Di_4_ANEPPS, which leads to signal too noisy to recognize, we smooth the data by averaging both spatially and temporally with a Gaussian filter and the remove drift using piece-wise linear function based on action potential period.

When calculating fraction of tissue excited (FTE), we first normalize the train of voltage signal of every pixel from 0.0 to 1.0. We pick 0.4 as the threshold and consider the pixel activated when the voltage is above that. We tested that changing the threshold from 30% to 50% does not change much of the results.

In general, activation time in literature such as APD is defined by different authors with different thresholds, typically 90%, 75% or 50% of the repolarization amplitude. In this study, we consider the cell activated when the membrane potential is well above Na^+

activation threshold (normally, action potential is from -80mV to 20mV; the activation threshold for Na^+ is -60mV; 40% of a normal action potential amplitude is -40mV).

F.6 Statistics analysis

Data are expressed as mean$\pm$SD. Two-Sample t-test is performed on:

1. Peak dFTE/dt during (i) LEAP (sample size: 30) and (ii) standard one-shock defibrillation (sample size: 19) in experiments;

2. Percentage of trials that terminate arrhythmia within 5 shocks during (i) upslope (sample size: 5) and (ii) downslope (sample size: 5) of FTE in LEAP simulations.

The first t-test is to determine whether LEAP and standard one-shock defibrillation synchronize tissue at the same rate in experiments. We use dFTE/dt as an indicator for how fast shocks synchronize tissue. The second t-test is to determine whether the LEAP efficiency is the same when the first shock is applied at the upslope of FTE or downslope of FTE in simulations. We use the percentage of trials successfully terminate arrhythmia within five shocks as an indicator for the shock efficiency. MATLAB function ttest2 is used for the significance level calculation. $P<0.05$ is considered significant.

APPENDIX G

MOVIES

Movie 1. Voltage and calcium in two consecutive beats for pacing cycle lengths from 350 to 140 ms when stimulation was applied at the base of the heart.
Link: https://youtu.be/PMdaUVDWXdo

Movie 2. Voltage and calcium in two consecutive beats for pacing cycle lengths from 350 to 140 ms when stimulation was applied at the apex of the heart.
Link: https://youtu.be/fHBApGL0G5k

Movie 3. Voltage and phase of LEAP terminating VF in Figure 6.1; E = 1.4V/cm.
Link: https://youtu.be/To-GMbOcyFk

Movie 4. Voltage of LEAP terminating AF in dog atria.
Link: https://youtu.be/XcNrPB2-UPo

Movie 5. Voltage and phase of LEAP failed to synchronize VF; E = 0.9V/cm.
Link: https://youtu.be/54TLDCfmSMo

Movie 6. Voltage and phase of LEAP terminating spiral waves in simulations in Figure 6.5; T = 190ms.
Link: https://youtu.be/7zdnROzUDks

Movie 7. Voltage and phase of LEAP failed to terminate the spiral waves with 10 shocks (T = 164ms) in simulation.
Link: https://youtu.be/5ki_uG7Jmrg

Movie 8. Voltage and FTE of LEAP terminating four spiral waves in simulation with pacing period T=201ms and first shock at tm=590ms.
Link: https://youtu.be/oKUUGj8Gsec

Movie 9. Voltage and FTE of LEAP terminating four spiral waves in simulation with T=181ms and tm=590ms.

Link: https://youtu.be/NubdY0scgPg

Movie 10. Voltage and FTE of LEAP terminating four spiral waves in simulation with T=221ms and tm=590ms.

Link: https://youtu.be/PRql5zkxbYU

Movie 11. Voltage and FTE of LEAP failed to terminate four spiral waves in simulation with T=181ms and tm=670ms.

Link: https://youtu.be/FVgv0nE9-U8

Movie 12. LEAP showed similar results as anti-tachycardia pacing (ATP) when terminating a single stable spiral and it has the advantage over ATP if the spiral is pinned to a heterogeneity. When fast multiple spiral waves are presented, the more complex the spirals are, the more energy will be required for LEAP. For example, in the 4-sprial wave system in simulation, LEAP with E=1.05V/cm failed to terminate the spirals with 10 shocks whereas in the 1-sprial wave system, the same electric field can terminate the spiral in 4 shocks. In both situations, the first shocks were applied on the downslope of FTE. Shock period is 221ms, 10% above the dominant period of the arrhythmia. Link: https://youtu.be/7V7QC0v6A64 https://youtu.be/OZQXe0LpgN0

REFERENCES

[1] J. Wikswo, S. Lin, and R. Abbas, "Virtual electrodes in cardiac tissue: A common mechanism for anodal and cathodal stimulation," *Biophysics Journal*, vol. 69, pp. 2195–2210, 6 1995.

[2] F. Fenton, S. Luther, E. Cherry, N. Otani, V. Krinsky, A. Pumir, E. Bodenschatz, and J. R. Gilmour, "Termination of atrial fibrillation using pulsed low-energy far-field stimulation," *Circulation*, vol. 120, pp. 467–476, 2009.

[3] S. Luther, F. Fenton, B. Kornreich, A. Squires, P. Bittihn, D. Hornung, M. Zabel, J. Flanders, A. Gladuli, L. Campoy, E. Cherry, G. Luther, G. Hasenfuss, V. Krinsky, A. Pumir, R. J. Gilmour, and E. Bodenschatz, "Low-energy control of electrical turbulence in the heart," *Nature*, vol. 475, pp. 235–239, 2011.

[4] E. J. Benjamin, M. J. Blaha, S. E. Chiuve, M. Cushman, S. R. Das, R. Deo, S. D. de Ferranti, J. Floyd, M. Fornage, C. Gillespie, C. R. Isasi, M. C. Jiménez, L. C. Jordan, S. E. Judd, D. Lackland, J. H. Lichtman, L. Lisabeth, S. Liu, C. T. Longenecker, R. H. Mackey, K. Matsushita, D. Mozaffarian, M. E. Mussolino, K. Nasir, R. W. Neumar, L. Palaniappan, D. K. Pandey, R. R. Thiagarajan, M. J. Reeves, M. Ritchey, C. J. Rodriguez, G. A. Roth, W. D. Rosamond, C. Sasson, A. Towfighi, C. W. Tsao, M. B. Turner, S. S. Virani, J. H. Voeks, J. Z. Willey, J. T. Wilkins, J. H. Wu, H. M. Alger, S. S. Wong, and P. Muntner, "Heart disease and stroke statistics—2017 update: A report from the american heart association," *Circulation*, 0009-7322 2017.

[5] S. Chugh, R. Havmoeller, K. Narayanan, D. Singh, M. Rienstra, E. Benjamin, R. Gillum, Y.-H. Kim, J. McAnulty, Z.-J. Zheng, M. Forouzanfar, M. Naghavi, G. Mensah, M. Ezzati, and C. Murray, "Worldwide epidemiology of atrial fibrillation: A global burden of disease 2010 study," *Circulation*, vol. 129, pp. 837–847, 2014.

[6] r. R. Ideke, X. Zhou, and K. S.B., "Correlation among fibrillation, defibrillation, and cardiac pacing," *Pacing Clin Electrophysiol PACE.*, vol. 18, pp. 512–525, 1995.

[7] R. Koster, P. Dorian, F. Chapman, P. Schmitt, S. OGrady, and R. Walker, "A randomized trial comparing monophasic and biphasic waveform shocks for external cardioversion of atrial fibrillation," *Am Heart J*, vol. 147, e20, 2004.

[8] G. Walcott, C. Killingsworth, and R. Ideker, "Do clinically relevant transthoracic defibrillation energies cause myocardial damage and dysfunction?" *Resuscitation*, vol. 59, pp. 59–70, 2003.

[9] W. Maisel, "Pacemaker and icd generator reliability: Meta-analysis of device registries," *JAMA*, vol. 295, pp. 1929–1934, 2006.

[10] S. Eysmann, F. Marchlinski, B. A.E., and J. M.E., "Electrocardiographic changes after cardioversion of ventricular arrhythmias," *Circulation*, vol. 73, pp. 73–81, 1986.

[11] A. Pumir, V. Nikolski, M. Hrning, A. Isomura, K. Agladze, K. Yoshikawa, R. Gilmour, E. Bodenschatz, and V. Krinsky, "Wave emission from heterogeneities opens a way to controlling chaos in the heart," *Phys Rev Lett.*, vol. 99, p. 208 101, 2007.

[12] P. Bittihn, M. Hrning, and L. S., "Negative curvature boundaries as wave emitting sites for the control of biological excitable media," *Phys Rev Lett.*, vol. 109, p. 118 106, 2012.

[13] M. Bishop, G. Plank, and E. Vigmond, "Investigating the role of the coronary vasculature in the mechanisms of defibrillation," *Circ Arrhythm Electrophysiol.*, vol. 5, pp. 210–219, 2012.

[14] E. M. Cherry and F. H. Fenton, "A tale of two dogs: Analyzing two models of canine ventricular electrophysiology," *Am. J. Physiol. Heart Circ. Physiol.*, vol. 292, H43–H55, 2007.

[15] D. Bers, "Cardiac excitationcontraction coupling," *Nature*, vol. 415, pp. 198–205, 6868 2002.

[16] J Ehrlich, T Cha, L Zhang, D Chartier, P Melnyk, S Hohnloser, and S Nattel, "Cellular electrophysiology of canine pulmonary vein cardiomyocytes: Action potential and ionic current properties," *Journal of Physiology*, vol. 551, pp. 801–813, 2003.

[17] C Pappone, G Vicedomini, F Manguso, M Saviano, M Baldi, A Pappone, C Ciaccio, L Giannelli, B Ionescu, A Petretta, R Vitale, A Cuko, Z Calovic, A Fundaliotis, M Moscatiello, L Tavazzi, and V Santinelli, "Wolff-parkinson-white syndrome in the era of catheter ablation: Insights from a registry study of 2169 patients," *Circulation*, vol. 130, pp. 811–9, 10 2014.

[18] F. Fenton, E. Cherry, and L Glass, "Cardiac arrhythmia," *Scholarpedia*, vol. 3, p. 1665, 7 2008.

[19] E. Cherry, and F. Fenton, "Visualization of spiral and scroll waves in simulated and experimental cardiac tissue," *New Journal of Physics*, vol. 10, p. 125 016, 2008.

[20] M. Guevara, G. Ward, and L. Glass, "Electrical alternans and period doubling bifurcations," *IEEE Comp. Cardiol.*, vol. 562, pp. 167–170, 1984.

[21] J. Nolasco and R. Dahlen, "A graphic method for the study of alternation in cardiac action potentials," *J. Appl. Physiol.*, vol. 25, pp. 191–196, 1968.

[22] J. Pastore, S. Girouard, K. Laurita, F. Akar, and D. Rosenbaum, "Mechanism linking t-wave alternans to the genesis of cardiac fibrillation," *Circulation*, vol. 99, pp. 1385–1394, 1999.

[23] A. Gizzi, E. Cherry, R. Gilmour, S. Luther, S. Filippi, and F. Fenton, "Effects of pacing site and stimulation history on alternans dynamics and the development of complex spatiotemporal patterns in cardiac tissue," *Front. Physiol.*, vol. 4, 2013.

[24] B. Choi, W. Jang, and G. Salama, "Spatially discordant voltage alternans cause wavebreaks in ventricular fibrillation," *Heart Rhythm*, vol. 4, pp. 1057–1068, 8 2007.

[25] F. Fenton, E. Cherry, H. Hastings, and S. Evans, "Multiple mechanisms of spiral wave breakup in a model of cardiac electrical activity," *Chaos*, vol. 12, pp. 852–892, 3 2002.

[26] H. Saitoh, J. Bailey, and B. Surawicz, "Alternans of action potential duration after abrupt shortening of cycle length: Differences between dog purkinje and ventricular muscle fibers," *Circ. Res.*, vol. 62, pp. 1027–1040, 5 1988.

[27] ——, "Action potential duration alternans in dog purkinje and ventricular muscle fibers. further evidence in support of two different mechanisms," *Circulation*, vol. 80, pp. 1421–1431, 5 1989.

[28] Z. Qu, A. Garfinkel, P. Chen, and J. Weiss, "Mechanisms of discordant alternans and induction of reentry in simulated cardiac tissue," *Circulation*, vol. 102, pp. 1664–1670, 14 2000.

[29] M. Watanabe, F. H. Fenton, S. Evans, H. Hastings, and A. Karma, "Mechanisms for discordant alternans," *J. Cardiovasc. Electrophysiol.*, vol. 12, pp. 196–206, 2 2001.

[30] J. Edwards and L. Blatter, "Cardiac alternans and intracellular calcium cycling," *Clin. Exp. Pharmacol. Physiol.*, vol. 41, pp. 524–532, 7 2014.

[31] J. Weiss, A. Karma, Y. Shiferaw, P.-S. Chen, A. Garfinkel, and Z. Qu, "From pulsus to pulseless: The saga of cardiac alternans," *Circ. Res.*, vol. 102, pp. 1244–1253, 14 2006.

[32] J. Weiss, M. Nivala, A. Garfinkel, and Z. Qu, "Alternans and arrhythmias: From cell to heart," *Circ. Res.*, vol. 108, pp. 98–112, 1 2011.

[33] W. Clusin, "Mechanisms of calcium transient and action potential alternans in cardiac cells and tissues," *Am. J. Physiol. Heart Circ. Physiol.*, vol. 294, H1–H10, 1 2008.

[34] D. Eisner, Y. Li, and S. ONeill, "Alternans of intracellular calcium: Mechanism and significance," *Heart Rhythm*, vol. 3, pp. 743–745, 6 2006.

[35] G. Kanaporis and L. Blatter, "The mechanisms of calcium cycling and action potential dynamics in cardiac alternans," *Circ. Res.*, vol. 116, pp. 846–856, 5 2015.

[36] K. Laurita and D. Rosenbaum, "Cellular mechanisms of arrhythmogenic cardiac alternans," *Prog. Biophys. Mol. Biol.*, vol. 97, pp. 332–347, 2-3 2008.

[37] R. Myles, F. Burton, S. Cobbe, and G. Smith, "The link between repolarisation alternans and ventricular arrhythmia: Does the cellular phenomenon extend to the clinical problem?" *J. Mol. Cell. Cardiol.*, vol. 45, pp. 1–10, 1 2008.

[38] L. Boersma, J. Brugada, C. Kirchhof, and M. Allessie, "Mapping of reset of anatomic and functional reentry in anisotropic rabbit ventricular myocardium," *Circulation*, vol. 89, pp. 852–862, 2 1994.

[39] A. Hollman, "The wolff-parkinson-white syndrome: A very long follow-up," *Americal Journal of Cardiology*, vol. 113, pp. 1751–1752, 10 2014.

[40] N Bursac and L Tung, "Acceleration of functional reentry by rapid pacing in anisotropic cardiac monolayers: Formation of multi-wave functional reentries," *Cardiovasc Res*, vol. 69, pp. 381–390, 2 2005.

[41] A. Adgey and S. Walsh, "Theory and practice of defibrillation: (1) atrial fibrillation and dc conversion," *Heart*, vol. 90, pp. 1493–1498, 12 2003.

[42] M. Hoffa and C Ludwig, "Eigige neue versuche über herzebewegung," *Z Rationelle Med*, vol. 9, pp. 107–144, 1850.

[43] J. Prevost and F. Battelli, "Sur quelques effects des décharges électriques sur le coeur des mammifères," *C R Acad Sci*, vol. 129, pp. 1267–1268, 1899.

[44] R Ideker, N. Chattipakorn, and R. Gray, "Defibrillation mechanisms: The parable of the blind men and the elephant," *Journal of Cardiovascular Electrophysiology*, vol. 11, pp. 1008–1013, 9 2000.

[45] J Dudel, "Elektrophysiologische grundlagen der defibrillation und künstlichen stimulation des herzens," *Med Klin*, vol. 52, pp. 2089–2091, 1968.

[46] W. C.J., "The physiologic basis for cardiac resuscitation from ventricular fibrillation: Method for serial defibrillation," *American Heart Journal*, vol. 20, pp. 413–422, 4 1940.

[47] D. Zipes, J. Fischer, K. R.M., A. Nicoll, and W. Jolly, "Termination of ventricular fibrillation in dogs by depolarizing a critical amount of myocardium," *American Journal of Cardiology*, vol. 36, pp. 37–44, 1 1975.

[48] M. Mower, M. Mirowski, J. Spear, and E. Moore, "Patterns of ventricular activity during catheter defibrillation," *Circulation*, vol. 49, pp. 858–861, 5 1974.

[49] S. Luther, F. Fenton, B. Kornreich, A. Squires, P. Bittihn, D. Hornung, M. Zabel, J. Flanders, A. Gladuli, L. Campoy, E. Cherry, G. Luther, G. Hasenfuss, V. Krinsky, A. Pumir, R. J. Gilmour, and E. Bodenschartz, "Low-energy control of electrical turbulence in the heart," *Nature*, vol. 475, pp. 235–239, 2011.

[50] W. Li, A. Janardhan, V. Fedorov, Q. Sha, R. Schuessler, and I. Efimov, "Low-energy multistage atrial defibrillation therapy terminates atrial firillation with less energy than a single shock," *Circ Arrhythm Electrophysiol*, vol. 4, pp. 917–925, 6 2011.

[51] A. Fabiato, P. Coumel, R. Gourgon, and R. Saumont, "Le seuil de réponse synchrone des fibres myocardiques," *Arch Mal Coeur*, vol. 60, pp. 527–544, 1967.

[52] A. T. Winfree, *When time breaks down: the three-dimensional dynamics of electrochemical waves and cardiac arrhythmias*. Princeton University Press, 1987.

[53] C. Wiggers and R. Wégria, "Ventricular fibrillation due to single localized induction and condenser shocks applied during the vulnerable phase of ventricular systole," *American Journal of Physiology*, vol. 128, pp. 500–505, 1940.

[54] S. Dillon, "Synchronized repolarization after defibrillation shocks: A possible component of the defibrillation process demonstrated by optical recordings in rabbit heart," *Circulation*, vol. 85, pp. 1865–1878, 1992.

[55] J. Jones, J. Swartz, R. Jones, and C. Sheffield, "Extracellular field stimulation with symmetrical biphasic defibrillation waveforms enhances refractory period responses," *Proc Am Assoc Med Inst*, vol. 25, p. 46, 1990.

[56] R. Sweeney, R. Gill, M. Steinberg, and P. Reid, "Ventricular refractory period extension caused by defibrillation shocks," *Circulation*, vol. 82, pp. 965–972, 3 1990.

[57] R. Plonsey, "The nature of sources of bioelectric and biomagnetic fields," *Biophysics Journal*, vol. 39, pp. 309–312, 1982.

[58] N. Trayanova and K. Skouibine, "Modeling defibrillation: Effects of fiber curvature," *Journal of electrocardiology*, vol. 31, Suppl: 23–29, 1998.

[59] V. Fast, S. Rohr, A. Gillis, and A. Kléber, "Activation of cardiac tissue by extracellular electrical shocks," *Circulation Res.*, vol. 82, pp. 375–385, 3 1998.

[60] S. Knisley, B. Hill, and R. Ideker, "Virtual electrode effects in myocardial fibers," *Biophysics Journal*, vol. 66, pp. 719–728, 3 1994.

[61] A. Sambelashivili, V. Nicolski, and I. Efimov, "Virtual electrode theory explains pacing threshold increase caused by cardiac tissue damage," *Am J Physiol Heart Circ Physiol*, vol. 286, H2183–H2194, 6 2004.

[62] M. A. Allessie, W. J. Lammers, I. M. Bonke, and J. Hollen, "Intra-atrial reentry as a mechanism for atrial flutter induced by acetylcholine and rapid pacing in the dog," *Circulation*, vol. 70, pp. 123–135, 1984.

[63] A. Pullan, L. Cheng, and M. Buist, *Mathematically Modelling the Electrical Activity of the Heart: From Cell to Body Surface and Back Again*. 27 Warren Street, Suite 401-402, Hackensack, NJ 07601: World Scientific, 2005.

[64] A. Xu and M. Guevara, "Two forms of spiral-wave reentry in an ionic model of ischemic ventricular myocardium," *Chaos*, vol. 8, pp. 157–174, 1 1998.

[65] B. Kogan, *Introduction to Computational Cardiology: Mathematical Modeling and Computer Simulation*. 233 Spring Street, New York, NY 10013: Springer Science, 2009.

[66] S. Niederer, T. Keurs, and N. Smith, "Modeling and measuring electromechanical coupling in the rat heart," *Experimental Physiology*, vol. 94, pp. 529–540, 5 2009.

[67] A. Hodgkin and A. Huxley, "A quantitative description of membrane currents and its application to conduction and excitation in nerve," *Journal of Physiology*, vol. 117, pp. 500–544, 4 1952.

[68] D. Noble, "A modification of the hodgkin–huxley equations applicable to purkinje fibre action and pace-maker potentials," *Journal of Physiology*, vol. 160, pp. 317–352, 2 1962.

[69] G. Beeler and H. Reuter, "Reconstruction of the action potential of ventricular myocardial fibres," *Journal of Physiology*, vol. 268, pp. 177–210, 1 1977.

[70] C. Luo and Y. Rudy, "A model of the ventricular cardiac action potential. depolarization, repolarization, and their interaction," *Circ Res*, vol. 68, pp. 1501–1526, 6 1991.

[71] D. DiFrancesco and D. Noble, "A model of cardiac electrical activity incorporating ionic pumps and concentration changes," *Philos Trans R Soc Lond B Biol Sci*, vol. 307, pp. 353–398, 1133 1985.

[72] D. Hilgemann and D. Noble, "Excitation-contraction coupling and extracellular calcium transients in rabbit atrium: Reconstruction of basic cellular mechanisms," *Proc R Soc Lond Ser B Contain Pap Biol Character R Soc G B*, vol. 230, pp. 163–205, 1259 1987.

[73] C. Luo and Y. Rudy, "A dynamic model of the cardiac ventricular action potential. i. simulations of ionic currents and concentration changes," *Circ Res*, vol. 74, pp. 1071–1096, 6 1994.

[74] J. Puglisi and D. Bers, "Labheart: An interactive computer model of rabbit ventricular myocyte ion channels and ca transport," *Am J Physiol Cell Physiol*, vol. 281, pp. C2049–C2060, 6 2001.

[75] K. ten Tusscher, D. Noble, P. Noble, and A. Panfilov, "A model for human ventricular tissue," *Am J Physiol Heart Circ Physiol*, vol. 286, H1573–H1589, 4 2004.

[76] S. Matsuoka, N. Sarai, S. Kuratomi, K. Ono, and A. Noma, "Role of individual ionic current systems in ventricular cells hypothesized by a model study," *Jpn J Physiol*, vol. 53, pp. 105–123, 2 2003.

[77] T. OHara, L. Virág, A. Varró, and Y. Rudy, "Simulation of the undiseased human cardiac ventricular action potential: Model formulation and experimental validation," *PLoS Comput Biol*, vol. 7, e1002061, 5 2011.

[78] V. Iyer, R. Mazhari, and R. Winslow, "A computational model of the human left-ventricular epicardial myocyte," *Biophys J*, vol. 87, 15071525, 3 2004.

[79] R. FitzHugh, "Impulses and physiological states in theoretical models of nerve membrane," *Biophysical Journal*, vol. 1, pp. 445–466, 6 1961.

[80] J. Rogers and A. McCulloch, "A collocation-galerkin finite element model of cardiac action potential propagation," *IEEE Trans Biomed Eng*, vol. 44, pp. 326–328, 4 1994.

[81] F. Fenton and A. Karma, "Vortex dynamics in three-dimensional continuous myocardium with fiber rotation: Filament instability and fibrillation," *Chaos*, vol. 8, pp. 20–47, 1 1998.

[82] R. LeVeque, *Finite Difference Methods for Ordinary and Partial Differential Equations*. Philadelphia, PA: SIAM, 2007.

[83] S. Rush and H. Larsen, "A practical algorithm for solving dynamic membrane equations," *IEEE Trans. Biomed. Eng.*, vol. BME-25, pp. 389–392, 4 1978.

[84] R. Roth, "Electrical conductivity values used with the bidomain model of cardiac tissue," *IEEE Trans Biomed Eng*, vol. 44, pp. 326–328, 4 1997.

[85] A. Pumir and V. Krinsky, "Unpinning of a rotating wave in cardiac muscle by an electric field," *J theor Biol*, vol. 199, pp. 311–319, 3 1999.

[86] J. Shea and M. Sweeney, "Cardiac resynchronization therapy. a patients guide," *Circulation*, vol. 108, e64–e66, 2003.

[87] D. Burkhoff and S. Ben-Haim, "Nonexcitatory electrical signals for enhancing ventricular contractility: Rationale and initial investigations of an experimental treatment for heart failure," *Am. J. Physiol. Heart Circ. Physiol.*, vol. 288, H2550–2556, 2005.

[88] R. Mentz and J. Butler, "Cardiac contractility modulation: The next cardiac resynchronization therapy or another renal sympathetic denervation?" *J. Card. Fail.*, vol. 21, pp. 24–26, 2015.

[89] A. Haisam Ismail, "Predictors of response to cardiac resynchronization therapy: The holy grail of electrophysiology," *Int. J. Cardiovasc Imaging*, vol. 26, pp. 197–198, 2015.

[90] V. Flore, J. Bartunek, M. Goethals, S. Verstreken, W. Timmermans, and F. e. a. De Pauw, "Electrical remodeling reflected by qrs and t vector changes following cardiac resynchronization therapy is related to survival in heart failure patients with left bundle branch block," *J. Electrocardiol.*, vol. 48, pp. 578–585, 2015.

[91] J. Van't Sant, I. ter Horst, S. Wijers, T. Mast, G. Leenders, and P. e. a. Doevendans, "Measurements of electrical and mechanical dyssynchrony are both essential to improve prediction of crt response," *J. Electrocardiol.*, vol. 48, pp. 601–608, 2015.

[92] D. Burkhoff, I. Shemer, B. Felzen, J. Shimizu, Y. Mika, and M. e. a. Dickstein, "Electric currents applied during the refractory period can modulate cardiac contractility in vitro and in vivo," *Heart Fail Rev.*, vol. 6, pp. 27–34, 2001.

[93] K. Blinova, J. Stohlman, V. Krauthamer, A. Knapton, E. Bloomquist, and R. Gray, "Acute effects of nonexcitatory electrical stimulation during systole in isolated cardiac myocytes and perfused heart," *Physiol. Rep.*, vol. 2, e12106, 2014.

[94] J. Kuschyk, S. Roeger, R. Schneider, F. Streitner, K. Stach, and B. e. a. Rudic, "Efficacy and survival in patients with cardiac contractility modulation: Long-term single center experience in 81 patients," *Int. J. Cardiol.*, vol. 183C, pp. 76–81, 2015.

[95] M. Borggrefe, T. Lawo, C. Butter, H. Schmidinger, M. Lunati, and B. e. a. Pieske, "Randomized, double blind study of non-excitatory, cardiac contractility modulation electrical impulses for symptomatic heart failure," *Eur. Heart J.*, vol. 29, pp. 1019–1028, 2008.

[96] C. Butter, J. Meyhofer, M. Seifert, M. Neuss, and H.-H. Minden, "First use of cardiac contractility modulation (ccm) in a patient failing crt therapy: Clinical and technical aspects of combined therapies," *Eur. J. Heart Fail.*, vol. 9, pp. 955–958, 2007.

[97] M. Potse, "Mathematical modeling and simulation of ventricular activation sequences: Implications for cardiac resynchronization therapy," *J. Cardiovasc. Transl. Res.*, vol. 5, pp. 146–158, 2012.

[98] R. Miri, I. Graf, and O. Dossel, "Efficiency of timing delays and electrode positions in optimization of biventricular pacing: A simulation study," *IEEE Trans. Biomed. Eng.*, vol. 56, pp. 2573–2582, 2009.

[99] M. Sermesant, R. Chabiniok, P. Chinchapatnam, T. Mansi, F. Billet, and P. e. a. Moireau, "Patient-specific electromechanical models of the heart for the prediction of pacing acute effects in crt: A preliminary clinical validation," *Med. Image Anal.*, vol. 16, pp. 201–215, 2012.

[100] C. De Lazzari, A. D'Ambrosi, F. Tufano, L. Fresiello, M. Garante, and R. e. a. Sergiacomi, "Cardiac resynchronization therapy: Could a numerical simulator be a useful tool in order to predict the response of the biventricular pacemaker synchronization?" *Eur. Rev. Med. Pharmacol. Sci.*, vol. 14, pp. 969–978, 2010.

[101] S. Niederer, G. Plank, P. Chinchapatnam, M. Ginks, P. Lamata, and K. e. a. Rhode, "Length-dependent tension in the failing heart and the efficacy of cardiac resynchronization therapy," *Cardiovasc. Res.*, vol. 89, pp. 336–343, 2011.

[102] T. C. project. (2014). Cellml.

[103] F. Fenton and E. Cherry. (2014). Models of cardiac cell.

[104] M. Cooper, "Postextrasystolic potentiation. do we really know what it means and how to use it?" *Circulation*, vol. 88, pp. 2962–2971, 6 1993.

[105] D. Yue, D. Burkhoff, M. Franz, W. Hunter, and K. Sagawa, "Postextrasystolic potentiation of the isolated canine left ventricle. relationship to mechanical restitution," *Circ Res.*, vol. 56, 340350, 1985.

[106] J. Negroni and E. Lascano, "A cardiac muscle model relating sarcomere dynamics to calcium kinetics," *J Mol Cell Cardiol.*, vol. 28, pp. 915–929, 5 1996.

[107] J. Rice, R. Winslow, and W. Hunter, "Comparison of putative cooperative mechanisms in cardiac muscle: Length dependence and dynamic responses," *Am J Physiol*, vol. 276, H1734–H1754, 1999.

[108] L. Dobrunz, P. Backx, and D. Yue, "Steady-state [ca2+]i-force relationship in intact twitching cardiac muscle: Direct evidence for modulation by isoproterenol and emd 53998," *Biophys. J.*, vol. 69, pp. 189–201, 1 1995.

[109] A. Landesberg and S. Sideman, "Mechanical regulation of cardiac muscle by coupling calcium kinetics with cross-bridge cycling: A dynamic model," *Am. J. Physiol.*, vol. 267, 2 Pt 2, 1 1994.

[110] W. Wier and D. Yue, "Intracellular calcium transients underlying the short-term force-interval relationship in ferret ventricular myocardium," *J. Physiol.*, vol. 376, pp. 507–530, 1986.

[111] G. Iribe, P. Kohl, and D. Noble, "Modulatory effect of calmodulin-dependent kinase ii (camkii) on sarcoplasmic reticulum ca2+ handling and interval-force relations: A modeling study," *Philos Transact A Math Phys Eng Sci.*, vol. 364, pp. 1107–1133, 1842 2006.

[112] G. Faber and Y. Rudy, "Action potential and contractility changes in [na(+)](i) overloaded cardiac myocytes: A simulation study," *Biophys J.*, vol. 78, pp. 2392–2404, 5 2000.

[113] L. Livshitz and Y. Rudy, "Regulation of ca2+ and electrical alternans in cardiac myocytes: Role of camkii and repolarizing currents," *Am J Physiol Heart Circ Physiol.*, vol. 292, H28542866, 6 2007.

[114] T. Shannon, F. Wang, J. Puglisi, C. Weber, and D. Bers, "A mathematical treatment of integrated ca dynamics within the ventricular myocyte," *Biophys J.*, vol. 87, 3351–3371, 5 2004.

[115] A. Mahajan, Y. Shiferaw, D. Sato, A. Baher, R. Olcese, L. Xie, M. Yang, P. Chen, J. Restrepo, A. Karma, A. Garfinkel, Z. Qu, and J. Weiss, "A rabbit ventricular action potential model replicating cardiac dynamics at rapid heart rates," *Biophys J.*, vol. 94, pp. 392–410, 2 2008.

[116] T. Hund and Y. Rudy, "Rate dependence and regulation of action potential and calcium transient in a canine cardiac ventricular cell model," *Circulation*, vol. 110, pp. 3168–3174, 20 2004.

[117] J. Fox, J. McHarg, and R. Gilmour, "Ionic mechanism of electrical alternans," *Am J Physiol Heart Circ Physiol.*, vol. 282, H516–H530, 2 2002.

[118] E. Grandi, F. Pasqualini, and D. Bers, "A novel computational model of the human ventricular action potential and ca transient," *J. Mol. Cell Cardiol.*, vol. 48, pp. 112–121, 1 2010.

[119] L. Priebe and D. Beuckelmann, "Simulation study of cellular electric properties in heart failure," *Circ. Res.*, vol. 82, pp. 1206–1223, 1998.

[120] K. ten Tusscher and A. Panfilov, "Alternans and spiral breakup in a human ventricular tissue model," *Am J Physiol Heart Circ Physiol.*, vol. 291, H1088–100, 3 2006.

[121] M. Fink, D. Noble, L. Virag, A. Varro, and W. Giles, "Contributions of HERG K^+ current to repolarization of the human ventricular action potential," *Prog. Biophys. Mol. Biol.*, vol. 96, pp. 357–376, 1-3 2008.

[122] C. J., "Automatic validation and optimisation of biological models," PhD thesis, University of Oxford, 2009.

[123] J. Cooper, A. Corrias, D. Gavaghan, and D. Noble, "Considerations for the use of cellular electrophysiology models within cardiac tissue simulations," *Prog. Biophys. Mol. Biol.*, vol. 107, pp. 74–80, 2011.

[124] A. Bueno-Orovio, E. Cherry, and F. Fenton, "Minimal model for human ventricular action potentials in tissue," *J. Theor. Biol.*, vol. 253, pp. 544–560, 2008.

[125] P. Schwartz, A. Moss, G. Vincent, and R. Crampton, "Diagnostic criteria for the long qt syndrome. an update," *Circulation*, vol. 88, pp. 782–784, 1993.

[126] P. J. Schwartz, "Idiopathic long qt syndrome: Progress and questions," *Am. Heart J.*, vol. 109, pp. 399–411, 1985.

[127] Food and D. Administration, "Guidance for industry e14 clinical evaluation of qt/qtc interval prolongation and proarrhythmic potential for non-antiarrhythmic drugs," *FDA*, 2005.

[128] W. Zareba, A. Moss, S. le Cessie, and W. Hall, "T wave alternans in idiopathic long qt syndrome," *J. Am. Coll. Cardiol.*, vol. 23, pp. 1541–1546, 1994.

[129] M. Jayakrishnan and P. Krishnakumar, "Macroscopic t wave alternans in long qt syndrome," *Indian J. Pediatr.*, vol. 73, pp. 539–540, 2006.

[130] L. Traube, "Ein fall von pulsus bigeminus nebst bemerkungen tiber die lebershwellungen bei klappenfehlern und uber acute leberatrophic," *Ber Klin Wschr*, vol. 9, 1872.

[131] R. L. Winslow, J. Rice, S. Jafri, E. Marbán, and B. ORourke, "Mechanisms of altered excitation-contraction coupling in canine tachycardia-induced heart failure, ii.," *Circ. Res.*, vol. 84, pp. 571–586, 1999.

[132] D. Sato, D. M. Bers, and Y. Shiferaw, "Formation of spatially discordant alternans due to fluctuations and diffusion of calcium," *PLOS One*, vol. 8, e85365, 2013.

[133] P. T. Sager, G. Gintant, J. R. Turner, S. Pettit, and N. Stockbridge, "Rechanneling the cardiac proarrhythmia safety paradigm: A meeting report from the cardiac safety research consortium," *Am. Heart J.*, vol. 167, pp. 292–300, 2014.

[134] A. Garzon and R. Grigoriev, "Memory effects, transient growth, and wave breakup in a model of paced atrium," *Chaos*, vol. 27, p. 093 917, 2017.

[135] P. S. Skardal, A. Karma, and J. G. Restrepo, "Spatiotemporal dynamics of calcium-driven cardiac alternans," *Phys. Rev. E Stat. Nonlin. Soft Matter Phys.*, vol. 89, p. 052 707, 2014.

[136] Y. Shiferaw and A. Karma, "Turing instability mediated by voltage and calcium diffusion in paced cardiac cells," *Proc. Natl. Acad. Sci. U.S.A.*, vol. 103, pp. 5670–5675, 2006.

[137] S. A. Gaeta, G. Bub, G. W. Abbott, and D. J. Christini, "Dynamical mechanism for subcellular alternans in cardiac myocytes," *Circ. Res.*, vol. 103, pp. 335–342, 2009.

[138] X. Zhao, D. G. Schaeffer, C. M. Berger, W. Krassowska, and D. J. Gauthier, "Cardiac alternans arising from an unfolded border-collision bifurcation," *J. Comput. Nonlinear Dyn.*, vol. 3, pp. 041 004–7, 2008.

[139] D. D. Chen, R. A. Gray, I. Uzelac, C. Herndon, and F. H. Fenton, "Mechanism for amplitude alternans in electrocardiograms and the initiation of spatiotemporal chaos," *Phys. Rev. Lett.*, vol. 118, p. 168 101, 2017.

[140] D. Sato, Y. Shiferaw, A. Garfinkel, J. Weiss, Z. Qu, and A. Karma, "Spatially discordant alternans in cardiac tissue: Role of calcium cycling," *Circ. Res.*, vol. 99, pp. 520–527, 2006.

[141] A. Nygren, C. Fiset, L. Firek, J. Clark, D. Lindblad, R. Clark, and W. Giles, "Mathematical model of an adult human atrial cell: The role of k^+ currents in repolarization," *Circ. Res.*, vol. 82, pp. 63–81, 1998.

[142] S. M.S. and P. Dolber, "Relating extracellular potentials and their derivatives to anisotropic propagation at a microscopic level in human cardiac muscle. evidence for electrical uncoupling of side-to-side fiber connections with increasing age.," *Circ. Res.*, vol. 58, pp. 356–371, 1986.

[143] J. Kneller, R. Zou, E. Vigmond, Z. Wang, L. Leon, and S. Nattel, "Cholinergic atrial fibrillation in a computer model of a two-dimensional sheet of canine atrial cells with realistic ionic properties.," *Circ. Res.*, vol. 90, E73–E87, 2002.

[144] S. Strogatz, "From kuramoto to crawford: Exploring the onset of synchronization in populations of coupled oscillators," *Phys. Nonlinear Phenom.*, vol. 143, pp. 1–20, 2000.

[145] G. Salama, A. Kanai, and E. I. R., "Subthreshold stimulation of purkinje fibers interrupts ventricular tachycardia in intact hearts. experimental study with voltage-sensitive dyes and imaging techniques.," *Circ. Res.*, vol. 74, pp. 604–619, 1994.

[146] B. P, G Luther, E. Bodenschatz, V. Krinsky, U. Parlitz, and S. Luther, "Far field pacing supersedes anti-tachycardia pacing in a generic model of excitable media.," *New J. Phys.*, vol. 10, p. 103 012, 2008.

[147] J. Keener, J. Sneyd, and editors, *Mathematical Physiology*. New York, NY: Springer New York, 2009.

[148] I. Turner, S. Turner, and A. A. Grace, "Timing of defibrillation shocks for resuscitation of rapid ventricular tachycardia: Does it make a difference?" *Resuscitation*, vol. 80, pp. 183–188, 2009.

[149] L. Rantner, B. Tice, and N. Trayanova, "Terminating ventricular tachyarrhythmias using far-field low-voltage stimuli: Mechanisms and delivery protocols," *Heart Rhythm*, vol. 10, pp. 1209–1217, 8 2013.

[150] N. Otani, K. Wheeler, V. Krinski, and S Luther, "Termination of multiple electrical vortices of unknown phase and location in three-dimensional excitable media," *Submitted manuscript*, 2018.

[151] B. Caldwell, M. Trew, and A. Pertsov, "Cardiac response to low-energy field pacing challenges the standard theory of defibrillation," *Circulation: Arrhythmia and Electrophysiology*, vol. 8, pp. 685–693, 2015.

[152] A. Clauset, C. Shalizi, and M. Newman, "Power-law distributions in empirical data," *SIAM Review*, vol. 51, pp. 661–703, 2009.

[153] G. Templeton, K. Wildenthal, J. Willerson, and W. Reardon, "Influence of temperature on the mechanical properties of cardiac muscle," *Circ. Res.*, vol. 34, pp. 624–634, 1974.

[154] G. Langer and A. Brady, "The effects of temperature upon contraction and ionic exchange in rabbit ventricular myocardium," *J Gen Physiol.*, vol. 52, pp. 682–713, 1968.

[155] F. Fenton, A. Gizzi, C. Cherubini, N. Pomella, and S. Filippi, "Role of temperature on nonlinear cardiac dynamics," *Phys Rev E.*, vol. 87, p. 042 717, 2013.

[156] S. Filippi, A. Gizzi, C. Cherubini, S. Luther, and F. Fenton, "Mechanistic insights into hypothermic ventricular fibrillation: The role of temperature and tissue size," *Europace*, vol. 16, pp. 424–434, 3 2014.

[157] M. Fink, S. Niederer, E. Cherry, F. Fenton, J. Koivumaki, and G. e. a. Seemann, "Cardiac cell modelling: Observations from the heart of the cardiac physiome project," *Prog Biophys Mol Biol*, vol. 104, pp. 2–21, 2011.

[158] J. Kentish, H. ter Keurs, J. Ricciardi L. Bucx, and M. Noble, "Comparison between the sarcomere length-force relations of intact and skinned trabeculae from rat right ventricle. influence of calcium concentrations on these relations," *Circ. Res.*, vol. 58, pp. 755–768, 1986.

[159] D. Yue, E. Marban, and W. Wier, "Relationship between force and intracellular ca in tetanized mammalian heart muscle," *J. Gen. Physiol.*, vol. 87, pp. 223–242, 1986.

[160] J. Negroni and E. Lascano, "Simulation of steady state and transient cardiac muscle response experiments with a huxley-based contraction model," *J. Mol. Cell Cardiol.*, vol. 45, pp. 300–312, 2008.

VITA

Vita may be provided by doctoral students only. The length of the vita is preferably one page. It may include the place of birth and should be written in third person. This vita is similar to the author biography found on book jackets.